

ELECTRONIC STRUCTURE AND PHOTOCHEMISTRY OF MOLECULAR AND
CLUSTER ANIONS VIA TANDEM TIME-OF-FLIGHT MASS SPECTROSCOPY
AND PHOTOELECTRON IMAGING

by

Terefe G Habteyes

A Dissertation Submitted to the Faculty of the

DEPARTMENT OF CHEMISTRY

In Partial Fulfillment of the Requirements
For the Degree of

DOCTOR OF PHILOSOPHY

In the Graduate College

THE UNIVERSITY OF ARIZONA

2008

THE UNIVERSITY OF ARIZONA
GRADUATE COLLEGE

As members of the Dissertation Committee, we certify that we have read the dissertation prepared by Terefe G. Habteyes entitled “Electronic Structure and Photochemistry of Molecular and Cluster Anions via Tandem Time-of-Flight Mass Spectroscopy and Photoelectron Imaging” and recommend that it be accepted as fulfilling the dissertation requirement for the Degree of Doctor of Philosophy

Date: April 16, 2008
Dr. Andrei Sanov

Date: April 16, 2008
Dr. Oliver L. A. Monti

Date: April 16, 2008
Dr. Mark A. Smith

Date: April 16, 2008
Dr. Indraneel Ghosh

Date: April 16, 2008
Dr. Vicki H. Wysocki

Final approval and acceptance of this dissertation is contingent upon the candidate’s submission of the final copies of the dissertation to the Graduate College.

I hereby certify that I have read this dissertation prepared under my direction and recommend that it be accepted as fulfilling the dissertation requirement.

Date: April 16, 2008
Dissertation Director: Dr. Andrei Sanov

STATEMENT BY AUTHOR

This dissertation has been submitted in partial fulfillment of requirements for an advanced degree at the University of Arizona and is deposited in the University Library to be made available to borrowers under rules of the Library.

Brief quotations from this dissertation are allowable without special permission, provided that accurate acknowledgment of source is made. Requests for permission for extended quotation from or reproduction of this manuscript in whole or in part may be granted by the head of the major department or the Dean of the Graduate College when in his or her judgment the proposed use of the material is in the interests of scholarship. In all other instances, however, permission must be obtained from the author.

SIGNED: Terefe G Habteyes

ACKNOWLEDGEMENTS

I would like to thank my advisor Dr. Andrei Sanov for his guidance, patience and support through out my research. Andrei first inspired me in his teaching of Introduction to Quantum Mechanics that I took in my first semester. His openness, clarity and enthusiast to scientific ideas and problems have encouraged me tremendously to maintain and develop interest in physical chemistry.

I am grateful to the past and present members of the Sanov Research Group (Emily Grumbling, Dr. Richard Mabbs, Kostya Pichugin, Dr. Eric Surber and Dr. Luis Velarde) for their friendship and for the spirited scientific discussions I have had with them. I am thankful to Emily for reading some portions of the dissertation that has helped me to eliminate errors.

I would like to thank Dr. Indraneel Ghosh, Dr. Stephen G. Kukolich, Dr. Oliver L. A. Monti, Dr. Mark A. Smith, Dr. Vicki H. Wysocki and Dr. Lucy M. Ziurys for their advice and comments. I would also like to express my appreciation to Dr. W. Ron Salzman who I would take as my role model for his detailed treatment of Statistical Mechanics and Quantum Mechanics courses.

I would also like to thank all the people who work at the Machine Shop and Electronic Shop in the Chemistry Department and the University of Arizona Instrument Shop where some of the components of the research apparatus were machined. I am particularly appreciative to Lee Macomber and Edward Autz in the Chemistry Department for the friendly interaction I have had with them.

I am thankful to many people who I befriended with during my stay in Tucson, Arizona. I was lucky to share office with Dr. Christopher Mullen who became my good friend and helped me in many ways. I would especially like to thank Jon Heine who picked me from the airport and provided me a room in his house that I stayed in for two weeks until I found a place. Jon saw me for the first time at the airport but it didn't take him long to make me feel home.

I would like to acknowledge the Department of Chemistry, University of Arizona, for accepting me to the graduate program, and the Imaging Fellowship Program of the University of Arizona for providing half of my RA support for the 2004/2005 academic year.

DEDICATION

To my mother Tirunesh and my brothers Negash and Tsedeke,
who gave me unconditional love and support

To Adanech, who gave me a life of love and support

To Mahlet, who gave meaning to my life

To the memory of my father Getaneh, who was determined to make my life better than
his own and who I missed very dearly at my early age.

TABLE OF CONTENTS

LIST OF FIGURES	10
LIST OF TABLES	18
ABSTRACT.....	19
Chapter 1 INTRODUCTION	
1.1 Atomic and Molecular Clusters	21
1.2 Photochemical Processes	24
1.3 Velocity-Map Photoelectron Imaging	25
1.4 Photodissociation and Tandem Time-of-Flight Mass Spectrometry	26
Chapter 2 INSTRUMENTATION, DATA ACQUISITION AND DATA ANALYSIS	
2.1 Overview	31
2.2 Ion Source	34
2.3 Primary TOF-MS	37
2.4 Reflectron TOF-MS	40
2.5 Ion Detection	44
2.6 Velocity Map Photoelectron Imaging System	46
2.7 Vacuum Systems	51
2.8 Laser System	51
2.9 Operation	52
2.10 Photoelectron Image Analysis	53
Chapter 3 PHOTOCHEMISTRY OF CO ₂ ⁻ IN WATER CLUSTERS	
3.1 Introduction	61
3.2 Experimental	65
3.3 Experimental Results	
3.3.1 Parent Ion Mass Spectra and Overview	66
3.3.2 355 nm Results	66
3.3.3 266 nm Results	73
3.4 Potential Energy Surfaces of CO ₂ ⁻ : The Need for Diffuse Basis Sets	74
3.5 Trapping the Excess Electron in CO ₂ ⁻ by Solvent Stabilization	77
3.6 Water Binding Energy	83
3.7 OC–O ⁻ Bond Energy in Water Cluster	86
3.8 Core-Dissociation Mechanism	88
3.9 Solvent-Evaporation Mechanism	97
3.10 Hydration versus Homogeneous Solvation	98

TABLE OF CONTENTS – Continued

3.11 Summary	99
Chapter 4 DFT AND <i>AB INITIO</i> STUDIES OF CS_2^- AND $(\text{CS}_2)_2^-$	
4.1 Introduction	101
4.2 Computational Methods and Procedures	105
4.3 Results and Discussion	
4.3.1 Electronic Potential Energy Curves of CS_2 and CS_2^-	106
4.3.2 Basis Set Effects	108
4.3.3 Optimized Structures and Stability Order	110
4.3.4 Ring Opening Barrier	112
4.3.5 Feasibility of the High Energy Isomers	115
4.4 Summary	121
Chapter 5 RELAXATION OF $(\text{CS}_2)_2^-$ TO ITS GLOBAL MINIMUM MEDIATED BY WATER MOLECULES: A PHOTOELECTRON IMAGING STUDY	
5.1 Introduction	123
5.2 Experimental	125
5.3 Photoelectron Imaging Results and Analysis	
5.3.1 Homogeneous and Heterogeneous Solvation of CS_2^-	127
5.3.2 Photoelectron Imaging of $(\text{CS}_2)_2^-$: The Effect of H_2O	133
5.4 Observation of Different Electron Binding Motifs in $(\text{CS}_2)_n^-$, $n > 4$	141
5.5 Discussion	144
5.6 Summary	147
Chapter 6 PHOTODISSOCIATION OF BARE AND SOLVATED $(\text{CS}_2)_2^-$: MANIFESTATION OF ELECTRONIC ISOMER COEXISTENCE AND SOLVENT-INDUCED CORE SWITCHING	
6.1 Introduction	149
6.2 Experimental	151
6.3 Results	
6.3.1 Overview	152
6.3.2 Photodissociation of Bare and Hydrated CS_2^-	153
6.3.3 Photofragmentation of $(\text{CS}_2)_n^-$ and $(\text{CS}_2)_2^-(\text{H}_2\text{O})_m$ Cluster Anions	153
6.3.4 The Effect of Water in the Ion Source.....	158
6.4 Discussion	
6.4.1 The Dissociation Channels of $\text{CS}_2^-(\text{H}_2\text{O})_m$	159
6.4.2 The Dissociation Channels $(\text{CS}_2)_2^-$	161
6.4.3 Fragment Origin and Mechanisms	
6.4.3.1 The S^- and CS_3^- Products	163

TABLE OF CONTENTS – Continued

6.4.3.2	The CS_2^- Product	165
6.4.3.3	The C_2S_2^- and S_2^- Products	166
6.4.4	Channel Switching versus $(\text{CS}_2)_2^-$ Electronic Isomer Coexistence.....	167
6.5	Summary	168
Chapter 7	OBSERVATION OF NOVEL ANIONS: PHOTOELECTRON IMAGING AND PHOTODISSOCIATION OF $\text{CS}_2 + \text{O}_2 + e^-$ REACTION PRODUCTS	
7.1	Introduction	170
7.2	Ion Formation Procedure	173
7.3	$\text{CS}_2^- \cdot \text{O}_2$ Ion-Neutral Complex	174
7.4	Anionic Products of $\text{CS}_2\text{-O}_2\text{-}e^-$ Reaction	
7.4.1	Overview	178
7.4.2	Low Mass Ions ($m/z < 90$)	180
7.4.3	Exotic and Novel Anion Formation	
7.4.3.1	$[\text{CS}_2\text{O}_2]^-$ versus CS_3^- (mass 108)	188
7.4.3.2	CS_3O^- (mass 124)	198
7.5	Photodissociation Pathways	202
7.6	Summary	205
Chapter 8	FUTURE DIRECTION	
8.1	Broader Perspective	207
8.2	Time-Resolved Photoelectron Imaging of CO_3^-	
8.2.1	Background	209
8.2.2	CO_3^- Ion Formation	211
8.2.3	Photodissociation of CO_3^- and Fragment Photodetachment	214
8.2.4	Laser Setup and the Choice of Pump-Probe Wave Lengths	214
8.3	Photoelectron Imaging of Fragment Ions at Infinite Time-Delay	219
8.4	Summary	222
Appendix A	ELIMINATION OF NOISE FROM PHOTOELECTRON IMAGES USING DIGITAL FILTERS	
A-1	Designing Two Dimensional Filters	224
A-2	Filter Implementation	230
A-3	Symmetrization of Photoelectron Image	236
A-4	Matlab Programs Used in the Image Analysis	236
REFERENCES	241

LIST OF FIGURES

- 1.1 Examples of different types of clusters: (a) metal cluster, (b) semiconductor cluster, (c) cluster cation, (d), (e) and (f) are examples of cluster anions. For $(\text{H}_2\text{O})_6^-$ and $\text{CO}_2^-(\text{H}_2\text{O})_6$, the orbital contour plots are shown in (d) and (f), respectively.23
- 1.2 Schematic illustrations of different possible dissociation routes of excited states. (a) An electronic transition takes place to a repulsive excited state where dissociation occurs directly. (b) A transition to a bound state. Through radiationless transition, the excited state population is transferred to a repulsive state where dissociation takes place. (c) A transition to a resonance (quasi-bound) state. The excited state decays either by tunneling or by internal vibrational energy redistribution. (d) The dissociation occurs in the ground electronic state following radiationless transfer from the bound excited state.28
- 2.1 Technical drawing of the outside view of the tandem time-of-flight mass spectrometer combined with photoelectron imaging assembly. The flanges where the diffusion and turbo pumps are connected are denoted as DP and TP, respectively. GV \equiv Gate Valve. CCD camera is not shown in this drawing.32
- 2.2 Technical drawing of the inside view of the tandem time-of-flight mass spectrometer combined with photoelectron imaging assembly.33
- 2.3 Simulation of fragment ion trajectories inside the reflectron field using Simion 7.0 for the parent ion of mass 404. The masses of the fragments are shown at the corresponding turning points. Only portion of the reflectron assembly is shown to magnify the trajectories.42
- 2.4 Schematics of circuit diagram showing the voltage application to the microchannel plate (MCP) and the parent and fragment ions mass spectra acquisition procedures. V_i , V_o and V_a are the voltages applied at the first MCP input, second MCP output and anode plate, respectively. $V_a \approx V_{in}$ (high voltage input), $V_o \approx V_{in} - 200$ V and $V_i \approx 0.36 (V_{in} - 200$ V).45
- 2.5 Photoelectron trajectory simulation using Simion 7.0 for parent ion photodetachment. The imaging assembly consists of four electrodes labeled as 1, 2, 3 and 4. The first three are used in the photoelectron imaging of parent ions. Electrode 4 is intended to be a repeller plate for fragment ion photoelectron imaging. The circle indicates the interaction spot of the parent ion and the laser beam. In the parent ion photoelectron imaging electrodes 2 and 4 are referenced to ground. The velocity mapping is achieved by varying the extraction-to-repeller voltage ($R = V_E/V_R$) ratio.48

LIST OF FIGURES – Continued

- 2.6 Schematics of voltage application to imaging detector and image acquisition procedures. V_i and V_o are the voltages applied to the input of the first and to the output of the second microchannel plates, respectively. $V_i \approx 2$ kV. $V_o \approx 3$ kV DC + 1kV pulse. Typically, 6.5 kV is applied to the phosphor screen.50
- 2.7 (a) Photoelectron image of CS_2^- acquired at 266 nm. (b) Inverse Abel transform of the image. (c) Photoelectron spectrum extracted from the image. The arrows indicate the correlation of the rings in the inverted image with the peaks in the spectrum.54
- 2.8 Photoelectron images of O^- , S^- and I^- acquired at 532, 355 and 266 nm. The raw and Abel inverted image at each wavelength are given at top and bottom, respectively.56
- 2.9 Photoelectron spectra of O^- , S^- and I^- extracted from the images displayed in Fig. 2.8.57
- 2.10 Examples of photodetachment transitions with perpendicular (a), isotropic (b) and parallel (c) photoelectron angular distribution. The 355 nm image of O^- shown (b) is the central transition band in Fig. 2.8 (the outer ring is cropped). The open circles in the plot are experimental data points. The solid lines are obtained by fitting $I(\theta) = (\sigma/4\pi)[1 + 0.5\beta(3\cos^2\theta - 1)]$ to the data. The values of the best fit anisotropy parameter (β) are shown on the corresponding plots.58
- 3.1 (a) Photoelectron images of $\text{CO}_2^-(\text{H}_2\text{O})_m$, $m = 2-6$, acquired at 400 nm. (b) Photoelectron images of $\text{CO}_2^-(\text{H}_2\text{O})_m$, $m = 4-6$, acquired at 266 nm. (c) Photoelectron images of $(\text{CO}_2)_m$, $m = 2-12$, acquired at 400 nm. The double headed arrow indicates the laser polarization direction.63
- 3.2 Parent ion mass-spectra of $\text{CO}_2^-(\text{H}_2\text{O})_m$ optimized for high mass (top) and low mass (bottom) ions.68
- 3.3 Photofragment-ion mass-spectra for the $\text{CO}_2^-(\text{H}_2\text{O})_m$ cluster anions at 355 nm. The numbers on the right and on the left indicate the number of water molecules, m , in the parent clusters. For clarity, the peaks assigned to the core-dissociation fragments, $\text{O}^- \cdot \text{W}_{m-k}$, are shown against the gray background. $\text{W} \equiv \text{H}_2\text{O}$69
- 3.4 Photofragment-ion mass-spectra for the $\text{CO}_2^-(\text{H}_2\text{O})_m$ cluster anions at 266 nm. The numbers on the right and on the left indicate the number of water molecules, m , in the parent clusters. For clarity, the peaks assigned to the core-dissociation fragments, $\text{O}^- \cdot \text{W}_{m-k}$, are shown against the gray background. $\text{W} \equiv \text{H}_2\text{O}$70

LIST OF FIGURES - Continued

- 3.5 Fractions of the $\text{O}^-(\text{H}_2\text{O})_{m-k}$ and $\text{CO}_2^-(\text{H}_2\text{O})_{m-k}$ products observed in the photofragmentation of $\text{CO}_2^-(\text{H}_2\text{O})_m$ at 355 nm (open circles) and 266 nm (solid circles), plotted as functions of the parent cluster size.71
- 3.6 Average numbers of water molecules evaporated in the core-dissociation and solvent-evaporation channels at 355 and 266 nm, as labeled. The dotted horizontal lines indicate the asymptotic values of $\langle k \rangle$ for each process.72
- 3.7 Potential energy curves of CO_2^-75
- 3.8 Calculated global minimum structures of $\text{CO}_2(\text{H}_2\text{O})_m$ neutral, $\text{CO}_2^-(\text{H}_2\text{O})_m$ anion and $\text{O}^-(\text{H}_2\text{O})_m$ anion. The structures are optimized using MP2/6-311++G** level of theory. For $\text{CO}_2^-(\text{H}_2\text{O})_m$, $m = 2$, two structures, labeled as 2-I and 2-II, are obtained with small energy difference: 2-II is ~ 0.02 eV higher in energy.78
- 3.9 The OCO bending angle dependence of the relative potential energies of $\text{CO}_2^-(\text{H}_2\text{O})_m$ versus $\text{CO}_2(\text{H}_2\text{O})_m$, $m = 0, 1, 2$ and 3, calculated using the *ab initio* and density-functional methods, as described in the text.79
- 3.10 Calculated enthalpy of evaporation (ΔH) of one water molecule as a function of $\text{CO}_2^-(\text{H}_2\text{O})_m$ cluster size: $\text{CO}_2^-(\text{H}_2\text{O})_m \rightarrow \text{CO}_2^-(\text{H}_2\text{O})_{m-1} + \text{H}_2\text{O}$, $\Delta H(m)$. The open and solid circles represent the values obtained using the B3LYP/6-311++G(3df,3pd) and MP2/6-311++G(3df,3pd) methods, respectively. The solid horizontal line indicates the asymptotic limit of $\Delta H(m)$ determined in the present experiments.85
- 3.11 A water molecule binding energy difference ($\Delta H' - \Delta H$) as a function of solvent cluster size, m . $\Delta H(m)$ and $\Delta H'(m)$ are defined in reaction equations (3.4a) and (3.4b), respectively. The energy is determined using MP2 method with aug-cc-pVTZ basis set.87
- 3.12 Optimized potential energy curves of the ground and first excited states for CO_2^- . The energy is calculated using MP2/6-311+G(3df) scanning one of the C-O distance while optimizing the other. The OCO angle is fixed at 138 degree (calculated equilibrium angle) throughout the calculations. The curve shown in dotted line is for the neutral state.95

LIST OF FIGURES - Continued

- 3.13 Schematics of potential energy curves for $\text{CO}_2^-(\text{H}_2\text{O})_m$, $m = 0, 1$ and 2 as functions of the OCO bending angle (a) and the OC–O bond length (b). The curves in (b) are generated at fixed equilibrium OCO angles. The vertical dotted lines in indicate the equilibrium OCO angle in (a) and equilibrium bond distance in (b).96
- 4.1 The electronic potential energy curves of CS_2 and its anion in C_{2v} symmetry as a function of SCS bending angle. The C–S distances are optimized at fixed angles using MP2/6-311+G(3df) followed by single point energy calculation at CCSD(T)/aug-cc-pVTZ.107
- 4.2 Basis set effect on the relative energy of two most stable $(\text{CS}_2)_2^-$ structures. The energy difference is obtained by subtracting the total energy of D_{2h} (${}^2B_{3g}$) structure from that of C_{2v} (2B_1) without including zero point energy. The region where the C_{2v} (2B_1) structure is more stable is shown against partially shaded background.109
- 4.3 Stable structures of $(\text{CS}_2)_2^-$ optimized using MP2 and B3LYP with aug-cc-pVTZ basis set. Bond lengths are in angstroms and bond angles are in degrees. The vertical detachment energy (VDE) is calculated using B3LYP/aug-cc-pVTZ and CCSD(T)/6-311+G(3df). The bond lengths, bond angles and VDEs obtained from B3LYP are provided in parenthesis.111
- 4.4 Potential energy curves of the C_{2v} (2B_1) and D_{2h} (${}^2B_{3g}$) calculated using B3LYP/6-311+G(3df) as a function of SCC angle (Θ) indicated on the structures. Constrained to the corresponding symmetries, all degrees of freedom are optimized at the fixed angles with 2 degree steps.113
- 4.5 Potential energy surface of the C_{2v} (2B_1) state as functions of SCC angle (Θ) and C–S distance (R) indicated on the structure. The energy calculation is performed using B3LYP/6-31+G(d) scanning Θ and R while optimizing all other degrees of freedom constrained to the C_{2v} symmetry.114
- 4.6 Potential energy curves of D_{2d} (2A_1) and D_{2h-3} (2A_g) states of $(\text{CS}_2)_2^-$ as a function of C–C distance. At fixed C–C separations all other molecular parameters are optimized constrained to the corresponding symmetries.117

LIST OF FIGURES - Continued

- 4.7 Potential energy curves of $D_{2d} (^2A_1)/D_2 (^2A)$ and $D_{2h-3} (^2A_g)/D_2 (^2A)$ states of $(CS_2)_2^-$ as a function of SCCS dihedral angle (Θ_D) calculated using the theory levels indicated on the figure. At fixed Θ_D all other molecular parameters are optimized. At $\Theta_D = 0$ and 180 degrees the anion has D_{2h} symmetry, and at $\Theta_D = 90$ and -90 degrees it has D_{2d} symmetry. At all other Θ_D it has D_2 symmetry, and as a result both A_1 and A_g states transform as 2A118
- 4.8 Highest occupied molecular orbital (HOMO) of the most viable structure of $(CS_2)_2^-$ dimer anion. The orbital surfaces are generated using SCF with aug-cc-pVTZ basis set. The HOMO of $(CO_2)_2^- [D_{2d}(^2A_1)]$ is included for comparison with the analogous structure of $(CS_2)_2^-$120
- 5.1 Representative mass spectra acquired under (a) dry and (b) wet source conditions, respectively.126
- 5.2 Photoelectron images of isolated and solvated CS_2^- acquired at 355 nm. The laser polarization is always vertical in the image plane. The results for the homogeneous solvation in (a) and heterogeneous solvation in (b) and (c) are presented together for comparison. In all cases, the $X^1A_1(^1\Sigma_g^+) \leftarrow X^2A_1$ transition band (band I) shifts to higher eBE, consistent with solvation energetics. Band II, which appears in $(CS_2)_n^-$, but not in $CS_2^-(CO_2)_m$ and $CS_2^-(H_2O)_m$, is assigned to a covalent dimer-anion structure. The $a^3B_2 \leftarrow X^2A_1$ transition band (band III) disappears upon the first addition of either CO_2 or H_2O . Since the solvation strength of CS_2 is slightly higher than CO_2 , band III must also disappear upon the addition of the first CS_2 solvent. Band IV is due to autodetachment from covalent structures.129
- 5.3 Vertical detachment energy corresponding to band I (see Fig. 5.2) as a function of the number of solvent molecules.130
- 5.4 (a) The 355 nm photoelectron spectra of $(CS_2)_n^-$, in comparison with (b) that of $(CS_2)_2^-(H_2O)_m$. The photoelectron spectrum extracted from the 266 nm image of $(CS_2)_2^-$ anion is included as a reference (shown as a red dotted line). As in Fig. 5.2 band I and II arise from direct photodetachment from $CS_2^- \cdot CS_2$ ion-neutral complex and $C_2S_4^-$ covalent structures, respectively. Band IV is due to autodetachment of covalent structures. Band II disappears almost completely when either CS_2 or H_2O solvent molecule is added to the dimer anion. The relative intensity differences of band I and II when the dimer anion is formed under (a) dry and (b) wet source conditions are clearly seen in the magnified spectra (shown in dotted lines) for $n = 2$ and $m = 0$131

LIST OF FIGURES - Continued

- 5.5 The 266 nm photoelectron images and the corresponding photoelectron spectra of $(\text{CS}_2)_2^-$ formed under (a) dry source condition, and (b) wet source condition. Also shown are the magnified portions of the spectra in the electron binding energy range of 0.5–3.5 eV. The photoelectron spectrum of CS_2^- extracted from 266 nm image is included (shown as dotted line) for reference.134
- 5.6 Photoelectron spectra of $(\text{CS}_2)_2^-$ and solvated CS_2^- extracted from 266 nm photoelectron images. The dotted line curve in (b)-(d) is shifted $\text{CS}_2^- \cdot \text{CO}_2$ spectrum from (a).137
- 5.7 Observation of a new photodetachment transition band for $(\text{CS}_2)_n^-$, $n > 4$. The new band is labeled as *S*.142
- 6.1 The 355 nm and 266 nm photofragment mass-spectra for the $\text{CS}_2^-(\text{H}_2\text{O})_m$ parent ions.154
- 6.2 The photofragment mass-spectra for (a) $(\text{CS}_2)_n^-$, $n = 2-4$ parent ions and (b) the $(\text{CS}_2)_2^-(\text{H}_2\text{O})_m$, $m = 0-2$ parent ions. The parent anions in (a) and (b) are formed under dry and wet source conditions, respectively.151
- 6.3 The $(\text{C}_2\text{S}_2^- + \text{S}_2^-)/\text{CS}_2^-$ product ratio for the $(\text{CS}_2)_n^-$, $n = 2-4$ and $(\text{CS}_2)_2^-(\text{H}_2\text{O})_m$, $m = 0-2$ parent ions, formed under the dry and wet source conditions, respectively.155
- 6.4 Energy diagram showing the correlations between the proposed reactant structures, intermediates and products for the bare $(\text{CS}_2)_2^-$ parent ion. The relative parent and product-channel energies are from the CCSD(T)/6-311+G(3df) calculations. The product channel correlations for the $\text{CS}_2^- \cdot \text{CS}_2$ ion-molecule complex and the D_{2d} (2A_1) structure are indicated by dashed lines, while those for the C_{2v} (2B_1) and D_{2h} ($^2B_{3g}$) isomers are indicated by solid lines.160
- 7.1 $\text{CS}_2\text{-O}_2$ reaction product temporal profile.172
- 7.2 Photoelectron images of mass selected $\text{CS}_2^-(\text{O}_2)_m$ ions acquired at 355 nm.175
- 7.3 Vertical detachment energies (VDEs) extracted from the 355 nm lowest binding energy photodetachment transition band of $\text{CS}_2^-(\text{M})_m$, $\text{M} \equiv \text{H}_2\text{O}, \text{O}_2, \text{CO}_2$. A quarter of the full width at half maximum is shown as an error bar.176

LIST OF FIGURES – Continued

- 7.4 Parent ion mass spectra. The anions are formed by supersonic expansion of 10% O₂ in argon (total pressure = 40 psi) over CS₂ liquid sample.179
- 7.5 Photoelectron images/spectra of m/z 32, 48, 64 and 80 formed by CS₂/O₂/Ar mixture expansion. The images are acquired at 532 nm.181
- 7.6 Dependence of anisotropy parameter (β) on kinetic energy. CZ is short for Cooper-Zare and l is effective angular momentum quantum number.182
- 7.7 Photoelectron images of S₂O⁻ acquired at 532, 355 and 266 nm. The 266 nm Abel inverted image is shown to the right side of the raw image showing the anisotropy parameter for each transition band.186
- 7.8 The 355 nm photoelectron images of [CS₂O₂]⁻ formed by expanding 10% O₂/Ar over CS₂ liquid sample. The image for isolated S⁻ is included for comparison with the S⁻ fragment image. A shaded bar is included in the spectra to show the energy matching between the isolated and fragment S⁻ bands. The variations of the transition patterns in the images shown in (a)-(c) is due to the change in the isomer populations distribution depending on source conditions.189
- 7.9 Photofragment ion mass spectra of m/z 108 and 140 ions excited at 355 nm laser radiation. LIS is short for laser independent signal.191
- 7.10 Photoelectron images/spectra of anions with m/z 108 and 140 acquired at 266 nm. In (a), the spectra shown in dotted and solid represent two extreme cases indicating the dominance and absence, respectively, of CS₂⁻·O₂ ion neutral complex in the ion beam as a result of existence of other competing isomer presumably CS₂O₂⁻ covalent structure.194
- 7.11 Optimized structures and SCF singly occupied molecular orbitals of [CS₂O₂]⁻. The optimization is performed using MP2/6-311+G(3df). For comparison the optimized structures of CS₂, CS₂⁻, O₂ and O₂⁻ are included. The SCF orbitals are generated using aug-cc-pVTZ basis set. Bond lengths are in angstrom and bond angles are in degrees. The vertical detachment energies are calculated using CCSD(T)/6-311+G(3df)//MP2/6-311+G(3df) and B3LYP/aug-cc-pVTZ.195
- 7.12 (a) Photoelectron image and spectra of CS₃O⁻ ion acquired at 266 nm. In the spectrum the open circles are the experimental data points; the dotted lines are Gaussian function fits to band I and II separately; and the solid line that fits the over all spectrum is the sum of the two Gaussian functions. (b) 355 nm fragment ions mass spectra for the CS₃O⁻ parent ions.200

LIST OF FIGURES - Continued

- 7.13 Optimized structures of CS_3O^- . Geometries are optimized using MP2/6-311+G(3df). The sum of the energies of separated $\text{SO}^- +$ and CS_2 is used as the origin.201
- 8.1 Reaction coordinate model of the CO_3^- ion proposed by Snodgrass et al. It is assumed that the D_{3h} symmetry lowers to C_{2v} as dissociation begins. The cross hatched region indicates the photon energy range covered in the experiment of ref. The circle indicates a conical intersection (avoided crossing) between $1\ ^2\text{B}_2$ and $2\ ^2\text{B}_2$ states.210
- 8.2 The top panel is the parent ion mass spectra obtained during supersonic expansion of a mixture of CS_2 vapor and $\sim 10\%$ O_2 in CO_2 . The lower panel shows the O^- fragment signal during the photodissociation of CO_3^- at 532 and 355 nm.212
- 8.3 Photoelectron image of O^- fragment at 355 nm. Both the dissociation and fragment photodetachment processes occur in a 355 nm laser pulse due to the long pulse width of the laser pulse output (~ 7 ns).213
- 8.4 Femtosecond laser setup for pump-probe experiment. The 400 nm laser pulse initiates the dissociation process and the reaction coordinate is sampled at different time delays probing with the 800 nm laser pulse. The progress of the reaction can be followed by photoelectron imaging of the excited complex and the O^- dissociation product.217
- 8.5 Photoelectron image of isolated O^- acquired at 800 nm using the femtosecond laser for a reference.218
- 8.6 Photoelectron imaging of fragment anions. The first laser pulse (Laser I) causes photofragmentation and the photofragments are separated in time and space according to their mass by the reflectron field. The second laser pulse (Laser II) is used to detach electron from the mass selected fragment ion. The detached electrons are accelerated towards the imaging detector.220
- 8.7 Simion trajectory simulation result for fragment ion photoelectron imaging. The focusing is achieved by varying electrode 1 to electrode 4 voltage ratio while referencing electrodes 2 and 3 to ground (G). When the hole in electrode 3 is open, the optimum ratio obtained from the simulation is 3.275, but when the hole is covered by a wire mesh the ratio is 1.725.221

LIST TABLES

3.1	Vertical detachment energies (VDE) of $\text{CO}_2^-(\text{H}_2\text{O})_m$, $m = 0-5$ calculated as described in the text using the MP2 and B3LYP methods with the aug-cc-pVTZ basis set, compared to the experimentally determined values.	82
4.1	Comparison of molecular properties of CO_2 and CS_2 molecules.	102
5.1	Solvation-induced shifts of the CS_2^- photodetachment bands.	138
7.1	Bimolecular reactions and rate constants for $\text{CS}_2\text{-O}_2$ system.	171

ABSTRACT

Molecular and cluster anions have been investigated using a newly built tandem time-of-flight mass spectrometer combined with photoelectron imaging system. Solvation particularly hydration is shown not only to stabilize metastable anions such as CO_2^- in their ground state and impede autodetachment but also to alter the dynamics in the excited states. For instance, the 355 nm photoelectron image of mass-selected $\text{CO}_2^-(\text{H}_2\text{O})_m$ evolves from anisotropic to isotropic as m increases indicating excited state decay via electron autodetachment. Dissociation channels open at $m=2$ at 266 nm, resulting in $\text{O}^-(\text{H}_2\text{O})_{m-k}$ and $\text{CO}_2^-(\text{H}_2\text{O})_{m-k}$ products, the later becoming dominant as m increases.

The photoelectron imaging of $(\text{CS}_2)_2^-$ has revealed the coexistence of four electronic isomers: $\text{CS}_2^- \cdot \text{CS}_2$ [$C_s(^2A')$] and three covalent C_2S_4^- [$C_{2v}(^2B_1)$, $D_{2h}(^2B_{3g})$, and $D_{2d}(^2A_1)$] structures. Water-mediated intermolecular interactions have been shown to facilitate the formation of the global minimum $C_{2v}(^2B_1)$ structure rather than the less stable local minima $C_s(^2A')$ and $D_{2d}(^2A_1)$ structures that are favored in the dry source condition. In the $(\text{CS}_2)_n^-$, $n \geq 3$ and $(\text{CS}_2)_2^-(\text{H}_2\text{O})_m$, $m > 0$ clusters, the population of the $C_{2v}(^2B_1)$ structure diminishes drastically due to more favorable solvent interactions with the CS_2^- monomer-core. Photoexcitation of the $(\text{CS}_2)_2^-$ also results in the formation of CS_2^- and C_2S_2^- at 532 nm, and C_2S_2^- , CS_2^- , CS_3^- , S_2^- , and S^- at 355 and 266 nm. The relative yields of C_2S_2^- is significantly higher when $(\text{CS}_2)_2^-$ is formed under wet source condition suggesting $C_{2v}(^2B_1)$ structure as the origin of C_2S_2^- . An abrupt decrease in the relative

yield of $C_2S_2^-$ is observed upon adding CS_2 or H_2O to $(CS_2)_2^-$. The CS_2^- based clusters are the likely origin of the S^- photoproduct, while CS_3^- is formed through the secondary S^-+CS_2 reaction.

Novel anions ($CS_2O_2^-$ and CS_3O^-) are observed in the $CS_2+O_2+e^-$ reaction. The photoelectron imaging and photodissociation results of these and other anionic products are presented. In addition, $CS_2^- \cdot O_2$ ion-neutral complex is formed depending on the conditions in the ion source. Despite the positive electron affinity of O_2 , no clear signature of $O_2^- \cdot CS_2$ ion-neutral complex is seen in the photoelectron image. CO_3^- ion is also formed abundantly as a result of $CS_2+CO_2+O_2+e^-$ reaction.

Chapter 1

INTRODUCTION

1.1 Atomic and Molecular Clusters

Although the concept of clusters in chemistry and physics is quite broad, atomic and molecular clusters can be thought of as aggregates of atoms or molecules bound together by different kinds of forces. The numbers of particles contained in the aggregate ranges from two to millions. Clusters are nanoparticles or even sub-nanoparticles, serving as intermediates between atoms/molecules and condensed matter. By measuring the chemical and physical properties of clusters as a function of size, one can infer the development of bulk properties starting from a single particle.

Conceptually, clusters have been around since the beginning of modern chemistry. Robert Boyle, the founder of modern chemistry, referred to clusters in his book *'Sceptical Chymist'* in 1661 saying *'...associated into minute masses or clusters.'*¹ The observation of clusters can be dated back to Faraday's times. What Faraday referred to as *'aggregates'* of *'proportionate size'* in his 1857 lecture are known as clusters today.² However, it was only after the 1950's that cluster science developed to its modern form after the advent of supersonic expansion sources.^{3,4} Cationic clusters of carbon dioxide, $(\text{CO}_2)_n^+$, $n = 2-23$, were observed in the mass spectrometry experiment in 1961.⁵ Around the same years, in the late 1950's and early 1960's, metal clusters were synthesized^{6,7} after which the word cluster as applied to chemistry became widespread. Review

articles^{8,9} and books^{10,11} that deals with cluster science are available for interested readers.

Examples of different types of clusters are shown in Fig. 1.1 for illustration. Despite their differences, all the clusters shown in the figure have common characteristics in that they all have defined coordination numbers, unlike bulk materials. Cobalt tetracarbonyl⁶, Fig. 1.1(a), is an example of metal cluster where constituent moieties are connected by metal-metal and metal-ligand bonds. Fullerene (C₆₀)^{12,13}, seen in Fig. 1.1(b), is an example for a semiconductor atomic cluster where the carbon atoms are connected by directional covalent bonds.

Neutral, cationic and anionic water clusters are well known examples of molecular clusters. The addition of the H₃O⁺ ion to the neutral water cluster to form H₃O⁺(H₂O)₂₀¹⁴, Fig. 1.1(c), is reminiscent of the hydronium ion hydration in aqueous solution. Although a water molecule has negative electron affinity, water cluster anions, (H₂O)_n⁻, $n \geq 2$, are known to form in the gas phase.^{15,16} An example is provided in Fig. 1.1(d) for six water molecules showing the contours of orbital for the surface bound excess electron.¹⁷ The excess electron binding motifs (surface versus cavity bound) as the cluster size increases has long been the subject of intellectual debate.¹⁸⁻²⁵ Doping the water cluster with a guest molecule (e.g. CS₂, CO₂, OCS) localizes the excess electron on the solute molecule.²⁶ An example is shown in Fig. 1.1(e) for CO₂.

Our research deals with the photodetachment and photofragmentation of molecular and cluster anions similar to the one shown in Fig. 1.1(e). In this type of cluster anions the

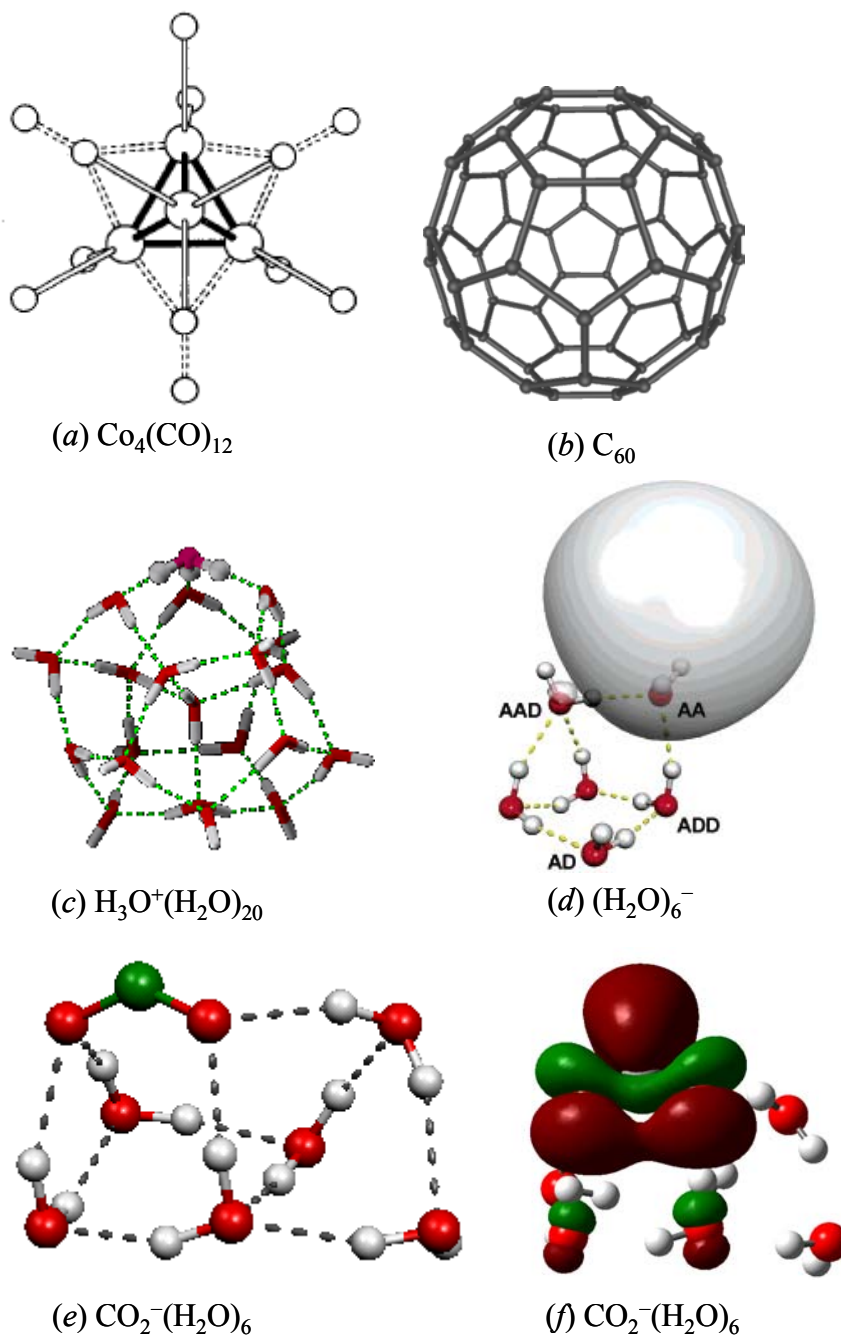


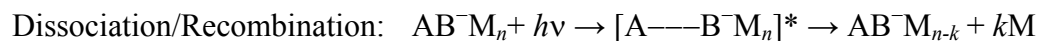
Figure 1.1 Examples of different types of clusters: (a) metal cluster (ref. ⁶), (b) semiconductor cluster (ref. ¹³), (c) cluster cation (ref. ¹⁴), (d), from ref. ¹⁷, (e) and (f) are examples of cluster anions. For $(\text{H}_2\text{O})_6^-$ and $\text{CO}_2^-(\text{H}_2\text{O})_6$, the orbital contour plots are shown in (d) and (f), respectively.

excess electron primarily reside on a cluster-core [e.g. CO_2^- is the cluster-core for $\text{CO}_2^-(\text{H}_2\text{O})_6$]. In the study of chemical dynamics, anions are convenient systems for two main reasons: (1) as they are charged, they can be separated according to their mass using time-of-flight mass spectrometer, and (2) the valence electronic structure and the fundamental chemical dynamics can be initiated by the excitation/detachment of the excess electron using commercially available laser systems. A pulsed laser light can be tuned in time to intersect mass selected cluster anion and the evolution of the cluster properties can be followed as a function of cluster size.

1.2 Photochemical Processes

Depending on the photon energy and transition probability, the interaction between the laser light and the cluster anions can result in different photochemical processes. Direct photodetachment and photodissociation are the straightforward outcomes. In the presence of solvent molecules, the dissociating species can recombine due to the solvent caging effect.²⁷⁻³¹ The photoabsorption can also create transient excited states that are prone to autodetachment.³² In addition, some anions can undergo dissociative photodetachment where the photodetachment and photodissociation take place simultaneously.^{33,34} The following photochemical reaction equations summarize the photoinduced chemical processes considering an arbitrary anion AB^- and a molecule M.





Where n and k are integer numbers indicating the number of solvent molecule M. Various techniques can be applied to study these photochemical processes. In this research we employ velocity-map photoelectron imaging and photofragmentation spectroscopies to investigate the electronic structures and photofragmentation dynamics of isolated and solvated anions. A Brief background of each technique is presented below.

1.3 Velocity-Map Photoelectron Imaging

Imaging of charged particles that result from interaction of linearly polarized light and molecular beams is a powerful spectroscopic technique providing both the kinetic energy and angular distribution of the photoproducts in a single measurement. The imaging technique was introduced in 1987 by Chandler and Houston³⁵ who applied it to study the state-selected photodissociation products of CH₃I detected by multiphoton ionization of the CH₃ fragment. In their experiment they used Wiley and McLaren time-of-flight technique, where grid electrodes were used, to accelerate the expanding ion cloud to a two dimensional detector. When the 3D ion distribution is projected on the 2D detector, the position at which the ions strike the detector is sensitive to the recoil velocity of the fragments.

The original imaging technique of Chandler and Houston yields images that are subject to spatial blurring due to the finite size of the laser-molecule interaction region. In 1997, Eppink and Parker improved the technique by introducing an electrostatic lens that consists of three electrode plates with no wire mesh on center holes of the extraction plates.³⁶ In the improved setup, by varying the ratio of the potential applied to the extraction and the repeller electrodes, charged particles with the same initial velocity vector can be mapped on the same point on the detector regardless of their initial spatial distribution. The technique of velocity-map imaging has been widely used since then.

The imaging technique was first applied to the study of photodissociation of neutral molecules ionizing the neutral photofragments via resonance-enhanced multiphoton ionization.^{35,37-40} The technique was adapted to the study of photodetachment of electrons from neutral molecules enabling simultaneous measurement of the kinetic energy and angular distribution of the photoelectrons.⁴¹⁻⁴⁷ For anions, photoelectron imaging was first applied to W_n^- and C_n^- clusters by Baguenard et al.^{48,49} to CS_2^- and $OCS^-(H_2O)_{1,2}$ by Surber and Sanov.⁵⁰ The application of imaging in chemical dynamics is growing in all aspects including fragment ion imaging⁵¹⁻⁵⁴, and photoelectron imaging of both neutral⁵⁵⁻⁶³ and anion⁶⁴⁻⁷² systems.

1.4 Photodissociation and Tandem Time-of-Flight Mass spectrometry

Photodissociation in general is an important molecular process relevant to atmospheric chemistry. It is important in fundamental understanding of photophysical and photochemical molecular properties. Photodissociation is the central part of

photochemistry. It provides excellent opportunity to investigate the molecular dynamics of different chemical systems. The study of photodissociation combines the principle of molecular spectroscopy, which is primarily focused on the absorption spectrum, and molecular scattering, which is focused on fragmentation of excited states. Understanding dissociation dynamics requires determining the initial electronic transition and the possible couplings between the nuclear and electronic motions. In polyatomic systems (such as cluster anions), there are several vibrational degrees of freedom that makes the dynamics interesting but challenging. Supporting the interpretation of experimental results with theoretical modeling valuable information can be obtained about the structure of the parent anions, potential energy surfaces and the dissociation mechanisms.

Photodissociation can be classified into different types depending on the dynamics involved between the initiation and product formation. The simplest type is a direct dissociation where the excited complex dissociates rapidly on a single repulsive electronic state potential energy surface. In most of the cases, however, dissociation proceeds through indirect processes where more than one electronic state is involved in the dissociation process. Schematics of potential energy surfaces that illustrate the different possibilities following photoexcitation are shown in Fig. 1.2.

In Fig. 1.2(a), the photon promotes the molecule from the ground state to a repulsive electronic potential energy surface where direct dissociation occurs as in the dissociation of water molecule into $\text{H} + \text{OH}$.⁷³ The photon energy in excess of the bond energy will be available as translational and internal energy (rotational, vibrational and electronic energy).

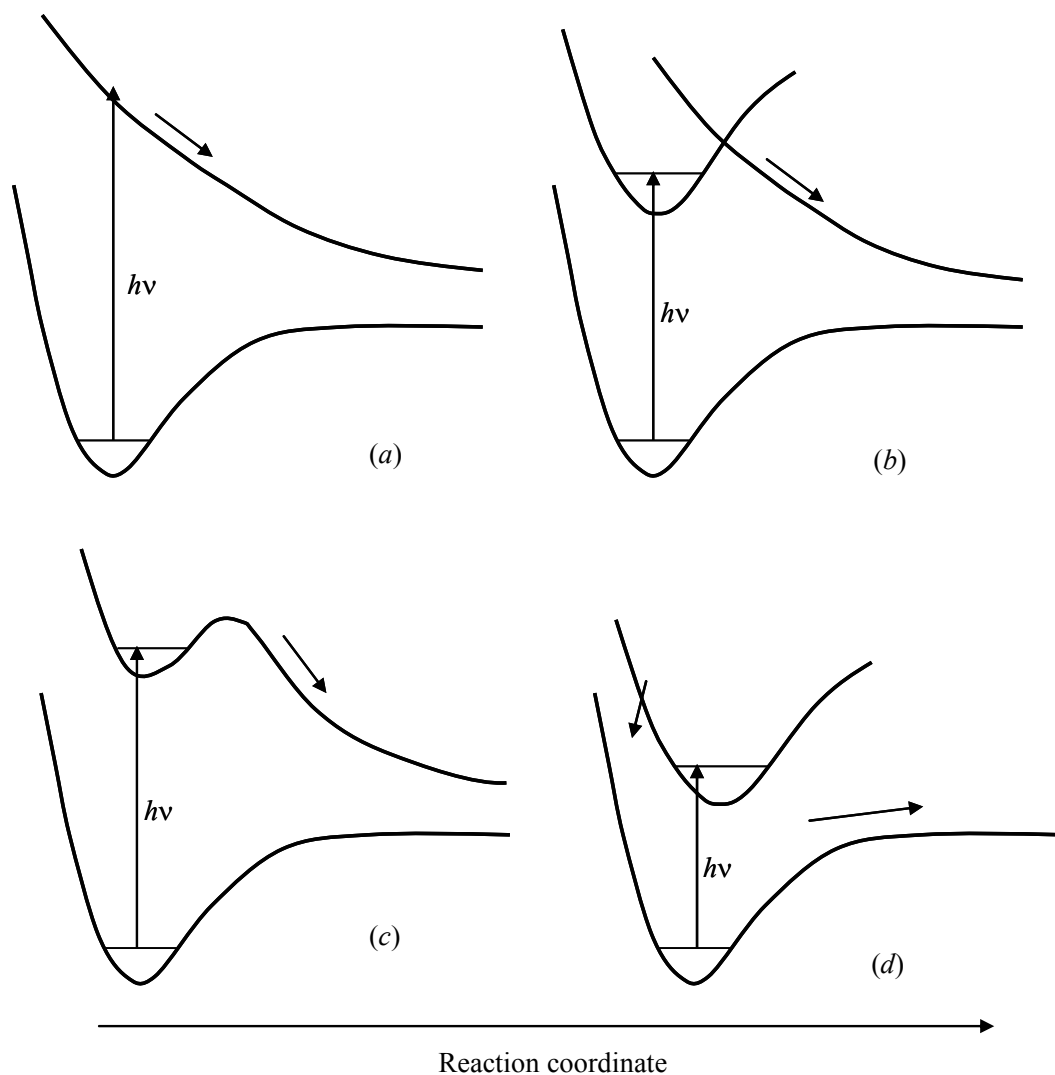


Figure 1.2 Schematic illustrations of different possible dissociation routes of excited states. (a) An electronic transition takes place to a repulsive excited state where dissociation occurs directly. (b) A transition to a bound state. Through radiationless transition, the excited state population is transferred to a repulsive state where dissociation takes place. (c) A transition to a resonance (quasi-bound) state. The excited state decays either by tunneling or by internal vibrational energy redistribution. (d) The dissociation occurs in the ground electronic state following radiationless transfer from the bound excited state.

$$E_{\text{excess}} = E_{\text{photon}} - D_0 = E_{\text{trans}} + E_{\text{int}}$$

Figures 1.2(b)-(d) illustrate different types of indirect photodissociations. In Fig. 1.2(b) the original excitation is to a bound state. The dissociation proceeds via electronic predissociation. That is, the dissociation process is mediated by the coupling between the initial bound excited electronic state and a repulsive electronic state which results in radiationless transition from the former to the later. The H₂S photodissociation^{74,75} is an illustrative example for this type of process. In Fig. 1.2(c) the photon excites the molecule to a *resonance* state where the wave packet decays by tunneling through the barrier or by internal vibrational redistribution as in the photodissociation of methyl nitrite, CH₃ONO.⁷⁶ The barrier can be a result of avoided crossing with upper lying excited states. Fig. 1.2(d) illustrates the case where the bound excited state relaxes to the ground state via radiationless transition and the dissociation occurs through a unimolecular reaction process. More detailed discussion of photodissociation dynamics is available in the classic book by Schinke.⁷⁷

Tandem time-of-flight mass spectrometer (TOF-MS) and pulsed laser light sources are an excellent combination to investigate the chemical dynamics initiated by photoexcitation of ionic systems. While the first stage of the tandem TOF-MS is used to separate the parent ions according to their masses, the second stage, a reflectron TOF-MS, is used to analyze the ionic fragments when the photoabsorption results in the photofragmentation of the parent ions. This approach enables determination of dissociation pathways and branching ratios.

Our research apparatus combines tandem time-of-flight mass spectrometer and photoelectron imaging assembly. Photoelectron imaging and photofragmentation experiments provide complimentary information on the electronic structure and dissociation dynamics. Therefore, we aim to investigate molecular and cluster anions applying both experimental methods. In addition, to assist the interpretation of the experimental data, *ab initio* and density functional theory calculations are performed to determine the equilibrium geometry, electron binding energy and potential energy surfaces of various anions.

The dissertation is organized as follows. In Chapter 2 the experimental apparatus and the data acquisition and data analysis procedures are described. The photofragmentation of mass selected $\text{CO}_2^-(\text{H}_2\text{O})_m$, $m = 2-40$, is presented in Chapter 3. The result in this chapter includes the first observation of CO_2^- dissociation into $\text{O}^- + \text{CO}$ in water clusters. The *ab initio* and density functional studies of the CS_2^- monomer and $(\text{CS}_2)_2^-$ dimer anions are discussed in Chapter 4 followed by photoelectron imaging studies of the isolated and solvated monomer and dimer anions in Chapter 5. The photofragmentation result presented in Chapter 7 compliments the photoelectron imaging result in Chapter 6. In Chapter 7, the photoelectron imaging and photodissociation of anions resulting from mixture of CS_2 vapor and $\sim 10\%$ O_2 in Ar are presented. The observation of CS_2O_2^- and CS_3O^- are reported for the first time. Brief descriptions of the ongoing research projects are presented in Chapter 8.

Chapter 2

INSTRUMENTATION, DATA ACQUISITION AND DATA ANALYSIS

2.1 Overview

A new tandem time-of-flight mass spectrometer coupled with photoelectron imaging assembly has been built as part of this research. All the photofragmentation and photoelectron imaging data that are presented in the subsequent chapters are produced using the new research apparatus. The apparatus has all the capabilities of the older negative ion photoelectron imaging apparatus^{32,78} built in the Sanov research group with the addition of a reflectron time-of-flight mass spectrometer (TOF-MS). The inside and outside views of the new machine are drawn to scale as shown in Fig. 2.1 and 2.2. The apparatus consists of (1) ion source chamber, (2) primary TOF-MS, (3) reflectron TOF-MS and (4) velocity-map imaging assembly. The first stage of the tandem TOF-MS is based on the principle of Wiley-McLaren time-of-flight mass spectrometer.⁷⁹ The general design of the tandem TOF-MS (primary and reflectron TOF-MS) is similar to the one described elsewhere.^{27,80} In principle the second stage, the reflectron, can be used to improve the resolution of the parent ion mass spectra. However, in our experiment the first stage is used to mass select the parent ion of interest for laser interaction and the second stage is used for the mass analysis of anionic photofragments. The ion source and the TOF-MS work in pulsed mode enabling us to target a mass selected ion beam with a pulsed laser light.

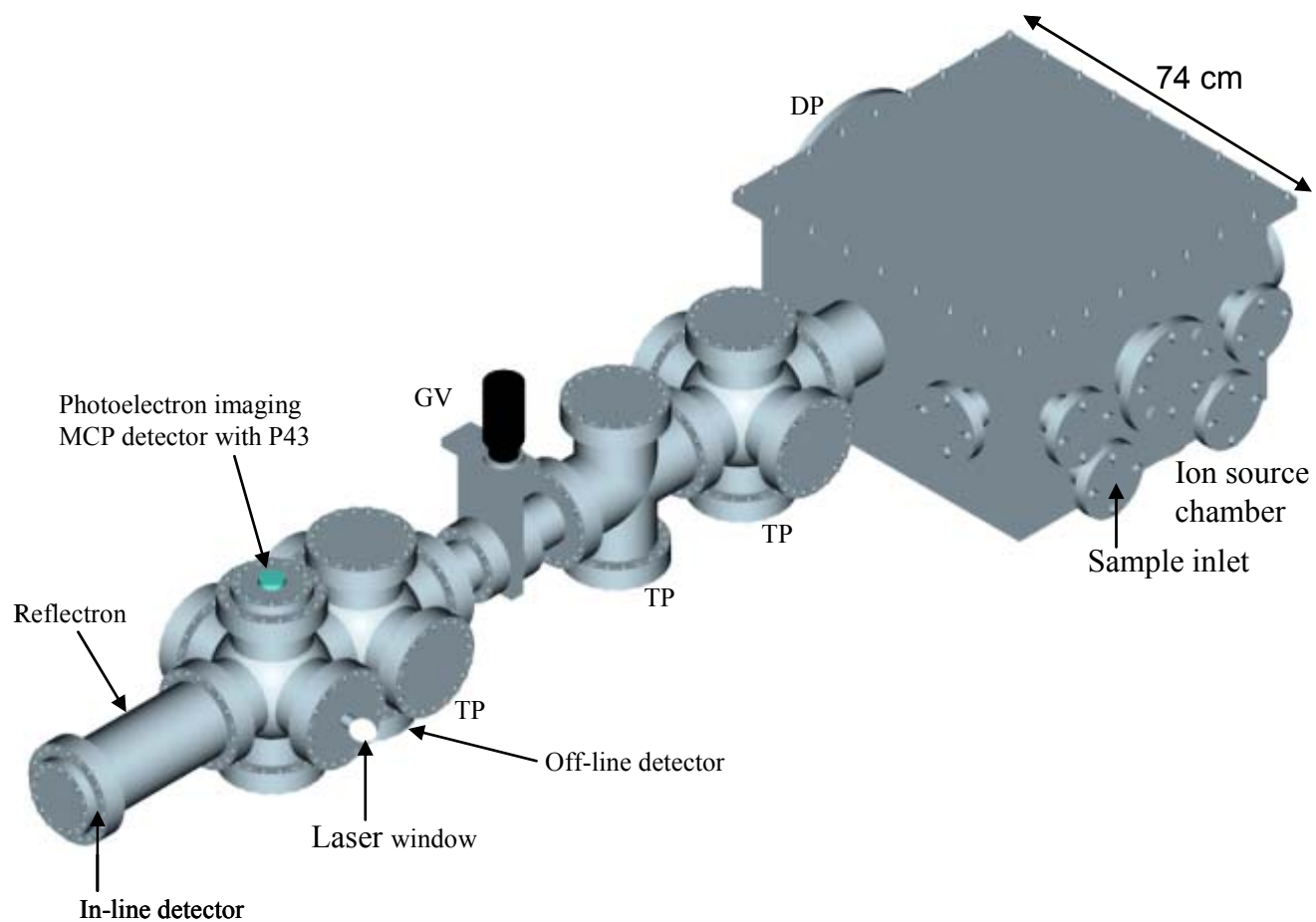


Figure 2.1 Technical drawing of the outside view of the tandem time-of-flight mass spectrometer combined with photoelectron imaging assembly. The flanges where the diffusion and turbo pumps are connected are denoted as DP and TP, respectively. GV \equiv Gate Valve. CCD camera is not shown in this drawing.

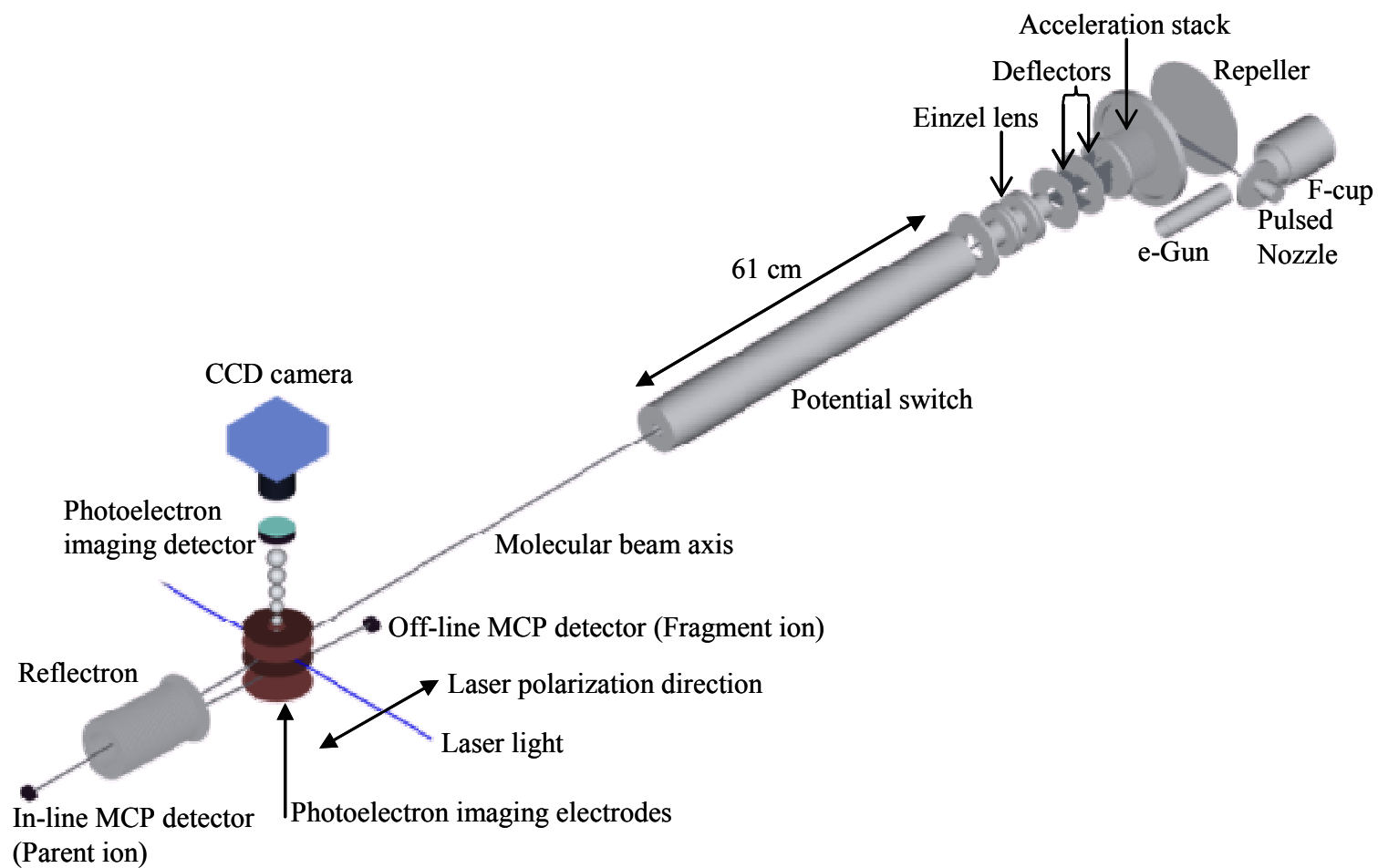


Figure 2.2 Technical drawing of the inside view of the tandem time-of-flight mass spectrometer combined with photoelectron imaging assembly.

The imaging technique is based on the principle developed by Chandler and Houston³⁶ and improved by Eppink and Parker.³⁵ In the improved technique, all charged particles with the same initial velocity vector hit the imaging detector at the same spot regardless of their initial spatial distribution. For this reason the technique is referred as velocity-map imaging.

2.2 Ion Source

The formation of ions and initiation of the TOF-MS take place inside the source chamber (see Fig. 2.1 and 2.2). The pulsed supersonic nozzle (General Valve Series 99, 0.8 mm orifice diameter), the electron gun (Southwest Vacuum Devices, Inc.), the Faraday cup, the repeller plate and extraction plates are enclosed inside the source chamber. While the first three components are used in the ion formation, the repeller and extraction plates are part of the time-of-flight spectrometer. Gaseous sample is introduced into the source chamber through a quarter inch outer diameter stainless steel tube. Inside the chamber, a Teflon tube is used to deliver the gas sample to the nozzle. The pulsed nozzle is driven by an Iota One pulse driver (Parker Hannifin Corp.), and it is set to operate at 50 Hz to synchronize with the laser pulsing rate. Typically 20-60 psi pressure of pure gas, mixture of gases or mixture of gases and vapor are backing the pulsed valve to form the supersonic expansion. When the voltage pulse is applied, the nozzle fires the supersonic gas pulse with full width at half maximum in the order of several hundred seconds.

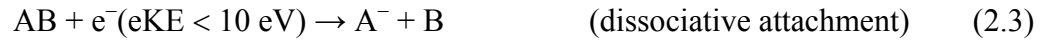
A constant current, typically 3-3.5 A, is supplied to the tungsten filament (cathode) of

the electron gun. The current supply is floated at -1 kV so that the emitted electron cloud is at 1 keV. A positive bias (control grid) potential, 80-160 V, is applied to the anode to extract the electrons from the emission region. The positive bias potential differs from the home built electron gun used with the older machine. The difference is due to the way the filament is mounted. In the home built electron gun the tip of the filament protrudes outside the anode plate towards the einzel lens while in the commercial electron gun the tip of the filament is just behind the anode plate. In addition, while some electron guns that were purchased from Southwest Vacuum Devices Inc. were performing consistently when the filaments were changed several times, others consistently failed regardless of the sign of the grid potential. Therefore, it appears to us that there is lack of consistency in the ion optics of Southwest electron gun. Ironically, with the commercial electron gun, the tungsten filament has longer life time than the thoriated iridium filament. The later tends to swell quickly causing arcing.

The electron beam is focused using an einzel lens applying ~ 1 kV. The electron gun is located such that the focal point of the electron beam is at the molecular beam supersonic free jet. The trajectory of the electron beam is fine adjusted on the horizontal and vertical axes using deflectors. The electron current is monitored by the Faraday cup which is mounted across the molecular beam free jet expansion axis collinear with the electron gun.

The electron beam crosses the expanding free jet expansion at ~ 4 mm (5 nozzle diameter) down stream from the nozzle orifice perpendicular to the direction of flow. The 1 keV electrons detach electrons from the neutral molecules/clusters generating cations

and slow secondary-electrons (with energy less than 10 eV). The resulting plasma has overall electrical neutrality with high charge density. Between the electron beam crossing and anion extraction into the TOF-MS the neutral plasma travels for 18 cm. Small cluster anions grow through three body collision association reaction. The ion formation mechanism is summarized in the following reaction equations considering arbitrary molecules AB and M:



In reaction (2.1) the high kinetic energy (eKE) electron ionizes the molecule M producing a slow secondary electron. While the high eKE electrons scatter away with slightly less energy the slower electrons becomes entrained inside the expansion free jet. The anions of interest are then formed through third-body stabilization (2.2), dissociative attachment (2.3) and evaporative attachment (2.4). The large drift distance before anion extraction (18 cm) results in long reaction time so that ion-molecule association reactions (2.5) take place. On the other hand, as the distance d increases from the nozzle orifice towards ion extraction, the beam diameter of the expansion free jet increases conically (see Fig. 2.2) and the molecular number density decreases as a function of $1/d^2$. Therefore, the long drift distance allows the plasma to dissipate and reduces the number of collisions at the time of extraction of the anions to the TOF-MS.

2.3 Primary TOF-MS

When the pulsed free jet passes by the midpoint of the repeller and extraction plates (~18 cm downstream), a pulsed -1 kV potential is applied on the repeller plate. Since the two plates are separated by 15 cm, a transverse electric field of ~67 V/cm is produced by the pulsed voltage. The anions are accelerated by the field into the time-of-flight tube. A small portion (cylindrical volume) of the anion beam passes through a 4 mm diameter hole in the extraction plate while most ions hit the wall and scatter. The ions leave the source chamber with ~500 eV of kinetic energy and are further accelerated by grid potential that increases up to 2500 V using evenly spaced serially connected (via 1.0 M Ω resistor) stack of 10 ring electrodes. This increases the beam's kinetic energy to 3.0 keV. The ion trajectory is adjusted with vertical and horizontal deflectors. Cylindrical focusing of the ion beam is achieved using an einzel lens⁸¹ which consists of three cylindrical electrodes arranged in series.

The acceleration stack, the vertical and horizontal deflector plates and the einzel lens are enclosed inside a metallic cylinder (10 cm diameter) that is floated at 2.5 kV. The power supplies of the ion deflectors are floated to the same potential as that of the 10 cm diameter metallic cylinder. The first and last electrodes of the einzel lens are in electrical contact with the metallic cylinder, and therefore they are at the beam's potential (2.5 kV). As a result the ion beam enters and exits the einzel lens with the same beam potential. Since a negative potential (typically -1 kV) is applied to the middle electrode, the einzel lens operates in a decelerating mode. That is, inside the einzel lens the ion beam is slowed down and accelerated back to its original kinetic energy although the velocity of

the outer particles will be altered such that they converge on to the beam axis.

After leaving the einzel lens, the ion beam (referenced to 2.5 kV) has to travel 193 cm flight length (referenced to ground) to arrive at the detector. Therefore, in order to achieve good focusing characteristics something has to be done. One possibility is electrical floating of the whole flight tube. However, the pulsed nature of the TOF-MS brings more convenient alternative by using a potential switch⁸² (see Fig. 2.2). In this technique, before the ions leave the 2.5 kV potential region, they enter into long metallic cylindrical tube (7.6 cm diameter x 61 cm length for our apparatus) which is also at 2.5 kV when the ions enter. Once the ions of interest enter the tube, the voltage is switched off so that they are referenced to ground when they exit. The ion beam has now its original kinetic energy but referenced to ground so that it passes straight to the in-line detector, mounted 2.3 m from the center of extraction region. Only those ions that are inside the potential switch when the voltage is on are detected. Ions with different mass range can be detected by adjusting the time at which the voltage is applied to the potential switch relative to the time the voltage is applied to the repeller plate. In other words, to detect larger mass ion both the repeller and potential switch should remain on for a longer time than for smaller mass ions.

The potential applied to the repeller plate (V) accelerates all ions to the same kinetic energy (U) independent of their mass, and for singly charged ions we have

$$U = \frac{1}{2}mv^2 = eV \quad (2.1)$$

where m is the mass of the ion, v is the velocity of the ion and e is the charge on an electron. Since all ions receive the same kinetic energy U , the ions separate in time

according to their masses (the speed of the ion is inversely proportional to the square root of its mass). As the ions pass through the acceleration stack their speed progressively increases. According to the Wiley-McLaren time-of-flight design, the ions then travel in a field free drift region up to the detector. The total flight time of the ion is the sum of its flight time through the source region, second acceleration region and field free drift region. For ion with zero initial kinetic energy, Wiley and McLaren⁷⁹ derived the following expression for the total flight time (t).

$$t = 1.02 \left(\frac{m}{2U} \right)^{1/2} \left(2k_0^{1/2} s_0 + \frac{2k_0^{1/2}}{k_0^{1/2} + 1} d + D \right) \quad (2.2)$$

where s_0 is the initial position in the ion source, d and D are the distances in the second acceleration and drift regions, respectively. $U = es_0E_s + edE_d$ (E_s and E_d are electric field strengths in the source and acceleration regions, respectively). $k_0 = 1 + dE_d/s_0E_s$. However, due to the addition of the einzel lens, equation (2.2) has to be modified to be applied to our TOF-MS design. The time the ions spend inside the einzel lens is longer than they would in the field free region.

In practice, however, we first calibrate the mass spectrum by recording the flight times of ions of known masses, and using a pair of peaks determine the constants a and t_0 in the following empirical equation.

$$t = a\sqrt{m} + t_0 \quad (2.3)$$

The masses of unknown ions can, then, be calculated using the values of the constants. The two constants depend on different potential settings particularly on the potentials

applied to the repeller plate and the acceleration stack. Therefore, the mass spectra have to be recalibrated whenever the settings are changed.

2.4 Reflectron TOF-MS

Single and multi stage ion reflectors (reflectron) have been widely used to improve the resolution of the primary TOF-MS.⁸³⁻⁸⁹ Mamyrin et al. who introduced the reflectron in 1973 were able to achieve a resolution improvement by about a factor of 10.⁸³ Since then the resolution has been improved tremendously.^{84,88} The application of reflectron for the analysis of fragmentation of the parent ion in the drift tube was realized in the multiphoton ionization experiment of Boesl et al⁹⁰ who used it to analyze metastable ion decay that occurred in the drift region. Similarly, the reflecting field was applied to study unimolecular and collision induced dissociation products following the multiphoton excitation of ammonia clusters.⁹¹ Lineberger and coworkers^{27,80,92} applied single stage reflectron in their photofragmentation study of ionic clusters.

In our experiment, the single stage reflectron time-of-flight mass spectrometer shown in Fig. 2.2 is used to mass analyze anionic fragments that result from interaction of the mass selected anions with the laser radiation. Excluding the first plate on the ion entrance side, the reflectron assembly consists of a stack of 27 stainless steel ring electrodes with inner and outer diameters of 5.1 cm and 9.0 cm, respectively. The electrode at the ion entrance and exit has outer diameter of 10.6 cm, and unlike the other electrodes it has small holes for ion entrance and exit. This electrode is referenced to ground and serves as a shield for the reflectron field. Equidistant spacing between consecutive electrode plates

is achieved by using a 0.5 cm long ceramic tube. The separation between the ground electrode and the next ring electrode is ~ 1 cm. Each electrode is connected to the next adjacent electrode by 1.0 M Ω metal film resistor. The electrode assembly is mounted on a wedge which is tilted by 2.5° with respect to the vertical axis so that the reflected ion trajectory is 175° relative to the incoming ion velocity direction and detected on the off-axis microchannel plate detector mounted 38 cm from the reflectron exit. High negative voltage is applied on the last electrode and successively drops across each resistor towards the ion entrance and exit. As the anions penetrate deeper into the reflectron field, the opposing force progressively increases. As a result, the anions are decelerated by the electric field, stop, turn around and re-accelerate to their original entrance speed. In effect, the ions have the same speed when they enter and exit the reflectron. Before they return the ions can travel inside the reflectron field as deep as $\sim 80\%$ of the total length.

The laser and molecular beam intersect 1.8 m from the extraction region and 19 cm from the reflectron entrance hole. When fragmentation of the parent anion occurs the fragment anion of mass m_f has a kinetic energy (U_f) proportional to its mass [$U_f = (m_f/m_p)U_p$], m_p = parent ion mass and U_p = parent ion kinetic energy] but its speed remain the same as that of the parent ion except negligible difference due to recoil energy. Therefore, the penetration depth of an individual fragment ion is proportional to its mass. This is illustrated in Fig. 2.3 using Simion 3D ion trajectory simulation. The

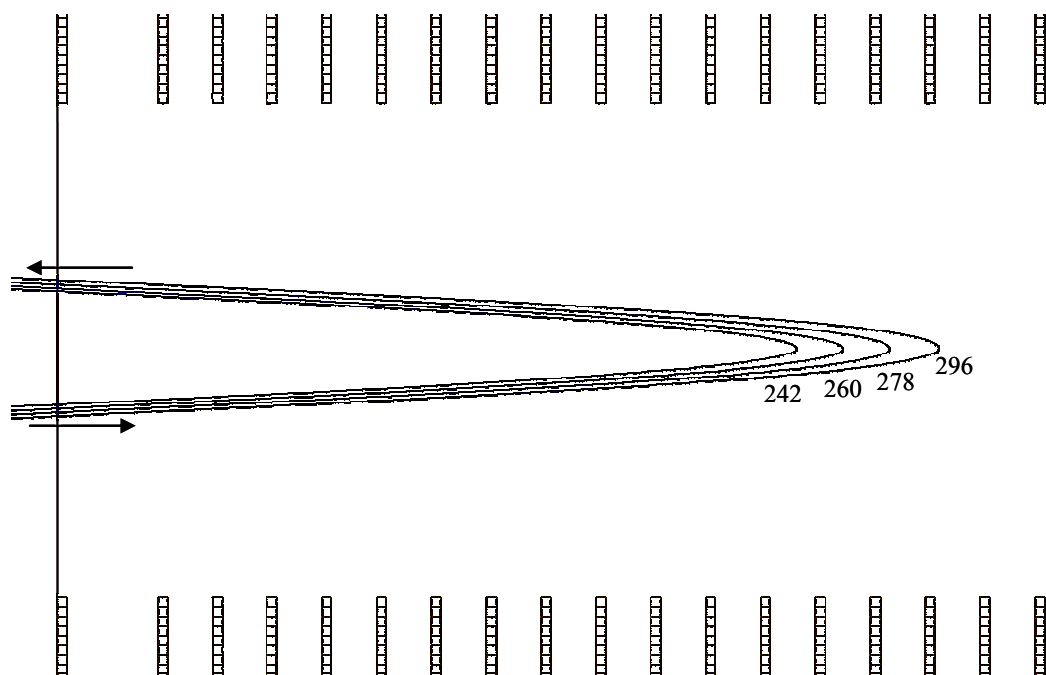


Figure 2.3 Simulation of fragment ion trajectories inside the reflectron field using Simion 7.0 for the parent ion of mass 404. The masses of the fragments are shown at the corresponding turning points. Only portion of the reflectron assembly is shown to magnify the trajectories.

trajectories of four fragment ions (mass: 296, 278, 260 and 242) of parent ion of mass 404 are shown. The fragment ion with the smallest mass (mass 242) will arrive at the detector first due to its shortest round trip inside the reflectron. The largest mass fragment ion (mass 296) has the largest penetration depth into the field and consequently arrives last at the detector.

The time (t) required for fragment ions to travel from the entrance of the reflectron to the ion detector can be written as⁸⁰

$$t = \frac{2m_f}{V_f \cos(\phi/2)} \sqrt{2U/m_p} + \frac{L}{\cos \phi \sqrt{2U/m_p}} \quad (2.4)$$

where ϕ is the tilt angle of the reflectron ($\phi = 2.5^\circ$ in design) and L is the distance from the reflectron to the ion detector. Equation (2.4) shows that flight time is directly proportional to the fragment mass (m_f). For a given m_p and fixed V_f , based on equation (2.4), the following empirical equation can be used to covert the fragment ion arrival time into mass.

$$t = a m_f + t_0 \quad (2.5)$$

The above discussion is based on detection of all fragment ions of a parent ion at one instance applying high enough potential on the reflectron. However, the reflectron field can be adjusted so that any fragment ion will follow the same trajectory, hitting the detector at the same spot as the parent ion. This approach is advantageous for determining the mass of the fragment ions unambiguously using the relation

$$m_f = \frac{V_f}{V_p} m_p \quad (2.6)$$

where m_f and m_p are masses of the fragment and parent ions, respectively, and V_f and V_p are the potential applied on the reflectron to focus the fragment and parent ions, respectively. The fragment ions can be identified based on their masses except when different ions have the same nominal mass (e.g. S^- and O_2^- , S_2^- and SO_2^-).

2.5 Ion Detection

The parent and fragment ions are detected on separate Chevron assembly 25 mm diameter dual microchannel plate (MCP) detectors (Burle, Inc.). The voltage application scheme and data acquisition procedures are shown in Fig. 2.4. The potentials applied to the first and second MCPs and anode plates are denoted as V_i , V_o and V_a , respectively. The nickel mesh (~96% transmittance) which is used to isolate the detector assembly from the external field and vice versa is referenced to ground. To increase the impact efficiency, after passing the mesh the ions are post accelerated by the voltage applied at the input of the first plate [$V_i \approx 0.36(V_{in}-200 \text{ V})$]. The impact of the ions inside the microchannels (12 μm diameter, 12° bias angle with respect to the detector surface normal) eject electrons from the surface which in turn eject more electrons thereby creating cascade of electrons inside the microchannels. The cascade of electrons at the output of the first plate is further accelerated by the bias potential created by applying V_o at the back of the second plate ($V_o \approx V_{in}-200 \text{ V}$ and $V_o-V_i \approx 0.64V_{in}$). Hence, the

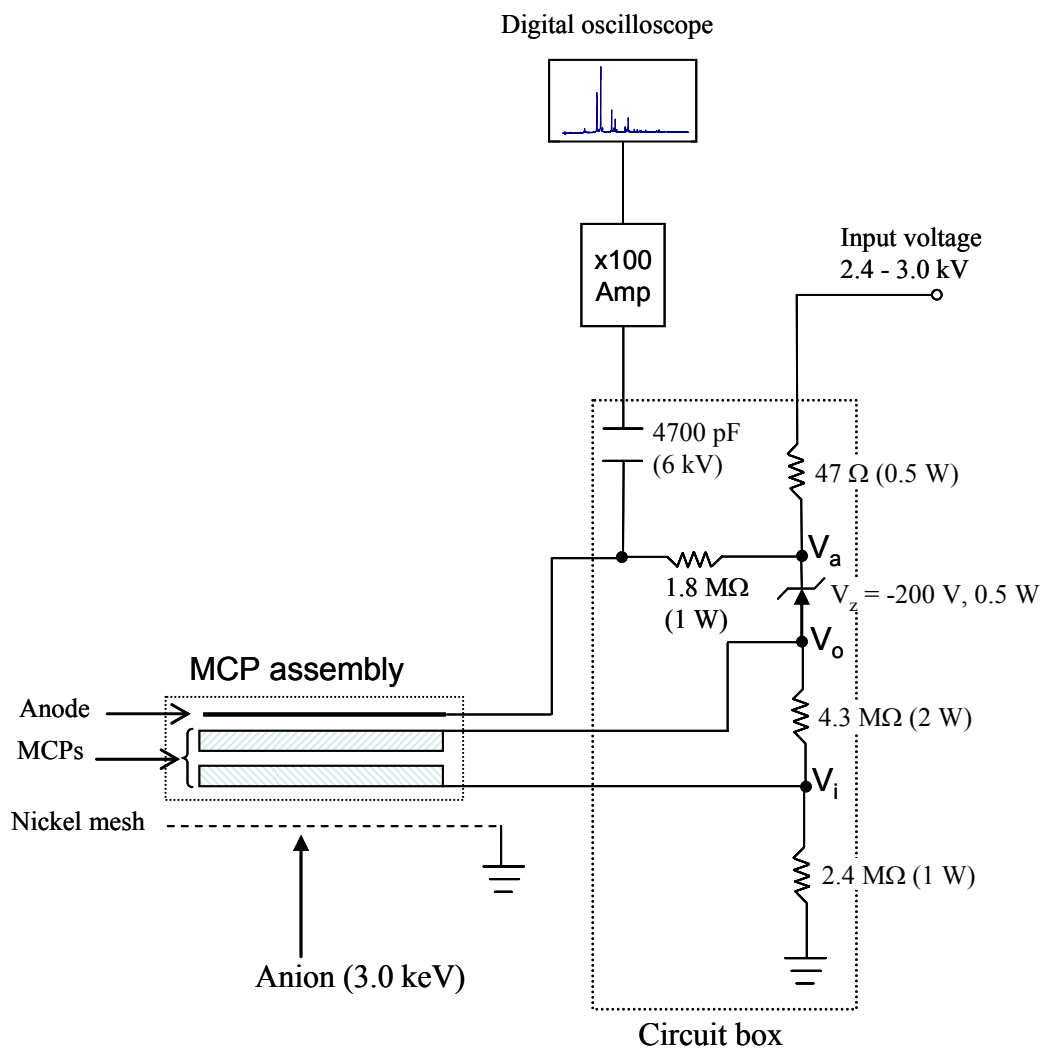


Figure 2.4 Schematics of circuit diagram showing the voltage application to the microchannel plate (MCP) and the parent and fragment ions mass spectra acquisition procedures. V_i , V_o and V_a are the voltages applied at the first MCP input, second MCP output and anode plate, respectively. $V_a \approx V_{in}$ (high voltage input), $V_o \approx V_{in} - 200$ V and $V_i \approx 0.36 (V_{in} - 200$ V).

cascade of electrons from the first plate initiates the cascade in the second plate. After exiting the second plate, the avalanche of electrons is collected on the anode plate to which $V_a \approx V_{in}$ is applied. The DC voltage is blocked by a capacitor, and the AC signal is preamplified and recorded as time-of-flight mass spectra on digital oscilloscope (Tektronix, Inc.). The digital oscilloscope allows to average up to 512 experimental cycles. The averaged spectrum is transferred to a computer via GPIB communication module.

2.6 Velocity Map Photoelectron Imaging System

One of the possible outcomes of the interactions between a photon and mass selected anion is photodetachment of electrons. The photo-detached/free electrons are referred as photoelectrons. The velocity distribution of the photoelectrons is defined by the laser polarization which is aligned parallel to the molecular beam axis and the surface of the detector. The photoelectrons are analyzed using velocity-map³⁶ photoelectron imaging³⁵ technique.

Velocity-map imaging maps all charged particles with the same initial velocity vector onto the same point on the imaging detector using an electrostatic lens. The electrostatic lens usually consists of three electrodes. In our imaging assembly (Fig. 2.2), four electrodes are shown, but only the top three are used in the imaging of the parent ions. The very bottom electrode (labeled as 4 in Fig. 2.5) is intended to be a repeller electrode for future photoelectron imaging of fragment anions. Electrodes 1, 2 and 3 are identical ring electrodes with inner and outer diameters of 2.5 and 7.6 cm. The photoelectrons are

accelerated to the detector by applying a negative potential to the repeller plate (V_R) and a positive potential on the extraction plate (V_E) while referencing electrodes 2 and 4 to ground (see Fig. 2.5).

The velocity mapping is achieved by varying the extraction-to-repeller voltage ($R = V_E/V_R$) ratio. The principle of velocity mapping is illustrated in the Simion 3D electron trajectory simulation results shown in Fig. 2.5(a)-(e) where the trajectories of electrons (1.0 eV) with different initial velocity and spatial distributions are considered. The dependence of the focusing on R is shown Fig. 2.5(a)-(c) including 5 trajectories with the same initial velocity vector but distributed evenly over 5 mm on the ion beam axis. For $R = 0.5$, seen in Fig. 2.5(a), a divergence is seen indicating that the electrostatic lens is out of focus. By repeating the simulation at different ratios the optimum focusing is obtained at $R = 1.91$ compared to 2.10 obtained from experiment (for a repeller plate without a hole at the center, the value is 2.70). When the ratio is further increased, the focal plane is at shorter distance than where the detector is mounted (example is shown in Fig. 2.5(c) for $R = 3$).

At the optimum ratio ($R = 1.91$), when the photoelectrons originate from the same point with different velocity vector they hit the detector at different places as shown in Fig. 2.4(d) for 45° elevation angle difference between the initial velocity vectors. The simulation result shown in Fig. 2.4(e) can be considered as the combination of the results shown in Fig. 2.4(b) and (d). As shown in the figure, the trajectories that originate from three points are shown. From each point there are three trajectories with 45° elevation angle difference (-45° , 0° and 45°). The trajectories with the same initial elevation angle

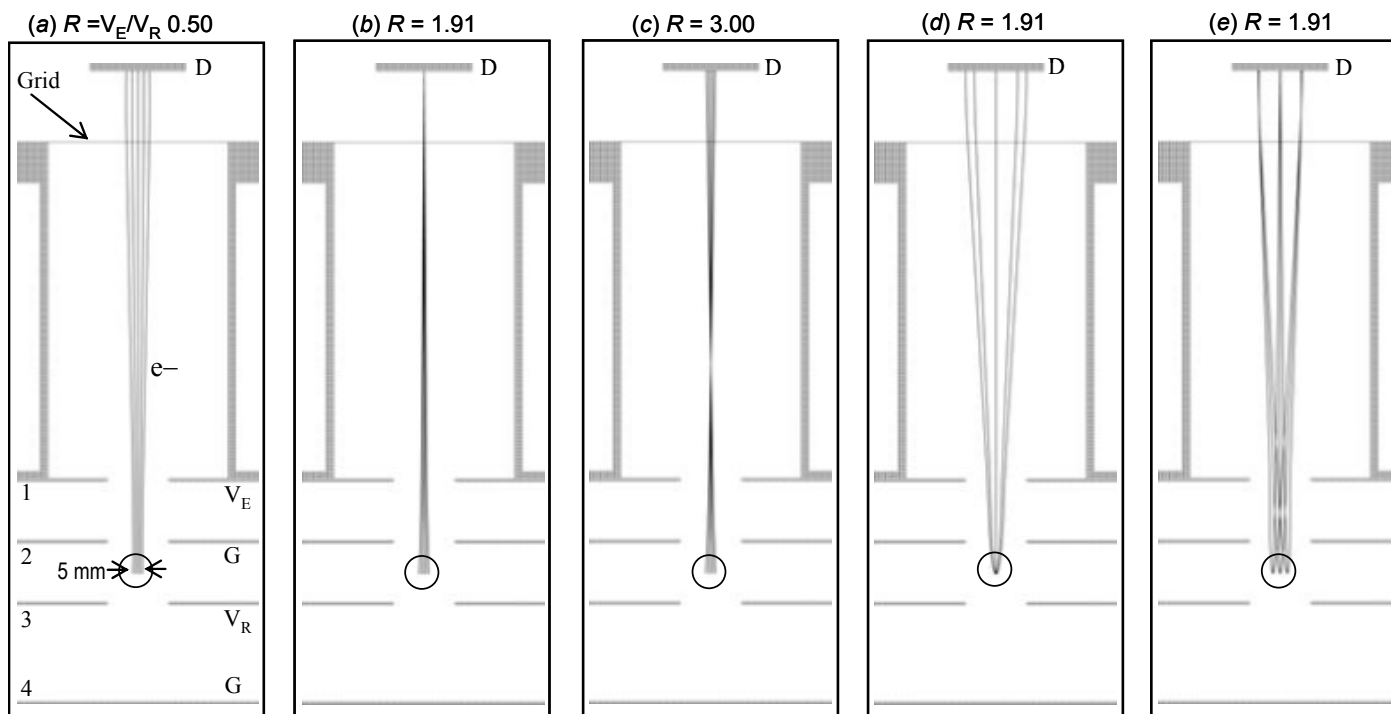


Figure 2.5 Photoelectron trajectory simulation using Simion 7.0 for parent ion photodetachment. The imaging assembly consists of four electrodes labeled as 1, 2, 3 and 4. The first three are used in the photoelectron imaging of parent ions. Electrode 4 is intended to be a repeller plate for fragment ion photoelectron imaging. The circle indicates the interaction spot of the parent ion and the laser beam. In the parent ion photoelectron imaging electrodes 2 and 4 are referenced to ground. The velocity mapping is achieved by varying the extraction-to-repeller voltage ($R = V_E/V_R$) ratio. The results shown in (b), (d) and (e) are obtained using the optimum R : (a) and (b) are included to illustrate how the focusing is affected by the ratio. In (a), (b) and (c) the five electrons have the same initial velocity vector but distributed over 5 mm distance along the horizontal axis. (d) All electrons originate from the same point with 45 degree elevation angle difference. (e) Three electrons originate from each of the three points and those with the same velocity vector focused at the same point on the detector D regardless of their initial spatial distribution.

that originate from three different points (3 mm difference between successive points) are mapped on the top of each other on the focal plane.

In our experiment, in order to minimize the distortion of the electron distribution due to the Earth's magnetic field, the interaction region is shielded by a μ -metal cup. In addition, the electron flight tube is wrapped inside and out by μ -metal. The electron cloud is accelerated vertically towards the detector (40 mm diameter) mounted at ~ 19 cm from the interaction spot. The detector assembly contains two imaging quality microchannel plates (MCPs) and P43 phosphor screen deposited on fiberoptic (Burle, Inc.).

The voltage application and imaging data acquisition procedures are shown in the schematic in Fig. 2.6. A DC potential of $V_i \approx 2$ kV is applied to the front MCP plate to post accelerate the electrons. The cascades of electrons produced in the front plate are further accelerated by applying $V_o \approx 3$ kV (DC) + 1 kV (pulse) potentials on the second plate. To discriminate noise from signal, the pulsed potential is on for only 200 ns when the photoelectrons arrive. No signal is observed when the pulsed potential is off. The electron cloud is accelerated onto the phosphor screen by a high voltage (~ 6.5 kV). When the cascade electrons impinge on the phosphor screen, the kinetic energy of the electrons is released as light. The light passing through the fiber optic bundle is captured by a CCD camera (Dalsa 1M30) which is linked to a computer through PICI[®] frame grabber (EPIX, Inc.) that comes with image processing "C" function library. A program called XCAP (EPIX, Inc.) is used to set the parameters for the camera. A data acquisition C++ program (written by Dr. Andreas Osterwalder, Neumark Group, Berkeley, CA) is used to read and integrate the data from the buffers on the frame grabber.

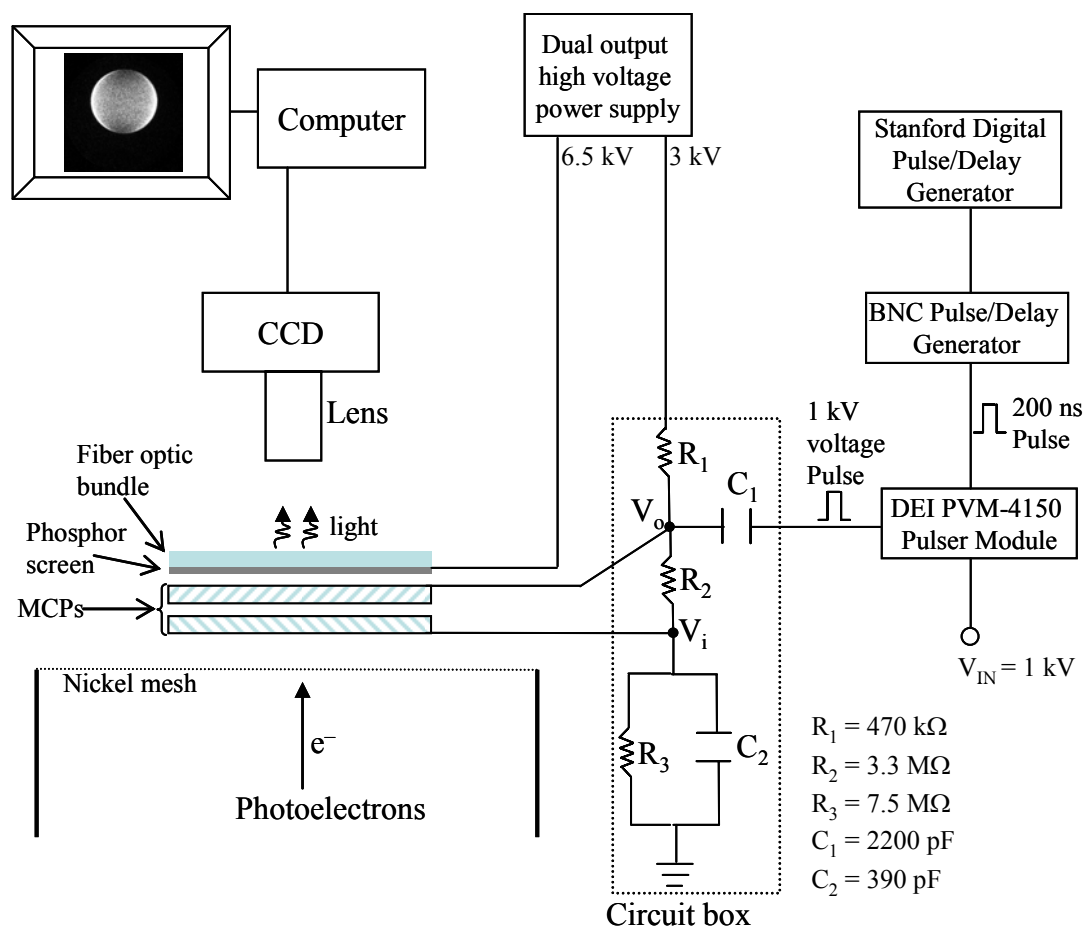


Figure 2.6 Schematics of voltage application to imaging detector and image acquisition procedures. V_i and V_o are the voltages applied to the input of the first and to the output of the second microchannel plates, respectively. $V_i \approx 2$ kV. $V_o \approx 3$ kV DC + 1kV pulse. Typically, 6.5 kV is applied to the phosphor screen.

2.7 Vacuum Systems

The ion source chamber is primarily pumped by a high-throughput diffusion pump (Varian, Inc. VHS-10, pumping speed ~ 7000 l/s) that is backed by a mechanical pump (Edwards High Vacuum, pumping speed 14 l/s). An elbow with 10 inch inner diameter connects the diffusion pump (DP) to a gate valve that separates the source chamber from the DP. The ion-optics region, where the acceleration stack, einzel lens and potential switch are located, is pumped by two turbomolecular pumps (Leybold TMP 361, pumping speed 400 l/s) backed by Trivac rotary pumps. The source chamber is also differentially pumped by the two turbo pumps through 4 mm hole. The detection region is separated from the ion-optics region by a 4 inch gate valve (Kurt Lesker Co.), and it is pumped by one turbo pump. When all the pumps are running and the nozzle is off the typical pressures in the source, ion-optics and detection regions are 4×10^{-7} , 3×10^{-8} and 5×10^{-9} Torr, respectively. When the nozzle is operating, the pressures increase typically to 2×10^{-5} , 8×10^{-8} and 2×10^{-8} Torr, in the respective order.

2.8 Laser System

A neodymium-doped yttrium aluminium garnet ($\text{Nd:Y}_3\text{Al}_5\text{O}_{12} \equiv \text{Nd:YAG}$) laser (Spectra Physics Lab 130-50) is used in the photoelectron and photofragmentation experiments. The outputs of the laser are 1064 nm (fundamental), 532 nm (second harmonic), 355 nm (third harmonic) and 266 nm (fourth harmonic) at a repetition rate of 50 Hz and pulse width 6-9 ns. The 532, 355 and 266 nm outputs, respectively, have 120,

56 and 15 mJ of energy per pulse. The power is optimized based on the need for different types of experiments. At the interaction region, the laser beam is brought to a ~4 mm diameter using a 2 m focal length lens.

2.9 Operation

Each experimental cycle is initiated when the pulsed nozzle is triggered by the Iota One driver. The Stanford delay/pulse generator (Stanford Research Systems DG535) is used to synchronize the delay and triggering time of the extraction plate, potential switch, laser lamp, laser Q-Switch and the imaging detector with reference to the nozzle driver. The repeller plate and potential switch are pulsed by PVM-4210 pulser module and PVX-4140 pulse generator (Directed Energy, Inc.), respectively, both of which are gated by the Stanford delay generator. The voltage pulse to the repeller plate and potential switch remains on until the ions of interest are in the potential switch tube and it is turned off before they exit the tube. The duration of the pulse increases with ion mass. The laser lamp and Q-switch are externally triggered by the delay generator. The overlap between the laser and the mass selected ion packet is controlled by following the neutral signal on the in-line detector while deflecting the ions using the reflectron (additional application of the reflectron!). The neutral species arrives at the in-line detector at the same time as the corresponding anion. As shown in Fig. 2.6, the 200 ns 1 kV pulse voltage is generated by the PVM-4150 pulse generator module which is gated by the BNC delay generator (Berkeley Nucleonics Corp.). The BNC delay generator is externally triggered by the

Stanford delay generator. The pulsed voltage is added to the 3 kV DC using the circuit shown in Fig. 2.6 and applied to the second plate of the imaging MCP detector.

2.10 Photoelectron Image Analysis

The raw photoelectron imaging data are 1024 x 1024 square matrices. The background subtraction is performed using the Matlab program. The Matlab programming environment is convenient to analyze the imaging data and to filter noise signal whenever necessary. There several types of digital filters incorporated in the program, and the choice of appropriate digital filter is discussed in appendix A.

The photoelectron image is a 2D projection of the 3D electron distribution. The 3D distribution is reconstructed from the 2D projection using the inverse Abel transformation⁹³ mathematical technique. The horizontal polarization of the photodetaching laser light imposes cylindrical symmetry on the photoelectron images. The 3D image reconstruction is performed using the Basis Set Expansion (BASEX)⁹⁴ which is suited for cylindrically symmetric images. The kinetic energy and the anisotropy parameter of the angular distribution of the detached electrons can easily be determined from the inversion results.

The 266 nm image of CS_2^- and its inverse Abel transform are shown in Fig. 2.7(a) and (b) for illustration. The inverted image is a slice through the 3D distribution of the electron cloud containing all the information that can possibly be obtained from the entire distribution. For every radius (r) of the inverted image the electron kinetic energy (eKE) is calculated using the relation $\text{eKE} \propto r^2$. The eKE is converted to the electron binding

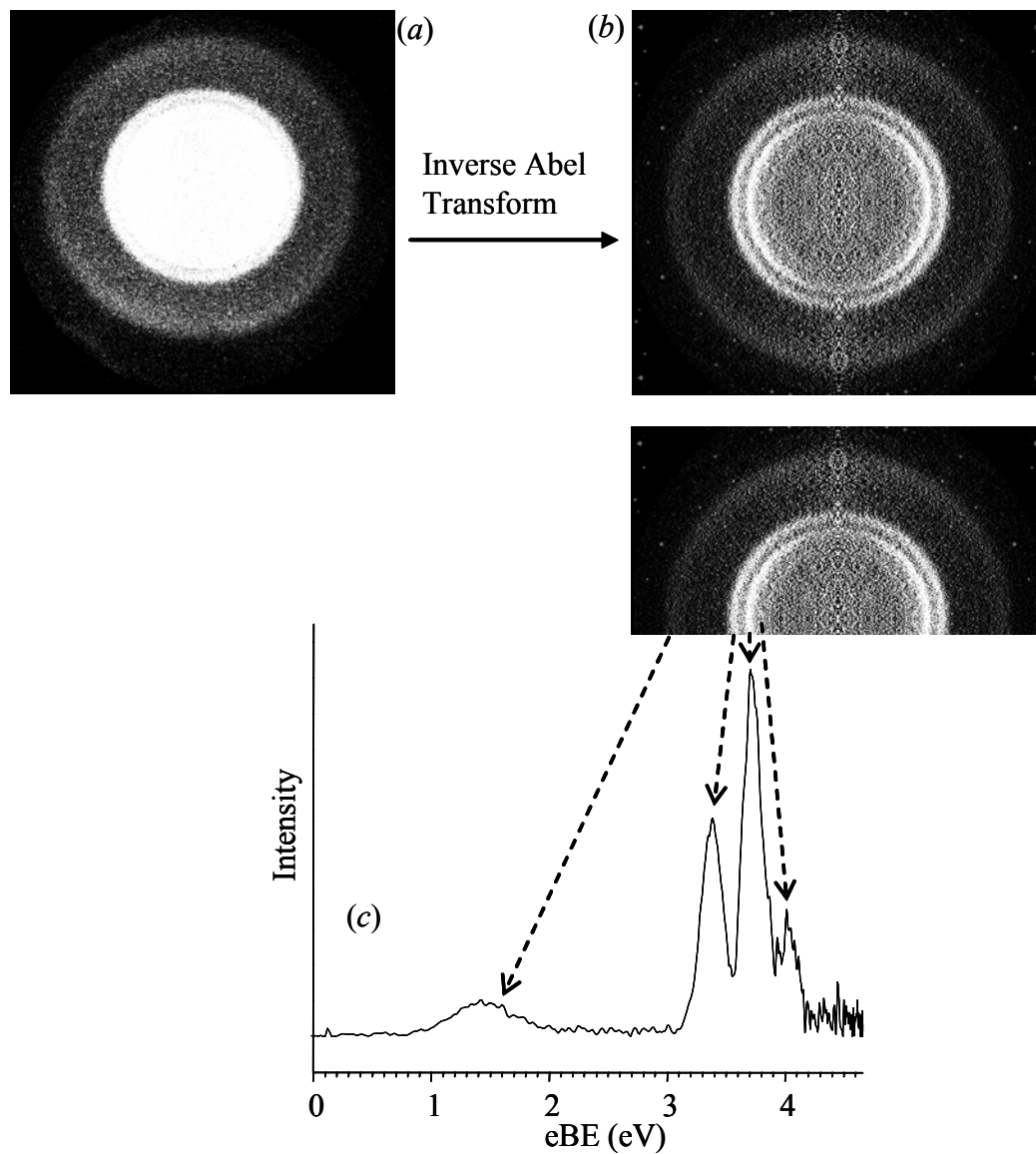


Figure 2.7 (a) Photoelectron image of CS_2^- acquired at 266 nm. (b) Inverse Abel transform of the image. (c) Photoelectron spectrum extracted from the image. The arrows indicate the correlation of the rings in the inverted image with the peaks in the spectrum.

energy (eBE) of the particle (atom, molecule or cluster) using the equation that Einstein applied in the analysis of photoelectric effect.

$$eKE = h\nu - eBE \quad (2.7)$$

where h is the Planck's constant and ν is the frequency of the electromagnetic light. The eBE is analogous to the work function for a bulk system. The eBE is characteristic of a chemical system while the eKE varies linearly as a function of photon energy for $h\nu > eBE$. The photoelectron spectrum of CS_2^- obtained from the Abel inverted image following the above procedure is shown in Fig. 2.7 (c). The lowest eBE (highest eKE) corresponds to the outer most ring in the image and so on.

The photoelectron images provided in Fig. 2.8 and the corresponding spectra in Fig. 2.9 are used as standards to calibrate the spectrometer. For each atomic anion at each wavelength, the Abel inverted image is shown below the raw image. In addition to calibration, the photoelectron imaging results on the atomic systems illustrate some fundamental trends of the energetics and angular distributions of the photoelectrons. As shown in the photoelectron spectra in Fig. 2.9, the photodetachment transition bandwidth increases with photon energy for all O^- , S^- and I^- emphasizing the fact that energy resolution decreases as the kinetic energy of the photoelectrons increases. For instance, in the 532 nm $S (^3P_{2,1,0}) \leftarrow S^- (^2P)$ transition, the spin-orbit splitting is partially resolved but this resolution is completely lost at 355 nm for the same transition. Regarding the angular distribution, except for the 355 nm $O (^1D_2) \leftarrow O^- (^2P)$ transition, the photoelectron images displayed in Fig. 2.8 are characterized by negative anisotropy, that is, the photoelectrons are preferentially ejected vertical to the laser polarization. In all the

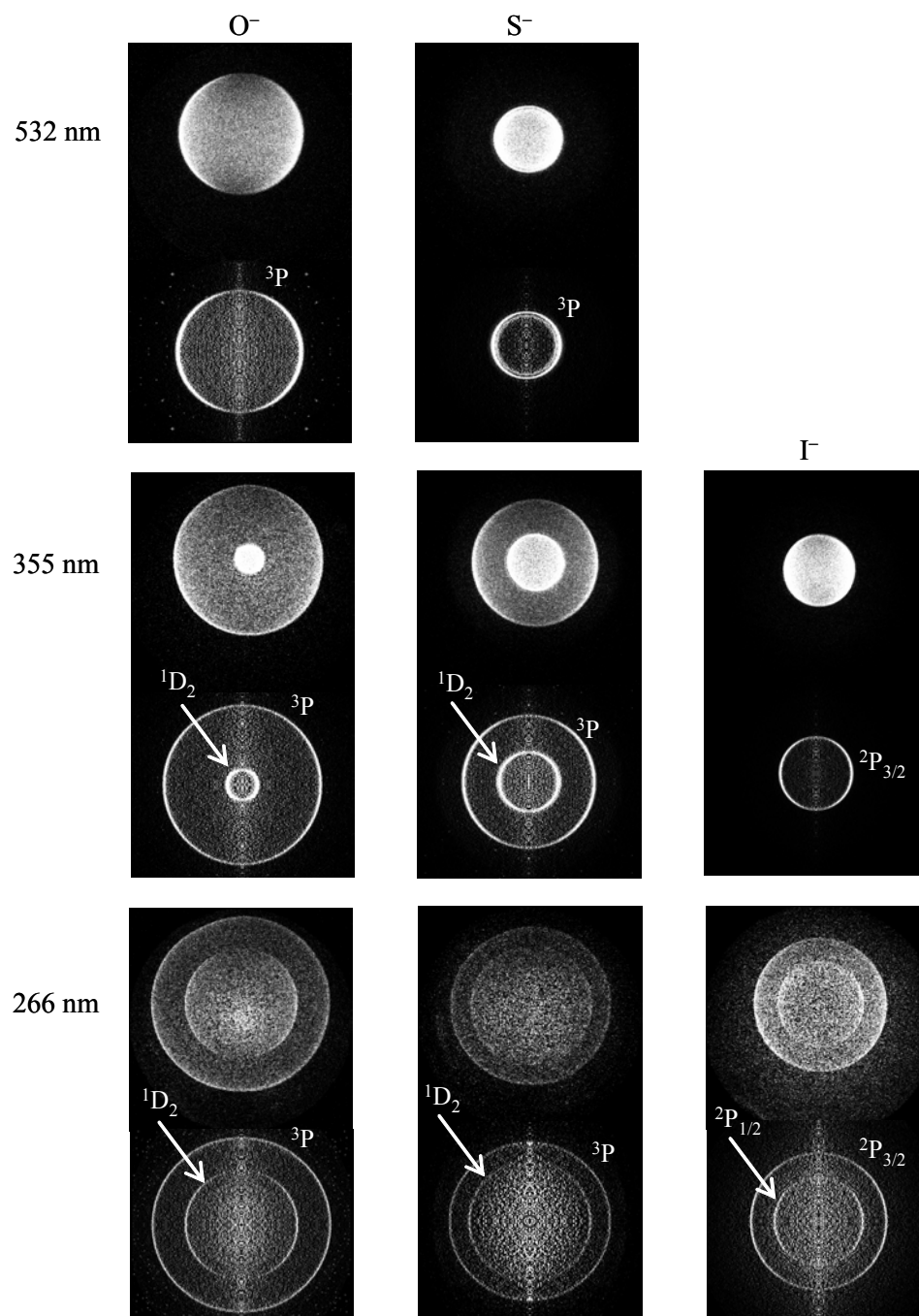


Figure 2.8 Photoelectron images of O^- , S^- and I^- acquired at 532, 355 and 266 nm. The raw and Abel inverted image at each wavelength are given at top and bottom, respectively.

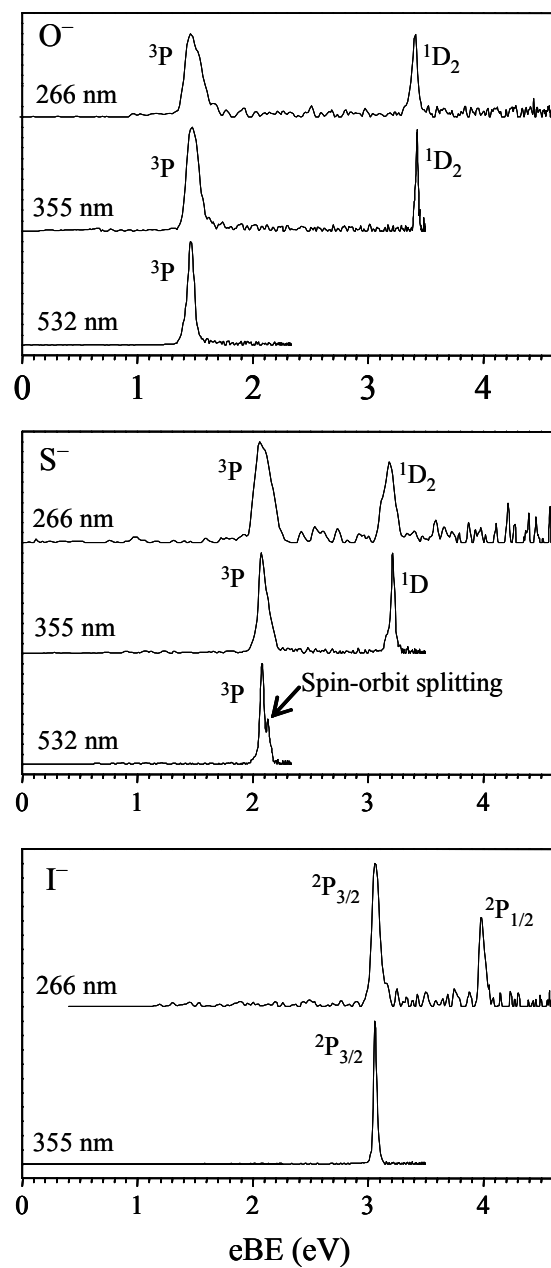


Figure 2.9 Photoelectron spectra of O^- , S^- and I^- extracted from the images displayed in Fig. 2.8.

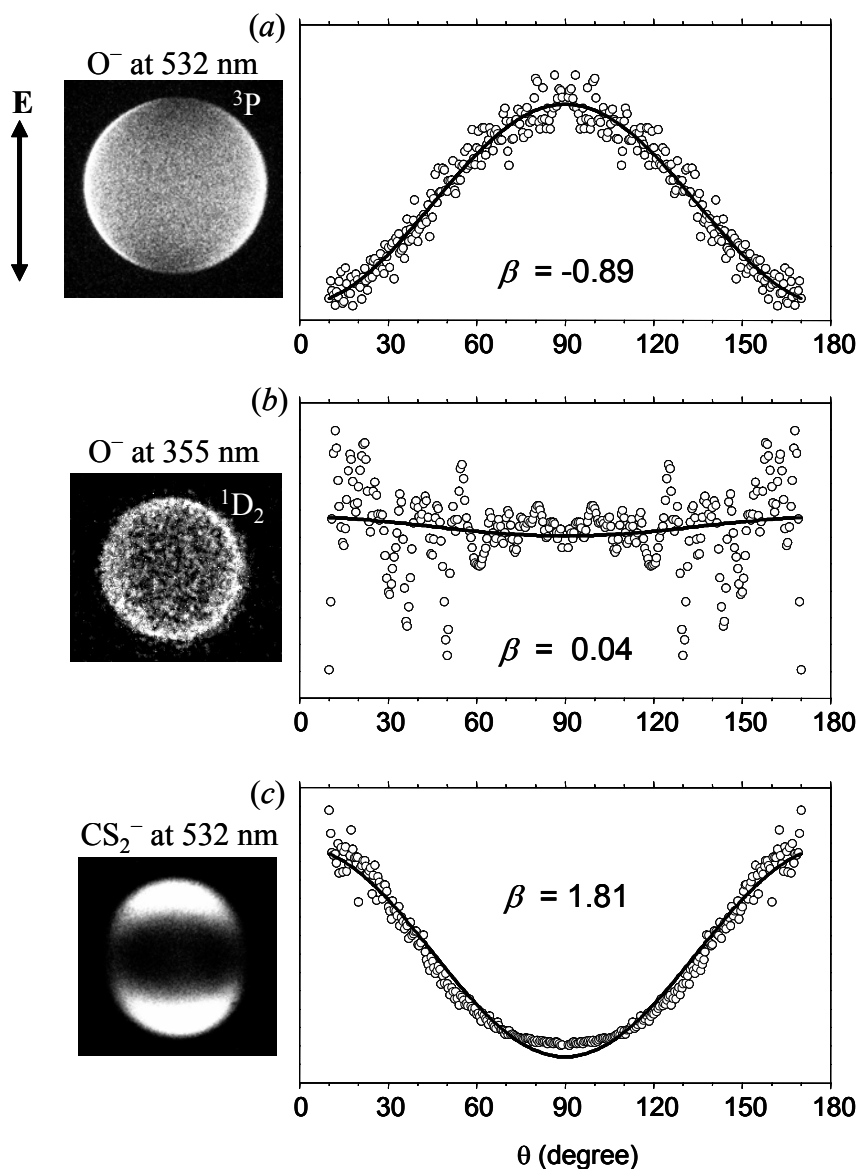


Figure 2.10 Examples of photodetachment transitions with perpendicular (a), isotropic (b) and parallel (c) photoelectron angular distribution. The 355 nm image of O^- shown (b) is the central transition band in Fig. 2.8 (the outer ring is cropped). The open circles in the plot are experimental data points. The solid lines are obtained by fitting $I(\theta) = (\sigma/4\pi)[1 + 0.5\beta(3\cos^2\theta - 1)]$ to the data. The values of the best fit anisotropy parameter (β) are shown on the corresponding plots.

atomic anions, the electron occupies the p -orbital. According to the electric-dipole selection rule, the outgoing electron is characterized by s & d partial waves. It is the interference between the two partial waves that determines the observed photoelectron angular distributions. For the 355 nm $O(^1D_2) \leftarrow O^-(^2P)$ photodetachment transition, the free electron has near zero kinetic energy. According to the Wigner threshold law⁹⁵, the d -wave is inaccessible at very low eKEs. Therefore, the photoelectron image becomes isotropic reflecting the s -wave character of the free electron.

For a one-photon transition resulting from using linearly polarized light, the intensity I of photoelectrons at a particular angle θ (the angle between the laser polarization axis and the photoelectron velocity vector) is given by

$$I(\theta) = \frac{\sigma}{4\pi} [1 + \beta P_2(\cos \theta)] \quad (2.8)$$

where σ is a constant related to the total detachment cross-section. P_2 is the second-order Legendre polynomial, $P_2(\cos \theta) = 1/2[3\cos^2 \theta - 1]$. The most useful parameter in equation (2.8) is the anisotropy parameter β which is very often used to describe the photoelectron angular distribution. For $\beta=0$, equation (2.8) reduces to $I(\theta) = \sigma/4\pi$ which is constant at all angles and referred as an isotropic distribution. For $\beta = -1$, $I(\theta) = (3\sigma/8\pi) \sin^2 \theta$ which peaks at $\theta = 90^\circ$, and it is referred as perpendicular transition. In the photoelectron images this corresponds to distribution of photoelectrons along the ‘equator’ or on the left and right side. For $\beta = 2$, $I(\theta) = (3\sigma/4\pi) \cos^2 \theta$ and the intensity peaks at $\theta = 0$ and 180 , and referred as parallel transition as the photoelectrons are preferentially distributed along the laser polarization axis.

Experimentally the anisotropy parameter is determined by fitting equation (2.8) to the experimental data. The different patterns of photoelectron angular distribution are illustrated in Fig. 2.8. As shown in the figure, the 532 nm O^- photodetachment signal peaks at 90° . The solid line is obtained by fitting equation (2.8) to the data yielding $\beta = -0.89$. This is an example of a perpendicular transition. The 532 nm photodetachment of CS_2^- has the opposite trend, with the electron distribution peaking along the laser polarization axis ($\beta = 1.81$). The 355 nm $O(^1D_2) \leftarrow O^- (^2P)$ photodetachment transition has a nearly uniform electron distribution along all angles ($\beta = 0.04$), which can be characterized as an isotropic distribution.

Chapter 3

PHOTOCHEMISTRY OF CO_2^- IN WATER CLUSTERS

3.1 Introduction

Solvent molecules interact more strongly with anions than with the neutral counterparts. As a result, metastable anions can be stabilized and electron autodetachment pathways can be closed upon solvation. When the solvent cluster size increases, the direct photodetachment channel also gradually diminishes. By stabilizing an anion in its ground state and by pulling down the excited states from the detachment continuum the solvent molecules can open up dissociation channels as the solvent cluster size increases. CO_2^- is an excellent system for illustrating these solvation effects. Gas phase hydration traps metastable CO_2^- in water clusters by minimizing the anion potential energy faster than the neutral counterpart, thereby decreasing the electron autodetachment probability close to the linear geometry.

The metastable anion of CO_2 has been observed in numerous processes. Examples include: CO_2^+ impact on metals;⁹⁶ electron impact on formic acid;⁹⁷ γ -ray irradiation of sodium formate crystals;⁹⁸ CO_2 adsorption on UV-irradiated MgO surface;⁹⁹ CO_2 reactions with negative-ions;¹⁰⁰ pulse radiolysis of aqueous solutions of carbon monoxide, carbon dioxide, sodium formate, formic acid, sodium bicarbonate and aliphatic acids;^{101,102} electron collisions with cyclic anhydrides.¹⁰³ Short-lived CO_2^- resonances are also implicated in electron scattering on neutral CO_2 .¹⁰⁴⁻¹⁰⁶ The lifetime of

relaxed CO_2^- against autodetachment is estimated at 60-90 μs ,^{103,107} which is rather long on the timescale of most gas-phase experiments. The autodetachment can be further slowed or even suppressed by the effect of homogeneous¹⁰⁸ or heterogeneous¹⁰⁹ solvation.

The homogeneous solvation in the $(\text{CO}_2)_n^-$ clusters is known to affect the constitution of the core anion, which switches between the CO_2^- and $[\text{O}_2\text{C}-\text{CO}_2]^-$ forms depending on the cluster size.¹¹⁰⁻¹¹² Unlike homogeneous solvation, in heterogeneous $[\text{CO}_2(\text{H}_2\text{O})_m]^-$ clusters, the extra electron is localized on CO_2 at least for small m ²⁶ despite the negative adiabatic electron affinity of bare CO_2 .¹² Hence, these clusters are properly described as $\text{CO}_2^-(\text{H}_2\text{O})_m$.

Considering the electron binding motifs in pure water clusters the localization of the extra electron on CO_2 should not be surprising. In $(\text{H}_2\text{O})_m^-$ cluster there are two major electron binding motifs: surface states and cavity states. Network permeating states have also been predicted to be stable states that may be formed initially before the cluster undergoes significant nuclear rearrangement to form the most stable surface and cavity states.²⁵ In all cases the excess electron does not reside on single molecular entity, but rather is bound by the cooperative effect of all the water molecules in highly diffuse orbital. Electrostatic interactions and electron correlations play important role in binding the excess electron. In the surface and cavity states the excess electron localizes in the vicinity of free OH groups that are not involved in H-bonding. In the network permeating states the electron binding interaction is dominated by correlation effects and the electron is delocalized over the cluster.²⁵ The interaction of surface state $(\text{H}_2\text{O})_m^-$ with another

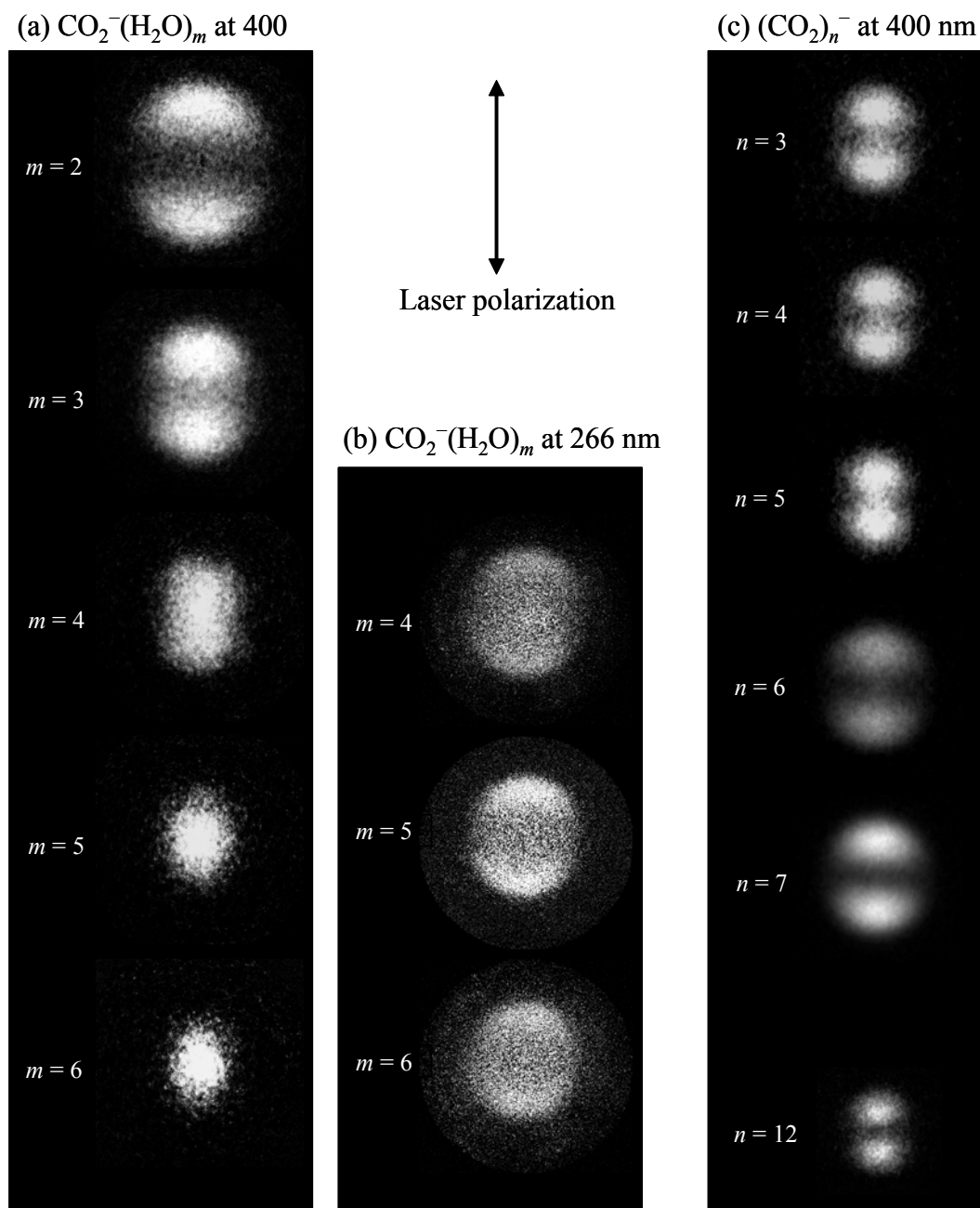


Figure 3.1 (a) Photoelectron images of $\text{CO}_2^-(\text{H}_2\text{O})_m$, $m = 2-6$, acquired at 400 nm. (b) Photoelectron images of $\text{CO}_2^-(\text{H}_2\text{O})_m$, $m = 4-6$, acquired at 266 nm. (c) Photoelectron images of $(\text{CO}_2)_m^-$, $m = 2-12$, acquired at 400 nm. The double headed arrow indicates the laser polarization direction.

atom/molecule M is dominated by the interaction between the excess electron and M.¹¹³ Consistent with this, a mixture of CO₂ and (H₂O)_m⁻ converts completely to the CO₂⁻(H₂O)_m cluster form within 0.5 sec.¹¹⁴ Therefore, in CO₂⁻(H₂O)_m cluster the excess electron localizes on the bound state of bent CO₂⁻ and the water molecules strengthen the localization.

In the anionic water clusters, (H₂O)_m⁻, the vertical detachment energies (VDEs) are rather modest, varying from 45 ± 5 meV for $m = 2$ to 0.79–1.92 eV in the $m = 11$ –69 range.^{8,15,16,19,115} The adiabatic electron affinity (EA_a) of (H₂O)₂⁻ has been estimated experimentally to be 17 meV.¹¹³ “Doping” the water cluster with CO₂ increases the detachment energies quite dramatically, i.e., to 1.96–3.46 eV for CO₂⁻(H₂O)_m, $m = 1$ –5.^{26,116} For bare CO₂⁻ the VDE is 1.4 eV. The large VDE values of isolated and hydrated CO₂⁻ compared to negative EA_a (-0.60 ± 0.20 eV)¹⁰⁷ of CO₂ is due to different equilibrium geometries of the anion ($\angle\text{OCO} < 138^\circ$) and the neutral. The stronger hydration interactions with a localized CO₂⁻ anionic core than with the neutral counterpart turns the EA_a values from negative to positive at $m = 1$ or 2 increasing as a function of m . The life time of isolated and hydrated CO₂⁻, especially for small m , is determined by tunneling to the neutral state in the proximity of the linear geometry.

The photoelectron images of CO₂⁻(H₂O)_m at 400 nm²⁶, shown in Fig. 3.1 (a), show loss of anisotropy as m increases. The observed change in the anisotropy could be attributed to the decrease of the photoelectron kinetic energy as a function of solvent cluster size. However, in the case of the homogeneous clusters, (CO₂)_n⁻, the anisotropy of the images

as shown in Fig. 3.1(c) essentially remains unaffected for all cluster size considered in the experiment. The difference underscores the remarkable role that hydration plays in stabilizing the excited states, opening new decay mechanisms such as electron autodetachment. The anisotropy of the 266 nm photoelectron images shown in Fig. 3.1(b) is less sensitive on solvent cluster size at least until $m = 6$ which indicates the dominance of direct photodetachment.

While electron detachment is the dominant photodepletion pathway in the small cluster-size range, the excited-state contribution to the photodetachment comes in the form of poorly structured autodetachment signal. However, with increasing hydration, the electron removal becomes progressively less favorable energetically, yielding stage to anionic rearrangements. This chapter focuses on the photofragmentation study of the mass selected $\text{CO}_2^-(\text{H}_2\text{O})_m$, $m = 2-40$, clusters at 355 and 266 nm radiations.¹¹⁷ The results illuminate the important role of the water molecules in controlling the excited-state decay channels. To assist interpretation of the experimental results *ab initio* and density functional theory (DFT) calculation results are presented for the smaller clusters.

3.2 Experimental

The $\text{CO}_2^-(\text{H}_2\text{O})_m$ cluster anions are prepared by expansion of undried CO_2 at a stagnation pressure of 2 atm through a pulsed supersonic nozzle into the vacuum chamber with a base pressure of 2×10^{-7} Torr. Few drops of water were introduced into the gas delivery line to maximize the abundance of hydrated CO_2^- . The mass-selected cluster anions of interest are interrogated using an appropriately timed pulsed laser beam. The

ionic photofragments are then analyzed using reflectron TOF-MS as described in Chapter 2. The third and fourth harmonic of a Nd:YAG laser are used in these experiments, giving 355 nm (~15 mJ) and 266 nm (~8 mJ) pulses, respectively, at a repetition rate of 50 Hz. The laser beam is brought to a ~4 mm diameter inside the vacuum chamber.

3.3 Experimental Results

3.3.1 Parent Ion Mass Spectra and Overview

A representative $\text{CO}_2^-(\text{H}_2\text{O})_m$ parent-ion mass-spectra optimized for small and high mass ions are shown in Fig. 3.2. The intensity pattern is reproducible at varying source conditions and consistent with the previous report by Tsukuda *et al.*¹¹⁶

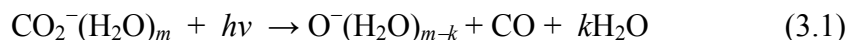
Absorption of a visible or UV photon by a negative ion generally leads to electron detachment or photofragmentation. The photodetachment process was the focus of previous work on $\text{CO}_2^-(\text{H}_2\text{O})_m$ ²⁶ in Sanov group, where we showed that the vertical detachment energy (VDE) increased with m , exceeding the 355 nm photon energy for $m > 6$. Accordingly, the overall photodetachment yield decreased with increasing m , shifting the photochemical process to the photofragmentation. Without quantifying this trend, in the present work we observed a sharp increase (with increasing m) in the photofragment ion yield relative to the total parent depletion in the $m = 2$ -10 range.

3.3.2 355 nm Results

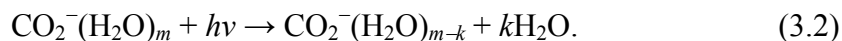
The photofragment-ion mass-spectra obtained from mass-selected $\text{CO}_2^-(\text{H}_2\text{O})_m$, $m = 3$ -

20 at 355 nm are shown in Fig. 3.3. The spectra are normalized to the same maximum intensity, not representative of the corresponding absolute cross-sections. We verified that the integrated peak intensities for selected fragment ions scale linearly with laser power, confirming the one-photon nature of the transitions. No anionic fragmentation of $\text{CO}_2^-(\text{H}_2\text{O})_m$ was observed at 532 nm.

The 355 nm spectra reveal two types of fragment anions: (1) $\text{O}^-(\text{H}_2\text{O})_{m-k}$, $1 \leq k \leq 3$, and (2) $\text{CO}_2^-(\text{H}_2\text{O})_{m-k}$, $4 \leq k \leq 9$. No hydrated electron clusters, $(\text{H}_2\text{O})_{m-k}^-$, are observed as fragments. The appearance of the $\text{O}^-(\text{H}_2\text{O})_{m-k}$ fragments implies the dissociation of the CO_2^- core of the cluster, followed by the escape of CO and evaporation of k H_2O molecules:



We will refer to all pathways defined by Eq. (1) collectively as the core-dissociation channel. The $\text{CO}_2^-(\text{H}_2\text{O})_{m-k}$ fragments will be described as water-evaporation products, formed via:



As evident from Fig. 3.3, the $\text{CO}_2^-(\text{H}_2\text{O})_m$, $m = 3-5$ cluster anions yield only the core-dissociation fragments. As the parent cluster size is increased, the water-evaporation fragments first appear at $m = 6$, with the smallest fragment of this type being $\text{CO}_2^-\cdot\text{H}_2\text{O}$. With m increasing further, the evaporation channel gradually takes over to become the dominant pathway for $m \geq 8$.

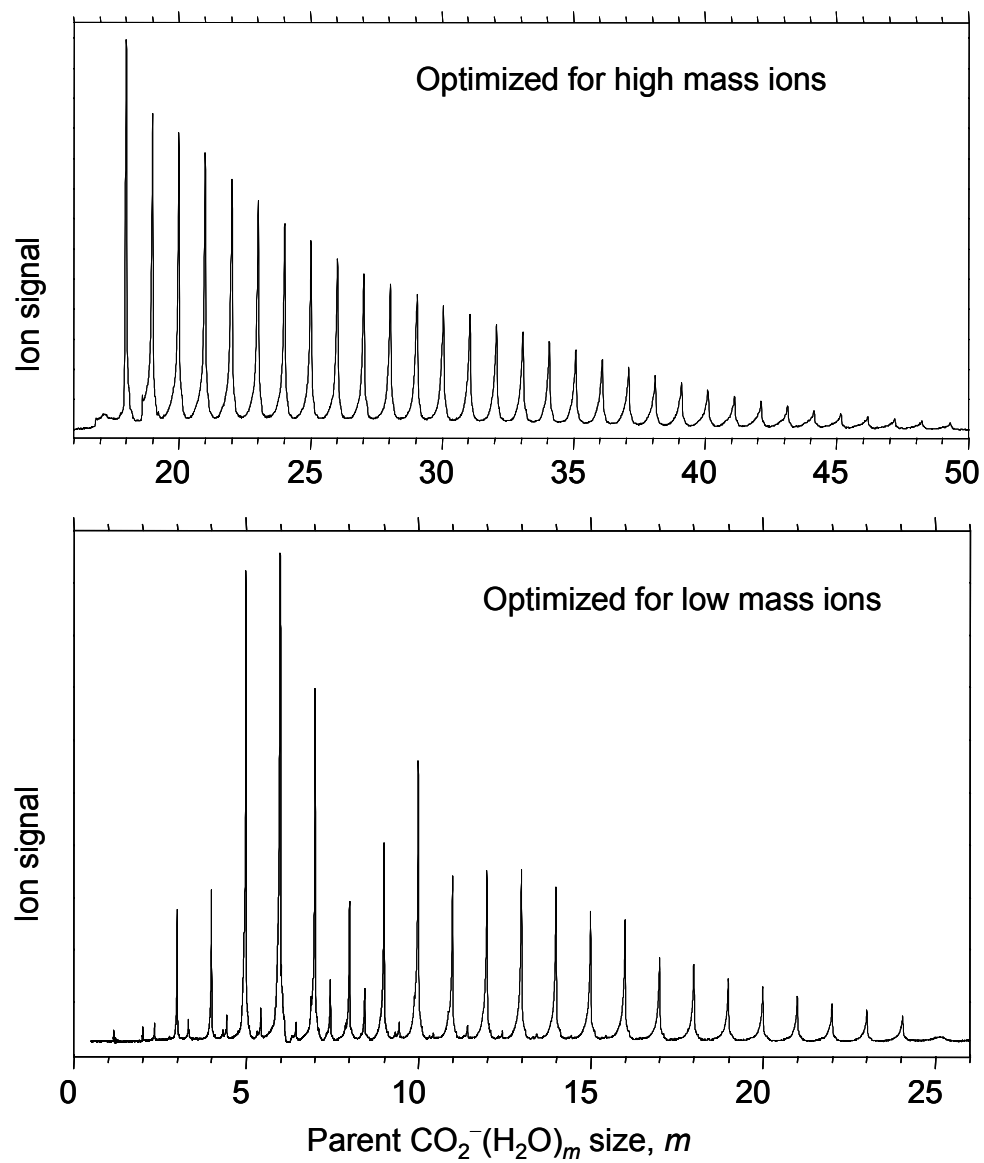


Figure 3.2 Parent ion mass-spectra of $\text{CO}_2^-(\text{H}_2\text{O})_m$ optimized for high mass (top) and low mass (bottom) ions.

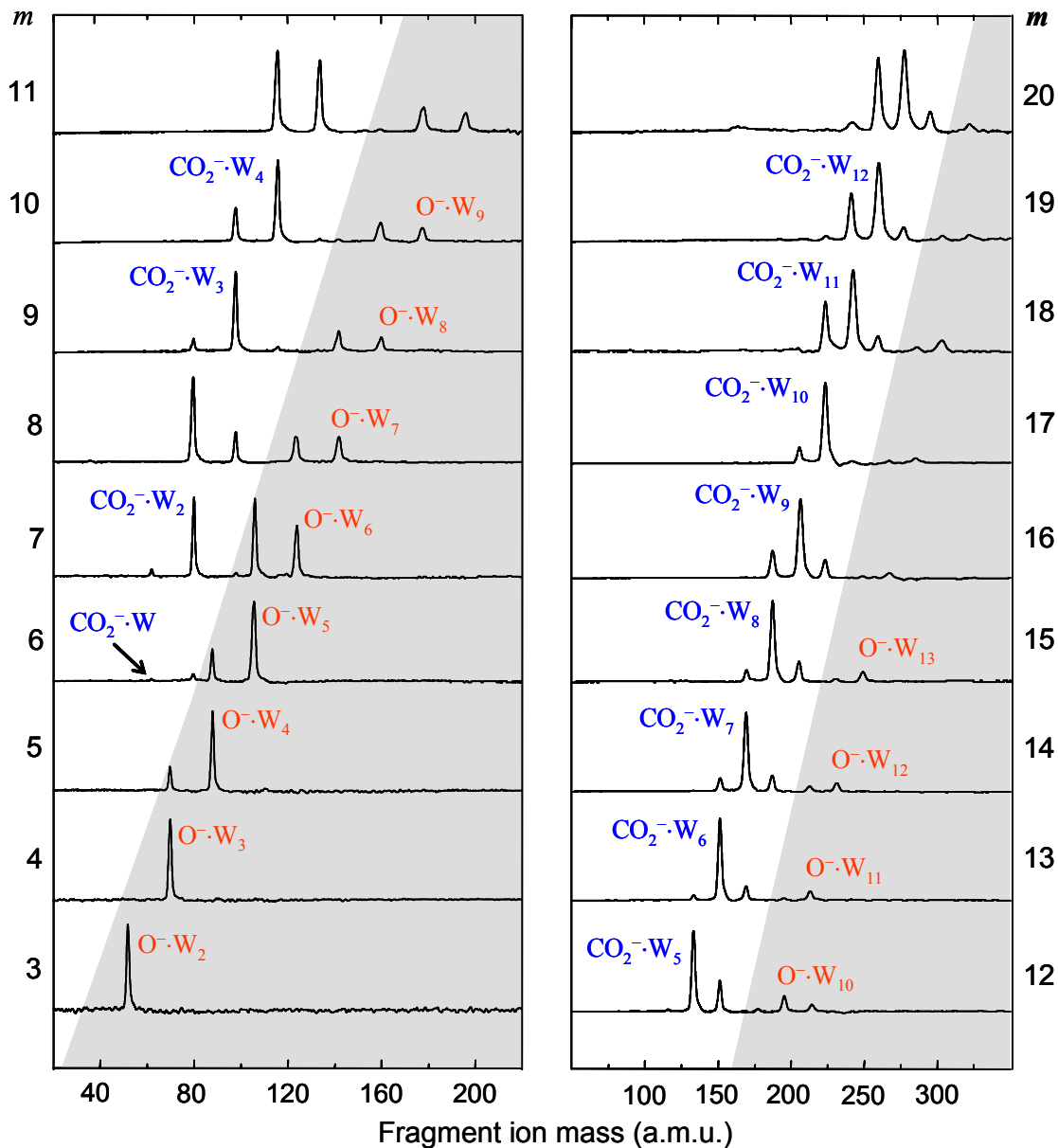


Figure 3.3 Photofragment-ion mass-spectra for the $\text{CO}_2^-(\text{H}_2\text{O})_m$ cluster anions at 355 nm. The numbers on the right and on the left indicate the number of water molecules, m , in the parent clusters. For clarity, the peaks assigned to the core-dissociation fragments, $\text{O}^-\cdot\text{W}_{m-k}$, are shown against the gray background. $\text{W} \equiv \text{H}_2\text{O}$.

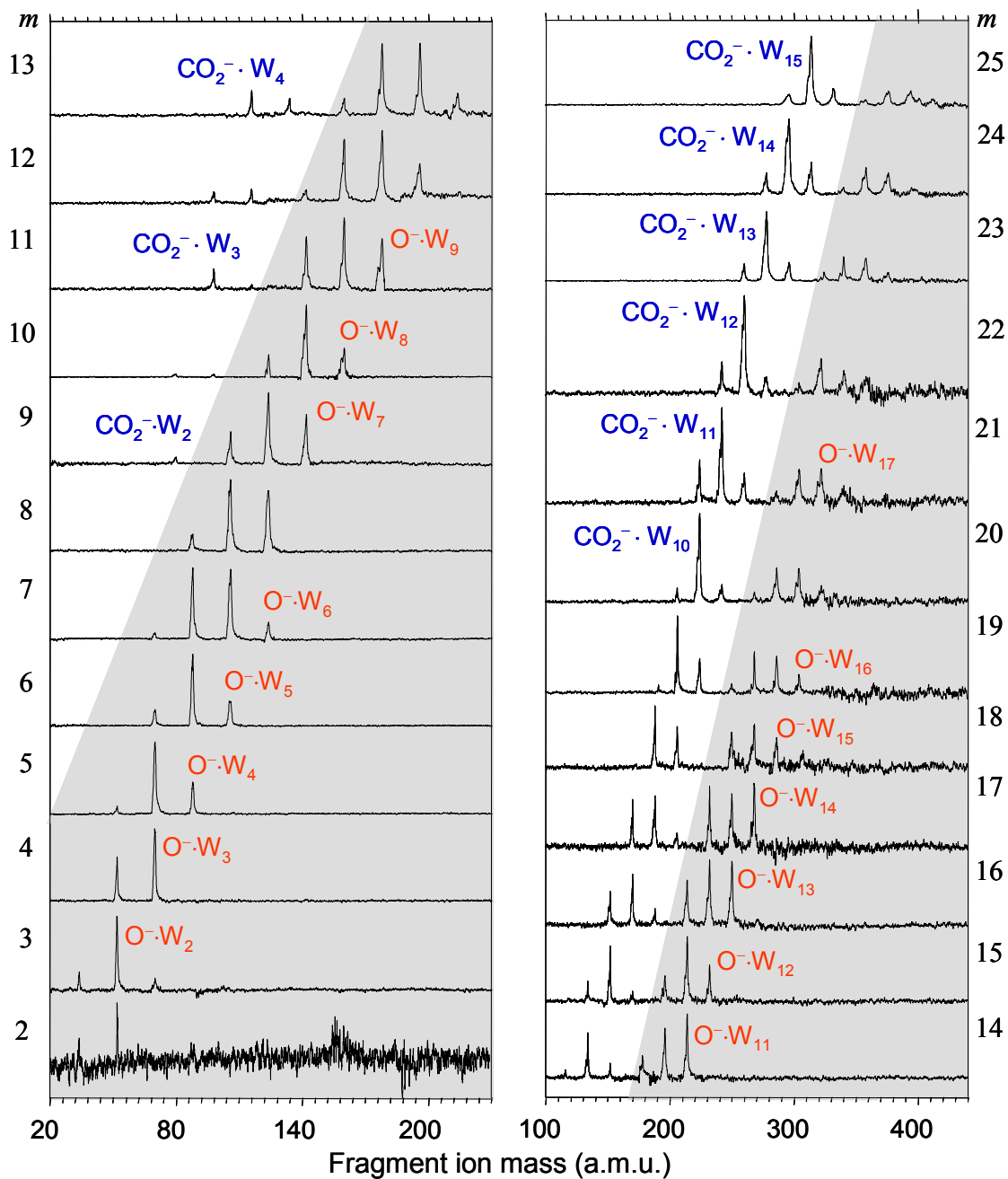


Figure 3.4 Photofragment-ion mass-spectra for the $\text{CO}_2^-(\text{H}_2\text{O})_m$ cluster anions at 266 nm. The numbers on the right and on the left indicate the number of water molecules, m , in the parent clusters. For clarity, the peaks assigned to the core-dissociation fragments, $\text{O}^-\cdot\text{W}_{m-k}$, are shown against the gray background. $\text{W} \equiv \text{H}_2\text{O}$.

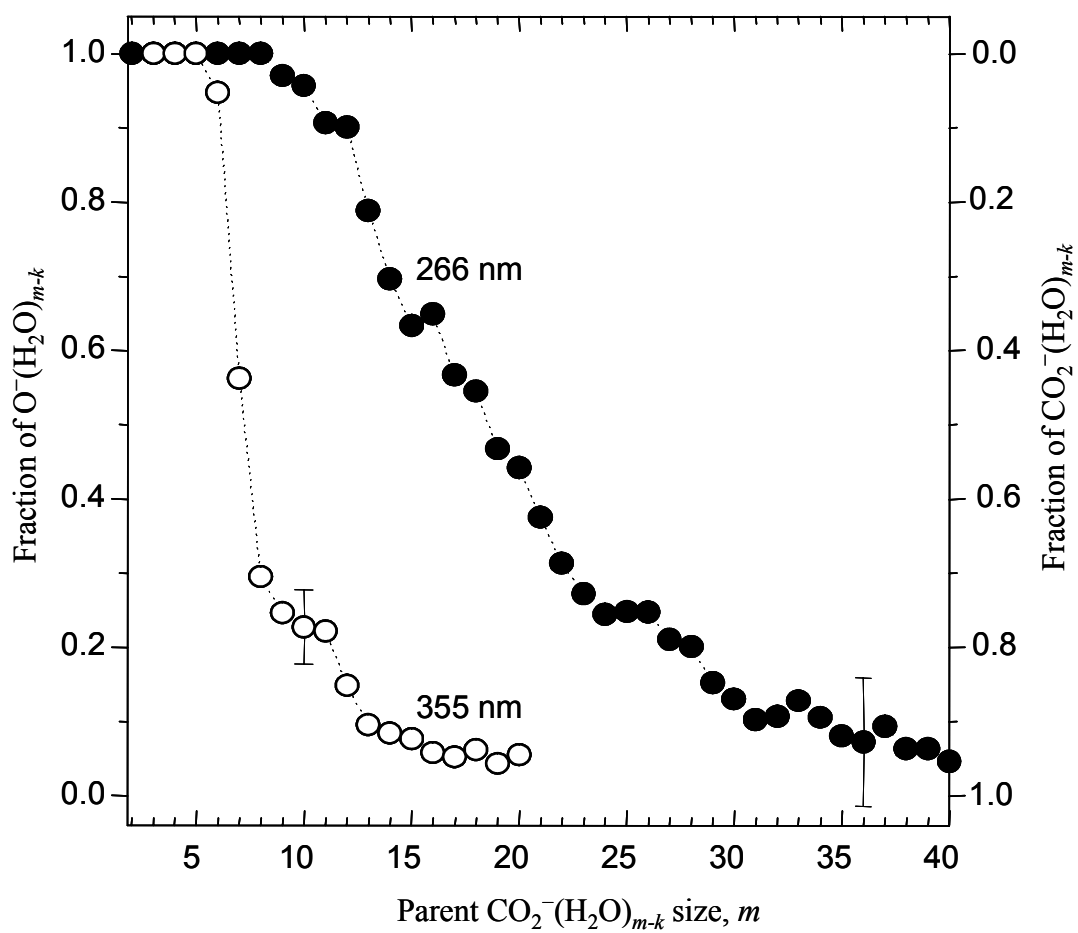


Figure 3.5 Fractions of the $\text{O}^-(\text{H}_2\text{O})_{m-k}$ and $\text{CO}_2^-(\text{H}_2\text{O})_{m-k}$ products observed in the photofragmentation of $\text{CO}_2^-(\text{H}_2\text{O})_m$ at 355 nm (open circles) and 266 nm (solid circles), plotted as functions of the parent cluster size.

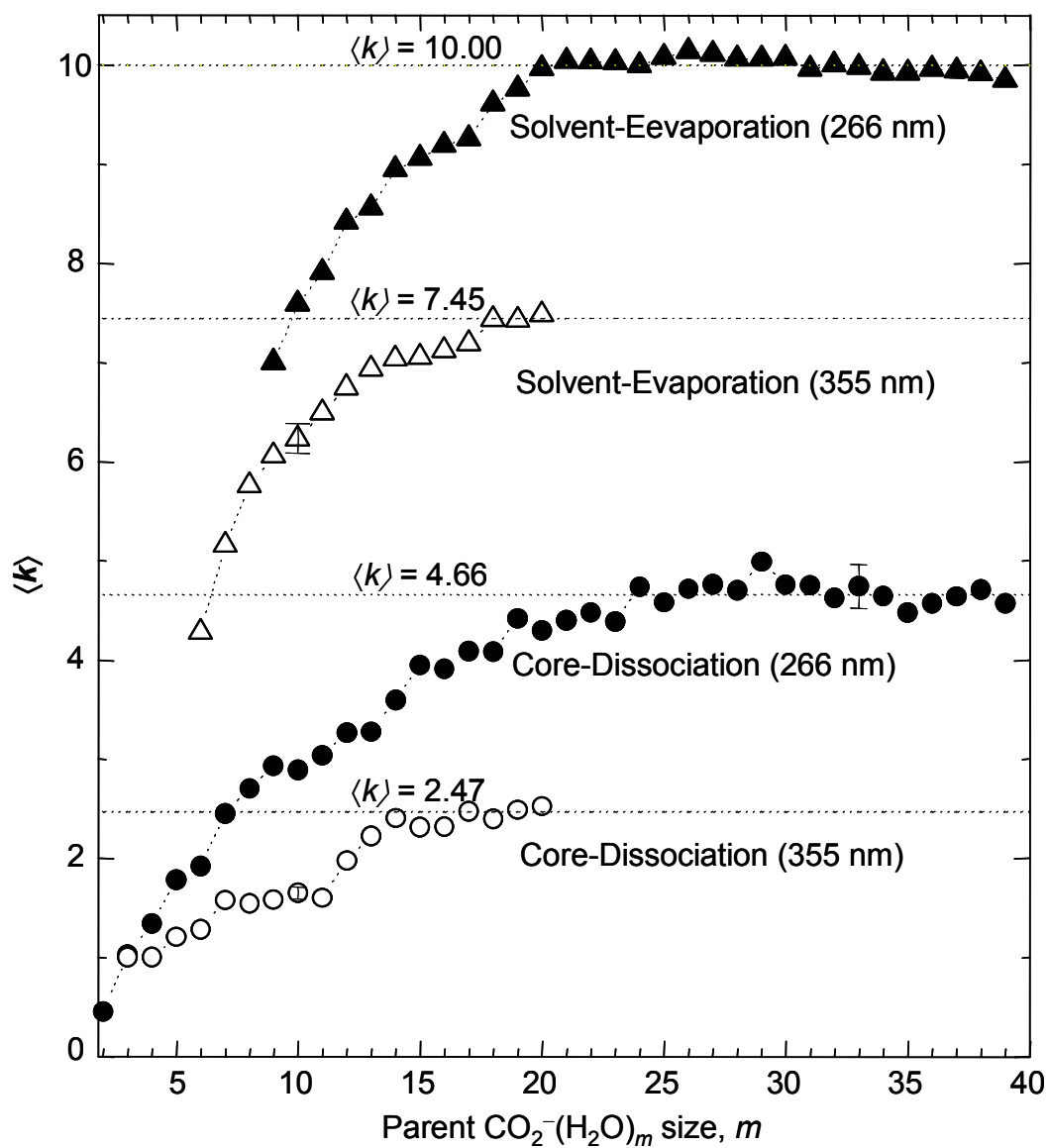


Figure 3.6 Average numbers of water molecules evaporated in the core-dissociation and solvent-evaporation channels at 355 and 266 nm, as labeled. The dotted horizontal lines indicate the asymptotic values of $\langle k \rangle$ for each process.

3.3.3 266 nm Results

The fragmentation measurements were performed at 266 nm on $\text{CO}_2^-(\text{H}_2\text{O})_m$ cluster anions with m up to 40. The photofragment-ion mass-spectra for $m = 2-25$ are shown in Fig. 3.4. The results for the larger clusters (up to $m = 40$) are included in the analysis, but the individual fragment mass-spectra are not shown to save space. The low signal-to-noise ratio apparent in the $m = 2$ spectrum reflects the weak intensity of the corresponding parent ion (as seen in Fig. 3.4), as well as the prevalence of the photodetachment.

Similar to the 355 nm study result,¹¹⁷ the observed fragmentation pattern can be summarized in terms of two types of anionic products: (1) $\text{O}^-(\text{H}_2\text{O})_{m-k}$ and (2) $\text{CO}_2^-(\text{H}_2\text{O})_{m-k}$. As the parent cluster size is increased, channel (2) opens at $m = 9$ (compared to $m = 6$ at 355 nm). The m dependent branching between channels (1) and (2) at 266 and 355 nm is summarized in Fig. 3.5.

The average loss of water molecules, $\langle k \rangle$, in different fragmentation channels is summarized in Fig. 3.6. For channel (1) at 266 nm, $\langle k \rangle$ varies between 0.5 and 4.7 depending on m (compared to $\langle k \rangle = 1.0 - 2.5$ at 355 nm), while channel (2) involves the average loss of between 7.0 and 10.0 (compared to $\langle k \rangle = 4.4 - 7.5$ at 355 nm) water molecules. $\langle k \rangle$ increases with m for small parent clusters, eventually approaching an asymptotic limit. Assuming that the asymptotic value of $\langle k \rangle = 10.0$ in channel (2) at 266 nm accounts for the dissipation of the entire photon energy, the average enthalpy of evaporation of one H_2O in the large-cluster limit is determined as 0.466 ± 0.001 eV (45.0

± 0.1 kJ/mol).

To shed light on the 266 and 355 nm fragmentation mechanisms, we compared the corresponding dissociation cross-sections using the integrated intensities of all photofragments normalized to the laser power and parent-ion intensity. For small parent clusters ($m = 3$), the 266 nm dissociation cross-section was found to exceed that at 355 nm by more than an order of magnitude. However, the ratio of the two decreases with m and for $m \approx 10$ the two cross-sections become approximately the same.

3.4 Potential Energy Surfaces of CO_2^- : The Need for Diffuse Basis Sets

The potential energy curves of CO_2^- ground and excited electronic states as a function of $\angle\text{OCO}$ bending angle and OC–O distance were calculated in 1970 using INDO semi-empirical method.¹¹⁸ This calculation predicted the energy curve of the anion as a function of the bending angle is be the neutral curve until an angle of 100° , which is not the case as we know now. The calculation by Krauss and Neumann¹¹⁹ using Hartre-Fock (HF) *ab initio* method with (9/5) atomic bases of Huzinaga predicted that the anion energy curve was indeed below the neutral energy curve for the bending angle less than $\sim 140^\circ$ as shown in Fig. 3.7(a). Both the INDO and HF calculations connect the anion ground state ($^2\text{A}_1$) and the first excited state $^2\text{B}_1$ to the $^2\Pi_u$ resonance state as the angle is increased towards the neutral geometry (180°). However, our calculation using the coupled-cluster method with single, double, and perturbative triple excitations, CCSD(T), with Dunning's aug-cc-pVTZ basis set revealed that the $^2\text{A}_1$ state does not correlate to the $^2\Pi_u$ state. This result is shown in Fig. 3.7(b).

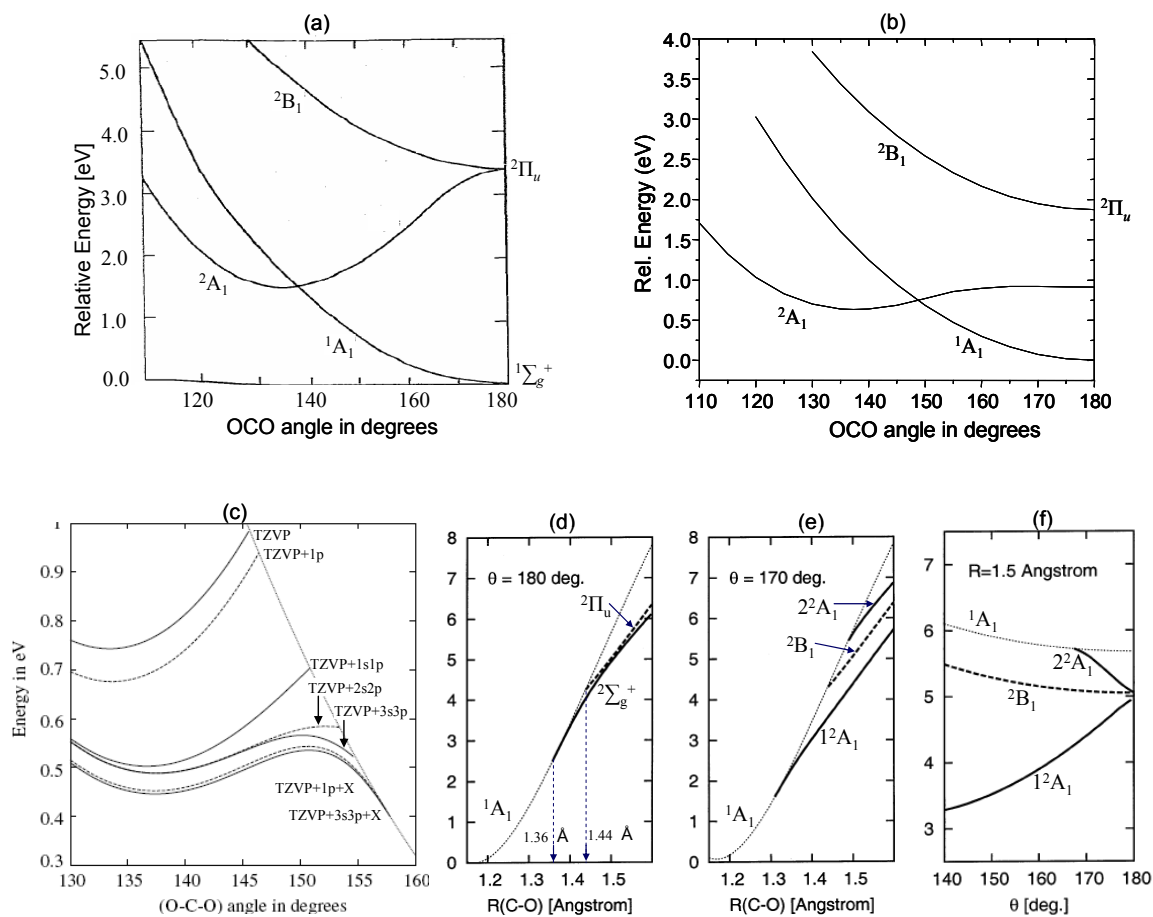


Figure 3.7 Potential energy curves of CO_2^- : (a) Using HF with small basis sets (ref. ¹¹⁹). (b) From this work using CCSD(T)/aug-cc-pVTZ. (c) From ref. ¹²⁰. (d)-(f) Using EOM-CCSD method with aug-cc-pVTZ+4s4p2d basis set (from ref. ¹²¹).

Calculating the EA of CO₂ using ADC(2) with different basis sets including diffuse functions [indicated on the curves in Fig. 3.7(c)] and then converting the results into potential energy curves using CCSD(T), Sommerfeld illustrated the basis set dependence of electronic ground state CO₂⁻ potential energy surface.¹²⁰ As shown in Fig. 3.7 (c) when very diffuse functions are used, the adiabatic anion potential energy surface increases to a barrier height and then drops even below the anion equilibrium energy before crossing with the neutral surface. This theoretical prediction has an earlier experimental backing; the electron scattering experiment by Allan¹⁰⁶ on CO₂ revealed vibrational structures in the 0.4-0.9 eV range, compared to for the ²Π_u resonance that appears above 3.2 eV. The calculation was later extended to include the components of ²Π_u using equation-of-motion CCSD (EOM-CCSD) method with aug-cc-pVTZ basis sets augmented with [4s4p2d] set of diffuse functions.¹²¹ The main results are shown in Fig. 3.7(d)-(f). Figure 3.7(d) illustrates that as the OC–O distance stretches the virtual ²Σ_g⁺ state becomes bound before the resonance ²Π_u state. At bent geometry the virtual ²Σ_g⁺ state converts to the ²A₁ state and the doubly degenerate ²Π_u state splits into ²A₁ and ²B₁ Renner-Teller components as shown in Figs. 3.7 (e) and (f). Sommerfeld *et al.* suggested that the three states are coupled by vibronic motions.¹²¹

Allan's experimental result and the results of the calculations suggest that in the proximity of the neutral states ($\angle\text{OCO} \geq 145^\circ$) the electronic state of CO₂⁻ can not be described using ordinary *basis sets* due to the extremely diffuse nature of the anionic state in this region. In our experiment, however, CO₂⁻ is trapped in water network. In the

following sections we will address the stabilization of the metastable anion by hydration.

3.5 Trapping the Excess Electron in CO_2^- by Solvent Stabilization

As seen in Fig. 3.7(c), the energy minimum of isolated CO_2^- is separated by a small energy barrier from the lower energy neutral CO_2 minimum. As a result the anion has a maximum life time of 90 μs against autodetachment. However, due to stronger interaction of water molecules with the CO_2^- anion than with the neutral, the anion can be stabilized in the presence of solvent molecules. The different pattern of interactions of the neutral and anion with water molecules can be realized by referring to the optimized (using MP2/6-311++G**) structures presented in Fig. 3.8. For $m = 1$, CO_2 is very weakly bound to H_2O forming a T-shaped structure^{122,123} while both oxygen atoms of CO_2^- are hydrogen bonded forming a C_{2v} ring structure. For $m \geq 2$, the structure of pure neutral water clusters, $(\text{H}_2\text{O})_m$,¹²⁴⁻¹²⁶ remains essentially unperturbed in the presence of neutral CO_2 . In contrast, in the $(\text{CO}_2^-\text{H}_2\text{O})_m$ cluster anions all the free OH's are pointing towards CO_2^- where the excess electron is localized, forming hydrogen bonds with the terminal oxygen atoms, and competing for the excess electron. The shorter OCO----HOH distances in the anion than in the neutral is the manifestation of the stronger electrostatic interaction in the former.

In terms of potential energy curves, the most obvious effect of hydration is the lowering of the equilibrium energy of metastable CO_2^- with respect to that of the neutral. Consequently, the height of the barrier also increases, impeding the anion tunneling into the region of the coordinate space where rapid autodetachment will occur, effectively

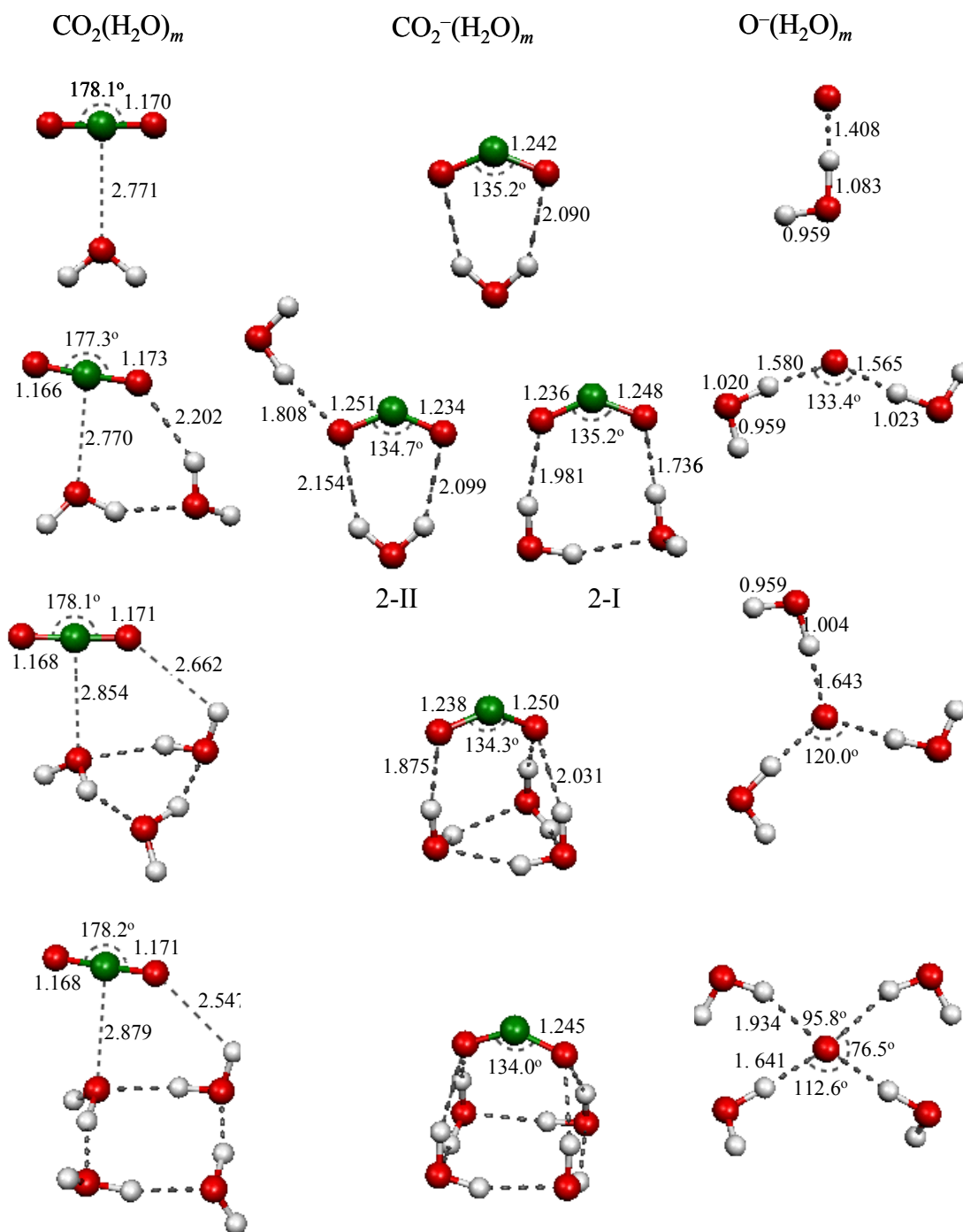


Figure 3.8 Calculated global minimum structures of $\text{CO}_2(\text{H}_2\text{O})_m$ neutral, $\text{CO}_2^-(\text{H}_2\text{O})_m$ anion and $\text{O}^-(\text{H}_2\text{O})_m$ anion. The structures are optimized using MP2/6-311++G** level of theory. For $\text{CO}_2^-(\text{H}_2\text{O})_m$, $m=2$, two structures, labeled as 2-I and 2-II, are obtained with small energy difference: 2-II is ~ 0.02 eV higher in energy.

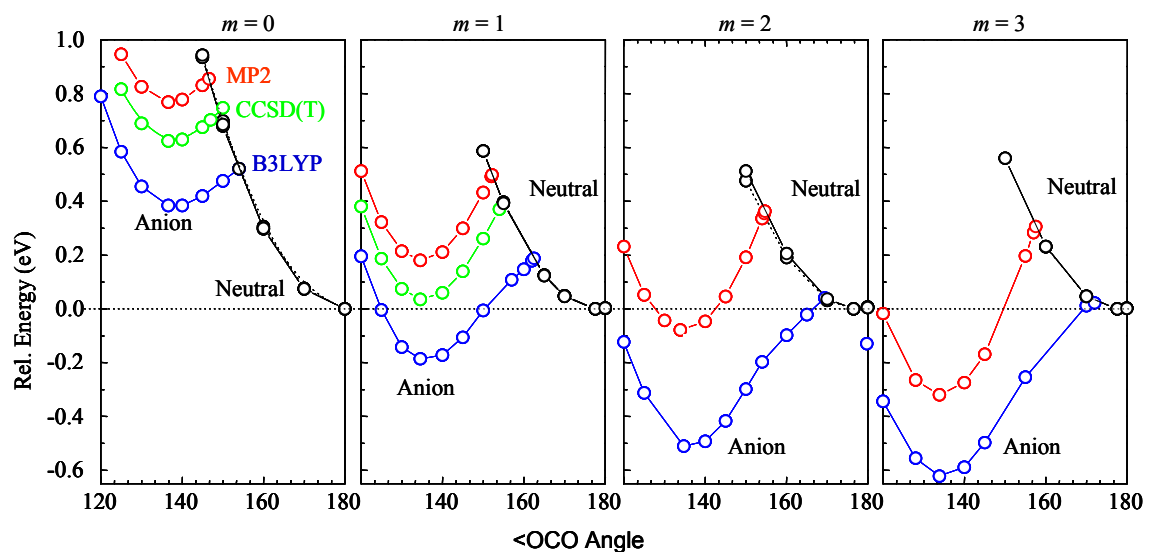


Figure 3.9 The OCO bending angle dependence of the relative potential energies of $\text{CO}_2^-(\text{H}_2\text{O})_m$ versus $\text{CO}_2(\text{H}_2\text{O})_m$, $m = 0, 1, 2$ and 3 , calculated using the *ab initio* and density-functional methods, as described in the text.

trapping the anion in its equilibrium nuclear configuration. The barrier plays a critical role in determining the anion stability. Referring to it as the autodetachment barrier, we explore how its height is affected by the hydration in the $\text{CO}_2^-(\text{H}_2\text{O})_m$ cluster anions.

As discussed in Sec. 3.4, modeling of the anionic states of carbon dioxide and its hydrates requires highly correlated methods and large basis sets including very diffuse functions, which are rather challenging to apply to large cluster anions. However, the approximate effect of stepwise hydration on the anion stability can be estimated using computationally inexpensive methods and basis sets. We calculated the bending potential energy curves for the anion and neutral species of interest using the following procedure.

First, the geometries of $\text{CO}_2^-(\text{H}_2\text{O})_m$, $m = 0-3$ and the corresponding neutral clusters were optimized using MP2/6-31+G* calculations. The global-minimum geometries of the $\text{CO}_2^-(\text{H}_2\text{O})_m$, $m = 0-3$ cluster anions are shown in Fig. 3.8. The geometries of the neutral species were optimized starting from the corresponding anion equilibria. The resulting structures of the $m = 1, 2$ neutral clusters compare favorably with the previous experimental^{122,123,127-130} and theoretical^{114,131-134} results (see structures in Fig. 3.8). There is no experimental data available for the $m = 3$ neutral structure, but our optimized geometry agrees with the previously reported B3LYP result.¹¹⁴

Then, the OCO bending angle was scanned in 5-10° steps, starting from the corresponding anion and neutral equilibrium geometries. At each fixed bending angle, all other cluster degrees of freedom were optimized at the MP2/6-31+G* level. The resulting geometries were used in single-point MP2, CCSD(T) and B3LYP calculations with aug-cc-pVTZ basis set to determine the corresponding potential energy values. The resulting

energy curves are shown in Fig. 3.9, where the neutral energy minima are set arbitrarily to zero. The calculations at CCSD(T) are limited to $m = 0$ and 1 due to computational cost.

As seen in Fig. 3.9 the minima of the anions with respect to the neutral various based on the method used. According to the result from B3LYP, MP2 and CCSD(T) the CO_2^- minimum (after correcting for the zero point energy) lies 0.34, 0.58 and 0.72 eV, respectively, above the neutral minimum. The CCSD(T) result is the closest to the experimental electron affinity value of -0.60 ± 0.2 eV.¹⁰⁷ Although the values differ depending on the level of theory used, in all cases the minima of the anions with respect to that of the neutral decreases as m increases. The electron affinity becomes positive for $m \geq 2$ regardless of the methods used.

In addition to minimizing the anion energy hydration also increases the autodetachment barrier height. Although the level of theories used are inadequate to accurately calculate the potential energy surfaces in the proximity of the neutral state, the barrier height can reasonably be approximated as the energy of the anion (relative to its minimum) at $\angle\text{OCO}$ angle where the anion and the neutral have nearly the same energy. Since both the anion and the neutral geometries are optimized independently at a fixed angle the energy can be viewed as a lower bound. The approximate energy barrier height (BH) for $m = 0-3$ obtained from the different methods is summarized as follows.

m	BH (meV)		
	CCSD(T)	MP2	B3LYP
0	96	87	136
1	355	319	374
2		441	550
3		626	644

Table 3.1 Vertical detachment energies (VDE) of $\text{CO}_2^-(\text{H}_2\text{O})_m$, $m = 0-5$ calculated as described in the text using the MP2 and B3LYP methods with the aug-cc-pVTZ basis set, compared to the experimentally determined values.

m	VDE (eV)		
	MP2	B3LYP	Expt
0	0.77	1.19	1.4 ^a
1	1.65	2.06	1.96 ^b
2	2.17	2.61	2.44 ^b
3	2.60	2.97	2.85 ^b
4	2.91	3.28	3.21 ^b
5	3.18	3.62	3.46 ^b

^a Reference ¹³⁵

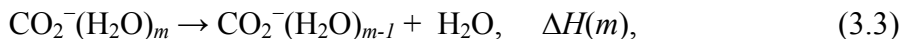
^b Reference ¹¹⁶

All the level of theories employed here show that the BH increases with m . In addition, the OCO angles where the anion and the corresponding neutral curves intersect increase with m . This trend suggests that for large m the optimized potential energy curve of anion state may lie below the neutral state curve for all OCO angles. In summary, the results presented in Fig. 3.9 reveal the dual effect of stepwise hydration: (1) the stabilization of the anion equilibrium relative to the neutral potential minimum, and (2) the increase in the autodetachment barrier height. Both of these factors contribute to the increased stability of hydrated CO_2^- .

The VDEs of $\text{CO}_2^-(\text{H}_2\text{O})_m$, $m = 0-5$ are calculated using B3LYP and MP2 with aug-cc-pVTZ basis set. The VDE is determined by calculating the single point energy of the anion and the neutral at the anion equilibrium geometry. For the DFT calculation the geometries in ref.¹¹⁴ optimized using B3LYP/6-311++G(3df,3pd) are used, and for MP2 we used the geometries optimized at MP2/6-311++G**. The conflicting VDE predictions by the MP2 and B3LYP methods for the $\text{CO}_2^-(\text{H}_2\text{O})_m$, $m = 0-5$ cluster anions are summarized in Table 3.1. For all cluster sizes the VDEs obtained from B3LYP are closer to the experimental values^{26,116,135} than the MP2 values, which are always less than the observed values. We note that similar discrepancies between MP2 and B3LYP were described previously in the case of OCS.¹³⁶

3.6 Water Binding Energy

The enthalpy of evaporation of a water molecule from $\text{CO}_2^-(\text{H}_2\text{O})_m$, $\Delta H(m)$, can be determined from the energy balance of the following reaction:



From the data in Fig. 3.6, the asymptotic limit of $\Delta H(m)$ is 45.0 kJ/mol (for $m \geq 20$). However, $\Delta H(m)$ is expected to deviate significantly from the asymptotic limit as m decreases, generally corresponding to larger values for smaller clusters.

From the B3LYP/6-311++G(3df,3pd) calculations, Bondybey and co-workers estimated the dissociation enthalpy of $\text{CO}_2^-(\text{H}_2\text{O})_m$, $m = 0-5$ at 1 atm and 298 K.¹¹⁴ Their results are plotted in Fig. 3.10 (open circles), with the horizontal line indicating the asymptotic limit of $\Delta H(m)$ derived from the present experiments. Despite the different pressure-temperature conditions, one should expect the size-dependent theoretical values to approach the experimental asymptotic limit from above, as m increases. As this is not what is seen in Fig. 3.10, we conclude that DFT underestimates the hydration energetics.

For comparison, after optimizing the $\text{CO}_2^-(\text{H}_2\text{O})_m$, $m = 0-5$ cluster structures at the MP2/6-311++G** level (giving the same geometries as in ref.¹¹⁴, except for $m = 5$, for which a more stable structure was found²⁶), we calculated single-point MP2 energies with the 6-311++G(3df,3pd) basis set. The corresponding $\Delta H(m)$ values are plotted in Fig. 10 (solid circles). The MP2 predictions are clearly in better agreement with the experiment than the B3LYP results. Combining this observation with the adiabatic electron affinity and VDE calculations in Sec. 3.5, we infer that B3LYP provides a fair estimate of the electron binding energy, but not the water binding energy. For the latter, the MP2 results are more consistent with our experimental observation.

The experimentally estimated asymptotic limit of $\Delta H \rightarrow 45.0$ kJ/mol for large m , is

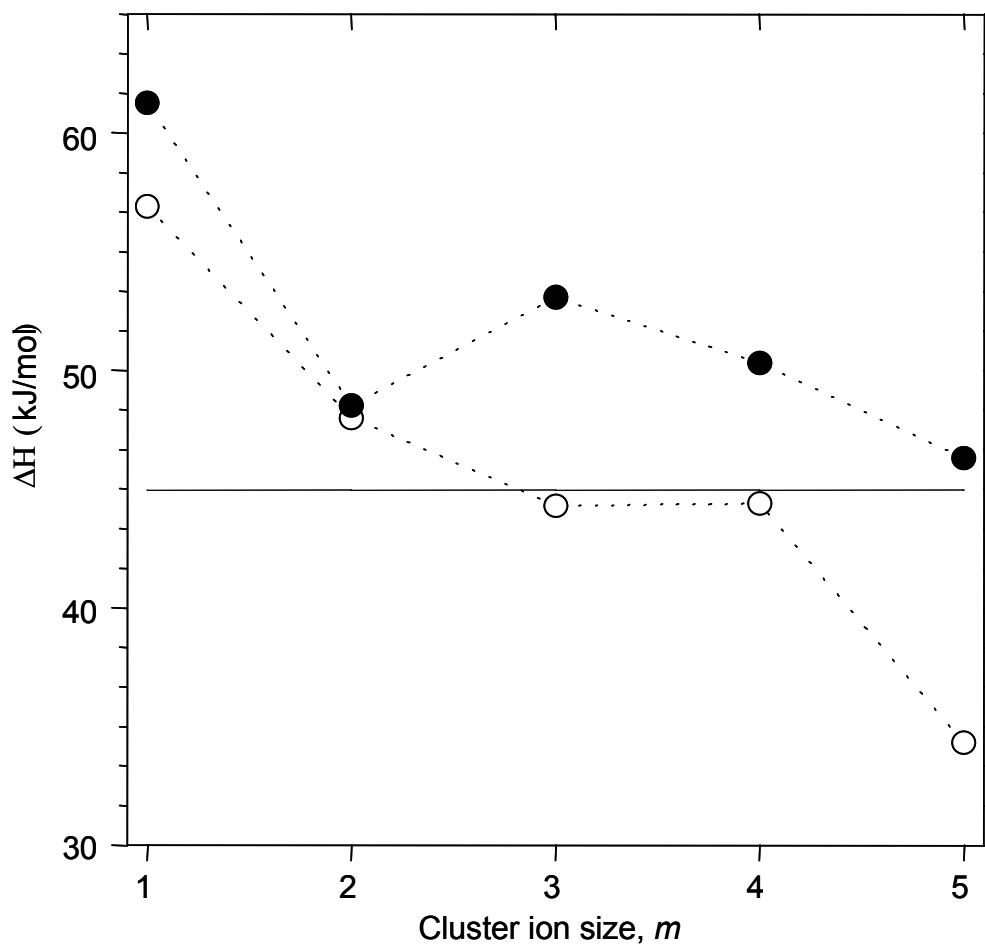


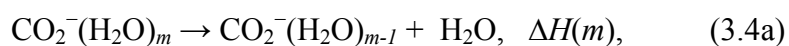
Figure 3.10 Calculated enthalpy of evaporation (ΔH) of one water molecule as a function of $\text{CO}_2^-(\text{H}_2\text{O})_m$ cluster size: $\text{CO}_2^-(\text{H}_2\text{O})_m \rightarrow \text{CO}_2^-(\text{H}_2\text{O})_{m-1} + \text{H}_2\text{O}$, $\Delta H(m)$. The open and solid circles represent the values obtained using the B3LYP/6-311++G(3df,3pd) and MP2/6-311++G(3df,3pd) methods, respectively. The solid horizontal line indicates the asymptotic limit of $\Delta H(m)$ determined in the present experiments.

very close to the heat of evaporation of bulk water at 25°C, 43.98 kJ/mol (0.456 eV per molecule).¹³⁷ This implies that in large $\text{CO}_2^-(\text{H}_2\text{O})_m$ clusters ($m > 20$), the outermost water molecules interact predominantly with the water network rather than with the anionic core of the cluster.

3.7 OC-O^- Bond Energy in Water Cluster

As seen in Fig. 3.5, in the large m limit of the core-dissociation channel, the average number of water molecules evaporated at 266 nm (4.66 eV) exceeds that at 355 nm (3.49 eV) by 2.2. This compares to the average difference of 2.5 molecules expected under the assumption that the evaporation of one H_2O requires 0.466 eV (see Sec. 3.3.3). This fairly close agreement confirms that the energetics are approximately accounted for and the core-dissociation pathways at both wavelengths yield fragments in the same electronic states.

In the 266 nm core-dissociation channel, the average number of evaporated water molecules is $\langle k \rangle = 4.66$ for $m \geq 20$. Given the estimated 0.466 eV evaporation energy per molecule, approximately $4.66 \times 0.466 \text{ eV} = 2.17 \text{ eV}$ of the 266 nm photon energy is spent on water evaporation and only the remaining 2.49 eV, at the most, is used to dissociate the OC-O bond. This estimate is meaningful only if the energetics of the following two reactions in large clusters are comparable:



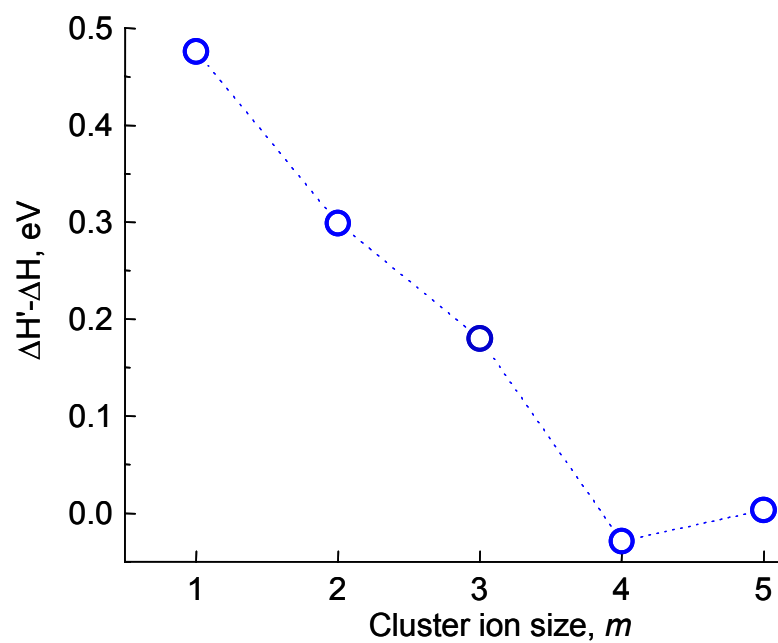


Figure 3.11 A water molecule binding energy difference ($\Delta H' - \Delta H$) as a function of solvent cluster size, m . $\Delta H(m)$ and $\Delta H'(m)$ are defined in reaction equations (3.4a) and (3.4b), respectively. The energy is determined using MP2 method with aug-cc-pVTZ basis set.

Using MP2/aug-cc-pVTZ single point energy calculations on the geometries optimized at MP2/6-311++G** (see structures in Fig. 3.8) $\Delta H'(m)$ at 298 K and 1 atm was estimated as 1.076, 0.791, 0.662, and 0.478 eV for $m = 0, 1, 2, 3$ and 4, respectively, including the zero-point energy corrections. Given the $\Delta H(m)$ values provided in Sec. 3.6, the difference between the water binding energies for the O^- and CO_2^- based clusters can be estimated as $\Delta H' - \Delta H = 0.476, 0.299, 0.180, -0.029,$ and 0.003 (plotted in Fig. 3.11) for $m = 0, 1, 2, 3, 4$ and 5, respectively. A similar trend can be obtained by combining the results of the density functional calculations by Balaj *et al.*¹¹⁴ on $\text{CO}_2^-(\text{H}_2\text{O})_m$, and by Seta *et al.*¹³⁸ on $\text{O}^-(\text{H}_2\text{O})_m$. Hence the difference between $\Delta H'$ and ΔH becomes small in the limit of large m . This is because the interaction of a water molecule in large cluster size is mainly with the water cluster rather than with the anion core. Therefore, the above estimate for the energy required to break the OC–O[−] bond in large $\text{CO}_2^-(\text{H}_2\text{O})_m$ clusters, 2.49 eV, is reasonable. This value is ~ 0.1 eV less than the OC–O bond dissociation energy of isolated CO_2^- (3.46 eV). The large difference in the bond energies for isolated and hydrated CO_2^- reflects the strong interaction between the water cluster and the anion core through H-bonding.

3.8 Core-Dissociation Mechanism

The first two absorption bands of CO_2^- trapped in crystalline sodium formate were observed at 340 and 250 nm and assigned to the ${}^2\text{B}_1 \leftarrow \text{X}^2\text{A}_1$ and ${}^2\text{A}_1 \leftarrow \text{X}^2\text{A}_1$ electronic transitions, respectively.¹³⁹ The former transition was also seen at 365 nm, under a

different procedure of crystal preparation.¹⁴⁰ The 250 nm transition was also observed in aqueous solution.^{101,102} The photofragmentation at 355 nm has been suggested to involve the ${}^2B_1 \leftarrow X^2A_1$ transition.¹¹⁷ The 266 nm wavelength is closer to the second, ${}^2A_1 \leftarrow X^2A_1$ band, leading us to believe that the $CO_2^-(H_2O)_m$ cluster fragmentation at 355 and 266 nm may proceed via different excited electronic states of hydrated CO_2^- .

The ${}^2B_1({}^2A'')$ state, which was suggested to be excited at 355 nm, does not correlate with the $O^- + CO$ product. As shown in Fig. 3.12 it correlates with the energetically inaccessible $CO^- + O$ products. The $X^2A_1({}^2A')$ state potential energy surface converges to $O^- + CO$ products in the limit of large $OC-O^-$ distance. Since the potential gradient of the excited state directs the excited complex towards the linear geometry, the dissociation was suggested to occur on the $X^2A_1({}^2A')$ surface after the excited state population is transferred to the ground state assuming that $X^2A_1({}^2A')$ and ${}^2B_1({}^2A'')$ belong to the resonance ${}^2\Pi_u$ state and are Renner-Teller coupled at linear geometry. However, as shown in Fig. 3.7(b) and (c), the ground state does not correlate with the ${}^2\Pi_u$ state at linear geometry. The ground adiabatic $X^2A_1({}^2A')$ potential energy surface is connected with the virtual ${}^2\Sigma_g^+$ state at linear geometry.¹²¹ On the other hand, even though the potential energy curve of X^2A_1 state is not connected to the ${}^2\Pi_u$ state adiabatically, it is believed that at the anion equilibrium the excess electron occupies the lowest unoccupied molecular orbital of the neutral CO_2 which is the X^2A_1 component of the ${}^2\Pi_u$. In other words, starting from the anion equilibrium as the OCO angle increases, the ground state curve may connect to the ${}^2\Pi_u$ resonance state diabatically. Therefore, one can infer a

conical intersection between the valence and the virtual state close to the nuclear configuration where the anion and the neutral states are crossing.

As mentioned above, in our first report¹¹⁷, we proposed that the 355 nm dissociation of CO_2^- in water cluster is mediated by the Renner-Teller coupling of the X^2A_1 ($^2A'$) and 2B_1 ($^2A''$) states. However, it appears now that this mechanism is inconsistent with our experimental observations. (i) If the dissociation is controlled by Renner-Teller interaction it also involves conical-intersection as mentioned above. Both of these interactions take place in the region of nuclear configurations where electron autodetachment competes effectively. Therefore, the dissociation cross-section would have been much weaker than it was observed. (ii) The Renner-Teller coupling occurs at $\angle\text{OCO} \approx 180^\circ$ where CO_2 does not have electron binding tendency. In this case, $(\text{H}_2\text{O})_{m-k}$ fragments should have been the major products because there would be probability of losing CO_2 neutral every time it passes linearity leaving the excess electron on the surface of water cluster.

Therefore, in order to propose more plausible dissociation mechanism it is important to take into account the perturbation effect of water molecule on the electronic structure of CO_2^- cluster core. To start with, the 355 nm photon energy (3.49 eV) is barely enough to initiate dissociation of bare CO_2^- into $\text{O}^- + \text{CO}$ (dissociation energy ≈ 3.46 eV). As discussed in Sec. 3.7, the dissociation energy decreases to 2.49 eV in water cluster, a consequence of strong weakening of $\text{OC}-\text{O}^-$ bond due to the interaction with the water cluster. The dissociation channel opens at $m = 3$ at 355 nm and the cross-section increases with m . The solvent molecules enable the dissociation by slowing down the

photodetachment channel and by differentially shifting the electronic states. In addition, the strength of the interaction of the solvent cluster with OC–O[−] cluster core depends on the dissociation reaction coordinate.

To shed light on the hydration effect on the CO₂[−](H₂O)_{*m*} excited state geometry as opposed to bare CO₂[−], we have optimized the global minimum structures of the ²B₁ excited state for *m* = 0 and 1 using MP2/6-311+G(3df). According to this theory the OCO angles are 180.0° and 175.8° for *m* = 0 and 1, respectively. The deviation from linearity is expected to remain approximately the same or higher in larger water clusters where our experiment is conducted. This is consistent with our intuition that in the presence of strong H-bonding to the terminal oxygen atoms, the energy partitioned into the bending mode motion may not be sufficient to take CO₂[−] cluster core to linear configuration. Although the deviation of the ²B₁ minimum may not be sufficient to impede the vibronic motion completely from reaching to the linear configuration (considering the zero point energy), it may reduce the strength of the Renner-Teller coupling interaction especially as the solvent cluster size increases.

There is no detailed theoretical work for the excited-state potential energy surfaces of CO₂[−] relevant to the 355 and 266 nm photodissociation in literature. As early as 1970, Claydon et al.¹¹⁸ used semi-empirical (INDO) methods to calculate the potential energy curves of CO₂[−]. Other theoretical studies on CO₂[−] targeted mainly the ground *X* ²A₁ and first excited ²B₁ states usually calculating the energy curves as a function of OCO angle.^{119-121,141-145} Therefore, we opted to examine the excited electronic states of CO₂[−] in the vicinity of equilibrium nuclear configuration using the configuration-interaction

method with single excitations (CIS). The calculations are carried out for both the isolated and hydrated anions, $\text{CO}_2^-(\text{H}_2\text{O})_m$, with $m = 0, 1$, and 2 . For $m = 2$, the planar isomer (structure 2-II shown in Fig. 3.8) is used in the calculation. For larger clusters, it is assumed that the main features of the electronic structure, dissociation mechanism, and hydration effects can be understood on the basis of the available results.

All molecular and cluster geometries were constrained to C_s symmetry, under which the irreducible representations of the C_{2v} point group transform as: $A_1, B_2 \rightarrow A'$; $A_2, B_1 \rightarrow A''$. The constrained $\text{CO}_2^-(\text{H}_2\text{O})_m$, $m = 0-2$ geometries were optimized at either fixed OCO bending angles or fixed OC–O bond distances. The results of these potential energy scans for the low-lying electronic states of $\text{CO}_2^-(\text{H}_2\text{O})_m$, $m = 0-2$ are shown in Fig. 3.13. Since the level of calculation employed provide only semi-quantitative information we consider the potential energy curves in Fig. 3.13 as a schematic representation. The schematics provide a qualitative guide to the electronic structure and dissociation dynamics of hydrated CO_2^- .

In addition to the electronic wave function symmetry, each state in Fig. 3.13 is assigned an *italic* label reflecting the energetic state ordering at the equilibrium geometry of bare CO_2^- . While the order of states may change with geometry and hydration, the italicized labels uniquely identify the relevant electronic states throughout the following discussion. For example, the 3^2B_2 state, which is the third excited state at the CO_2^- equilibrium geometry, is found below the X^2A_1 state for bending angles less than $\sim 101^\circ$, as seen in Fig. 3.13(a) for $m = 0$. This change in the 2B_2 and 2A_1 state ordering is similar to that in the isoelectronic NO_2 .¹⁴⁶⁻¹⁴⁹ (No attempt was made to explore the X^2A_1 and 3^2B_2

states crossing region in the presence of water molecules.) It is interesting to note that the energy gaps between X^2A_1 ($^2A'$) and I^2B_1 ($^2A''$) increase with m reflecting the different extent of solvent interaction with different electronic states. The CIS result for X^2A_1 ($^2A'$), I^2B_1 ($^2A''$) and 4^2A_2 ($^2A''$) shown in Fig. 3.13(b) for $m = 0$ qualitatively agrees with the MP2/6-311+G(3df) result shown in 3.12.

For small m at the anion equilibrium geometry all the anionic excited electronic states lie above the neutral state, see Fig. 3.12. However, although photodetachment (and or autodetachment) of electron is the dominant channel, dissociation channel is observed for parent clusters as small as $m = 2$ (see Fig. 3.4). This implies that despite the fact that the neutral state lies below the anion excited states the water molecules enable the interaction of the anionic excited states that leads to the dissociation. As m increases first the autodetachment of the ground state through tunneling is prevented. One water molecule is enough for this purpose.¹⁰⁹ Although direct photodetachment is dominant until $m \approx 6$ at 266 nm, the competition with photodissociation channel starts at $m = 2$. At lower photon energy, 355 nm, the excited state can also decay through autodetachment as reflected in the loss of the anisotropy of the photoelectron images with increasing m as seen in Fig. 1 (a). As m increases further dissociation becomes the important channel.

In view of the potential energy curves in Fig. 3.12 and Fig. 3.13(a) and (b), the 355 nm $CO_2^- \rightarrow O^- + CO$ dissociation dynamics following the I^2B_1 excitation can proceed via the genuine conical intersection between the I and 4 states, both of which are of the same $^2A''$ electronic symmetry for C_s geometries, but of different, 2B_1 and 2A_2 symmetries in C_{2v} . The potential energy curves corresponding to these states are indicated in Fig. 3.13

by dotted lines. As seen in the lower panel of the Fig. 3.13 and also in Fig. 3.12, the 4 state does indeed correlate to the $O^- + CO$ dissociation limit.

At 266 nm, the $2^2A_1 \leftarrow X^2A_1$ transition in CO_2^- is believed to be excited. The initially prepared 2 state or the core anion does not correlate with the $O^- + CO$ dissociation limit. However, it intersects (conically) with the dissociative $3^2B_2(2^2A')$ state. For $m = 2$, the oscillator strengths of the $1^2A'' \leftarrow X^2A'$ and $2^2A' \leftarrow X^2A'$ transitions, as estimated using the CIS calculations, are 0.0093 and 0.0223, respectively. These values are consistent with the relative 266 and 355 nm dissociation cross-sections observed in this work. The higher dissociation cross-section (especially for small m) at 266 nm than at 355 nm can be explained by referring to the conical intersection regions in Fig. 3.13(a) and (b). The crossing of the $2^2A'$ and $3^2A'$ states relevant to the 266 nm dissociation occurs around the Franck-Condon region (indicated by dash vertical line in each plot) of the anion where the two solid lines intersect without requiring much nuclear rearrangement. In contrast, the crossing of $2^2A''$ and $3^2A''$ states relevant to the 355 nm dissociation occurs at smaller bending angle than the anion equilibrium where the bending potential gradient acts in opposite direction.

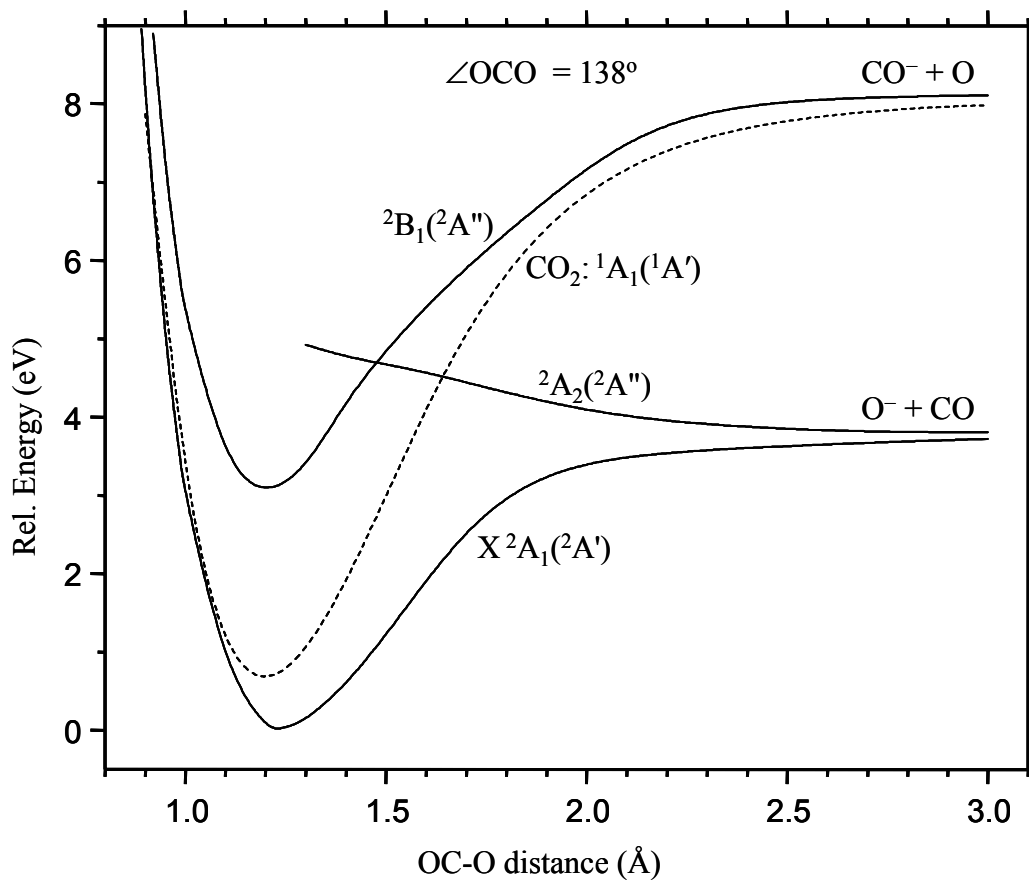


Figure 3.12 Optimized potential energy curves of the ground and first excited states for CO_2^- . The energy is calculated using MP2/6-311+G(3df) scanning one of the C-O distance while optimizing the other. The OCO angle is fixed at 138 degree (calculated equilibrium angle) throughout the calculations. The curve shown in dotted line is for the neutral state.

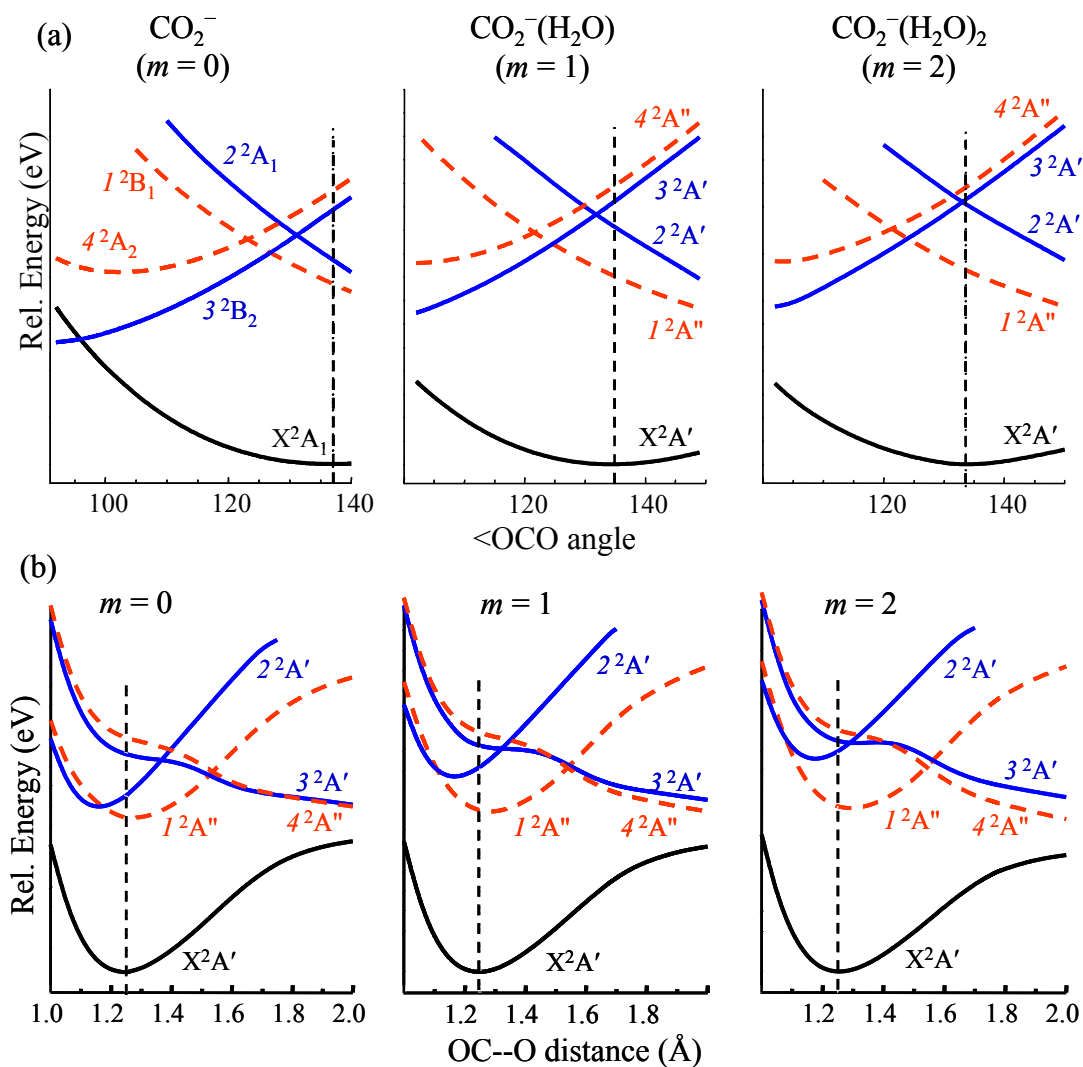


Figure 3.13 Schematics of potential energy curves for $\text{CO}_2^-(\text{H}_2\text{O})_m$, $m = 0, 1$ and 2 as functions of the OCO bending angle (a) and the OC--O bond length (b). The curves in (b) are generated at fixed equilibrium OCO angles. The vertical dotted lines in indicate the equilibrium OCO angle in (a) and equilibrium bond distance in (b).

3.9 Solvent-Evaporation Mechanism

The electronic excitation responsible for the observed fragmentation of the CO_2^- $(\text{H}_2\text{O})_m$ cluster anions by UV light can either be localized on the CO_2^- core of the cluster or involve a charge transfer to solvent (CTTS). Either type of excitation may be followed by anionic fragmentation or autodetachment, provided there is enough energy for the removal of the electron.

The core-dissociation channels (1) definitely involve the excitation of the CO_2^- core of the cluster. The water-evaporation pathways, on the other hand are consistent with three distinct mechanisms: (2-i) cluster predissociation via electronic excitation of CO_2^- followed by energy transfer to inter-molecular degrees of freedom; (2-ii) photodissociation of CO_2^- followed by its recombination or trapping of the CO fragment within the cluster; (2-iii) a CTTS transition followed by the evaporation of several H_2O molecules. Since no $(\text{H}_2\text{O})_{m-k}^-$ fragments are observed, the possible CTTS process is likely reversed by electron recapture by the CO_2 .

The decrease in the fraction of core-dissociation fragments with increasing parent cluster size (Fig. 3.5) is consistent with all of these mechanisms. For example, in (2-iii) the increase in the relative yield of the water-evaporation fragments in larger parent clusters may reflect the closing of the indirect detachment channel. Without autodetachment, the evaporation becomes the main decay mechanism for the CTTS states. The sharp increase in the water-evaporation fraction at 355 nm occurring between $m = 6$ and 8 seen in Fig. 3.5 coincides with the size range where we expect the autodetachment pathway to

close in 355 nm experiments.²⁶

3.10 Hydration versus Homogeneous Solvation

It is instructive to compare $\text{CO}_2^-(\text{H}_2\text{O})_m$ to pure $(\text{CO}_2)_n^-$ cluster anions. Lineberger and co-workers found that UV fragmentation of $(\text{CO}_2)_n^-$, $n \geq 13$ occurs via the sequential ejection of CO_2 monomers.¹⁵⁰ Intriguingly, the onset of this channel coincides, approximately, with the reverse core-switching from the monomer-based $\text{CO}_2^-(\text{CO}_2)_{n-1}$, $7 \leq n \leq 13$ clusters to dimer-based $(\text{O}_2\text{CCO}_2)^-(\text{CO}_2)_{n-2}$, $n > 13$.¹¹² $(\text{CO}_2)_{13}^-$ is believed to be a mix of the monomer and dimer-based structures. The dominant mechanism of $(\text{CO}_2)_n^-$, $n \geq 13$ dissociation likely involves the dissociation of the order-of-1/2 C–C bond in the covalently bound $(\text{O}_2\text{CCO}_2)^-$ dimer-anion,¹⁵¹ yielding $\text{CO}_2^- + \text{CO}_2$ (followed by the evaporation of some solvent CO_2). Hence, even though the dissociation of the anionic core of the cluster does occur, the fragments are not distinguishable from the mere solvent evaporation. For $(\text{CO}_2)_n^-$, $n < 13$ only a minor CO_3^- channel was observed.^{150,152} The CO_3^- products can be attributed to $\text{CO}_2^- \rightarrow \text{O}^- + \text{CO}$ dissociation followed by a bimolecular association reaction $\text{O}^- + \text{CO}_2 \rightarrow \text{CO}_3^-$. This channel is most relevant for comparison with $\text{CO}_2^-(\text{H}_2\text{O})_m$. For $n \geq 14$, following the core-switching to dimer-anion based $(\text{CO}_2)_n^-$ cluster structures, the CO_3^- channel is replaced by $(\text{CO}_2)_m^-$ products.

Our 355 nm fragmentation experiment on mass selected $(\text{CO}_2)_2^-(\text{H}_2\text{O})_m$ has shown three fragmentation pathways: $\text{CO}_3^-(\text{H}_2\text{O})_{m-k}$ for $m = 3-6$, $\text{O}^-(\text{H}_2\text{O})_{m-k}$ for all cluster size, and $\text{CO}_2^-(\text{H}_2\text{O})_{m-k}$ for $m > 4$.¹⁵³ Particularly interesting is the observation of CO_3^- based

products involving an intra-cluster ion-molecule reaction of the nascent O^- with the second CO_2 .

3.11 Summary

The photofragmentation of the mass-selected $\text{CO}_2^-(\text{H}_2\text{O})_m$, $m = 2-40$ cluster anions proceeds via two types of pathways: the core-dissociation channel resulting in the formation of $\text{O}^-(\text{H}_2\text{O})_{m-k}$, and the solvent-evaporation channel, which is manifest in the loss of several water molecules from the parent cluster. The average number of water molecules, $\langle k \rangle$, lost in the fragmentation process depends on the photon energy. At 266 nm $\langle k \rangle$ varies between 0.5 and 4.7 in the core-dissociation channel and between 7.0 and 10.0 in the solvent-evaporation channel. From the asymptotic value of $\langle k \rangle$, the enthalpy of H_2O evaporation from the cluster is determined as 0.466 ± 0.001 eV, compared to the heat of evaporation of bulk water, 0.456 eV at 25°C. The C–O bond dissociation energy of the CO_2^- core in the $\text{CO}_2^-(\text{H}_2\text{O})_m$, $m \geq 20$ cluster anions is estimated as 2.49 eV, compared to 3.46 eV for bare CO_2^- . *Ab initio* and density-functional calculations illuminate the twofold effect of stepwise hydration: (1) the stabilization of the anion equilibrium relative to the neutral potential minimum; and (2) the increase in the autodeachment barrier height.

Although 355 and 266 nm excitations produce the same types of anionic fragments, different electronic transitions and dissociation mechanisms are implicated in the two excitation regimes. The 355 nm excitation involves the $I^2B_1 \leftarrow X^2A_1$ electronic

transition at the bent CO_2^- geometry. The 266 nm dissociation is initiated by $2^2\text{A}_1 \leftarrow X^2\text{A}_1$ electronic transition. In both cases the dissociation dynamics is suggested to involve conical intersections: at 355 nm between $1^2\text{B}_1(^2\text{A}'')$ and $4^2\text{A}_2(^2\text{A}'')$ dissociation happening on the $4^2\text{A}_2(^2\text{A}'')$ potential energy surface, and at 266 nm between $2^2\text{A}_1(^2\text{A}')$ and $3^2\text{B}_2(^2\text{A}')$ dissociation happening on the $3^2\text{B}_2(^2\text{A}')$ potential energy surface.

Chapter 4

DFT AND *AB INITIO* STUDIES OF CS_2^- AND $(\text{CS}_2)_2^-$

4.1 Introduction

In order to facilitate the analysis of the photoelectron imaging (Chapter 5) and the photofragmentation (Chapter 6) data, this chapter describes the theoretical study of the electronic structures of CS_2^- and $(\text{CS}_2)_2^-$ anions. As it will be evident in the experimental and theoretical results the CS_2 based anions have very versatile electronic structural properties. We will attempt to investigate particularly the dimer anion in detail applying both density functional theory (DFT) and *ab initio* theory.

The molecular properties of CS_2 in comparison with that of CO_2 are summarized in Table 4.1. Although CS_2 is isovalent with CO_2 and has zero dipole moment, its polarizability is about 3 times that of CO_2 . The signs of the quadrupole moments for CS_2 and CO_2 are opposite. The positive electron affinity of CS_2 (0.89 ± 0.02 eV)¹⁵⁴ is in contrast with the negative electron affinity of CO_2 (-0.6 ± 0.2 eV).¹⁰⁷ The comparable VDE values are due to similar bent equilibrium structures of the anions compared to the linear geometry of the neutrals.

Metastable CO_2^- can hardly be produced through direct electron attachment to the neutral CO_2 ; it was first observed in gas phase in the dissociative electron attachment to organic molecules (such as maleic anhydrides) that contains OCO unit in bent arrangement. Stable CS_2^- is generated through direct electron attachment to the neutral

Table 4.1 Comparison of molecular properties of CO₂ and CS₂ molecules.

Molecular properties	CO ₂	<i>reference</i>	CS ₂	<i>reference</i>
Bond length (r_e)	1.1600 Å	¹³⁷	1.5526 Å	¹³⁷
Electronegativity difference between C and O (S) atoms	0.89		0.03	
Polarizability	2.911 Å ³	¹³⁷	8.86 Å ³	¹³⁷
Electric Quadrupole moment	-4.3×10^{-26} esu cm ²	¹⁵⁵	1.8×10^{-26} esu cm ²	¹⁵⁵
Electron Affinity	-0.6 ± 0.2 eV	¹⁰⁷	0.895 ± 0.020 eV	¹⁵⁴
VDE (CO ₂ ⁻ or CS ₂ ⁻)	1.4 eV	¹³⁵	1.48 eV (from our data)	

molecule in the presence of third body molecules. In fact, in the mass spectra recorded in our lab, the strongest signal in the $(\text{CS}_2)_n^-$ series is due to the isolated CS_2^- ion. Rydberg atom collisions with the CS_2 lead to the formation of two groups of long-lived metastable CS_2^- ions that undergo electric field induced electron detachment under different field strengths.^{156,157} In the first group, the excess electron detaches when $\leq 3 \text{ kV}\cdot\text{cm}^{-1}$ of electric field is applied, and in the second group it requires above $10 \text{ kV}\cdot\text{cm}^{-1}$ of field strength. The formation of the two groups of CS_2^- anions was attributed to the formation of the anion close to linear geometry with different extent of bending excitation.

For the $(\text{CS}_2)_2^-$ dimer anion, different structures have been suggested in the interpretations of various experimental results. In the gas phase clustering reaction experiments of Hiraoka *et al.* the dissociation energy of the dimer anion was discussed in terms of the four-membered C_2S_4^- [$C_{2v}({}^2\text{B}_1)$] structure in comparison with $\text{CS}_2^- \cdot \text{CS}_2$ ion-molecule complex.¹⁵⁸ The photoelectron imaging experiment of Tsukuda *et al.* confirmed the coexistence of the ion-neutral complex and the $C_{2v}({}^2\text{B}_1)$ covalent structures.¹⁵⁹ Maeyama *et al.* explained the photodissociation of $(\text{CS}_2)_2^-$ into $\text{CS}_2^- + \text{CS}_2$ and $\text{C}_2\text{S}_2^- + \text{S}_2$ considering the $C_{2v}({}^2\text{B}_1)$ covalent structure.¹⁶⁰ The photoelectron imaging experiment carried out in Sanov research group¹⁶¹ showed that the covalent dimer anions of CO_2 and CS_2 have different electronic-structural properties. Yu *et al.* recorded infrared spectra of the dimer anion formed by high-frequency discharge in CS_2 and trapped in solid neon and argon.¹⁶² Using the MP2/6-311+G(d) and B3LYP/6-311+G(d) predictions to aid the spectroscopic assignment, they identified the C_2S_4^- [$D_{2h}({}^2\text{B}_{3g})$] covalent structure as the only structure of $(\text{CS}_2)_2^-$, whose calculated vibrational frequencies matched the observed

spectral features.

Several isomeric structures have been reported for $(\text{CS}_2)_2^-$ based on *ab initio* and density functional theory calculations.^{158,162-164} Using the restricted open-shell Hartree-Fock method with the 6-31G basis set, Hiraoka *et al.* proposed the four-membered ring covalent structure of C_{2v} symmetry with the 2B_1 ground electronic state.¹⁵⁸ An MP2/6-31+G(d) investigation revealed several additional structures, of which two were nearly degenerate, corresponding to the C_{2v} symmetry 2B_1 and 2B_2 electronic states.¹⁶³ Zhang *et al.*¹⁶⁴ found that at the B3LYP/6-31+G(d) level, the C_{2v} (2B_2) structure converts to the higher-symmetry D_{2h} geometry with ${}^2B_{3g}$ electronic state. That is, the 2B_2 electronic state in C_{2v} symmetry correlates with the ${}^2B_{3g}$ electronic state in the D_{2h} symmetry. At the B3LYP/6-31+G(d) level, the D_{2h} (${}^2B_{3g}$) structure was claimed to be more stable than the C_{2v} (2B_1) isomer.¹⁶⁴ In addition to the stability order, the possibility of a D_{2d} (2A_1) structure for $(\text{CS}_2)_2^-$, which would be analogous to the most stable isomer of $(\text{CO}_2)_2^-$ anion¹⁵¹, remained controversial. Some theoretical calculations indicate that the D_{2d} (2A_1) is a stable electronic structure for the $(\text{CS}_2)_2^-$ anion,^{162,163} while other authors argue that $(\text{CS}_2)_2^-$ has no stable D_{2d} electronic isomer.¹⁶⁴

CS_2 has high degree of polarizability and yet the basis sets used in all of the past theoretical works are very poorly polarized placing only one ‘d’ function per heavy atom. It is not expected, therefore, that the previous calculations reliably predict the relative stability order of the isomers. This may have also contributed to the uncertainty regarding the electronic and geometric structures of the dimer anion including the D_{2d} (2A_1) and D_{2h} (2A_g) structures. This chapter revisits the calculations on CS_2^- and $(\text{CS}_2)_2^-$ anions. The

effects of basis sets particularly the polarization functions are illustrated considering the relative stability order of C_{2v} (2B_1) and D_{2h} (${}^2B_{3g}$) electronic structures whose stability order has remained controversial to date. The basis set that gives reliable result is then used to optimize the geometries of other isomers. The feasibility of high energy isomers are evaluated by calculating their potential energies as functions of critical molecular parameters.

4.2 Computational Methods and Procedures

The calculations are performed using Gaussian 03 software package¹⁶⁵ on the University of Arizona High Performance Computer (Marin). The potential energy curves for the CS_2 (${}^1\Sigma_g^+ / {}^1A_1$) ground state, and the (2A_1) ground and the (2B_1) excited states of the CS_2^- are generated using CCSD(T)/aug-cc-pVTZ//MP2/6-311+G(3df). That is, the energy calculation is performed using the coupled-cluster theory with single, double (and triple) excitations, CCSD(T), with Dunning's aug-cc-pVTZ basis set on the structures optimized using the second order Møller-Plesset perturbation (MP2) theory with 6-311+G(3df) basis set. The basis set effect is illustrated on the stability order of $(CS_2)_2^-$ electronic structures considering the 6-31+G(d), 6-311+G(d), 6-311+G(df), 6-311+G(2df), 6-311+G(3df) and aug-cc-pVTZ basis sets. These basis sets are used with B3LYP, MP2 and CCSD(T)//MP2 methods. The geometries of all other isomers then are optimized using both B3LYP and MP2 with aug-cc-pVTZ basis set followed by CCSD(T)//MP2 single point energy calculations. The stabilities of the structures are checked through frequency calculations with aug-cc-pVDZ basis set on the geometries

optimized at the same level of theory. The correlation between different electronic isomers is evaluated through potential energy calculations as functions of selected parameters. The electron detachment energy (VDE) for each optimized structure is calculated using B3LYP and CCSD(T)//MP2 theories.

4.3 Results and Discussion

4.3.1 Electronic Potential Energy Curves of CS₂ and CS₂⁻

The behavior of the CS₂⁻ anionic states as a function of ∠SCS angle are shown in Fig. 4.1. It is interesting to note that while the adiabatic ground electronic state potential energy of CO₂⁻ connects to the virtual ²Σ_g⁺ state at linear geometry (see Chapter 3), the CS₂⁻ ground state correlates with the ²Π_u resonance state. The ground state (*X* ²A₁) and the first excited state (²B₁) of CS₂⁻ are coupled through glancing intersection (Renner-Teller coupling) at linear geometry. Both states lie below the CS₂ (¹A₁) neutral state for all ∠SCS angles at which C–S distances are optimized constrained to the C_{2v} symmetry.

In the previous work by Gutsev *et al.*, at linear geometry the anion was found to be stable towards autodetachment by ~16 meV.¹⁶⁶ Based on this calculation, the Rydberg electron transfer experiment by Dunning and coworkers¹⁵⁷ was interpreted as the formation of CS₂⁻ in the ground electronic state by electron attachment to CS₂ at near-linear geometry with subsequent relaxation towards the bent CS₂⁻ (²A₁) equilibrium. The observation of two forms of metastable CS₂⁻ in this experiment was then attributed to different degrees of bending mode excitation. However, the previous calculation

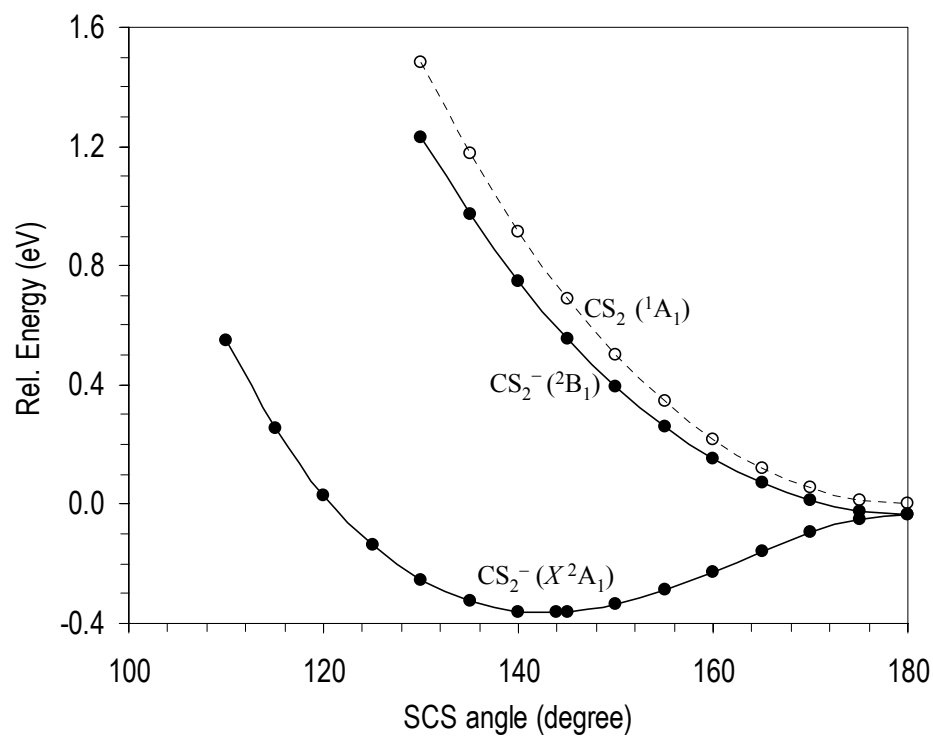


Figure 4.1 The electronic potential energy curves of CS₂ and its anion in C_{2v} symmetry as a function of SCS bending angle. The C–S distances are optimized at fixed angles using MP2/6-311+G(3df) followed by single point energy calculation at CCSD(T)/aug-cc-pVTZ.

considers only the ground state adiabatic potential energy curve. As shown in Fig. 4.1, in addition to the X^2A_1 ground state the 2B_1 excited state also lie below the neutral state at the same nuclear configuration. Therefore, since initially the anion can be formed in either of the two states we suggest that, the role of Renner-Teller coupling in the relaxation dynamics should be considered in the interpretation of the Rydberg electron transfer experimental results.⁴

4.3.2 Basis Set Effects

The basis set effect is illustrated in Fig. 4.2 considering the relative stability of the C_{2v} (2B_1) and D_{2h} ($^2B_{3g}$) structures, previously identified as the two most stable structures of $(CS_2)_2^-$ anion. In the figure, the energy differences between their total electronic energies without the zero-point vibrational energy corrections are plotted. With the 6-31+G(d) and 6-311+G(d) basis sets, which were used in all of the previous calculations, the D_{2h} ($^2B_{3g}$) structure is more stable than the C_{2v} (2B_1), regardless of the theory level used. However, with the application of the df polarization functions, i.e. the 6-311+G(df) basis set, the C_{2v} (2B_1) isomer becomes more stable than the D_{2h} ($^2B_{3g}$) structure, at least according to the CCSD(T) result. The addition of more polarization functions, through the use of the 6-311+G(2df) and 6-311+G(3df) basis sets, reinforces this trend: both CCSD(T) and B3LYP now indicate that the C_{2v} (2B_1) structure is more stable than D_{2h} ($^2B_{3g}$), while MP2 continues to predict the reverse order. The MP2 and B3LYP calculations using Dunning's aug-cc-pVTZ basis set yield the relative isomer energetics that are similar to the corresponding 6-311+G(3df) results. The CCSD(T)/aug-cc-pVTZ calculations could

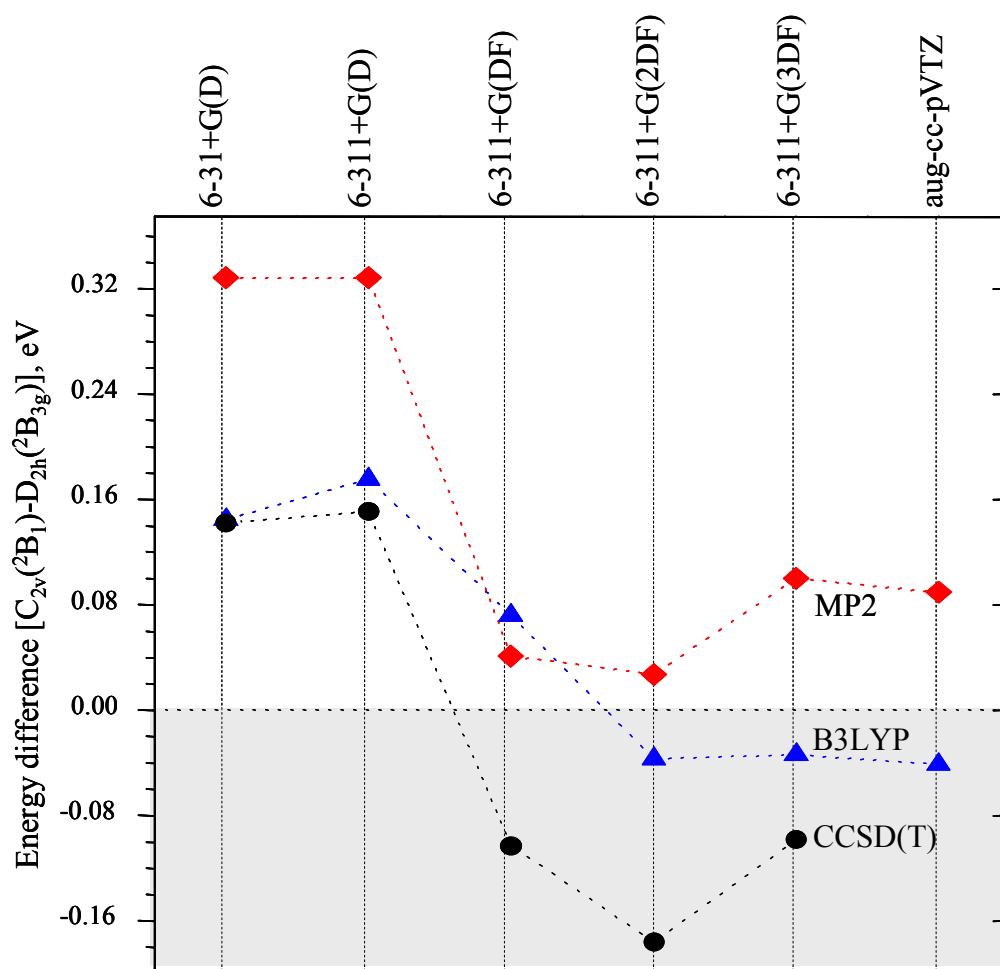


Figure 4.2 Basis set effect on the relative energy of two most stable $(\text{CS}_2)_2^-$ structures. The energy difference is obtained by subtracting the total energy of $D_{2h} (^2B_{3g})$ structure from that of $C_{2v} (^2B_1)$ without including zero point energy. The region where the $C_{2v} (^2B_1)$ structure is more stable is shown against partially shaded background.

not be carried out due to their high computational cost.

4.3.3 Optimized Structures and Stability Order

In view of the importance of the basis set size particularly the polarization functions, we optimized the other $(\text{CS}_2)_2^-$ structures using B3LYP and MP2 methods with the aug-cc-pVTZ basis set. The optimized geometries are shown in Fig. 4.3, with the corresponding CCSD(T)/6-311+G(3df)//MP2/aug-cc-pVTZ and B3LYP/aug-cc-pVTZ energy levels indicated on the left and right axes, respectively. Although the zero point energies are not included in Fig. 4.3, we have confirmed that it does not change the energetic state ordering. The zero of energy in Fig. 4.3 corresponds to $\text{CS}_2^- + \text{CS}_2$ dissociation limit. The vertical detachment energies (VDEs), obtained as the difference between the neutral energy calculated at the anion equilibrium geometry and the anion minimum energy, are included in Fig. 4.3.

All the structures reported for $(\text{CS}_2)_2^-$ previously are found to be stable according to the frequency calculations. Among the six isomers, four [labeled as C_{2v-1} (2B_1), D_{2h-1} (${}^2B_{3g}$), D_{2h-2} (${}^2B_{2g}$) and D_{2d} (2A_1)] contain covalently bonded CS_2 moieties and the other two [C_s (${}^2A'$) and D_{2h-3} (2A_g)] are ion-neutral complexes. In the C_s (${}^2A'$), D_{2d} (2A_1) and D_{2h-3} (2A_g) structures, the excess electron occupies the lowest unoccupied molecular orbital (LUMO) of the neutral state. The formation of the C_{2v-1} (2B_1), D_{2h-1} (${}^2B_{3g}$) and D_{2h-2} (${}^2B_{2g}$) electronic structures must involve electron rearrangement after the electron enters the neutral cluster. The most stable $(\text{CS}_2)_2^-$ isomer is predicted to be the C_{2v} (2B_1) structure, with the D_{2h} (${}^2B_{3g}$) structure lying ~ 0.1 eV higher. In contrast with $(\text{CO}_2)_2^-$, the

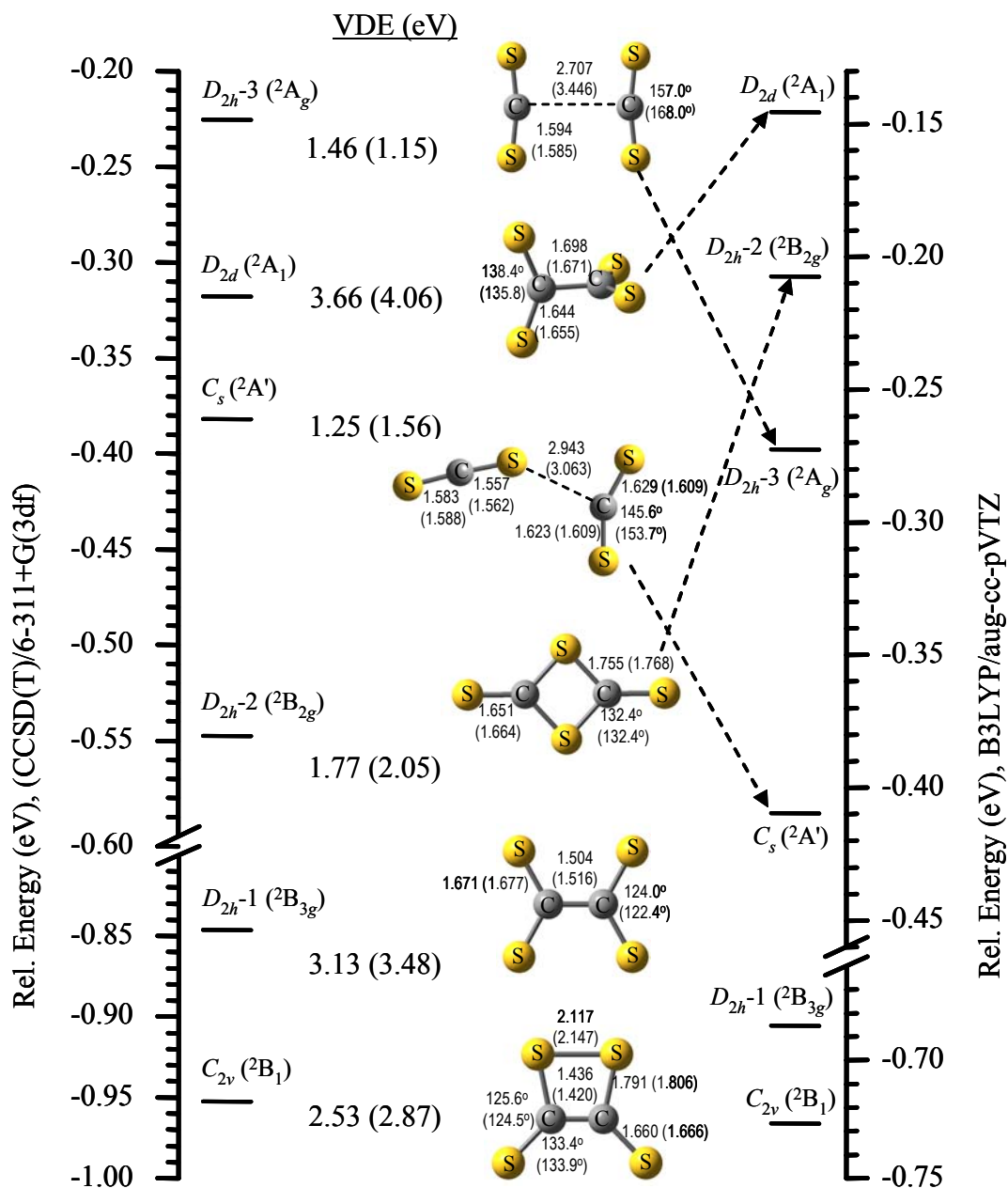


Figure 4.3 Stable structures of $(\text{CS}_2)_2^-$ optimized using MP2 and B3LYP with aug-cc-pVTZ basis set. Bond lengths are in angstroms and bond angles are in degrees. The vertical detachment energy (VDE) is calculated using B3LYP/aug-cc-pVTZ and CCSD(T)/6-311+G(3df). The bond lengths, bond angles and VDEs obtained from B3LYP are provided in parenthesis. The energies are given with reference to $\text{CS}_2^- + \text{CS}_2$ dissociation limit. Note: In the text unless it is specified otherwise $D_{2h} \equiv D_{2h-1}$.

total energy of the D_{2d} structure for $(\text{CS}_2)_2^-$ is ~ 0.6 eV higher than the most stable structure.

4.3.4 Ring Opening Barrier

For the C_{2v} ($^2\text{B}_1$) structure, the barrier against opening the four-membered ring is estimated by scanning the $\angle\text{SCC}$ angle, Θ , in 2° increment while optimizing all other degrees of freedom (subject to the C_{2v} symmetry constraint). Similar calculation is performed on the D_{2h-1} ($^2\text{B}_{3g}$) structure that converts to C_{2v} ($^2\text{B}_2$) when the D_{2h} constraints are removed. The resulting potential energy curves are shown in Fig. 4.4. The energy of the C_{2v} ($^2\text{B}_1$) structure is sensitively dependent on Θ and increases until $\sim 120^\circ$ where the C_{2v} ($^2\text{B}_1$) and D_{2h-1} ($^2\text{B}_{3u}$) states become degenerate. In other words, the $^2\text{B}_{3u}$ excited state of the D_{2h-1} electronic isomer is correlated with the $^2\text{B}_1$ ground state of the C_{2v} isomer. As seen in Fig. 4.4, the C_{2v} ($^2\text{B}_1$) structure has two equivalent C_{2v} ($^2\text{B}_1$) minima, separated by a ~ 0.8 eV barrier without correcting for zero point energy. Since the 0.8 eV barrier energy is obtained when all degrees of freedom are optimized at fixed $\angle\text{SCC}$, it is an estimate for the barrier along the minimum energy path. The potential barrier corresponds to breaking the bond between one pair of the sulfur atoms, resulting in covalent ring opening, and forming an equivalent bond between the opposing pair (ring closing). Therefore, it is referred as ring opening barrier energy. The $^2\text{B}_{3g}$ state correlates with the $^2\text{B}_2$ state when the D_{2h-1} is lowered to the C_{2v} symmetry. The potential energy curve of the $^2\text{B}_2/^2\text{B}_{3g}$ state appears as a flat plateau centered at $\Theta \approx 120^\circ$ on this energy scale. In the magnified scale shown in the lower panel in Fig. 4.4, the D_{2h-1} ($^2\text{B}_{3g}$) structure is seen

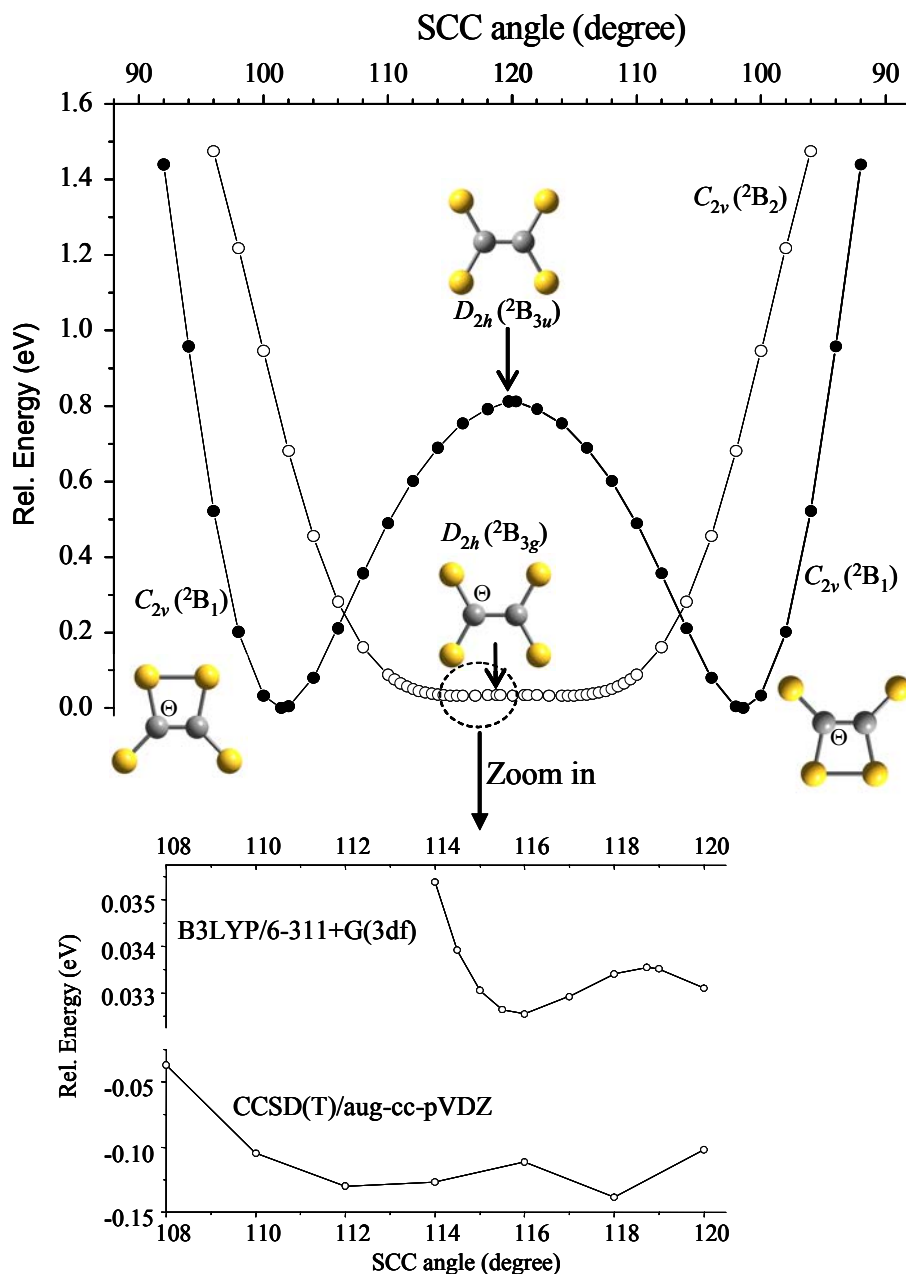


Figure 4.4 Potential energy curves of the $C_{2v} (^2B_1)$ and $D_{2h} (^2B_{3g})/C_{2v} (^2B_2)$ calculated using B3LYP/6-311+G(3df) as a function of $\angle SCC = \Theta$. Constrained to the corresponding symmetries, all degrees of freedom are optimized at the Θ with 0.5-2 degree steps. The zoom in shows the trend in the plateau region of the $D_{2h} (^2B_{3g})/C_{2v} (^2B_2)$ curve comparing with the result obtained from single point energy calculation using CCSD(T)/aug-cc-pVDZ. The negative of energy from the couple-cluster method is due to the limitation of the aug-cc-pVDZ basis set that predicts the D_{2h} as a more stable structure than the C_{2v} (the $C_{2v} (^2B_1)$ minimum is the zero of energy).

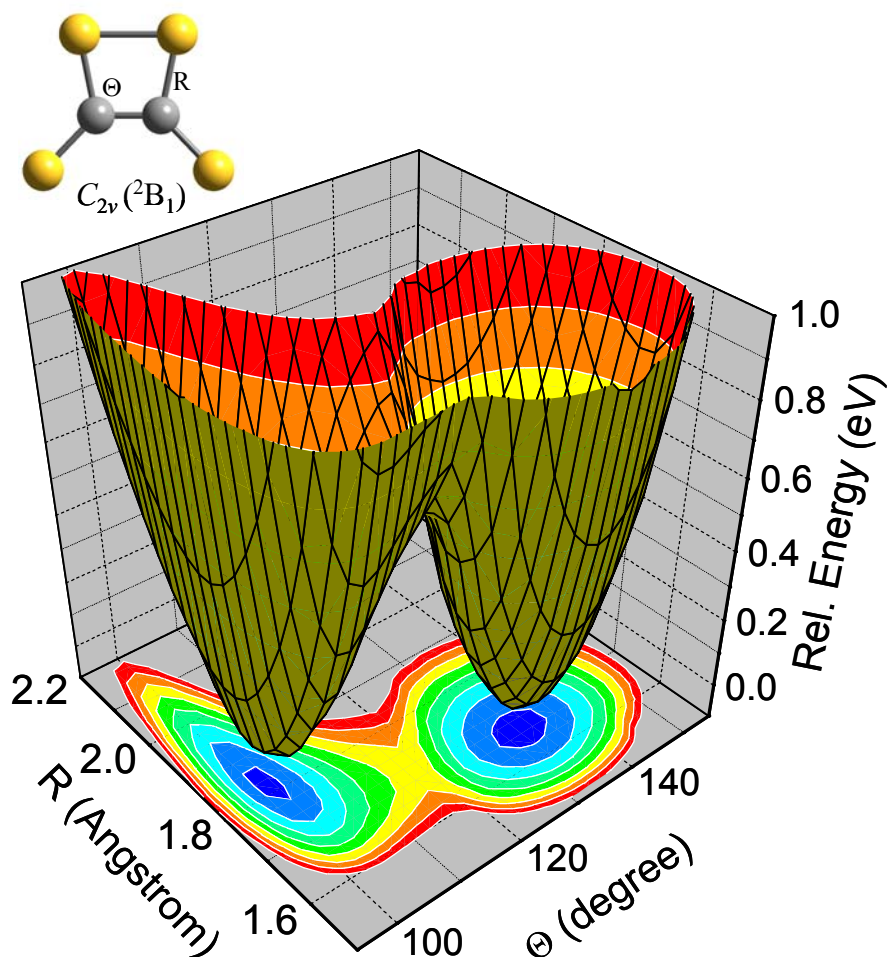


Figure 4.5 Potential energy surface of the $C_{2v} (^2B_1)$ state as functions of SCC angle (Θ) and C-S distance (R) indicated on the structure. The energy calculation is performed using B3LYP/6-31+G(d) scanning Θ and R while optimizing all other degrees of freedom constrained to the C_{2v} symmetry.

as a transition state lying ~ 0.5 meV above the double minima of the C_{2v} -2 (2B_2) structure. However, the result obtained from CCSD(T)/aug-cc-VDZ does not show similar barrier. In fact the later method indicate deeper minimum at the D_{2h} -1 (${}^2B_{3g}$) configuration. The barrier obtained from the B3LYP method may be an artifact of the DFT method although the barrier height is practically insignificant considering the zero point energy.

Similar ring opening and closing also occurs when one pair of C–S bonds are simultaneously stretched while the other pair is compressed. Therefore, the inversion from one minimum to the second also depends on C–S bond length denoted as R in Fig. 4.5. Potential energy calculations are performed scanning Θ and R while optimizing all other degrees of freedoms constrained to the C_{2v} symmetry and the resulting energy surface is shown in Fig. 4.5.

4.3.5 Feasibility of the High Energy Isomers

The minima of the D_{2d} (2A_1) and D_{2h} -3 (2A_g) electronic isomers lie 0.63 and 0.73 eV above the most stable isomer and 0.06 and 0.16 eV above the C_s (${}^2A'$) ion-neutral complex isomer, respectively. As in C_s (${}^2A'$), the extra electron in the two isomers occupies the LUMO of the CS₂ neutral molecule. This implies that the D_{2d} (2A_1), D_{2h} -3 (2A_g) and C_s (${}^2A'$) states lie on the same adiabatic potential energy surface, separated by energy barriers. Therefore, through thermalization the higher energy isomers can relax to the lower ones provided that the barrier is comparable to the thermal energy, without undergoing nonadiabatic transitions.

The main structural differences between the D_{2d} and D_{2h-3} are the $\angle\text{SCCS} = \Theta_D$ dihedral angle and the C–C distance (see structures in Fig. 4.3). Therefore, the relation between the two electronic isomers on the adiabatic energy surface can be revealed by calculating the potential energy as functions of the two parameters while optimizing the other molecular parameters. The potential energy as a function of Θ_D shows a barrier against internal rotation along C–C internuclear axis, while the potential energy as a function of C–C distance indicates the energy required for the dissociation of the dimer into $\text{CS}_2^- + \text{CS}_2$. The calculation as a function of C–C distance is performed fixing the structures in the corresponding symmetries (Fig. 4.6), and as a function of dihedral angle (Fig. 4.7) reducing the symmetry from D_{2h-3} to D_2 (or from D_{2d} to D_2). In Fig. 4.7 the curves that are calculated starting from D_{2h-3} equilibrium geometry ($\Theta_D = 0^\circ$) are labeled as $D_{2h-3} (^2A_g)/D_2 (^2A)$, and the curves calculated starting from D_{2d} equilibrium ($\Theta_D = 90^\circ$) are labeled as $D_{2d} (^2A_1)/D_2 (^2A)$.

According to the result from the B3LYP energy calculation, the $D_{2d} (^2A_1)$ lies above the $D_{2h-3} (^2A_g)$. The DFT predicts that the $D_{2d} (^2A_1)$ structure has very small barrier against dissociation of the dimer into $\text{CS}_2^- + \text{CS}_2$ as seen in Fig. 4.6(a). This barrier height is expected to be smaller when smaller basis sets are used. This may be why Zhang *et al.* did not find stable D_{2d} structure for the $(\text{CS}_2)_2^-$ anion using B3LYP/6-31+G(d).¹⁶⁴ The $D_{2h-3} (^2A_g)$ structure is also essentially barrierless towards dissociation according to the DFT result. As seen in Fig. 4.7(a) at $\Theta_D = 90^\circ$, the minimum energy of the $D_{2d} (^2A_1)$ structure lies at the transition state of the $D_{2h-3} (^2A_g)/D_2 (^2A)$ state.

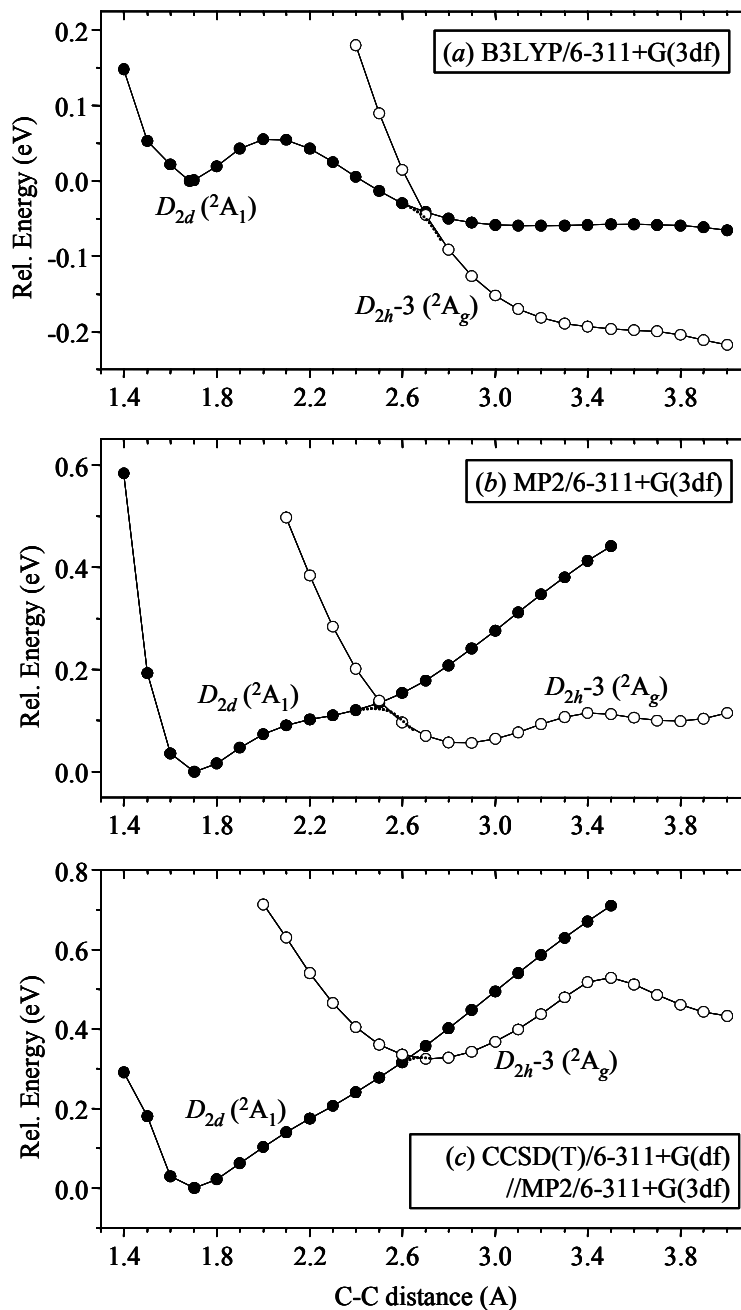


Figure 4.6 Potential energy curves of $D_{2d} (^2A_1)$ and $D_{2h-3} (^2A_g)$ states of $(CS_2)_2^-$ as a function of C-C distance. At fixed C-C separations all other molecular parameters are optimized constrained to the corresponding symmetries.

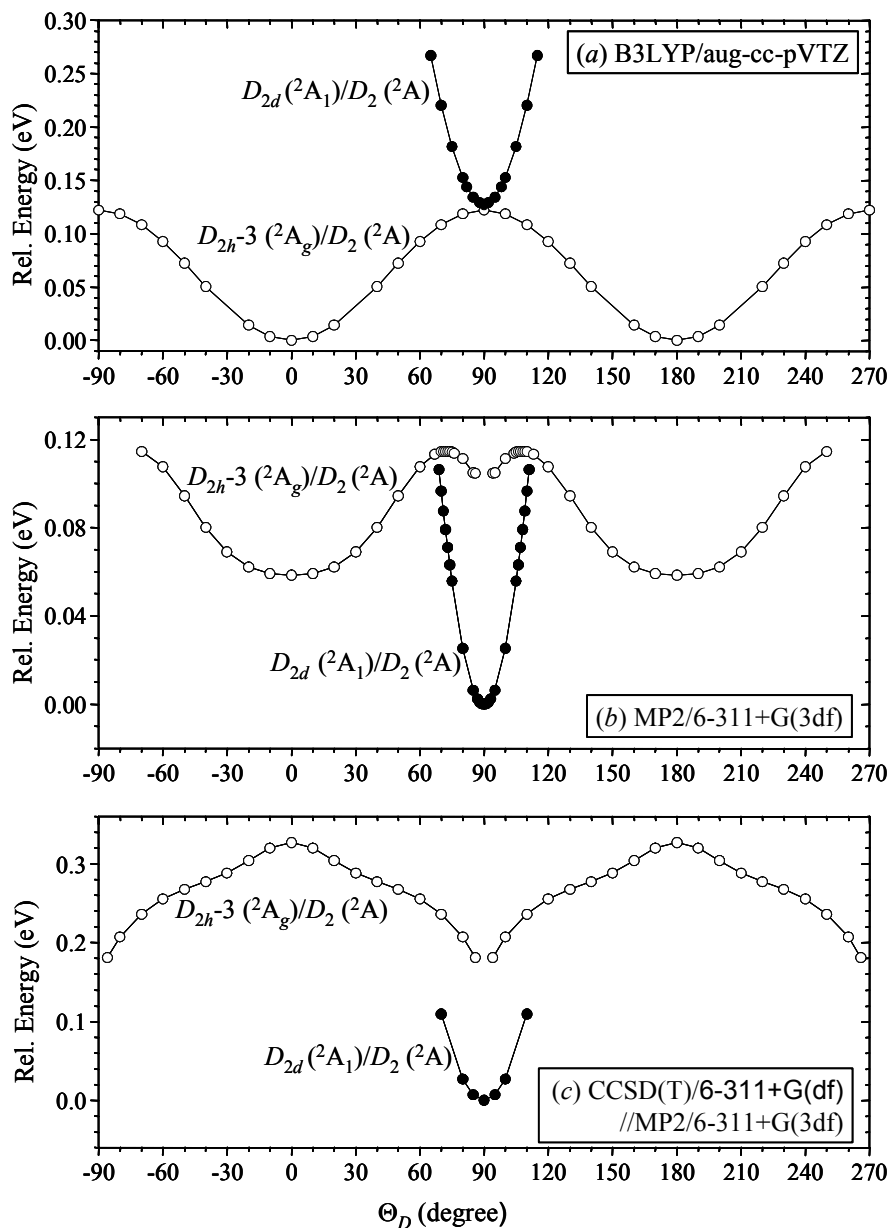


Figure 4.7 Potential energy curves of $D_{2d}(^2A_1)/D_2(^2A)$ and $D_{2h-3}(^2A_g)/D_2(^2A)$ states of $(CS_2)_2^-$ as a function of SCCS dihedral angle (Θ_D) calculated using the theory levels indicated on the figure. At fixed Θ_D all other molecular parameters are optimized. At $\Theta_D = 0$ and 180 degrees the anion has D_{2h} symmetry, and at $\Theta_D = 90$ and -90 degrees it has D_{2d} symmetry. At all other Θ_D it has D_2 symmetry, and as a result both A_1 and A_g states transform as 2A .

Therefore, although diabatically the $D_{2d} (^2A_1)/D_2(^2A)$ curve appears to be bound, it has no barrier against internal rotation along the C–C internuclear axis on the adiabatic potential energy curve, see Fig. 4.7(a).

The results of the *ab initio* calculations (MP2 and CCSD(T)) are in direct contrast with the DFT prediction as shown in Figs. 4.6(b) and (c) and Figs. 4.7(b) and (c). Both MP2 and CCSD(T) place the D_{2d} structure at lower energy than the D_{2h-3} , and both structures are stable towards dissociation into the $CS_2^- + CS_2$ products. On the adiabatic potential energy curve calculated as a function of C–C distance using MP2 (Fig. 4.6(b)), there is negligible barrier between the $D_{2d} (^2A_1)$ and the $D_{2h-3} (^2A_g)$ isomers, and there is no barrier according to the CCSD(T) result as shown in Fig. 4.6(c). Therefore, the D_{2h-3} isomer, if formed at all, should automatically relax to the D_{2d} minimum.

The qualitative trend of the $D_{2h-3} (^2A_g)/D_2 (^2A)$ curve, shown in Fig. 4.7(c), obtained from the CCSD(T) calculation contradicts the results given in Figs. 4.7(a) and (b), obtained from both MP2 and B3LYP, respectively. According to the CCSD(T) result shown in Fig. 4.7(c), the $D_{2h-3} (^2A_g)$ is a transition state. On the other hand, consistent with the geometry optimization result given in Fig. 4.3, the B3LYP and MP2 methods produce bound $D_{2h-3} (^2A_g)/D_2 (^2A)$ energy curves as functions of Θ_D . This striking difference is attributed to the electron correlation effect. In contrast to the B3LYP result, both MP2 and CCSD(T) predict that the $D_{2d} (^2A_1)$ state is more stable than the $D_{2h-3} (^2A_g)$. In addition, even though the diabatic $D_{2h-3} (^2A_g)/D_2 (^2A)$ curve obtained from MP2 is bound as shown in Fig. 4.7(b), on the adiabatic energy curve, no barrier is expected to

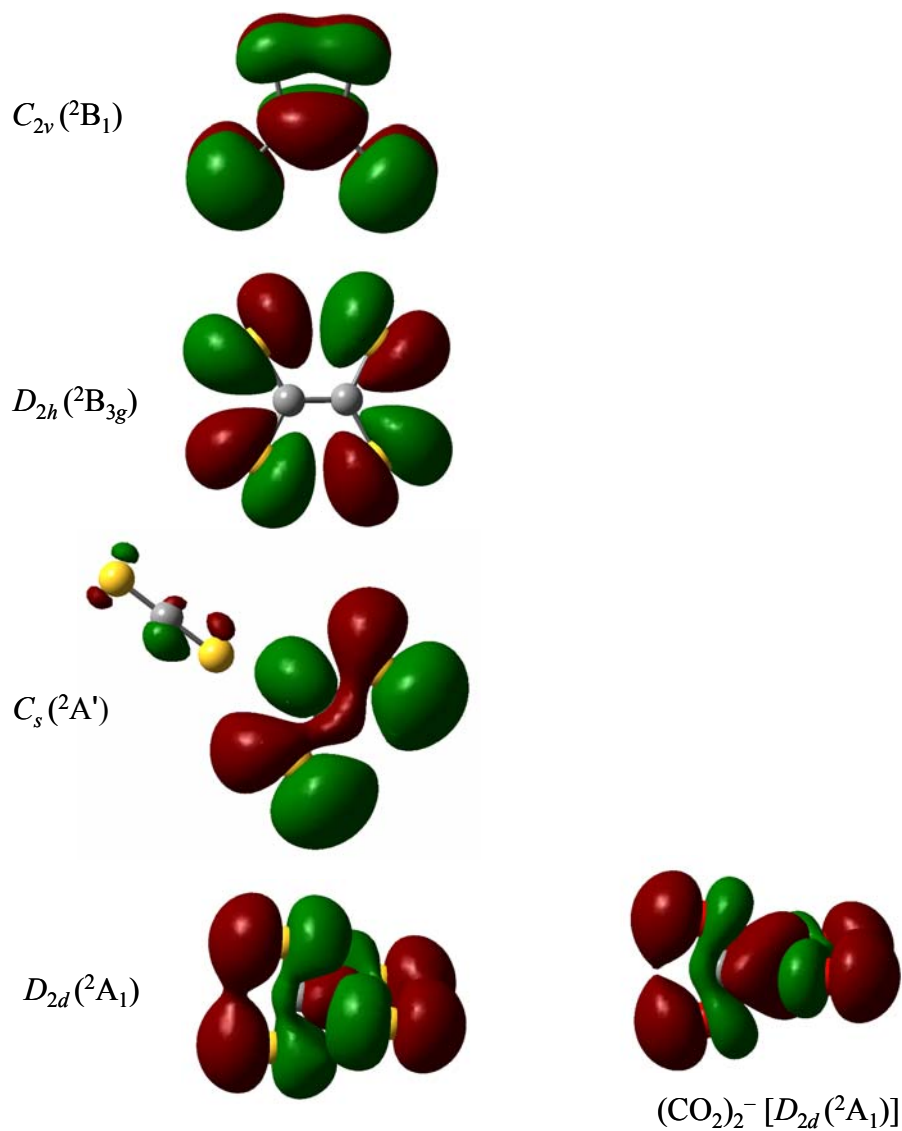


Figure 4.8 Highest occupied molecular orbital (HOMO) of the most viable structure of $(CS_2)_2^-$ dimer anion. The orbital surfaces are generated using SCF with aug-cc-pVTZ basis set. The HOMO of $(CO_2)_2^- [D_{2d} (^2A_1)]$ is included for comparison with the analogous structure of $(CS_2)_2^-$.

separate the D_{2h-3} (2A_g) electronic structure from the D_{2d} (2A_1). Therefore, the energy calculations as a function of the \angle SCCS dihedral angle and the C–C distance suggest that the D_{2h-3} (2A_g) is not a stable structure for $(CS_2)_2^-$ dimer anion.

In principle the possibility of relaxation of the D_{2d} structure to the more stable C_s (${}^2A'$) structure can be evaluated in a similar manner. In practice, however, the choice of appropriate parameters is not obvious as the two isomers have significant structural differences. Therefore, based on the present calculation we cannot be certain about the possibility of the D_{2d} structure for the $(CS_2)_2^-$ ion. The above results and the frequency calculation indicate that the D_{2d} (2A_1) is a stable electronic structure for the $(CS_2)_2^-$ dimer anion.

The ${}^2B_{2g}$ state of D_{2h-2} structure correlates with the 2B_1 state in the C_{2v} symmetry. Consequently, the two electronic isomers should be on the same adiabatic potential energy surface. The D_{2h-2} (${}^2B_{2g}$) isomer is ~ 0.4 eV above the C_{2v} (2B_1) isomer. Although there is similar ring strain in both structures the former, if formed, is expected to relax to the later for in a ‘warm’ cluster environment. The stable structures for the $(CS_2)_2^-$ dimer anion are summarized in Fig. 4.8 showing the contours of the singly occupied molecular orbitals (SOMO) of the ground electronic states. For comparison the orbital shape for the most stable form of $(CO_2)_2^-$ is also included in the figure.

4.4 Summary

Both the 2A_1 and 2B_1 components of the ${}^2\Pi_u$ resonance state of CS_2^- are found to be

below the neutral (${}^1\Sigma_g^+ / {}^1A_1$) state for all SCS angles at which the C–S distances are optimized constrained to the C_{2v} symmetry. At linear geometry the anion is stable towards autodetachment by ~ 90 meV. The 2A_1 and 2B_1 states of the CS_2^- are coupled by Renner-Teller interaction at linear geometry.

Based on geometry optimization and frequency calculation using MP2 and B3LYP methods six stable structures are obtained for $(CS_2)_2^-$. Due to large polarizability of CS_2 molecule, increasing the polarization function in the basis sets is shown to have significant effect in some cases reversing the stability orders of the isomers predicted previously.¹⁶²⁻¹⁶⁴ The importance of the electron correlation in the dimer anion is reflected on the results obtained from the B3LYP, MP2 and CCSD(T) methods where the results for the $D_{2h-3} ({}^2A_g) / D_2 ({}^2A)$ energy curve as a function of the SCCS dihedral angle obtained from the couple-cluster method is strikingly different from that obtained from the other two methods. Based on the analysis of the diabatic and adiabatic potential energy surfaces some of the predicted structures are found to be unlikely candidates for $(CS_2)_2^-$ ion. The stable electronic structures of the $(CS_2)_2^-$ dimer anion are $C_{2v} ({}^2B_1)$, $D_{2h} ({}^2B_{3g})$, $C_s ({}^2A')$, and $D_{2d} ({}^2A_1)$.

Chapter 5

RELAXATION OF $(\text{CS}_2)_2^-$ TO ITS GLOBAL MINIMUM MEDIATED BY WATER
MOLECULES: A PHOTOELECTRON IMAGING STUDY

5.1 Introduction

One obvious effect of solvation is the shifting of the electronic transition bands of a chemical system due to differential solvation of the ground and the excited states. Solvent molecules stabilize metastable species and control the photochemical processes by switching from electron autodetachment to direct photodetachment and to photodissociation channels as the solvent cluster size increases.^{117,167} In addition to these well known effects of solvation, this chapter demonstrates the intriguing role of water in mediating the intermolecular interactions that lead to the formation of the global-minimum structure of the $(\text{CS}_2)_2^-$ anion..

The study of the electronic structure of the $(\text{CS}_2)_2^-$ dimer anion has been the focus of both experimental and theoretical studies.^{32,135,158-164,168} The similarity of the photoelectron spectra of CS_2^- and $(\text{CS}_2)_2^-$ at 2.54 eV photon energy and the magnitude of the dissociation energy (0.176 ± 0.025 eV) led Bowen and Eaton¹³⁵ to suggest an ion-molecule complex, $\text{CS}_2^- \cdot \text{CS}_2$, structure for the dimer anion.¹³⁵ Tsukuda *et al* measured the photoelectron spectra of $(\text{CS}_2)_n^-$ ($n = 1-6$) at 266 nm and based on the observed photoelectron bands predicted the coexistence of ion-neutral complex, $\text{CS}_2^- \cdots \text{CS}_2$, and covalent structure, C_2S_4^- , electronic isomers for $n \geq 2$.¹⁵⁹ In addition, the Sanov group carried out a photoelectron imaging study of $(\text{CS}_2)_n^-$, $n = 2-4$, at 800, 532, and 400 nm,³²

emphasizing the distinct electronic-structural properties of the covalent dimer anions of CO_2 and CS_2 .¹⁶¹

The geometric and electronic structures of $(\text{CS}_2)_2^-$ have been the focus of numerous experimental and theoretical studies.^{32,135,158-164,168,169} The similarity of the photoelectron spectra of CS_2^- and $(\text{CS}_2)_2^-$ at 2.54 eV photon energy and the small magnitude of the dissociation energy (0.176 ± 0.025 eV) led Bowen and Eaton to suggest an ion-molecule complex, $\text{CS}_2^- \cdot \text{CS}_2$, structure for the dimer anion.¹³⁵ In the gas phase clustering reaction experiments of Hiraoka *et al.*, the dissociation energy of $(\text{CS}_2)_2^-$ was discussed in terms of the four-membered-ring, C_{2v} symmetry C_2S_4^- structure, corresponding to the ${}^2\text{B}_1$ electronic state, contrasting the C_s (${}^2\text{A}'$) ion-molecule complex structure of $\text{CS}_2^- \cdot \text{CS}_2$.¹⁵⁸ The photoelectron spectroscopy experiment of Tsukuda *et al.* confirmed the coexistence of the ion-molecule complex and the C_{2v} (${}^2\text{B}_1$) covalent structure.¹⁵⁹ The latter was also considered by Maeyama *et al.* in their interpretation of $(\text{CS}_2)_2^-$ photodissociation into $\text{CS}_2^- + \text{CS}_2$ and $\text{C}_2\text{S}_2^- + \text{S}_2$.¹⁶⁰ The photoelectron imaging study by Sanov group emphasized the distinct electronic-structural properties of the covalent dimer anions of CO_2 and CS_2 .^{32,161} In the infrared study of the dimer anion by Yu *et al.*, a D_{2h} (${}^2\text{B}_{3g}$) covalent structure was found as the only electronic ground state of $(\text{CS}_2)_2^-$, whose calculated vibrational frequencies matched the observed spectral features.¹⁶² In the calculation described in chapter 4, four stable electronic structures are found for the dimer anion: C_{2v} (${}^2\text{A}_1$), D_{2h} (${}^2\text{B}_{3g}$), C_s (${}^2\text{A}'$) and D_{2d} (${}^2\text{A}_1$).

The diverse findings of the previous experimental studies indicate that the electronic

and geometric structures and, therefore, the photochemical properties of $(\text{CS}_2)_2^-$ are dependent on its environment and the intermolecular interactions involved. In this chapter, we investigate the effects of water-mediated interactions and solvation on the CS_2^- and $(\text{CS}_2)_2^-$ anions. Using photoelectron imaging, we elucidate the coexistence of several isomers of $(\text{CS}_2)_2^-$ and the corresponding larger cluster anions. The ion source conditions, particularly the presence of water in the precursor gas delivery line, are shown to have a pronounced effect on the observed isomer distribution, even for $(\text{CS}_2)_2^-$, which itself contains no water molecules.

5.2 Experimental

The experiments are carried out using the tandem time-of-flight mass spectrometer coupled with photoelectron imaging assembly as described in Chapter 2. Neutral clusters of CS_2 are formed by expanding Ar carrier gas at 40 psi backing pressure over carbon disulfide liquid sample. The CS_2/Ar mixture then supersonically expands through a 0.8 mm orifice pulsed nozzle into a vacuum chamber with a base pressure of 2×10^{-7} Torr. The $(\text{CS}_2)_n^-$ anion clusters are formed by secondary electron attachment to the neutral clusters. The $(\text{CS}_2)_2^-(\text{H}_2\text{O})_m$ clusters are formed through the same procedure in the presence of water vapor in the precursor gas mixture.

In the subsequent discussion, the term “dry source conditions” refers to the experimental regime where moisture in the neutral precursor gas expansion line has been removed (as much as possible) by means of baking and pumping. Otherwise, the experiments are referred to as performed under the “wet source conditions”. Figure 5.1

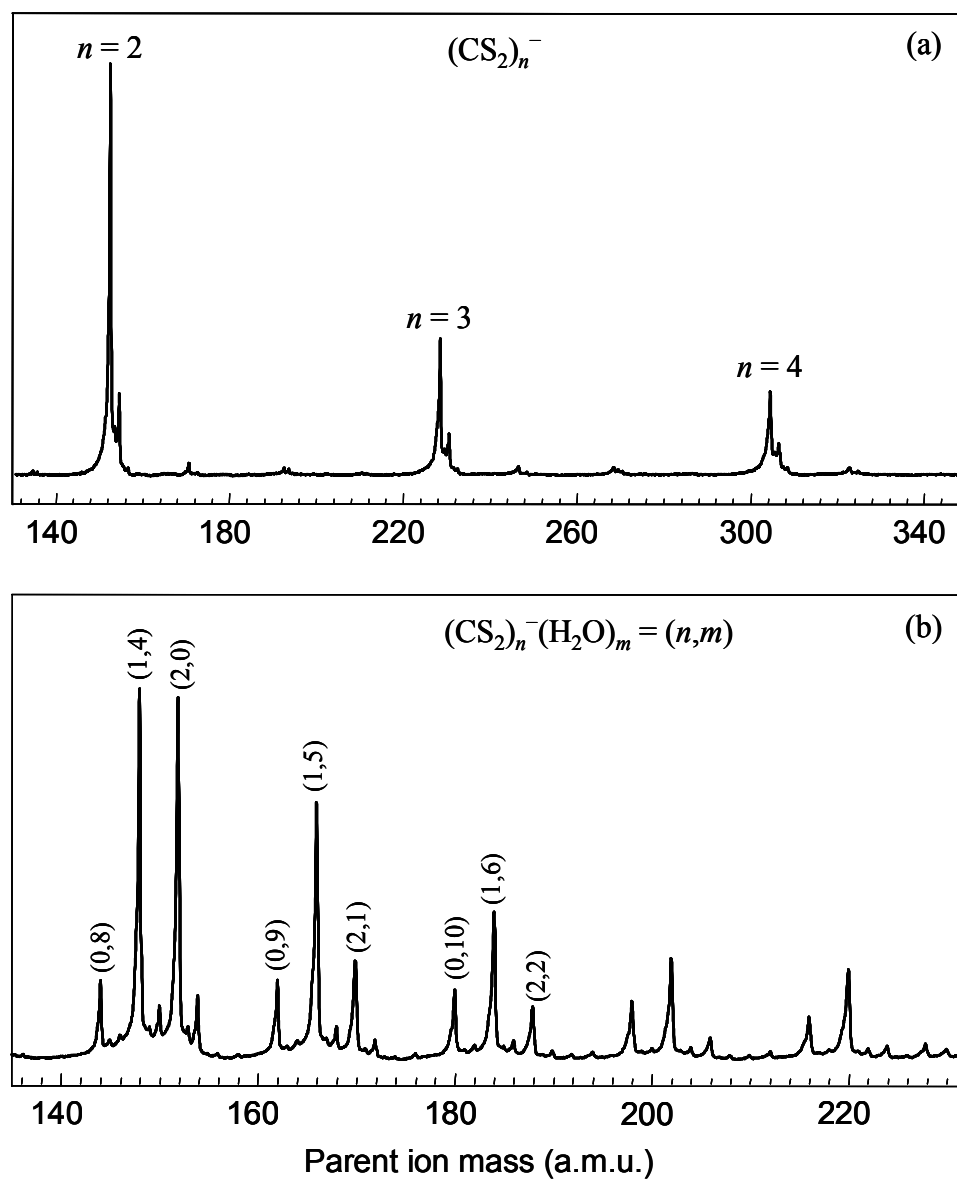


Figure 5.1 Representative mass spectra acquired under (a) dry and (b) wet source conditions, respectively.

displays the representative mass spectra of the cluster anions generated under the two regimes. The spectrum acquired under the wet source conditions shows intense $(\text{CS}_2)_n^-(\text{H}_2\text{O})_m$ peaks, while only $(\text{CS}_2)_n^-$ are prominent under the dry conditions.

Photoelectron images are acquired at 532, 355 and 266 nm output of Nd:YAG laser (Spectra Physics Lab 130-50). The images are typically accumulated over 25,000 to 100,000 photodetachment events.

5.3 Photoelectron Imaging Results and Analysis

5.3.1 Homogeneous and Heterogeneous Solvation of CS_2^-

The 355 nm photoelectron images of $(\text{CS}_2)_n^-$, $n = 1-4$, $\text{CS}_2^-(\text{CO}_2)_m$, $m = 1-3$ and $\text{CS}_2^-(\text{H}_2\text{O})_m$, $m = 1-3$, are shown in Fig. 5.2(a), (b) and (c), respectively. These and all other photoelectron images presented in this work are recorded with the laser polarization set vertical in the figure plane. The photoelectron spectra are extracted from the images using the inverse Abel transformation technique. The transformation is performed using the Basis Set Expansion program.⁹⁴

In all cases shown in Fig. 5.2(a)–(c), the $X^1\text{A}_1(^1\Sigma_g^+) \leftarrow X^2\text{A}_1$ transition band in CS_2^- , denoted as band I, shifts progressively to higher binding energies upon the addition of solvent molecules, which is consistent with solvation energetics. The solvation-induced shifts observed for band I in the presence of varying numbers of CS_2 , CO_2 , and H_2O solvent molecules are summarized in Fig. 5.3. Band II, which appears in $(\text{CS}_2)_n^-$ (most prominently for $n = 2$), but not in $\text{CS}_2^-(\text{CO}_2)_m$ and $\text{CS}_2^-(\text{H}_2\text{O})_m$, is assigned to a covalent

structure of $(\text{CS}_2)_2^-$, i.e. C_2S_4^- . The $a^3\text{B}_2 \leftarrow X^2\text{A}_1$ transition (band III) is prominent in the low electron kinetic energy (eKE) region of the CS_2^- spectrum, but disappears almost completely upon solvation by CO_2 or H_2O , as seen in Fig. 5.2(b) and (c). Most strikingly, the anion stabilization with the addition of just one, relatively weakly bound CO_2 solvent molecule appears to be enough to make the photodetachment transition (band III) in solvated CS_2^- practically inaccessible at 355 nm [Fig. 5.2(b), $m = 1$]. As seen in Fig. 5.3, the solvation shift of band I due to CS_2 is larger than that due to CO_2 . Since a qualitatively similar trend is expected for band III, it should also disappear from the 355 nm spectra upon the addition of the first CS_2 solvent molecule. Therefore, despite its similarity (on a coarse inspection) to band III in CS_2^- , the slow-electron band appearing near the centers of the $(\text{CS}_2)_n^-$, $n = 2-4$ images in Fig. 5.2(a) cannot be due to solvated CS_2^- . Hence, we give this band a distinct label, band IV.

In Fig. 5.4, the 355 nm photoelectron spectra obtained for (a) $(\text{CS}_2)_n^-$, $n = 2-4$ are compared to those for (b) $(\text{CS}_2)_2^-(\text{H}_2\text{O})_m$, $m = 0-2$. The results for the two cluster series were obtained under the dry and wet source conditions, respectively. Similar to the data in Fig. 5.2(a) for $n = 2-4$, all spectra in Fig. 5.4 show intense low-eKE bands (band IV). To provide further evidence that this band is distinct from band III, or other higher-energy bands attributed to CS_2^- , Figs. 5.4(a) and (b) also show (as red dotted lines) the photoelectron spectra of $(\text{CS}_2)_2^-$ obtained at 266 nm under the corresponding ion-source conditions. It is clear that in $\text{CS}_2^- \cdot \text{CS}_2$, the $a^3\text{B}_2 \leftarrow X^2\text{A}_1$ transition, responsible for band III, appears at binding energies that exceed the 355 nm photon energy.

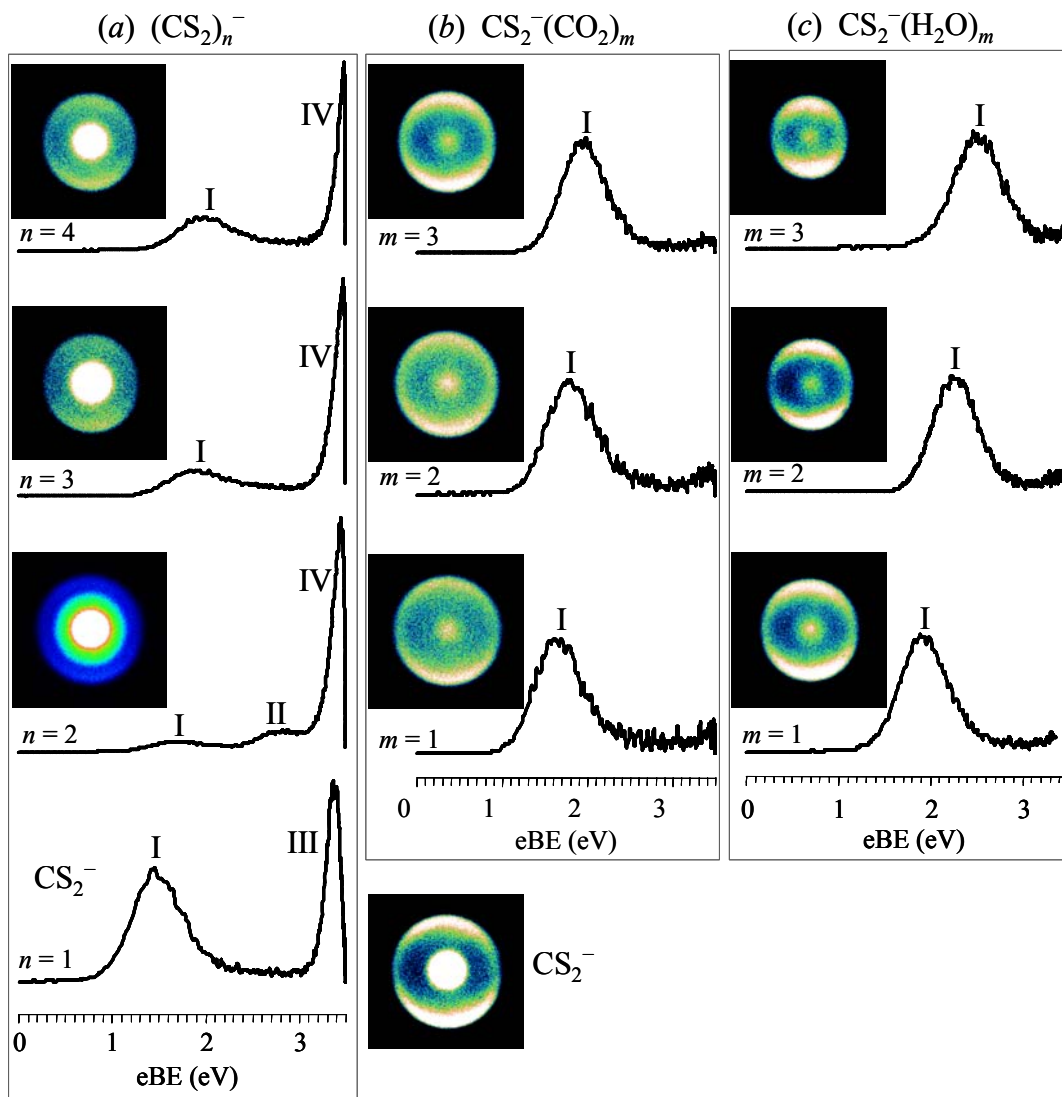


Figure 5.2 Photoelectron images of isolated and solvated CS_2^- acquired at 355 nm. The laser polarization is always vertical in the image plane. The results for the homogeneous solvation in (a) and heterogeneous solvation in (b) and (c) are presented together for comparison. In all cases, the $X^1\text{A}_1(1\Sigma_g^+) \leftarrow X^2\text{A}_1$ transition band (band I) shifts to higher eBE, consistent with solvation energetics. Band II, which appears in $(\text{CS}_2)_n^-$, but not in $\text{CS}_2^-(\text{CO}_2)_m$ and $\text{CS}_2^-(\text{H}_2\text{O})_m$, is assigned to a covalent dimer-anion structure. The $a^3\text{B}_2 \leftarrow X^2\text{A}_1$ transition band (band III) disappears upon the first addition of either CO_2 or H_2O . Since the solvation strength of CS_2 is slightly higher than CO_2 , band III must also disappear upon the addition of the first CS_2 solvent. Band IV is due to autodetachment from covalent structures.

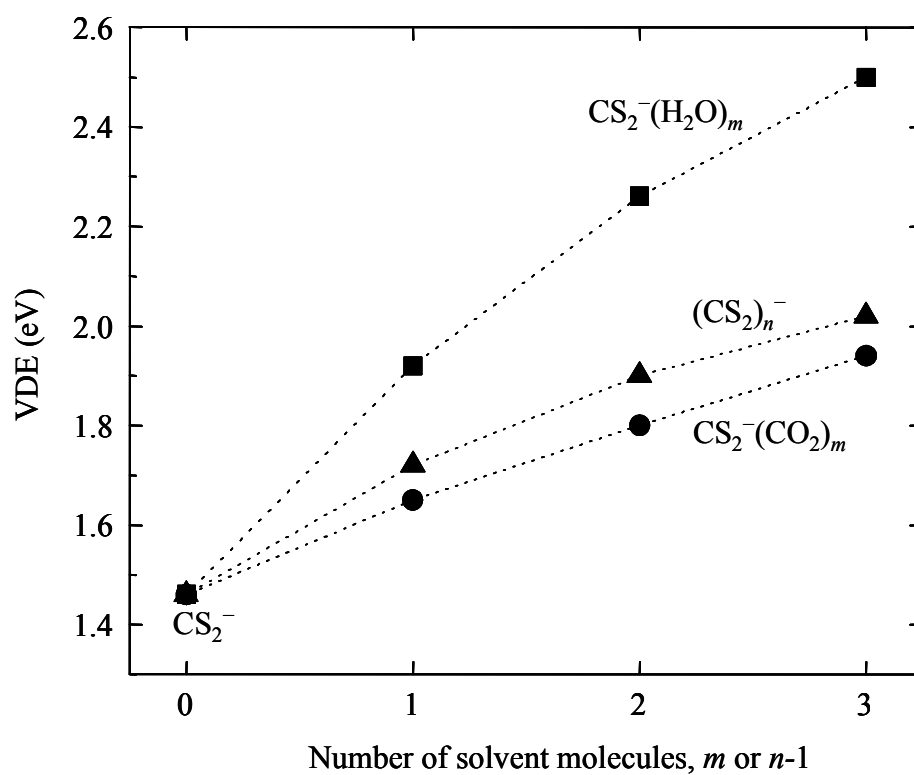


Figure 5.3 Vertical detachment energy corresponding to band I (see Fig. 5.2) as a function of the number of solvent molecules.

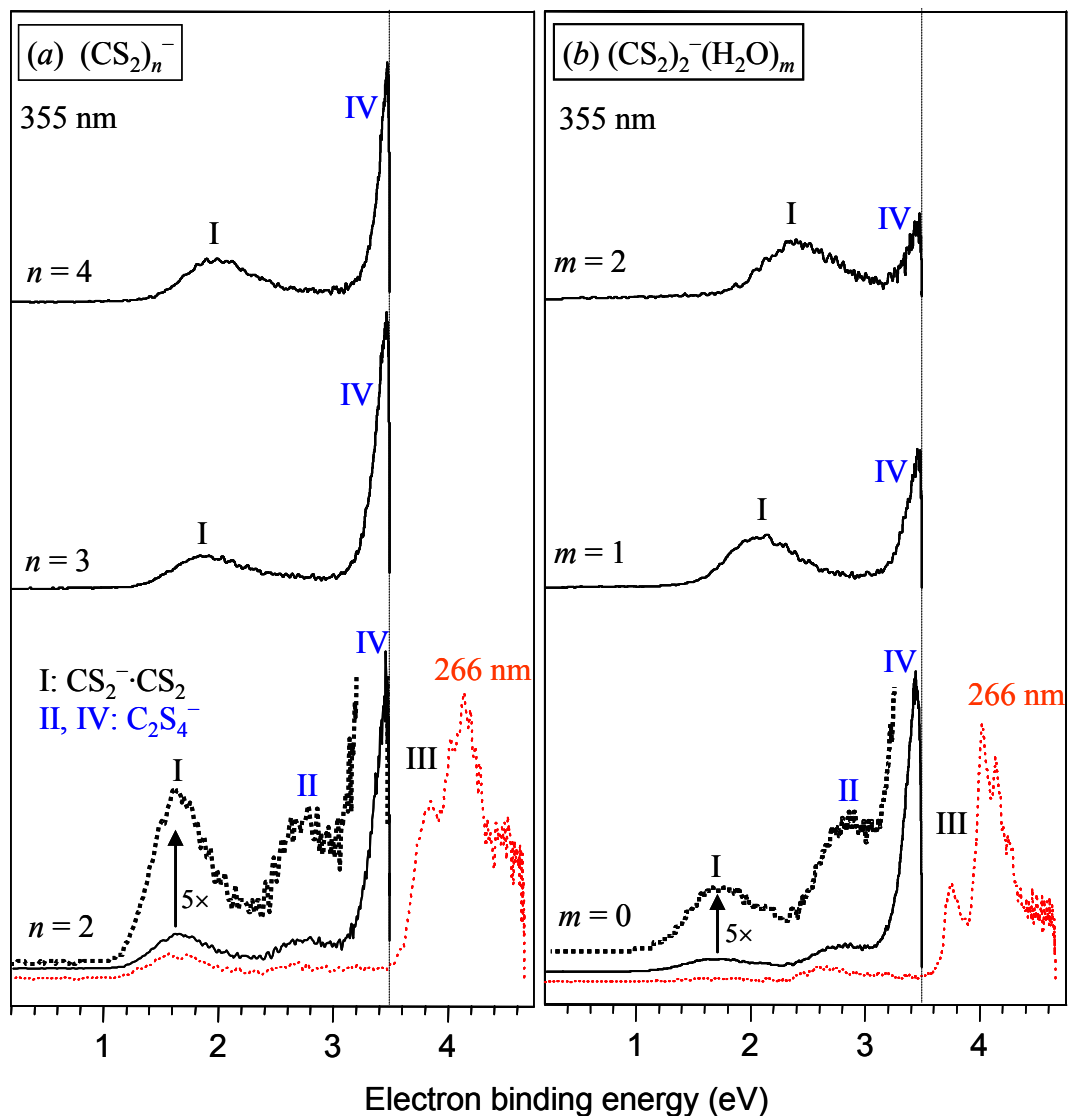


Figure 5.4 (a) The 355 nm photoelectron spectra of $(\text{CS}_2)_n^-$, in comparison with (b) that of $(\text{CS}_2)_2^-(\text{H}_2\text{O})_m^-$. The photoelectron spectrum extracted from the 266 nm image of $(\text{CS}_2)_2^-$ anion is included as a reference (shown as a red dotted line). As in Fig. 5.2 band I and II arise from direct photodetachment from $\text{CS}_2^- \cdot \text{CS}_2$ ion-neutral complex and C_2S_4^- covalent structures, respectively. Band IV is due to autodetachment of covalent structures. Band II disappears almost completely when either CS_2 or H_2O solvent molecule is added to the dimer anion. The relative intensity differences of band I and II when the dimer anion is formed under (a) dry and (b) wet source conditions are clearly seen in the magnified spectra (shown in dotted lines) for $n = 2$ and $m = 0$.

Since band IV appears only in cluster anions with two or more CS₂ moieties, its likely origin is the covalent dimer-anion. Past measurements on (CS₂)_n⁻, $n = 2-4$ at several wavelengths have also indicated intense, isotropic low-eKE signals,^{32,161} similar to band IV in Figs. 5.2(a) and 4. In general, autodetachment bands are quite common in the low-eKE regions of cluster-anion photoelectron spectra. Their origin is traced to the optical preparation and subsequent decay (e.g., via dissociative autodetachment) of excited anionic states. Depending on the energetics and relative cross-sections, this process may compete favorably with direct photodetachment. However, we expect autodetachment to take place when the photon energy falls below the VDE for the direct photodetachment. With these considerations in mind, a possible origin of band IV is a covalent (CS₂)₂⁻ structure with a VDE in excess of the 355 nm photon energy. The 266 nm photoelectron imaging results (presented next) will provide a direct photodetachment signature of this covalent species.

Comparing the relative intensities of bands I and II in Fig. 5.4(a) for $n = 2$ and Fig. 5.4(b) for $m = 0$, it can be seen that band I is more intense when (CS₂)₂⁻ is prepared in the dry source condition, while band II is more intense under the wet conditions. At first, this observation may appear surprising, since the (CS₂)₂⁻ anion itself does not include a water moiety. Band II diminishes in intensity upon the addition of either a CS₂ or H₂O solvent molecule to (CS₂)₂⁻. The band's disappearance could be attributed, in part, to a solvation-induced spectral shift: while band II is expected to move to higher electron binding energies (eBEs) with the addition of solvent molecules, band IV always peaks near eKE = 0. Therefore, in larger clusters band II will eventually overlap with the more

intense band IV. However, the projected spectral shift is not sufficient to explain band II's near-absence in $(\text{CS}_2)_3^-$ and $(\text{CS}_2)_2^-\cdot\text{H}_2\text{O}$. Hence, we attribute this band's behavior to a decrease in the relative abundance of the corresponding core-anion isomer(s) in larger clusters.

5.3.2 Photoelectron Imaging of $(\text{CS}_2)_2^-$: The Effect of H_2O

We now turn to a detailed discussion of the photoelectron imaging results for the $(\text{CS}_2)_2^-$ dimer, focusing on the sharp, reproducible variations in the $(\text{CS}_2)_2^-$ isomer population balance depending on the ion source conditions, particularly the presence of water in the precursor gas delivery line. Figures 5.5(a) and (b) show the 266 nm photoelectron images and spectra of $(\text{CS}_2)_2^-$ formed under the dry and wet source conditions, respectively. The left and right halves of the images shown represent the raw and Abel-inverted data, respectively.

Even though both datasets in Figs. 5.5(a) and (b) correspond to (nominally) the same anion, there are significant differences between the spectra. The differences in the relative band intensities reflect the variation in the isomer distribution depending on the ion source conditions. To facilitate the analysis, the $(\text{CS}_2)_2^-$ data are compared to the photoelectron spectrum of CS_2^- , shown in both Figs. 5.5(a) and (b) by dotted lines. The CS_2^- spectrum is derived from a 266 nm photoelectron image, not included here due to its similarity with the past result.¹⁷⁰ Following the previous studies,^{50,159,170} the CS_2^- bands peaking at eBE = 1.46, 3.38, 3.72, and 4.03 eV are assigned to transitions from the X^2A_1 state of CS_2^- to the $X^1A_1(1\Sigma_g^+)$, a^3B_2 , b^3A_2 , and A^1A_2 neutral states, respectively. Of

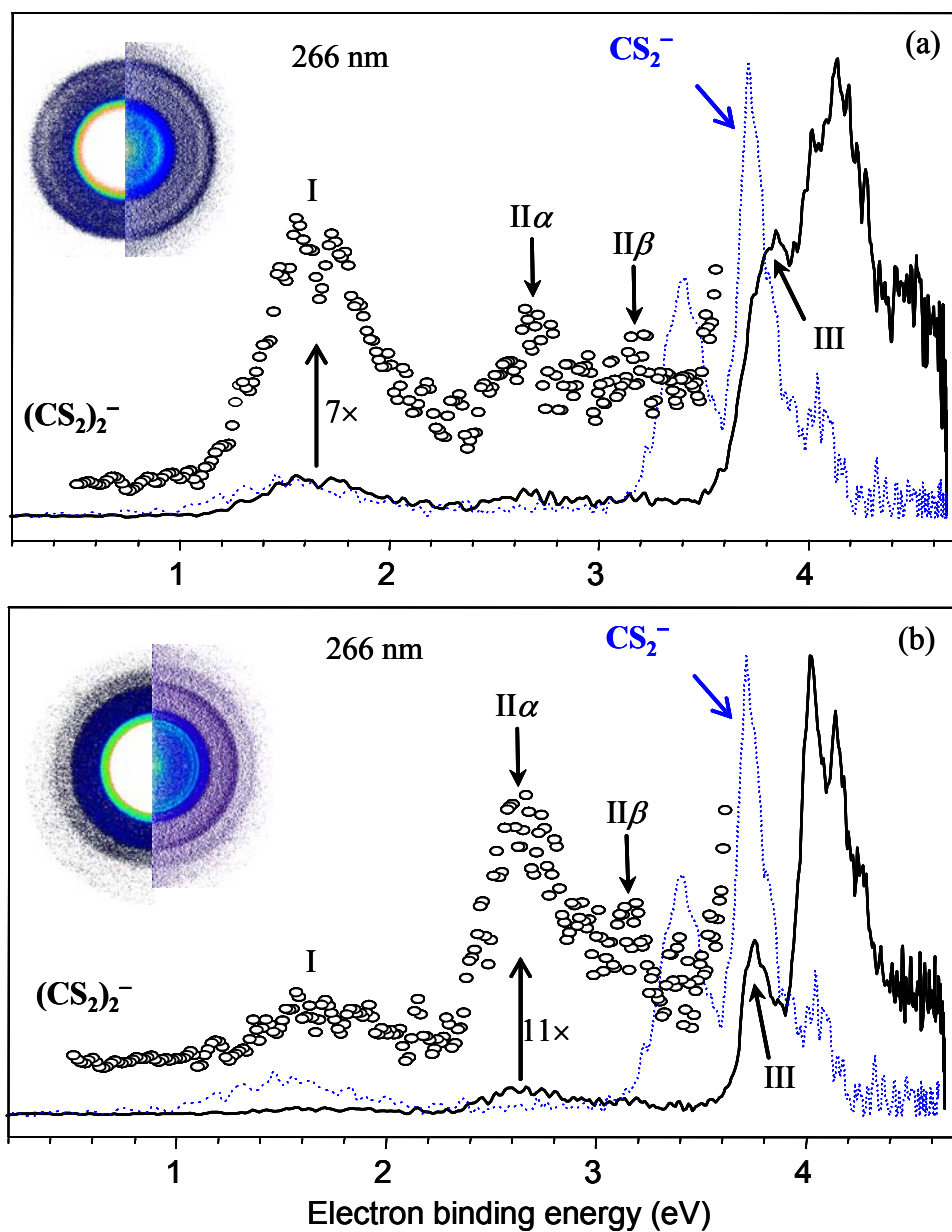


Figure 5.5 The 266 nm photoelectron images and the corresponding photoelectron spectra of $(\text{CS}_2)_2^-$ formed under (a) dry source condition, and (b) wet source condition. Also shown are the magnified portions of the spectra in the electron binding energy range of 0.5–3.5 eV. The photoelectron spectrum of CS_2^- extracted from 266 nm image is included (shown as dotted line) for reference.

these, only the first two transitions were accessible at 355 nm (see Fig. 5.2). Following the adopted nomenclature, these two lowest-energy CS_2^- transitions, $X^1\text{A}_1(^1\Sigma_g^+) \leftarrow X^2\text{A}_1$ and $a^3\text{B}_2 \leftarrow X^2\text{A}_1$, are responsible for the bands labeled as I and III, respectively, in the photoelectron spectra presented throughout this Chapter.

Examining the $(\text{CS}_2)_2^-$ spectra in Figs. 5.5(a) and (b) in comparison with the CS_2^- spectrum, the $(\text{CS}_2)_2^-$ bands centered at eBE = 1.69 eV (band I), 3.79 eV (band III), and 4.02 eV are unambiguously assigned to the $\text{CS}_2^- \cdot \text{CS}_2$ ion-molecule complex. These bands are shifted by 0.25–0.41 eV, relative to CS_2^- , consistent with the expected solvation energetics. Band II, assigned to covalent C_2S_4^- , exhibits a partially resolved doublet character, which was not clear in the 355 nm results [Fig. 5.2(a)], presumably due to the overlap with the intense autodetachment transition, band IV. The two components of band II, seen at 266 nm, are labeled in Fig. 5.5 as $\text{II}\alpha$ and $\text{II}\beta$.

As in the previous studies,^{32,159,161} the $(\text{CS}_2)_2^-$ band at eBE = 2.69 eV (band $\text{II}\alpha$ in Fig. 5.5) is assigned to a C_2S_4^- covalent structure. The location of this band is in reasonable agreement with the VDE estimated for the C_{2v} ($^2\text{B}_1$) C_2S_4^- anion based on the CCSD(T)/6-311+G(3df) and B3LYP/aug-cc-pVTZ calculations (2.53 and 2.87 eV, respectively – see Fig. 4.3). The band at 3.17 eV (band $\text{II}\beta$) has not been assigned before, although the doublet structure of the spectrum in this spectral region is discernable in the past data.¹⁵⁹ We assign band $\text{II}\beta$ to direct photodetachment from the D_{2h} ($^2\text{B}_{3g}$) covalent structure shown in Fig. 4.3, as the location of the band's maximum is in good agreement with the VDE values for this structure obtained from both the CCSD(T) (3.13 eV) and B3LYP

(3.48 eV) calculations. (As I was finalizing this dissertation for submission to the Graduate College at the University of Arizona, a manuscript by Matsuyama and Nagata¹⁶⁹ became available online, suggesting the same assignment of this band).

Comparing the photoelectron spectra of $(\text{CS}_2)_2^-$ obtained under the dry and wet source conditions [Figs. 5.5(a) and (b), respectively], it is clear that the presence of water in the precursor gas mixture enhances the formation of the global-minimum C_{2v} (2B_1) covalent structure relative to $\text{CS}_2^- \cdot \text{CS}_2$. Figures 5.5(a) and (b) include magnified portions of the spectra in the $e\text{BE} = 0.5\text{--}3.5$ eV range. Under the dry source conditions [Fig. 5.5(a)], band I, assigned to $\text{CS}_2^- \cdot \text{CS}_2$, is more intense than both bands $\text{II}\alpha$ and $\text{II}\beta$, assigned to C_2S_4^- . In contrast, under the wet source conditions [Fig. 5.5(d)], the covalent bands, especially $\text{II}\alpha$, are markedly more intense than band I.

The CS_2^- spectrum included in Figs. 5.5(a) and (b) features three intense partially resolved bands in the range of $e\text{BE} = 3.2$ to 4.2 eV. These CS_2^- transitions, after accounting for the solvation-induced shift, dominate the $e\text{BE} \geq 3.6$ eV region of the $(\text{CS}_2)_2^-$ spectrum. However, carefully inspecting the $(\text{CS}_2)_2^-$ spectra in Figs. 5.5(a) and (b), we observe an additional band, peaking at $e\text{BE} = 4.15$ eV, that cannot be ascribed to $\text{CS}_2^- \cdot \text{CS}_2$.

To clarify the spectral assignment in this congested region ($e\text{BE} \geq 3.6$ eV), we acquired 266 nm photoelectron images of CS_2^- solvated by CO_2 , H_2O , and O_2 . The photoelectron spectra for the CO_2 and H_2O solvents are presented in Figs. 5.6(a) and (b), respectively (the corresponding spectra for $\text{CS}_2\text{--O}_2$ system is provided in Chapter 7), and

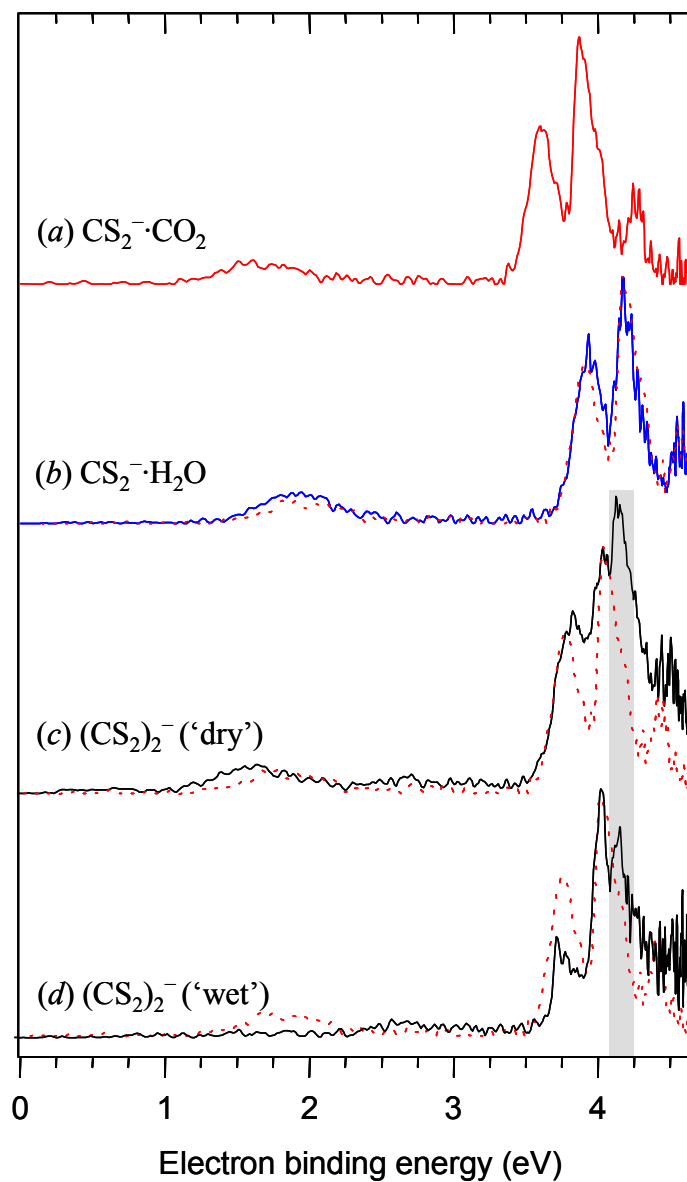


Figure 5.6 Photoelectron spectra of $(\text{CS}_2)_2^-$ and solvated CS_2^- extracted from 266 nm photoelectron images. The dotted line curve in (b)-(d) is shifted $\text{CS}_2^- \cdot \text{CO}_2$ spectrum from (a). The shaded band centered at 4.15 eV in (c) and (d) does not originate from $\text{CS}_2^- \cdot \text{CS}_2$; it is attributed to a $\text{C}_2\text{S}_4^- [D_{2d} (^2A_1)]$ covalent structure.

Table 5.1. Solvation-induced shifts of the CS_2^- photodetachment bands.

Neutral state	VDE (eV)	VDE (eV) shift due to solvation of CS_2^- by			
		CO_2	CS_2	O_2	H_2O
$X^1\text{A}_1(^1\Sigma_g)$	1.46	0.21	0.24	0.46	0.46
$a^3\text{B}_2$	3.38	0.23	0.41	0.45	0.56
$b^3\text{A}_2$	3.72	0.15	0.30	0.37	0.44
$A^1\text{A}_2$	4.03	0.23	-	0.43	0.57

are compared to the $(\text{CS}_2)_2^-$ data obtained under the dry and wet source conditions as shown in Figs. 5.6(c) and (d), respectively. Although these $(\text{CS}_2)_2^-$ spectra are very similar to the respective results in Figs. 5.5(a) and (b), they in fact represent different experimental runs under the respective source conditions. The duplicate datasets are shown to demonstrate the reproducibility of the experimental observations.

The motivation for the supplementary measurements presented in Fig. 5.6 is that, on the one hand, the $\text{CS}_2^- \cdot \text{CO}_2$ and $\text{CS}_2^- \cdot \text{H}_2\text{O}$ photoelectron spectra are expected to be affected by solvation in a manner similar to that of the $\text{CS}_2^- \cdot \text{CS}_2$ ion-molecule complex. On the other hand, the CO_2 and H_2O molecules are not expected to form favorable covalent bonds with CS_2^- . Hence, by comparing the spectra of $(\text{CS}_2)_2^-$ to those of $\text{CS}_2^- \cdot \text{CO}_2$ and $\text{CS}_2^- \cdot \text{H}_2\text{O}$ it should be possible to identify the signatures of the covalent dimer anion in the congested $(\text{CS}_2)_2^-$ spectra.

The observed solvation shifts of the CS_2^- photodetachment bands due to different solvent molecules are summarized in Table 5.1. The VDE values listed are determined by fitting the sum of individual Gaussians, corresponding to each of the observed spectral band, to the experimental spectra. From Table 5.1, the solvating strength towards CS_2^- can be ordered as $\text{H}_2\text{O} > \text{O}_2 > \text{CS}_2 > \text{CO}_2$. We note, however, that the individual bands in the same photoelectron spectra are not shifted by the same amounts. In particular, for all solvent molecules considered, the $a^3\text{B}_2 \leftarrow X^2\text{A}_1$ transition (band III in Figs. 5.2, 5.4, and 5.5) exhibits a greater (by ~ 0.1 eV on average) solvent-induced shift, compared to the $b^3\text{A}_2 \leftarrow X^2\text{A}_1$ transition (the middle of the three CS_2^- photodetachment bands in the eBE

= 3.2 – 4.2 eV range, as seen, for example, in Fig. 5.5). We believe that this effect is due to more favorable interaction of solvent molecules with the in-plane b_2 molecular orbital of CS_2^- , compared to the out-of-plane a_2 orbital.

As seen in Figs. 5.6(a) and (b), the three characteristic CS_2^- bands at $eBE > 3.2$ eV remain resolved upon solvation. The overall spectral patterns remain similar despite the difference in the solvation energies for CO_2 and H_2O . To emphasize this point, the $\text{CS}_2^- \cdot \text{CO}_2$ spectrum, shifted by 0.30 eV to higher energy, is superimposed (dotted line) in Fig. 5.6(b) with the $\text{CS}_2^- \cdot \text{H}_2\text{O}$ spectrum (solid line). There are no significant differences between the shifted $\text{CS}_2^- \cdot \text{CO}_2$ and the $\text{CS}_2^- \cdot \text{H}_2\text{O}$ spectra. Similarly, in Figs. 5.6(c) and (d), the same $\text{CS}_2^- \cdot \text{CO}_2$ spectrum, only shifted by 0.16 eV, is superimposed with the dry and wet source conditions $(\text{CS}_2)_2^-$ spectra. Now, significant differences can be seen comparing the band structures of homogeneously and heterogeneously solvated CS_2^- . In particular, there is an additional $(\text{CS}_2)_2^-$ band in the shaded area that peaks at 4.15 eV. This is the same band that was first noted in the similar spectra shown in Fig. 5.5. Since this additional band does not correspond to any feature in the $\text{CS}_2^- \cdot \text{CO}_2$ and $\text{CS}_2^- \cdot \text{H}_2\text{O}$ spectra, it cannot be attributed to the $\text{CS}_2^- \cdot \text{CS}_2$ ion-neutral complex.

Comparing the spectra in Fig. 5.5(a) vs. 5.5(b), as well as Fig. 5.6(c) vs. 5.6(d), we further note that the relative intensity of the 4.15 eV band is reproducibly greater under the dry, compared to wet, source conditions. This trend is opposite of that displayed by bands $\text{II}\alpha$ and $\text{II}\beta$, suggesting that the 4.15 eV band arises from a different covalent $(\text{CS}_2)_2^-$ isomer. Among the structures in Fig. 4.3, the D_{2d} (2A_1) structure is the only

electronic isomer with a comparatively high VDE (3.66 eV according to CCSD(T) and 4.06 eV according to B3LYP). Therefore, we suggest that the photoelectron spectra of $(\text{CS}_2)_2^-$ include previously unidentified spectral features of the D_{2d} (2A_1) isomer in the eBE = 3.75-4.3 eV region. Due to its relatively large VDE, this isomer may also be responsible for the (dissociative) autodetachment transition observed at 355 nm in the low-eKE region [band IV in Fig. 5.2(a)].

5.4 Observation of Different Electron Binding Motifs in $(\text{CS}_2)_n^-$, $n > 4$

The photoelectron imaging results for $(\text{CS}_2)_n^-$ acquired at 532 nm (for $n = 4-8$), and 355 nm (for $n = 8-12$) are presented in Fig. 5.7. The strong intensity band with the higher binding energy is the same as band I in Fig. 5.2 and 5.4. Band I is the lowest energy transition band for $n \leq 4$. However, for $n \geq 4$ a new transition band with weak intensity is observed at a binding energy smaller than that of band I. The new transition band is labeled as *S* in Fig. 5.7.

Although detailed analysis of the *S* band requires investigation of the electronic states using theoretical modeling, possible electron binding motifs that differ from smaller size clusters can be suggested based on the known properties of the CS_2 molecule and its anion. Previous studies have shown that Rydberg electron transfer leads to the formation of two forms of long-lived metastable CS_2^- with different degrees of stability as determined from electric field strength that is required to induce electron detachment.^{156,157} In the first form, the excess electron detaches below $3 \text{ kV}\cdot\text{cm}^{-1}$ while the second form requires more than $10 \text{ kV}\cdot\text{cm}^{-1}$ of field strength. It takes up to ~ 2 ms for

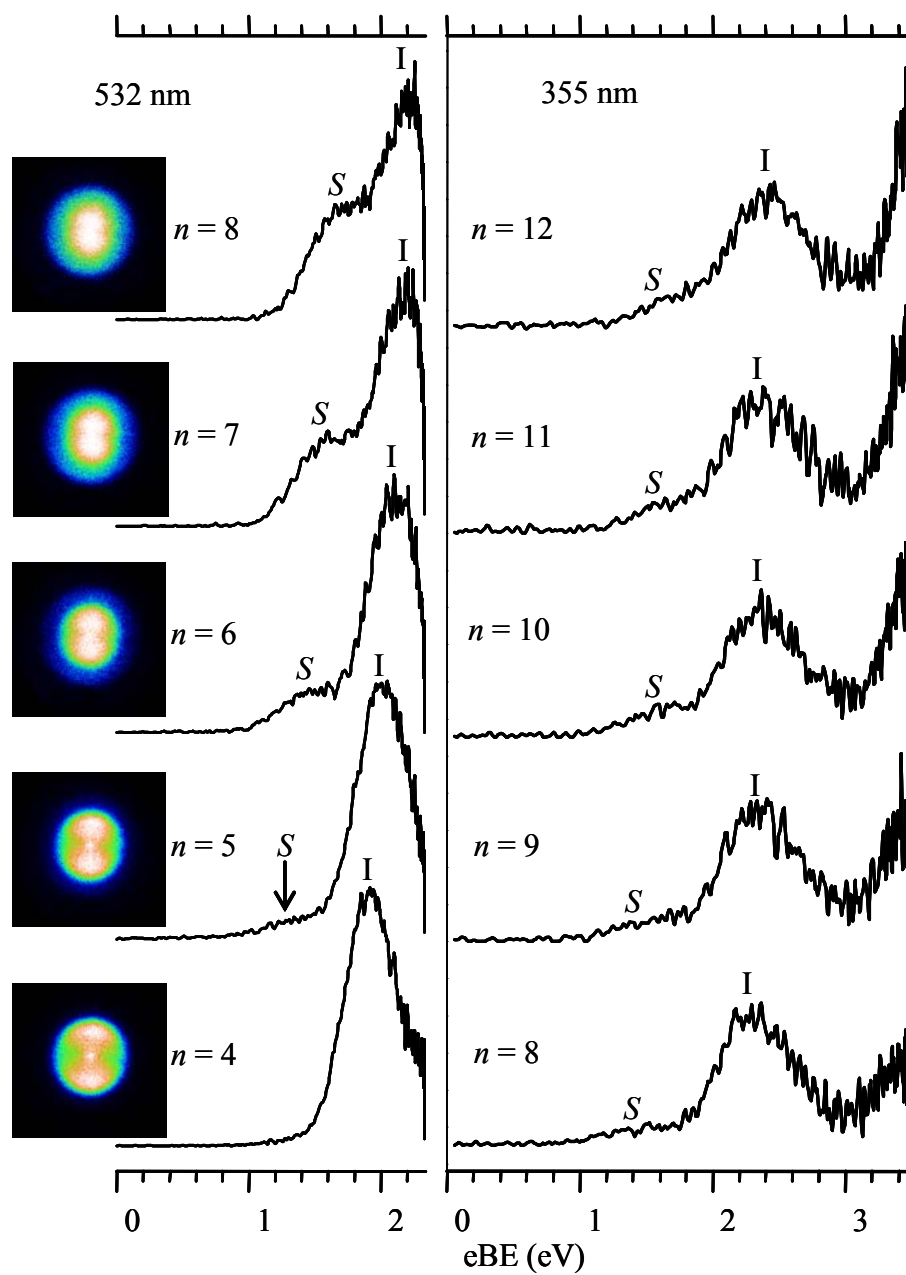


Figure 5.7 Observation of a new photodetachment transition band for $(\text{CS}_2)_n^-$, $n > 4$. The new band is labeled as *S*.

the metastable forms to convert to stable CS_2^- that does not exhibit field induced detachment even at $18 \text{ kV}\cdot\text{cm}^{-1}$. On the other hand theoretical calculation indicated that the anion at linear geometry is stable towards autodetachment by $\sim 16 \text{ meV}$.¹⁶⁶ Our calculation (Chapter 4) with different better basis set increases the anion (with linear geometry) stability against autodetachment to $\sim 90 \text{ meV}$. Based on the earlier calculation the formation of the two groups of CS_2^- ions with different field detachment characteristics were attributed to near-linear configuration with different amounts of bending excitations. Radiative decay to lower vibrational levels was suggested as a stabilization mechanism.

Although the previous calculation by Gutsev *et al.*¹⁶⁶ compares only the ground state potential energy curve of the anion with that of the neutral, our calculation described in Chapter 4 shows that both the $^2\text{A}_1$ and $^2\text{B}_1$ lie below the $^1\text{A}_1$ neutral state at all SCS angles at which the C–S distances are optimized constrained to the C_{2v} symmetry (see Fig. 4.1). Therefore, as the CS_2^- leaves linearity following electron capture the anion can be formed in $X^2\text{A}_1$ and $^2\text{B}_1$ states. Since the potential energy gradient for the $^2\text{B}_1$ state is directed towards linearity, eventually, the population in $^2\text{B}_1$ state is funneled to the $X^2\text{A}_1$ state through the Renner-Teller coupling. This population transfer is expected to take place rapidly in $(\text{CS}_2)_n^-$ for small n . Keeping this in mind we suggest two possibilities that account for the appearance of S band.

The first one is based on the fact that CS_2 can bind electron at linear geometry where the $^2\text{A}_1$ and $^2\text{B}_1$ convert to $^2\Pi_u$ resonance state. When the electron is captured in large clusters of CS_2 , it is possible that the excess electron would hop from one CS_2 moiety to

another before the nuclear configuration takes to the anionic equilibrium geometry. In this regard, the network permeating states predicted for $(\text{H}_2\text{O})_n^-$ by Sommerfeld and Jordan²⁵ seem even more appropriate for $(\text{CS}_2)_n^-$ clusters. This state is expected to have low relatively electron binding energy.

The second possibility is that since ${}^2\text{B}_1$ state is also below the neutral state it may have some contribution as the cluster size increases. Although, for the isolated CS_2^- , the minimum of ${}^2\text{B}_1$ state is at linear geometry it may move towards bent structure as the cluster size increases, similar to CO_2^- in water cluster (Sec. 3.8). This situation slows down the population transfer from ${}^2\text{B}_1$ to the $X\ {}^2\text{A}_1$ ground state. Therefore, albeit its contribution is expected to be small, the homogeneously solvated CS_2^- ion can be formed in a distinct ${}^2\text{B}_1$ state as the solvent cluster size increases giving rise to the photodetachment transition band denoted as *S* in Figs. 5.7(a) and (b).

5.5 Discussion

The results presented in Sec. 5.3 indicate that the $(\text{CS}_2)_2^-$ anion, as well as the larger CS_2 based cluster anions, exists in several isomeric forms. The point-group symmetries (and the corresponding electronic states) of the proposed $(\text{CS}_2)_2^-$ electronic structures are C_s (${}^2\text{A}'$), C_{2v} (${}^2\text{B}_1$), D_{2h} (${}^2\text{B}_{3g}$), and D_{2d} (${}^2\text{A}_1$). The corresponding geometries and relevant energetics are summarized in Fig. 4.3, along with other structures not observed in this experiment. The coexistence of several isomers for $(\text{CS}_2)_2^-$ is in marked contrast with $(\text{CO}_2)_2^-$, for which only the D_{2d} (${}^2\text{A}_1$) structure has been observed experimentally for the

dimer anion.¹¹⁰

The presence of water molecules in the neutral precursor gas (wet source conditions) enhances the formation of cluster isomers that give rise to bands II, particularly II α . This band is assigned to the most stable covalent structure of $(\text{CS}_2)_2^-$, C_{2v} (${}^2\text{B}_1$), while its satellite band II β is ascribed to the D_{2h} (${}^2\text{B}_{3g}$) isomer. Dry source conditions, on the other hand, favor (in relative terms) the formation of the $\text{CS}_2^- \cdot \text{CS}_2$ ion-neutral complex and the D_{2d} (${}^2\text{A}_1$) electronic structures.

The accepted mechanism of cluster anion formation involves the attachment of slow secondary electrons to neutral clusters in the supersonic expansion,⁸⁰ while the resulting anions are stabilized by solvent evaporation. In this light, it is intriguing to note that from the electronic structure perspective¹⁶³ both the C_s (${}^2\text{A}'$) and D_{2d} (${}^2\text{A}_1$) local minima of $(\text{CS}_2)_2^-$ correlate to the $\text{CS}_2^- + \text{CS}_2$ dissociation limit. The C_s (${}^2\text{A}'$) and D_{2d} (${}^2\text{A}_1$) dimer anions can be thought of as resulting from the addition of an electron to the lowest unoccupied molecular orbital (LUMO) of $(\text{CS}_2)_2$ in its ground electronic state, corresponding to the neutral van der Waals dimer. Hence, the formation of the C_s (${}^2\text{A}'$) and D_{2d} (${}^2\text{A}_1$) dimer anions from the neutral clusters can be described as straightforward electron capture, followed by the anion stabilization by neutral solvent evaporation.

On the other hand, the electron configurations of the C_{2v} (${}^2\text{B}_1$) and D_{2h} (${}^2\text{B}_{3g}$) structures of $(\text{CS}_2)_2^-$, at least within the single-reference picture, are both based on the “doubly excited” neutral species, which can be thought of as resulting from singlet coupling of two CS_2 moieties, individually promoted to their respective triplet states.¹⁶³ Although the C_{2v} (${}^2\text{B}_1$) isomer is predicted to be the global-minimum $(\text{CS}_2)_2^-$ structure, its electronic

state does not correlate to the $\text{CS}_2^-(X^2A_1) + \text{CS}_2(X^1\Sigma_g^+)$ dissociation limit or to the C_s ($^2A'$) and D_{2d} (2A_1) electronic states. Therefore, the formation of the C_{2v} (2B_1) structure, as well as the D_{2h} ($^2B_{3g}$) structure, by electron addition to neutral CS_2 clusters must proceed via nonadiabatic transitions and potential energy barriers.

The observed variations in the photoelectron spectrum of $(\text{CS}_2)_2^-$, depending on the presence of water molecules, can be rationalized with the assumption that in the absence of water the newly formed cluster anions are stabilized more efficiently in the local minima corresponding to the C_s ($^2A'$) and D_{2d} (2A_1) dimer-anion structures. Initially, we expect the excess electron to occupy the LUMO of one or two CS_2 molecules within the cluster, leading to the formation of the C_s ($^2A'$) or D_{2d} (2A_1) dimer-anion structures. The efficiency of relaxation towards the global minimum C_{2v} (2B_1) structure depends on the strength of the nonadiabatic couplings and the availability of excess energy to overcome the potential energy barriers separating the local and global minima.

The expected neutral clusters in the dry and wet source conditions may be described as $(\text{CS}_2)_n\text{Ar}_k$ and $((\text{CS}_2)_n(\text{H}_2\text{O})_m)\text{Ar}_k$, respectively. In the dry source condition, the anion stabilization involves evaporation of the weakly bound CS_2 and Ar moieties. Since the highest internal temperature of the cluster can only be as high as the binding energy of Ar atom or CS_2 molecule, the dimer anion can effectively be stabilized in the C_s ($^2A'$) or D_{2d} (2A_1) initially formed local minima structures. In the absence of other weakly bound solvent molecules, the $(\text{CS}_2)_2^-$ anions hydrated by water molecules can be formed with very high internal temperatures and possess an excess of internal energy as large as the binding energy of one H_2O . Thus, the presence of water may facilitate the nonadiabatic

interactions leading to the formation of the global-minimum anionic structure, even if H₂O is evaporated once the ground electronic state is formed. In addition, higher internal temperatures in the presence of H₂O may facilitate surmounting potential energy barriers, enabling the anion relaxation from the initial local minima to the global minimum structure. The heat released during the formation of the more stable structure may then lead to the evaporation of the remaining water molecule(s), ultimately yielding an unhydrated C₂S₄⁻ anion.

On the other hand, if water molecules are present in the final cluster after equilibration, another factor comes into play. The excess electron will then tend to localize on the CS₂ monomer, due to more favorable interaction of H₂O with the more localized charge distribution of CS₂⁻, compared to C₂S₄⁻. This effect is reflected in Fig. 5.4(b) where the relative intensity of the C_{2v} (²B₁) band decreases in the photoelectron spectra of (CS₂)(H₂O)_m for m ≥ 1. This also holds true for the homogenous solvation as it can be seen in Figs. 5.2(a) and 5.4(a), where the relative intensity of the corresponding band declines similarly in the photoelectron spectra of (CS₂)_n⁻ for n > 2. The photodissociation results described in Chapter 6 provide additional evidence of this effect.

5.6 Summary

The photoelectron imaging results highlight the structural complexity of the (CS₂)₂⁻ dimer anion. Several (CS₂)₂⁻ isomers are generated in the ion source, with their population distribution depending sensitively on the source conditions, particularly the presence of water vapor in the precursor gas mixture. Based on the assignment of the

bands in the photoelectron spectra, the coexistence of the following isomers is proposed for $(\text{CS}_2)_2^-$: the $\text{CS}_2^- \cdot \text{CS}_2$ [C_s ($^2A'$)] ion-molecule complex and three covalent structures [C_{2v} (2B_1), D_{2h} ($^2B_{3g}$) and D_{2d} (2A_1)]. The presence of water in the precursor gas mixture enhances the formation of the global-minimum C_{2v} (2B_1) structure, particularly relative to C_s ($^2A'$) and D_{2d} (2A_1). It is proposed that the formation of the global-minimum structure is facilitated by the hydration-induced nonadiabatic interactions and the higher internal temperature expected for the initially formed (metastable) cluster anions containing water molecules. In the equilibration process leading to the formation of the C_{2v} (2B_1) cluster core, the H_2O and/or CS_2 solvent molecules will tend to evaporate. If some solvents remain within the cluster, their stronger interactions with the more localized charge distribution of CS_2^- , compared to C_2S_4^- , favor the monomer-anion based structures for the $(\text{CS}_2)_n^-$, $n > 2$ and $(\text{CS}_2)_2^-(\text{H}_2\text{O})_m$, $m > 0$ cluster anions.

In the $(\text{CS}_2)_n^-$ anion a new isomer with very low binding energy is observed for $n \geq 5$. Two types of electron binding motifs are proposed for the new isomer: (i) electron permeating state where the electron freely distributed in $(\text{CS}_2)_n^-$ cluster network, and (ii) formation of homogeneously solvated CS_2^- in 2B_1 state in a slightly bent geometry.

Chapter 6

PHOTODISSOCIATION OF BARE AND SOLVATED $(\text{CS}_2)_2^-$: MANIFESTATION OF ELECTRONIC ISOMER COEXISTENCE AND SOLVENT-INDUCED CORE SWITCHING

6.1 Introduction

Carbon disulfide is used as a solvent and a building block in the synthesis of many organic compounds. The reactivity of CS_2 can be contrasted with that of isovalent CO_2 by referring to the thermochemical data on ion-molecule association and clustering reactions.¹⁷¹ Carbon dioxide forms weak complexes with positive ions due to the poor Lewis basicity of oxygen atoms, but it forms covalent bonds with negative ions (such as O^-) through nucleophilic attack on the carbon atom.^{153,172} The CS_2 molecule, on the other hand, exhibits amphoteric character, forming covalent bonds with both positive and negative ions through its sulfur and carbon atoms, respectively.¹⁵⁸ For the gas-phase clustering reactions of CS_2 in a pulsed electron-beam high-pressure mass spectrometer, the S_2^- , $\text{S}_2^-\cdot\text{CS}_2$ and CS_3^- ions were observed as minor products, in addition to the $(\text{CS}_2)_n^-$ clusters.¹⁵⁸ In the gas-phase drift-tube study of the $^{34}\text{S}^- + \text{CS}_2$ reaction, the isotope-exchange ($\text{S}^- + ^{34}\text{SCS}$) and sulfur abstraction ($^{34}\text{SS}^- + \text{CS}$) products were observed.¹⁷³ Although CS_3^- was not detected directly, the formation of the long-lived CS_3^{-*} complex was suggested in the isotope-exchange process. However, in the S_2^- channel, which was observed at collision energies above 0.3 eV, the $^{32}\text{S}^{32}\text{S}^-$ product was not observed, ruling out the formation of an intermediate CS_3^{-*} collision complex.¹⁷³

Maeyama *et al.* studied the photodissociation of $(\text{CS}_2)_n^-$, $n = 1-4$ by tuning the photon energy in the $\sim 1.0-2.8$ eV range.¹⁶⁰ In their experiment, two dissociation channels, $\text{CS}_2^- + \text{CS}_2$ and $\text{C}_2\text{S}_2^- + \text{S}_2$, were observed, although the channel branching ratio could not be quantified. Nonetheless, the total photodepletion cross-section peaked between 1.6-1.8 eV for all $n \geq 2$, suggesting that the same cluster core was involved in the fragmentation of all clusters. These results were interpreted considering the C_{2v} (${}^2\text{B}_1$) structure of the dimer anion, C_2S_4^- , where the two CS_2 moieties are initially bound by the covalent C-C and S-S bonds. In the intracuster reactions of $(\text{CS}_2)_n^-$ induced by surface impact at a collision energy of 50 eV, Kondow and coworkers observed the S^- , C_2S^- , S_2^- , CS_2^- and C_2S_2^- fragments for $n = 2$, and S^- , S_2^- , and CS_2^- for $n = 3$.¹⁶⁸

Although the past photodissociation results were interpreted by considering only the C_{2v} (${}^2\text{B}_1$) structure of the dimer-anion,¹⁶⁰ other isomeric structures have been proposed for $(\text{CS}_2)_2^-$, including several distinct covalently bound isomers.^{159,161-164} The stability and the photochemical properties of these anions are strongly affected by their immediate surroundings and also by the manner in which they are formed. For example, Yu *et al.* recorded infrared spectra of the dimer anion, which was formed by high-frequency electric discharge in CS_2 and trapped in solid neon and argon matrices.¹⁶² Using the MP2/6-311+G(d) and B3LYP/6-311+G(d) predictions to aid the spectroscopic assignment, they identified the D_{2h} symmetry structure (${}^2\text{B}_{3g}$ electronic state) as the only structure of $(\text{CS}_2)_2^-$, whose calculated vibrational frequencies matched the observed spectral features. This assignment contrasts the C_{2v} (${}^2\text{B}_1$) structure identified in the gas-phase studies described above.

In Chapter 5, the photoelectron imaging study of $(\text{CS}_2)_2^-$ under varying ion-source and solvation conditions are presented. Assisted by the theoretical calculations, described in Chapter 4, the bands in the images and spectra are assigned to the $\text{CS}_2^- \cdot \text{CS}_2$ ion-molecule complex and three distinct covalent structures: C_{2v} (${}^2\text{B}_1$), D_{2h} (${}^2\text{B}_{3g}$), and D_{2d} (${}^2\text{A}_1$). The C_{2v} (${}^2\text{B}_1$) isomer is confirmed as the global-minimum structure, but the actual isomer distribution depends sensitively on the ion source conditions, particularly the presence of water in the precursor gas mixture.

In this Chapter, we explore the manifestations of the different electronic-structural properties of the coexisting (and competing) $(\text{CS}_2)_2^-$ isomers in their photochemistry. The photodissociation of $(\text{CS}_2)_2^-$, as well as the $(\text{CS}_2)_n^-$, $n \leq 4$ and $(\text{CS}_2)_2^- \cdot (\text{H}_2\text{O})_m$, $m \leq 2$ cluster anions is investigated using tandem time-of-flight parent and fragment mass-spectroscopy. The channel branching ratios are analyzed depending on the ion source conditions (and hence the parent isomer distribution) and the cluster solvation. The results shed light not only on the photoinduced dynamics, but also on the structure of the parent anions, complementing the photoelectron imaging study (Chapter 5).

6.2 Experimental

The experiments are carried out using the tandem time-of-flight mass spectrometer described in Chapter 2. The ions are formed following the same procedure described in Chapter 5. In the subsequent discussion, the term “dry source conditions” refers to the experimental regime where moisture in the neutral precursor gas delivery line has been removed (as much as possible) by means of baking and pumping. Alternatively, in order

to generate hydrated cluster anions, a small droplet of water is added to the precursor delivery line, corresponding to the so-called “wet source conditions”. Under the dry conditions, the $(\text{CS}_2)_n^-$ cluster progression is most abundant in the parent-ion mass-spectra. With the “wet” source, the $(\text{CS}_2)_n^-(\text{H}_2\text{O})_m$ cluster anions are most prominent (see Fig. 5.1).

The experiments are performed with the 532, 355 and 266 nm harmonics of the Nd:YAG laser (Spectra Physics Lab 130, 50 Hz pulse repetition rate). The photofragment mass spectra are recorded by accumulating the pre-amplified ion signals from the off-axis MCP detector over 512 experimental cycles using a digital oscilloscope.

6.3 Results

6.3.1 Overview

The representative mass-spectra of the $(\text{CS}_2)_n^-$ and $(\text{CS}_2)_n^-(\text{H}_2\text{O})_m$ parent anions recorded under dry and wet source conditions, respectively, are shown in Fig. 5.4 in Chapter 5. For most cluster anions considered here both electron photodetachment and photodissociation channels compete in the 532 - 266 nm regions of laser radiations. The photodetachment channel was the focus of the photoelectron imaging experiment in the previous chapter. Here we consider the competition between different photofragmentation channels.

We begin by describing the photofragmentation pathways of the hydrated CS_2^- anions in Sec. 6.3.2). These results set the stage for the discussion of the contrasting

fragmentation patterns characteristic of the CS_2^- and C_2S_4^- based cluster anions (Sec. 6.3.3). In Sec. 6.3.4, the effect of the cluster formation conditions on the fragmentation pathways of (nominally) the same cluster anions is considered.

6.3.2 Photodissociation of Bare and Hydrated CS_2^-

The photofragment-ion mass-spectra for the $\text{CS}_2^-(\text{H}_2\text{O})_m$ parent anions collected at 355 and 266 nm are presented in Figs. 6.1(a) and (b), respectively. The spectra are normalized to the same maximum intensity, not representative of the absolute dissociation cross-sections. At 355 nm, the S^- based products appear for $m = 0-5$. The CS_2^- fragment is first seen for $m = 2$ and its hydrates become the only observed product type for $m = 6-8$. At 266 nm, no anionic photofragments are observed for $m = 0$ and 1, indicating that a minimum of two water molecules are required to enable the 266 nm photodissociation of CS_2^- , as opposed to the photodetachment. The 266 nm fragments observed for $m \geq 2$ are similar to the 355 nm results, with a slight variation in the relative peak intensities.

6.3.3 Photofragmentation of $(\text{CS}_2)_n^-$ and $(\text{CS}_2)_2^-(\text{H}_2\text{O})_m$ Cluster Anions

The photofragment mass-spectra for the $(\text{CS}_2)_n^-$, $n = 2-4$ and $(\text{CS}_2)_2^-(\text{H}_2\text{O})_m$, $m = 0-2$ parent anions obtained at 532, 355 and 266 nm are presented in Figs. 6.2(a) and (b), respectively. While the fragment distributions depend, as expected, on photon energy and the number of solvating CS_2 or H_2O molecules, they also exhibit a less intuitive, yet significant dependence on the ion source conditions, specifically the presence of water in the precursor gas mixture. The spectra in Fig. 6.2(a) were obtained under the dry source

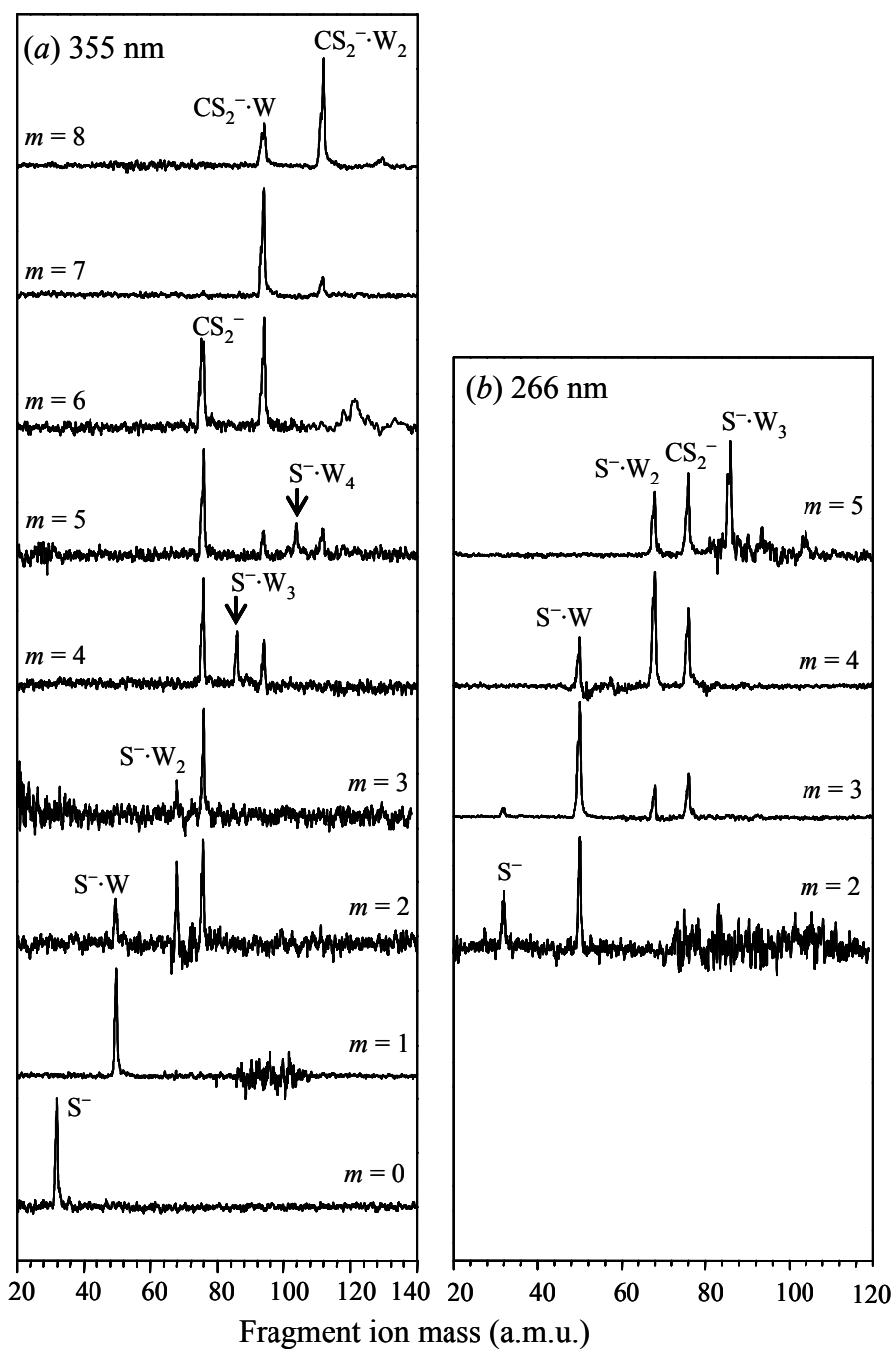


Figure 6.1 The 355 nm and 266 nm photofragment mass-spectra for the $\text{CS}_2^-(\text{H}_2\text{O})_m$ parent ions. $\text{W} \equiv \text{H}_2\text{O}$.

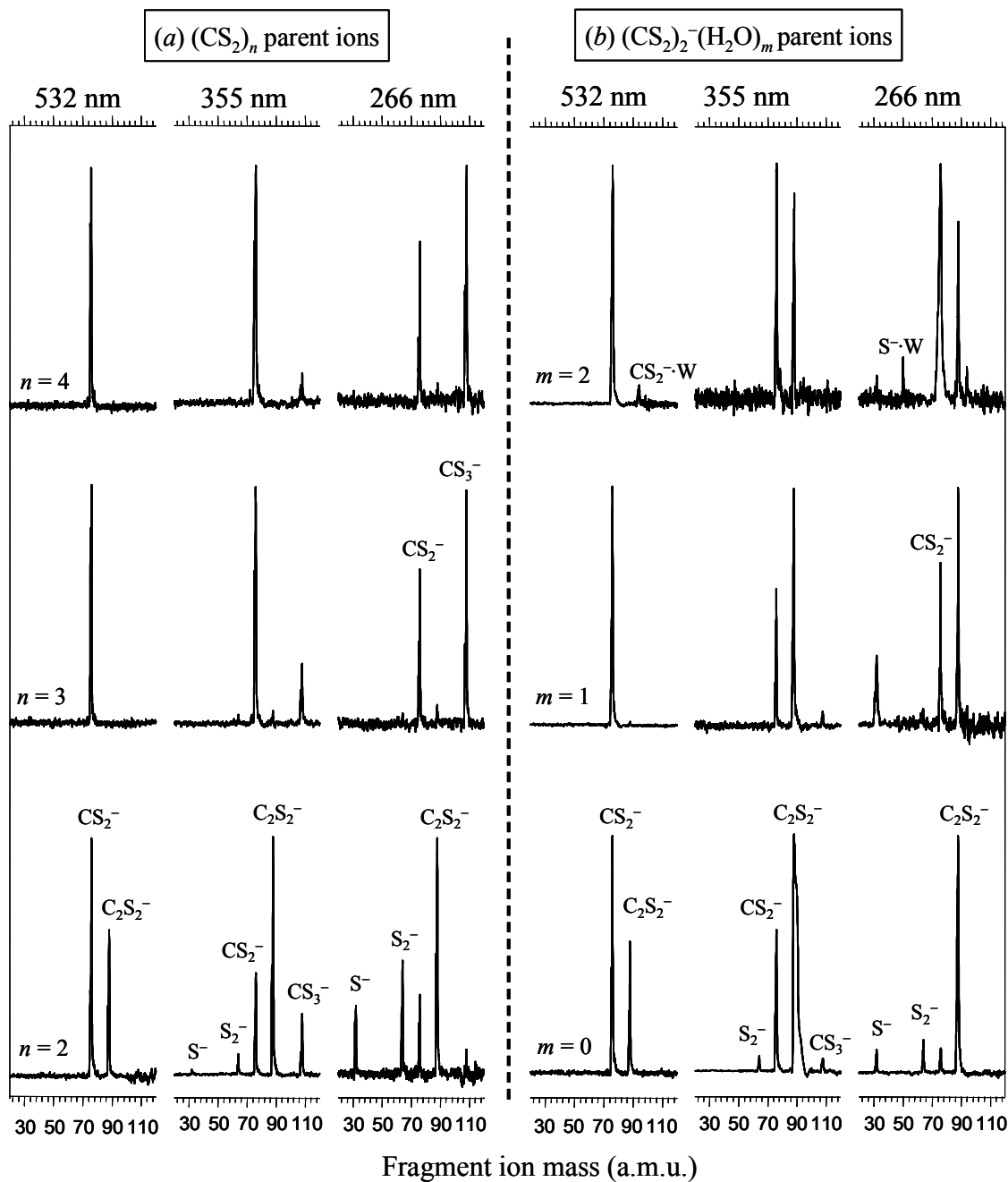


Figure 6.2 The photofragment mass-spectra for (a) $(\text{CS}_2)_n^-$, $n = 2-4$ parent ions and (b) the $(\text{CS}_2)_2(\text{H}_2\text{O})_m^-$, $m = 0-2$ parent ions. The parent anions in (a) and (b) are formed under dry and wet source conditions, respectively.

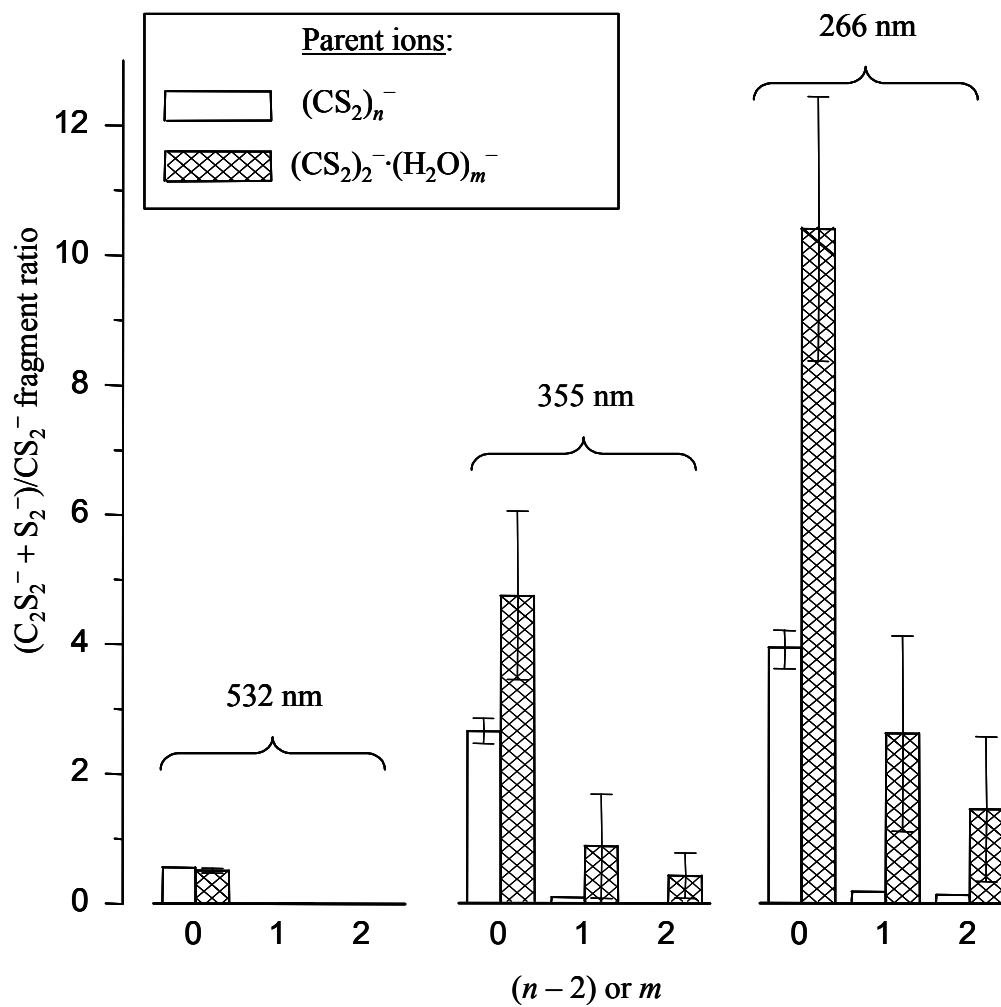


Figure 6.3 The $(\text{C}_2\text{S}_2^- + \text{S}_2^-)/\text{CS}_2^-$ product ratio for the $(\text{CS}_2)_n^-$, $n = 2-4$ and $(\text{CS}_2)_2^-\cdot(\text{H}_2\text{O})_m^-$, $m = 0-2$ parent ions, formed under the dry and wet source conditions, respectively.

conditions, while those in Fig. 6.2(b) correspond to the wet source conditions. The moisture effect on the fragmentation of the (nominally) same parent anion, $(\text{CS}_2)_2^-$, can be seen by comparing the $n = 2$ spectra in Fig. 6.2(a) to the corresponding $m = 0$ spectra in Fig. 6.2(b). Of the several photofragment types, we particularly emphasize the relative yields of CS_2^- , on one hand, and C_2S_2^- and S_2^- , on the other. The $(\text{C}_2\text{S}_2^- + \text{S}_2^-)/\text{CS}_2^-$ product ratios determined for the different wavelengths and parent ions are summarized in a histogram form in Fig. 6.3.

As seen in Fig. 6.2, the simplest fragmentation patterns are observed at 532 nm. At this wavelength, $(\text{CS}_2)_2^-$ dissociation yields the CS_2^- and C_2S_2^- fragment ions, with comparable intensities regardless of the source conditions. However, upon solvation with additional CS_2 or H_2O molecules, the C_2S_2^- channel is effectively turned off, as reflected in the 532 nm spectra in Fig. 6.2(a) for $n = 3-4$ and Fig. 6.2(b) for $m = 1-2$.

At 355 nm, two additional anionic fragments, S_2^- and CS_3^- , are observed for $(\text{CS}_2)_n^-$, in addition to the CS_2^- and C_2S_2^- products. The C_2S_2^- ion is the most intense 355 nm photofragment for the $(\text{CS}_2)_2^-$ parent anion. However, with the addition of just one more CS_2 solvent molecule, the C_2S_2^- and S_2^- product channels are almost completely turned off. Similar to the 532 nm result, in larger clusters the CS_2^- fragment takes a central stage, as seen in Fig. 6.2(a) for $n = 3-4$.

At 266 nm, the C_2S_2^- channel remains dominant for fragmentation of $(\text{CS}_2)_2^-$ under both the dry and wet source conditions, while the CS_2^- yield diminishes further, compared to the 355 and 532 nm results. This trend is accompanied by a relative increase in

S_2^- and the appearance of the S^- product. Again, the addition of the CS_2 solvent turns off, nearly completely, the S_2^- and $C_2S_2^-$ product channels, along with the S^- , while enhancing the relative intensities of CS_2^- and CS_3^- .

6.3.4 The Effect of Water in the Ion Source

As seen in Figs. 6.2(a) and (b), CS_2^- is the only 532 nm anionic product for the $(CS_2)_n^-$, $n = 3-4$ and $(CS_2)_2^-(H_2O)_m$, $m = 1-2$, cluster anions, with the exception of a minor $CS_2^- \cdot H_2O$ signal observed for $(CS_2)_2^-(H_2O)_2$. At 355 and 266 nm, however, the fragmentation patterns of the hydrated clusters are drastically different from those of $(CS_2)_n^-$. Even the unhydrated $(CS_2)_2^-$ parent anion exhibits different channel branching ratios depending on the ion source conditions. The $C_2S_2^-$ product fraction is larger with the “wet” source, as seen by comparing the 355 and 266 nm results for $m = 0$ in Fig. 6.2(b) to those for $n = 2$ in Fig. 6.2(a). This trend persists in the $(CS_2)_n^-$, $n = 3-4$ and $(CS_2)_2^-(H_2O)_m$, $m = 1-2$, clusters. As seen in Fig. 6.3, the $(C_2S_2^- + S_2^-)/CS_2^-$ product ratio is always larger within the hydrated cluster series (generated under the wet source conditions) compared to the $(CS_2)_n^-$ series (formed in a dry source).

The large error bars in Fig. 6.3 for the $(CS_2)_2^-(H_2O)_m$ parent-ion series reflect the variation in the photofragment yields between different experimental runs. These variations reflect the day-to-day fluctuations in the concentration of H_2O in the gas delivery lines. No variations of such significant magnitude were observed in the fragmentation patterns when the ion source was kept consistently moisture-free. This obser-

vation itself indicates that not just the relative intensities, but also the structural and, therefore, photochemical properties of the $(\text{CS}_2)_2^-$ and $(\text{CS}_2)_2^-(\text{H}_2\text{O})_{1-2}$ cluster anions are affected by the presence of H_2O at the ion formation stage.

The fractional yield of C_2S_2^- from $(\text{CS}_2)_2^-$ is positively correlated with the intensity of the C_{2v} (${}^2\text{B}_1$) band in the corresponding photoelectron spectrum.¹⁷⁴ Both the C_2S_2^- fragment fraction (at 355 and 266 nm) and the relative intensity of the photoelectron band increase under the wet source conditions. Hence, we conclude that the presence of H_2O in the ion source enhances the formation of the C_{2v} (${}^2\text{B}_1$) isomer of C_2S_4^- that in turn gives rise to the C_2S_2^- photofragments.

Summarizing the results: (i) The fractional yield of C_2S_2^- and S_2^- from the bare $(\text{CS}_2)_2^-$ parent anion increases in the presence of H_2O at the ion formation stage; and (ii) solvation by additional CS_2 or H_2O decreases the fractional yield of the C_2S_2^- and S_2^- fragments, mainly in favor of the CS_2^- channel. Comparing Figs. 6.2(a) and (b), particularly the 355 nm data, it may appear that H_2O is less effective in turning off the C_2S_2^- and S_2^- channels, compared to the CS_2 solvent. However, this is largely due to the more abundant presence of the C_{2v} (${}^2\text{B}_1$) isomer under the wet source conditions.

6.4 Discussion

6.4.1 The Dissociation Channels of $\text{CS}_2^-(\text{H}_2\text{O})_m$

Similar to the photodissociation of hydrated CO_2^- in water clusters,^{117,167} two types of dissociation channels are observed for $\text{CS}_2^-(\text{H}_2\text{O})_m$ at 355 and 266 nm: (i) the core-

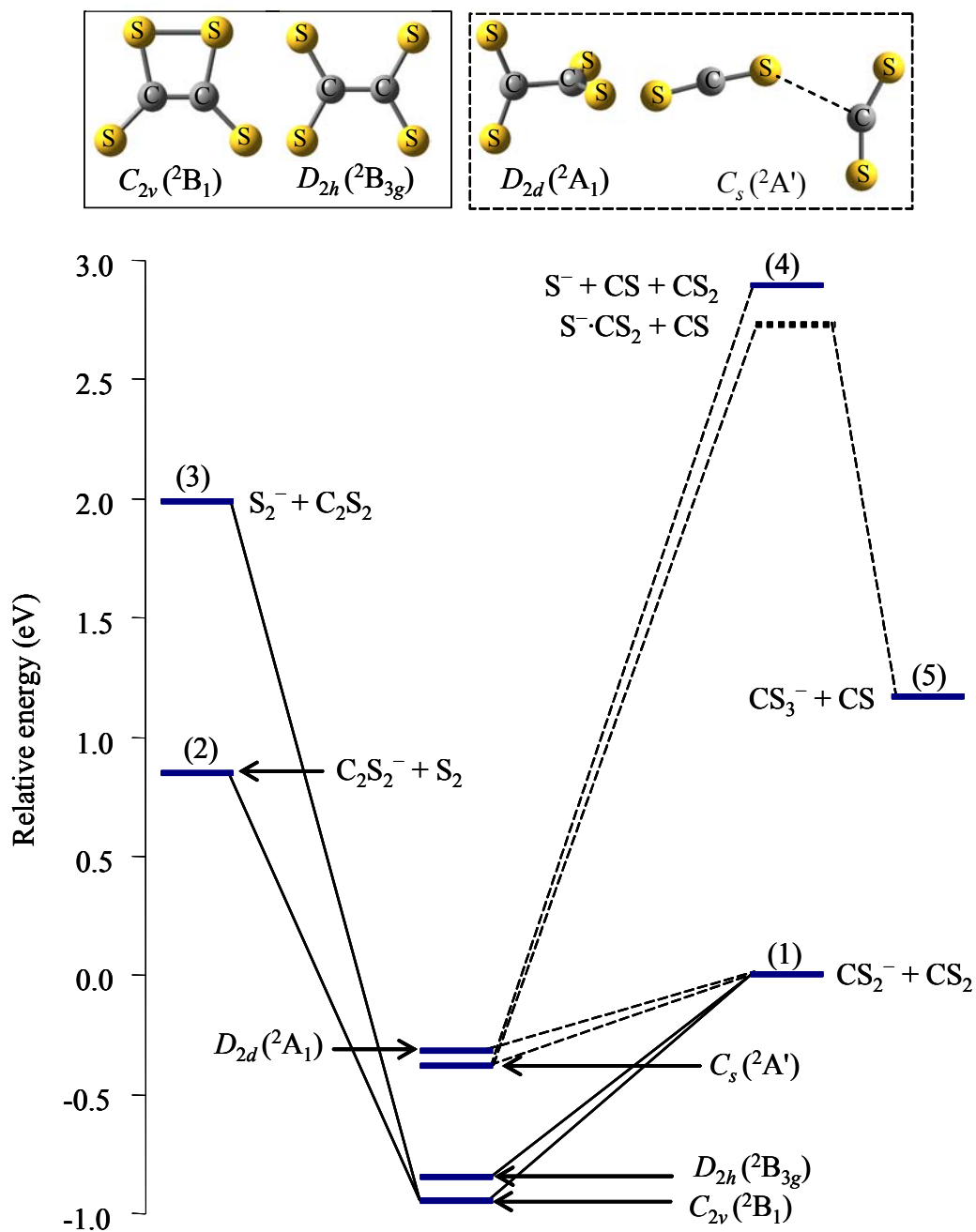


Figure 6.4 Energy diagram showing the correlations between the proposed reactant structures, intermediates and products for the bare $(\text{CS}_2)_2^-$ parent ion. The relative parent and product-channel energies are from the CCSD(T)/6-311+G(3df) calculations. The product channel correlations for the $\text{CS}_2^- \cdot \text{CS}_2$ ion-molecule complex and the $D_{2d} (^2A_1)$ structure are indicated by dashed lines, while those for the $C_{2v} (^2B_1)$ and $D_{2h} (^2B_{3g})$ isomers are indicated by solid lines.

dissociation channel, where the CS_2^- cluster core dissociates into $\text{S}^- + \text{CS}$ accompanied by loss of several water molecules, and (ii) the solvent-evaporation channel where, the photon energy is dissipated by the evaporation of several solvent molecules, while the CS_2^- anion remains intact.

6.4.2 The Dissociation Channels of $(\text{CS}_2)_2^-$

In the first photofragmentation experiment on $(\text{CS}_2)_2^-$ at photon energies of up to ~ 2.8 eV, Maeyama et al.¹⁶⁰ observed only the CS_2^- and C_2S_2^- fragmentation products. Our present findings at 532 nm (2.33 eV) are in line with this result. However, the present experiments at 355 and 266 nm reveal additional processes that were not observed previously. First, the C_2S_2^- product channel becomes dominant as the photon energy increases. Second, in addition to CS_2^- and C_2S_2^- , we observe new S^- , S_2^- and CS_3^- products.

These photofragments can be associated with the following plausible pathways:¹⁵⁶



These dissociation channels are summarized in Fig. 6.4, which shows the proposed reactant structures, intermediates, and product correlations for the $(\text{CS}_2)_2^-$ parent ion.

Similar pathways, involving additional solvent molecules, are expected for the larger $(\text{CS}_2)_n^-$ and $(\text{CS}_2)_2^-(\text{H}_2\text{O})_m$ clusters.

The parent electronic structures included in Fig. 6.4 are selected based on the photoelectron imaging results.¹⁷⁴ The structures shown, as well as the relative parent and product-channel energies are from the CCSD(T)/6-311+G(3df) calculations.^{174,175} The C_{2v} (2B_1) isomer is predicted to be the most stable $(\text{CS}_2)_2^-$ structure.^{158,174,175} Both this isomer and the next higher-lying structure, D_{2h} ($^2B_{3g}$), are characterized by the “doubly excited” electron configuration of the neutral core. That is, the removal of the excess electron from the highest occupied molecular orbital (HOMO) of either of these anions (in the single-reference picture) yields a doubly excited neutral configuration, rather than that corresponding to two CS_2 molecules in their ground electronic states.¹⁶³ The solid lines in Fig. 6.4 indicate the fragment channel correlations for these exotic anionic structures. The dashed lines show the $\text{CS}_2^- \cdot \text{CS}_2$ correlations, as well as those involving the D_{2d} (2A_1) anion, since both $\text{CS}_2^- \cdot \text{CS}_2$ and the D_{2d} (2A_1) structure correspond to the unexcited (“van der Waals” type) neutral-core configurations.¹⁶³

It follows from Fig. 6.4 that the appearance of only two anionic fragments, CS_2^- and C_2S_2^- , at 532 nm (2.33 eV) is accounted for by the dissociation energetics. From the mechanistic perspective, channels (1)–(3) are most feasible in the covalent dimer ions, C_2S_4^- . It may also be possible to form the CS_2^- photoproduct by predissociation of the $\text{CS}_2^- \cdot \text{CS}_2$ complex or by solvent caging of the $\text{S}^- + \text{CS}$ photofragments of its anionic core. Hence, channel (1) can, in principle, involve any of the proposed $(\text{CS}_2)_2^-$ isomers. Channels (2) and (3), on the other hand, are most consistent with the lowest-energy C_{2v}

(2B_1) structure, which contains a preexisting S–S bond.

The straightforward mechanism accounting for channel (4) (the S^- fragments) is the dissociation of CS_2^- based clusters, analogous to $CO_2^- \rightarrow CO + O^-$ dissociation studied previously.^{117,167} Channel (5), yielding the CS_3^- photofragments, is also possible in CS_2^- based clusters, assuming that the core dissociation is followed by an ion-molecule association reaction with solvent CS_2 . This two-step process is analogous to the CO_3^- channel in $(CO_2)_n^-$ and $(CO_2)_2^-(H_2O)_m$.^{150,153}

6.4.3 Fragment Origins and Mechanisms

6.4.3.1 The S^- and CS_3^- Products

In the photodissociation of $CS_2^-(H_2O)_m$, the S^- product is observed for $m = 0-5$ at 355 nm [Fig. 6.1(a)] and for $m = 2-5$ at 266 nm [Fig. 6.1(b)]. For $(CS_2)_2^-$ prepared under the dry source conditions, the S^- product is essentially absent at 355 nm and CS_3^- is observed instead [Fig. 6.2(a)]. The formation of S^- from solvated CS_2^- is possible when, first, the photon energy is large enough to overcome the dissociation threshold and, second, there is sufficient solvent-induced stabilization of excited CS_2^- states (CS_2^{-*}) enabling the $CS_2^{-*} \rightarrow CS + S^-$ dissociation to compete successfully with CS_2^{-*} autodetachment.

By comparing the 266 nm spectra in Fig. 6.2(a) for $n = 2$ and Fig. 6.2(b) for $m = 0$, both of which correspond to (nominally) the same $(CS_2)_2^-$ parent anions, a larger S^- fragment fraction is observed under the dry source conditions. In light of the proposed channel (4) mechanism, this observation parallels the conclusion drawn from the

accompanying photoelectron imaging study:¹⁷⁴ namely, the presence of water in the ion source enhances the formation of the more stable covalent $C_2S_4^-$ dimers over $CS_2^- \cdot CS_2$, of which the later is primarily responsible for the S^- photofragments. The disappearance of S^- in the $(CS_2)_n^-$, $n = 3-4$ fragment mass-spectra in Fig. 6.2(a) reflects, in part, the competition with channel (5), involving a secondary reaction of nascent S^- with the CS_2 solvent.

Based on the mechanism suggested for channel (5), the CS_3^- product intensity should reflect the populations of the CS_2^- based parent clusters, $CS_2^-(CS_2)_{n-1}$ or $CS_2 \cdot CS_2^-(H_2O)_m$. Indeed, in Fig. 6.2(a) and (b) the intensity of CS_3^- relative to other photofragments is consistently higher under the dry source conditions, compared to the results in a “wet” ion source. Again, this indicates a positive correlation between a process involving a monomeric CS_2^- cluster core and the absence of water in the ion source (even when the parent anions themselves do not contain H_2O).

The largest relative yield of CS_3^- is observed at 266 nm for $(CS_2)_n^-$, $n = 3$ and 4, where it is in fact the dominant product. On the other hand, no CS_3^- is observed at the same wavelength from any of the $(CS_2)_2^-(H_2O)_m$ clusters studied, despite the presence of S^- fragments and the availability of a solvent CS_2 molecule for a secondary $S^- + CS_2 \rightarrow CS_3^-$ reaction. This may be a consequence of the structural differences between the two types of clusters. In $CS_2^-(CS_2)_{n-1}$, more CS_2 molecules become available with increasing n for the secondary $S^- + CS_2$ association step in Eq. (5), resulting in the observed increase in the CS_3^- fragment intensity from $n = 2$ to $n = 3-4$. In $CS_2 \cdot CS_2^-(H_2O)_m$, on the other

hand, the water molecules occupying the most favorable solvation sites near CS_2^- will hinder the secondary reaction.

Although CS_3^- is stable by ~ 1.7 eV with respect to $\text{S}^- + \text{CS}_2$, it was not observed in the drift-tube experiment by Lee and Bierbaum.¹⁷³ The authors suggested that due to the large polarizability of CS_2 and relatively low center-of-mass energy, long-lived CS_3^{-*} collision complex could be formed through nucleophilic attack on the carbon. In their experiment, the isotope exchange reaction was observed at collision energies below 0.3 eV, while both the isotope exchange and sulfur abstraction took place above 0.3 eV. The absence of the $^{32}\text{S}^{32}\text{S}^-$ products above 0.3 eV indicates that the sulfur abstraction occurs through direct attack on the sulfur atom, ruling out the formation of CS_3^{-*} . The observation of CS_3^- in our experiment signals a greater efficiency of the association reaction within a cluster environment, compared to the drift tube experiment.

6.4.3.2 The CS_2^- Product

In the photofragmentation of the $\text{CS}_2^-(\text{H}_2\text{O})_m$ clusters, CS_2^- fragments are observed for $m \geq 2$ at 355 nm and for $m \geq 3$ at 266 nm (see Fig. 6.1). The photoinduced excitation of the cluster core should lead to $\text{CS}_2^{-*} \rightarrow \text{CS} + \text{S}^-$ dissociation and/or CS_2^{-*} autodetachment.¹⁷² Since water does not absorb at these wavelengths, the plausible mechanism for CS_2^- fragment formation is via the solvent-induced relaxation of CS_2^{-*} or fragment caging.

The fractional yields of CS_2^- from $(\text{CS}_2)_n^-$ and $(\text{CS}_2)_2^-(\text{H}_2\text{O})_m$ (see Fig. 6.2) are

generally much larger, than those from $\text{CS}_2^-(\text{H}_2\text{O})_m$. This is to be expected, as the dimer based cluster anions are more likely to yield CS_2^- via $\text{C}_2\text{S}_4^- \rightarrow \text{CS}_2^- + \text{CS}_2$ dissociation. As seen in Fig. 6.2, upon addition of CS_2 or H_2O to $(\text{CS}_2)_2^-$, the relative yields of the C_2S_2^- and S_2^- channels tend to decrease in favor of CS_2^- . This channel switching is in positive correlation with the decline in the relative intensity of the C_{2v} (${}^2\text{B}_1$) photoelectron band.¹⁷⁴ This observation indicates the reduced presence of the C_{2v} (${}^2\text{B}_1$) core-anion isomer in the larger clusters, compared to the CS_2^- monomer core. There is no clear evidence if the D_{2h} (${}^2\text{B}_{3g}$) and D_{2d} (${}^2\text{A}_1$) structures are also affected by solvation in a similar manner. On other hand, the photoelectron imaging results unambiguously show that the fraction of the CS_2^- based parent cluster increases upon solvation.

6.4.3.3 The C_2S_2^- and S_2^- Products

These fragments are expected to be formed from the global-minimum C_{2v} (${}^2\text{B}_1$) structure of the C_2S_4^- cluster core. The channel mechanisms may in fact be similar, with the difference being the final localization of the excess electron. The greater (overall) yield of C_2S_2^- and the observed increase in the $\text{S}_2^-/\text{C}_2\text{S}_2^-$ product ratio with increasing photon energy (Fig. 6.2) are consistent with the S_2^- channel being significantly more endothermic than the C_2S_2^- pathway (Fig. 6.4).

The $(\text{C}_2\text{S}_2^- + \text{S}_2^-)/\text{CS}_2^-$ product ratio plotted in Fig. 6.3 reflects three important trends:

First, in all the cluster anions studied, the ratio increases with increasing photon energy. This trend is consistent with the channel energetics shown in Fig. 6.4 and

therefore favors a statistical mechanism of cluster core photodissociation.

Second, for $(\text{CS}_2)_2^-$ the above ratio tends to be significantly larger under the wet source conditions, compared to the dry source. The difference is nearly three-fold at 266 nm! This observation reinforces our conclusion that the presence of water in the ion source enhances the formation of the most stable C_{2v} (2B_1) dimer-based clusters, which are responsible for the $C_2S_2^-$ and S_2^- products.

Third, solvation of $(\text{CS}_2)_2^-$ either by additional CS_2 or by H_2O leads to a drastic decrease in the $C_2S_2^-$ and S_2^- product yields, relative to the CS_2^- photofragment. The drop in the $C_2S_2^-$ and S_2^- yields is sharper in the CS_2 solvent case: e.g., at all wavelengths studied the $C_2S_2^-$ and S_2^- fragments disappear almost completely with the addition of just one extra CS_2 molecule. This is due to a more abundant formation of the C_{2v} (2B_1) dimer-based clusters under the wet source conditions compared to that in the dry source.

6.4.4 Channel Switching versus $(\text{CS}_2)_2^-$ Electronic Isomer Coexistence

The variation in the fragment intensities in $(\text{CS}_2)_2^-$ dissociation depending on the parent ion source conditions, as well as the observed dominant channel switching from $C_2S_2^-$ and S_2^- to CS_2^- upon solvation are easily reconciled with the variations in the corresponding photoelectron spectra, reported separately.¹⁷⁴ The dependence of the $(\text{CS}_2)_2^-$ fragmentation pattern on the presence of water in the precursor gas line is due to the role of H_2O in facilitating the formation of the global minimum structure of the dimer anion, which dissociates mainly into $C_2S_2^- + S_2$ or $S_2^- + C_2S_2$. In addition to mediating

the formation of the equilibrium structure, the water molecules serve as an effective heat sink, stabilizing the final products by evaporation. As the photoelectron imaging results indicate,¹⁷⁴ the $(\text{CS}_2)_2^-$ anions formed in the dry source are more likely to be trapped in the initially formed, yet less stable C_s ($^2A'$) $\text{CS}_2^- \cdot \text{CS}_2$ and/or D_{2d} (2A_1) structures, both of which are less likely to give rise to the C_2S_2^- and S_2^- products. The formation of the less stable structures, more abundant under the dry source conditions, is attributed to the anion stabilization processes after electron attachment, which mainly involves evaporation of the weakly bound CS_2 molecules or Ar atoms leading to an efficient trapping of the dimer anion in its initially accessible local minima.

When one or more solvent molecules (CS_2 or H_2O) are added to $(\text{CS}_2)_2^-$, the relative population of the dimer-core isomers declines due to more favorable solvation of CS_2^- vs. C_2S_4^- . The observed decrease in the $(\text{C}_2\text{S}_2^- + \text{S}_2^-)/\text{CS}_2^-$ product ratio reflects the diminishing presence of the global-minimum C_{2v} (2B_1) core anions upon solvation.

6.5 Summary

The photodissociation of $(\text{CS}_2)_2^-$ at 532, 355 and 266 nm has been investigated using tandem time-of-flight ion mass-spectroscopy. Several fragmentation channels are observed, yielding the CS_2^- , C_2S_2^- , CS_3^- , S_2^- , and S^- products. The channel branching ratios vary significantly depending on the presence of water in the precursor gas mixture. Although $(\text{CS}_2)_2^-$ itself does not contain H_2O , the observed variations in the fragmentation patterns reflect the effect of water presence at the ion formation stage on

the resulting $(\text{CS}_2)_2^-$ isomer distribution. Specifically, the $(\text{C}_2\text{S}_2^- + \text{S}_2^-)/\text{CS}_2^-$ channel ratio exhibits striking positive correlation with the relative intensity of the photoelectron band attributed to the C_{2v} (2B_1) covalent dimer-anion structure. This C_2S_4^- structure is therefore identified as the primary origin of the C_2S_2^- and S_2^- photoproducts, while the $\text{CS}_2^- \cdot \text{CS}_2$ ion-molecule complex is seen as the origin of S^- and CS_3^- . The fragmentation patterns also change drastically with the addition of solvent molecules (CS_2 or H_2O) to $(\text{CS}_2)_2^-$. Especially striking is the abrupt decrease in the yield of C_2S_2^- and the corresponding increase in the CS_2^- fragment. This solvent-induced channel switching is interpreted in terms of the diminished presence of the covalent C_2S_4^- cluster-core isomer relative to the CS_2^- based clusters, due to the more effective solvation of the monomer anion. These results underline the structural complexity of the $(\text{CS}_2)_2^-$ anions and complement the parallel photoelectron imaging findings.¹⁷⁴

Chapter 7

OBSERVATION OF NOVEL ANIONS: PHOTOELECTRON IMAGING AND
PHOTODISSOCIATION OF $\text{CS}_2 + \text{O}_2 + \text{e}^-$ REACTION PRODUCTS

7.1 Introduction

The chemical interaction that arises when an extra electron enters heterogeneous neutral clusters of molecules, all with positive electron affinities, is intriguing. We choose to consider $\text{CS}_2\text{-O}_2$ system as a starting point to study electron attachment, competition and transfer processes that play important roles in many areas of chemistry. The adiabatic electron affinities of CS_2 and O_2 are 0.89 ± 0.02 eV¹⁵⁴ and 0.448 ± 0.006 eV,¹⁷⁶ respectively. Since both molecules have positive electron affinity, when an electron enters the neutral heterogeneous clusters, the smallest cluster anions are expected to be $\text{O}_2^-\cdot\text{CS}_2$ and $\text{CS}_2^-\cdot\text{O}_2$ ion-neutral complexes, and possibly a covalent CS_2O_2^- structure. In addition to these expectations, exotic and novel anions are identified, and their electronic structures and photochemistries are investigated experimentally via photoelectron imaging and photofragmentation spectroscopies. Theoretical calculations are performed to assist the interpretation of the experimental results.

Carbon disulfide and oxygen gaseous mixture is known to ignite even below 100 °C and low pressure.¹⁷⁷ Since the 1930's there have been great research interests on the

Table 7.1 Bimolecular reactions and rate constants for CS₂-O₂ system (adapted from ref. ¹⁷⁸).

Number	Reaction	Rate constant (cm ³ mol ⁻¹ s ⁻¹)	ΔH° (kJ mol ⁻¹)
1	CS ₂ + O ₂ → CS + SO ₂	$k_1 = 1(10^{12}) \exp(-43/RT)$	-133.4
2	CS + O ₂ → CO + SO	$k_2 = 5.5(10^{10}) \exp(-2/RT)$	-385.9
3	CS + O ₂ → OCS + O	$k_3 = 1(10^{13}) \exp(-12/RT)$	-169.6
4	O + CS ₂ → CS + SO	$k_4 = 5(10^{13}) \exp(-8/RT)$	-80.8
5	O + CS ₂ → OCS + S	$k_5 = 1(10^{14}) \exp(-1.9/RT)$	-227.4
6	SO + O ₂ → SO ₂ + O	$k_6 = 3.5(10^{11}) \exp(-6.5/RT)$	-52.6
7	S + O ₂ → SO + O	$k_7 = 1(10^{12})$	-23.0
8	CS + O → CO(v) + S	$k_8 = 2.4(10^{14}) \exp(-2/RT)$	-362.9
9	S + CS ₂ → CS + S ₂	$k_9 = 1(10^{14}) \exp(-4/RT)$	14.8
10	O + S ₂ → SO + S	$k_{10} = 4(10^{12})$	-95.6
11	O + OCS → CO + SO	$k_{11} = 1.9(10^{13}) \exp(-4.5/RT)$	-216.3
12	S + OCS → CO + S ₂	$k_{12} = k_{11}$	-120.7
13	CS + SO → CO + S ₂	$k_{13} = 1(10^9)$	-267.3
14	O + CS ₂ → CO + S ₂	—	-348.1

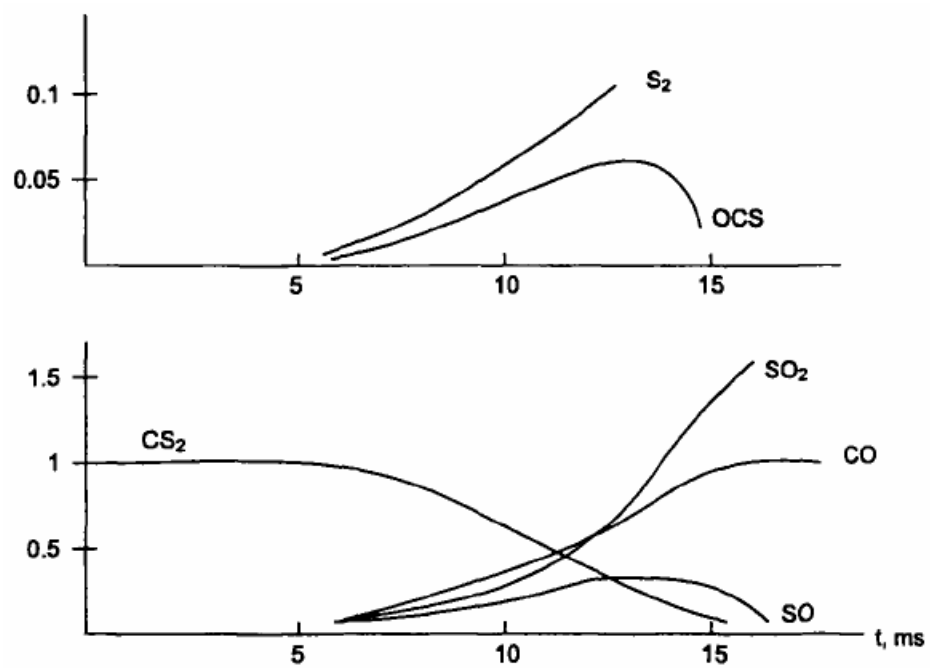


Figure 7.1 CS_2 - O_2 reaction product temporal profiles (from ref. ¹⁷⁹).

oxidation of CS₂.¹⁷⁷⁻¹⁸⁶ This is partly due to the environmental implication of the reaction in the atmosphere causing acid rain, and partly due to the advent of CS₂/O₂ chemical laser based on CO product of the reaction.¹⁸⁷⁻¹⁸⁹ The reaction of CS₂ with O₂ is a chain reaction involving avalanche multiplication of reactive intermediate species. Some of the bimolecular reactions are summarized in Table 7.1 (detailed consideration of the reactions is available in ref. ¹⁷⁸). The enthalpy of the reactions (ΔH) determined from gas phase thermochemical data¹⁹⁰ indicate that the initiation, branching and propagation steps are exothermic. The activation energy is given in the rate constant expressions in kcal/mol. Figure 7.1 shows the time profile of the intermediates and end products for CS₂-O₂ reaction at low pressure.

Therefore, the types of anions formed in the supersonic expansion depend not only on the presence of CS₂ and O₂ molecules but also on the CS₂-O₂ reactions in the neutral medium. Based on the reactions shown in Table 7.1, in addition to CS₂ and O₂, the neutral medium is mainly composed of CO, SO, OCS, S₂ and SO₂ molecules. Although the concentrations of CS₂ and intermediate species appear to decline after some time as seen in Fig. 7.1, due to the steady supply of CS₂ and O₂ reactants, no significant variation is expected in the partial pressures of the reactants and intermediate species. We further assume that compared to that of CS₂ and O₂, the concentration of the reactive intermediate species remain small.

7.2 Ion Formation Procedure

The experiment on the CS₂-O₂ based anions was started by forming the anions by

simply expanding argon carrier gas at 40 psi over liquid CS₂ sample. The ambient air trapped in the gas delivery line was the source of oxygen. The photoelectron images were acquired before the ion signals disappeared due to limited supply of oxygen. The photoelectron image of each ion is recorded by accumulating the photoelectrons from 25,000 events.

Next the ions were formed by expanding ~10% O₂/Ar mixture (total pressure 40 psi) over CS₂ liquid sample. The photoelectron images of the [CS₂(O₂)_m]⁻ ions have different transition characteristics from the ions prepared as described in the previous paragraph. In addition, the mass spectra are richer than in the first case showing several types of C_xS_yO_z⁻ ions where *x*, *y*, *z* = 0, 1, 2, etc. The photoelectron images of this group of ion are representative of more than 100,000 events.

7.3 CS₂⁻·O₂ Ion-Neutral Complex

The 355 nm photoelectron images and the corresponding spectra of [CS₂(O₂)_m]⁻ ions prepared using ambient atmosphere as an oxygen source, are presented in Fig. 7.2. The images/spectra are primarily characteristics of the CS₂⁻ ion, except the solvation induced shift of the transition band to higher energy. Therefore, this cluster series can be described as CS₂⁻(O₂)_m. To illustrate the solvation induced shift, the vertical detachment energy (VDE) determined as the maximum position of the lower electron binding energy (eBE) photodetachment transition band is plotted in Fig. 7.3 as a function of solvent cluster size, *m*. The corresponding results for CS₂⁻(CO₂)_m and CS₂⁻(H₂O)_m (from Chapter

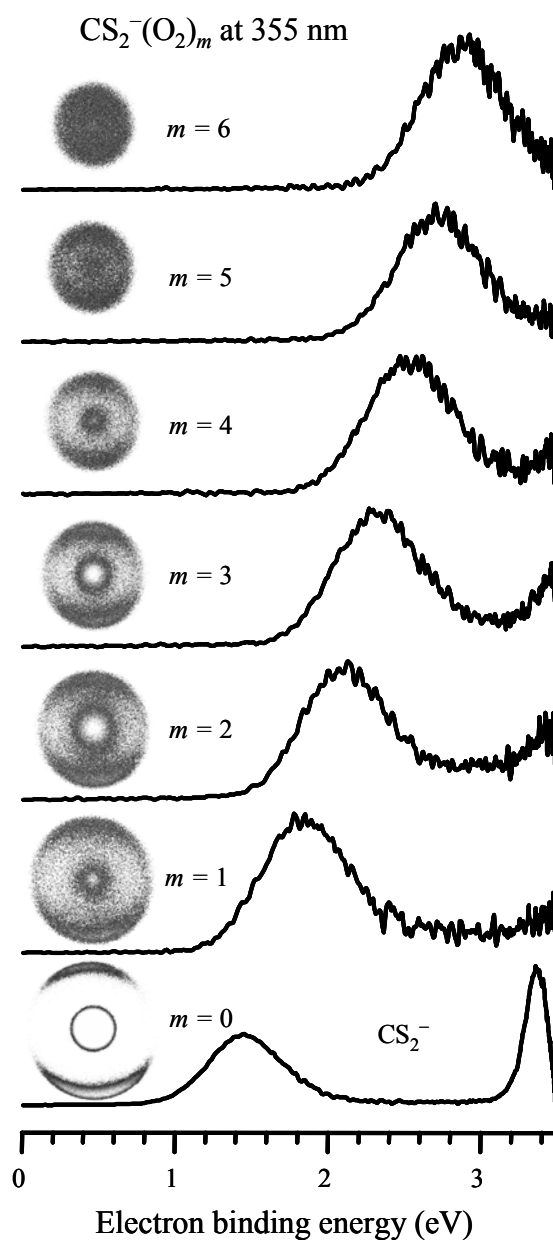


Figure 7.2 Photoelectron images/spectra of mass selected $\text{CS}_2^-(\text{O}_2)_m$ ions acquired at 355 nm.

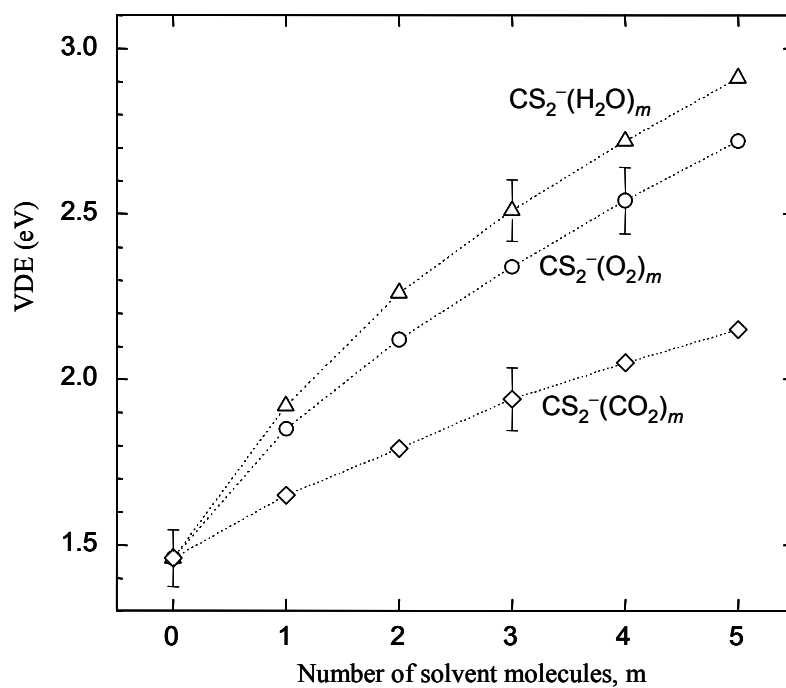


Figure 7.3 Vertical detachment energies (VDEs) extracted from the 355 nm lowest binding energy photodetachment transition band of $\text{CS}_2^-(\text{M})_m$, $\text{M} \equiv \text{H}_2\text{O}, \text{O}_2, \text{CO}_2$. A quarter of the full width at half maximum is shown as an error bar.

5) are also shown for comparison. As seen in the figure, the solvation strength of O_2 towards the CS_2^- solute is stronger than that of CO_2 but slightly weaker than that of H_2O . Due to the relaxation of the neutral CS_2 state from bent ($\angle SCS \approx 144^\circ$) to linear geometry, band I is very broad. The band width remains approximately constant upon solvation. Quarters of the half widths at half maximum are shown in Fig. 7.3 as error bars on arbitrarily selected data points.

As seen in Fig. 5.1 of Chapter 5, just one CO_2 or H_2O solvent molecule is enough to make the higher-eBE photodetachment transition in CS_2^- inaccessible at 355 nm. The same should hold true when an O_2 molecule acts as a solvent for the CS_2^- solute, as its solvation strength is higher than that of CO_2 (Fig. 7.3). However, compared to the $CS_2^-(H_2O)_m$ and $CS_2^-(CO_2)_m$ images (Fig. 5.1(b) and (c), Chapter 5), the central spots in the $CS_2^-(O_2)_m$ photoelectron images are more prominent as can also be seen from the corresponding bands in the low electron kinetic energy (eKE) region in the photoelectron spectra. This is particularly apparent for $m = 2$ and 3, above which the transition is barely accessible. This feature is an indication of a different electron binding pattern by CS_2-O_2 (both molecules with positive adiabatic electron affinity) system, compared to the CS_2-H_2O and CS_2-CO_2 combinations where both H_2O and CO_2 have negative electron affinities.

7.4 Anionic Products of $\text{CS}_2 + \text{O}_2 + \text{e}^-$ Reaction

7.4.1 Overview

When CS_2 is expanded in argon through a dried gas delivery line in the absence of oxygen the prominent mass peaks correspond to the $(\text{CS}_2)_n^-$, $n = 0, 1, 2 \dots$ cluster series (see top panel of Fig. 7.4 for a representative mass spectrum). CS_2^- is essentially the only observed ion with a mass to charge (m/z) ratio less than 100, giving the strongest signal in the overall spectrum. When oxygen is seeded into the carrier gas even in a small proportion (2% O_2 in Ar) the mass spectrum is inundated with ion signals virtually at every multiple of $m/z = 16$, excluding carbon mass. Representative mass spectra optimized for low and high masses are given in the lower panel of Fig. 7.4. The assignment of the observed peaks is ambiguous due to the same nominal mass of O_2 and S atoms. However, identification of the ions is, however, possible via photoelectron imaging. The photofragmentation experiment has also provided important and complementary information in the identification of the parent ions. Although the main interest here is in the ions with $m/z > 100$, particularly the $[\text{CS}_2(\text{O}_2)_m]^-$ and other exotic and novel anions, the smaller mass ions are analyzed first to shed light on the $\text{CS}_2\text{-O}_2$ reaction pathways occurring before/after intersection of the molecular and electron beam.

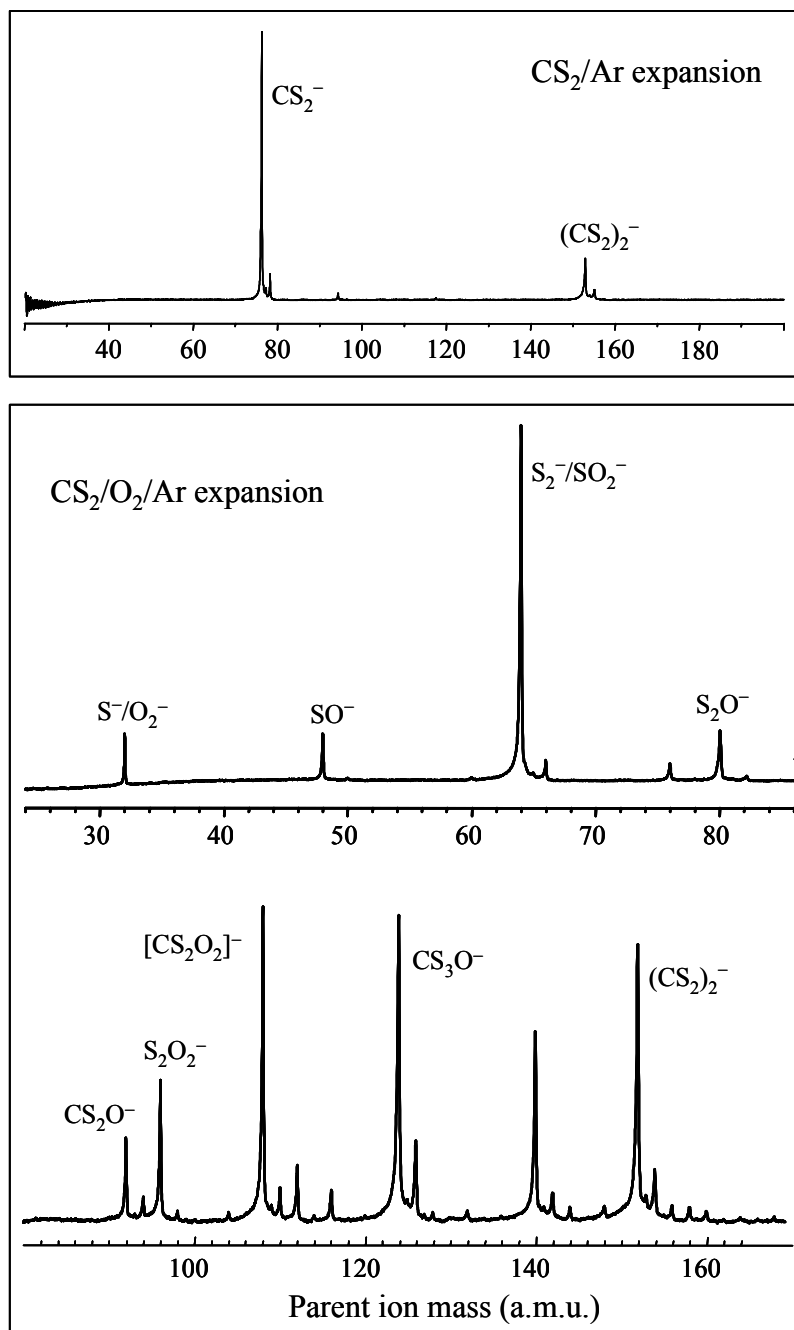


Figure 7.4 Parent ion mass spectra. The mass spectrum in the top panel is obtained by expanding CS₂ vapor in argon carrier gas (total pressure = 40 psi). The spectra in the lower panel are obtained during expansion of a mixture of CS₂ vapor and 10% O₂ in argon (total pressure = 40 psi).

7.4.2 Low Mass Ions ($m/z < 90$)

The 532 nm photoelectron images and spectra of the low mass ions are displayed in Fig. 7.5. For $m/z = 32$ anion the photoelectron image, displayed in Fig. 7.5(a), shows the prominence of S (3P) \leftarrow S $^-$ (2P) atomic transition band over broadly distributed O $_2^-$ molecular anion photodetachment signal. Although the image clearly reflects the contribution of O $_2^-$, in the corresponding photoelectron spectrum on a coarse examination, it appears as if only the S $^-$ band was present. This is due to the narrow band width of atomic transition compared to the molecular anion which is characterized by the broad photodetachment transition band involving several excited vibrational states in the neutral ground and excited electronic states. As seen in the inset in Fig. 7.5(a), the O $_2^-$ bands are revealed when the spectrum is magnified in the range where there is no overlap with the S $^-$ band.

The most likely candidate for $m/z 48$ is SO $^-$. However, O $_3^-$ can also be formed through O $^-$ + O $_2$ reaction (in the presence of a third body) in the plasma before extraction of the anions to the ion flight tube. From past measurements at 2.98 eV of photon energy, O $_3^-$ is known to have transition bands between 2.0 and 2.8 eV of eBE.¹⁹¹ In the present photoelectron imaging experiment at 532 nm (2.33 eV) the O $_3^-$ ion, if exists in the ion beam, may contribute only in the low-eKE range (eBE > 2.0 eV). Therefore, all the bands seen in the photoelectron spectrum (Fig. 7.5(b)) at eBE < 2.0 eV can be attributed to SO $^-$

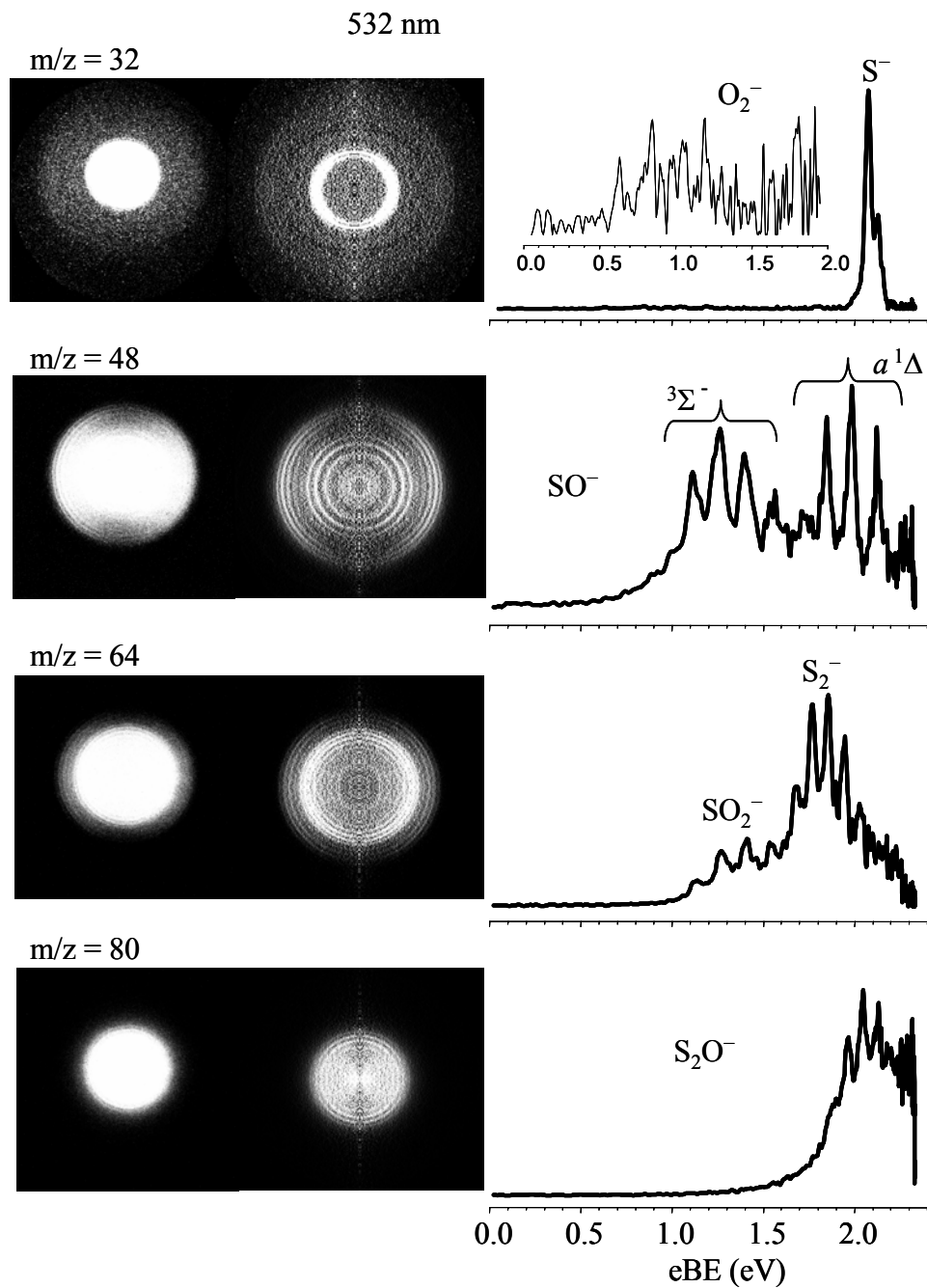


Figure 7.5 Photoelectron images/spectra of m/z 32, 48, 64 and 80 formed by $CS_2/O_2/Ar$ mixture expansion. The images are acquired at 532 nm.

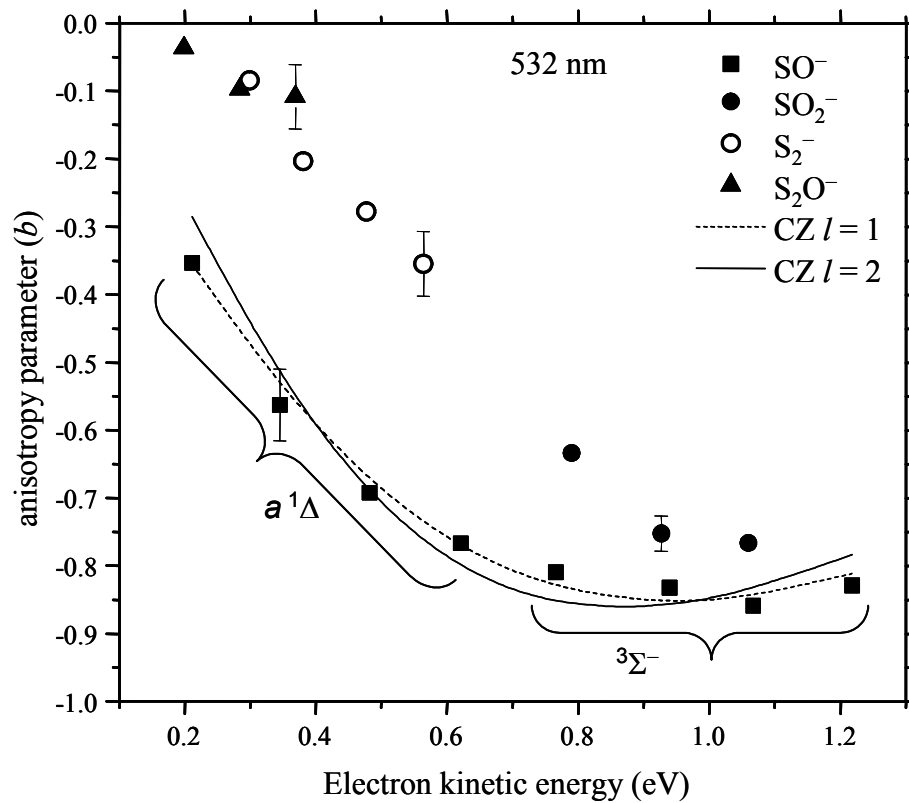


Figure 7.6 Dependence of anisotropy parameter (β) on kinetic energy. CZ is short for Cooper-Zare and l is effective angular momentum quantum number.

unambiguously. The overall spectrum is in good agreement with the previously reported photoelectron spectrum of SO^- .¹⁹² Following the previous assignments the bands in the $\text{eBE} < 1.6 \text{ eV}$ region is assigned to $\text{SO} (^3\Sigma^-) \leftarrow \text{SO}^- (X^2\Pi)$ photodetachment transitions, and the band above 1.7 eV of eBE is assigned to $\text{SO} (a^1\Delta) \leftarrow \text{SO}^- (X^2\Pi)$ transitions. The average peak to peak separation ($1107 \pm 36 \text{ cm}^{-1}$) in the photoelectron spectrum agrees reasonably with the vibrational frequencies of SO in the $^3\Sigma^-$ and $a^1\Delta$ electronic states which, respectively, are 1149.2 cm^{-1} ¹⁹³ and 1115.3 cm^{-1} .¹⁹⁴

For the vibrationally resolved SO^- photodetachment transitions the anisotropy parameter (β) is plotted in Fig. 7.6 as a function of peak kinetic energy. The negative values reflect the angular distribution of the photoelectrons preferentially in the axis perpendicular to the laser polarization. The kinetic energy dependence of β can be approximated using the Cooper-Zare (CZ) model.¹⁹⁵ The model was developed for atomic systems and was further simplified by Hanstorp *et al.*¹⁹⁶ ignoring the interaction of the departing electron with the neutral molecule. The simplified version of the model is given as

$$\beta = \frac{l(l-1) + (l+1)(l+2)A^2\varepsilon^2 - 6l(l+1)A\varepsilon \cos\phi}{(2l+1)[l + (l+1)A^2\varepsilon^2]}$$

where l is the effective angular momentum quantum number of the parent orbital, $\varepsilon = \text{eKE}$, $A\varepsilon = R_{l+1}/R_{l-1}$ is the ratio of the dipole radial matrix element, A is proportionality constant and ϕ is the relative phase of the $l' = l \pm 1$ partial waves. Similar to the previous studies of S_2^- ,¹⁷⁰ O_2^- ¹⁹⁷ and NO^- ,⁶⁴ the π^* HOMO of SO^- may be approximated as a d -

like orbital with $l=2$. On the other hand, due to lack of inversion symmetry and size difference between the two atoms, there is greater probability for the extra electron to occupy the p -orbital of sulfur than that of oxygen which gives it a p -like wave character with $l=1$. The solid and dotted line curves in Fig. 7.6 are obtained by fitting equation (7.1) to the SO^- data using nonlinear least square curve fitting procedure. For $l=2$, the CZ curve (solid line) corresponds to $\cos \phi = 0.91 \pm 0.01$ for the relative phase ϕ of the $l' = l \pm 1$ partial waves and $A = 0.76 \pm 0.03 \text{ eV}^{-1}$ for the coefficient related to the spatial extent of the negative ion. For $l=1$, $\cos \phi = 0.891 \pm 0.007$ and $A = 0.51 \pm 0.01 \text{ eV}^{-1}$.

The photoelectron image/spectrum of m/z 64 anion is given in Fig 7.5(c). The formation of both S_2^- and SO_2^- ion in the ions source is plausible. Both ions have known photodetachment transition bands at 532 nm. The photoelectron spectra of S_2^- ¹⁹⁸ and SO_2^- ¹⁹⁹ recorded at 488 nm (2.54 eV) was reported in the past. At this photon energy vibrationally resolved bands were observed in the eBE range of 1.5-2.4 eV for S_2^- and 1.0-2.0 eV for SO_2^- . As seen in Fig. 7.5(c), the photoelectron spectrum obtained from this experiment shows photodetachment transition bands that span from 1.0 eV of eBE up to the limit of the photon energy, 2.33 eV. The faster electron transition band in the photoelectron image (corresponding to the fastest electron) cannot be due to S_2^- for energetic reasons. In addition, the average anisotropy parameter ($\beta = -0.8$) is incomparably more negative than previously reported value ($\beta = -0.3$) determined from S_2^- photoelectron image recorded at 530 nm.¹⁷⁰ Therefore, the lower eBE and lower intensity band in the photoelectron spectrum shown in Fig. 7.5 for m/z 64 is attributed to

SO_2^- for which this is the first photoelectron imaging result. The average peak to peak separation ($\sim 1170 \pm 22 \text{ cm}^{-1}$) is in agreement with the vibrational mode symmetric stretch frequency (1151.4 cm^{-1}) of SO_2 neutral.²⁰⁰ Although the SO_2^- transition band is expected to extend up to 2.0 eV of eBE, beyond 1.6 eV the photoelectron spectra is dominated by S_2^- transition bands. Therefore, above 1.6 eV of eBE the spectrum is mainly characteristic of S_2^- . The anisotropy parameters of the individual peaks that appear in the $\text{eBE} > 1.6$ region (open circles in Fig. 7.6) compare favorably with the previous result of S_2^- .¹⁷⁰ The average peak to peak separation ($718 \pm 38 \text{ cm}^{-1}$) agrees with the ground state vibrational frequency (725.65 cm^{-1}) of S_2 neutral.¹⁹³

The two possibilities for m/z 80 are SO_3^- and S_2O^- . Since the detachment energy of SO_3^- is well above the 532 nm photon energy with vertical detachment energy (VDE) of 3.41 eV,²⁰¹ the transition bands for mass 80 ion in Fig. 7.5(d) is exclusively the signature of S_2O^- . Although this is the first photoelectron imaging result for S_2O^- ion, the photoelectron spectrum extracted from the image is consistent with the published traditional photoelectron spectrum.¹⁹⁹ As seen in the raw and Abel inverted images, in contrast to the other anions discussed above; the photodetachment of S_2O^- has nearly isotropic angular distribution of detached electrons. The average β value obtained by integrating the 532 nm S_2O^- photoelectron angular distribution over the entire Franck-Condon envelopes is -0.12. The β values determined for resolved vibrational structures are plotted in Fig. 7.6 (solid triangles) as a function of kinetic energy. The average peak

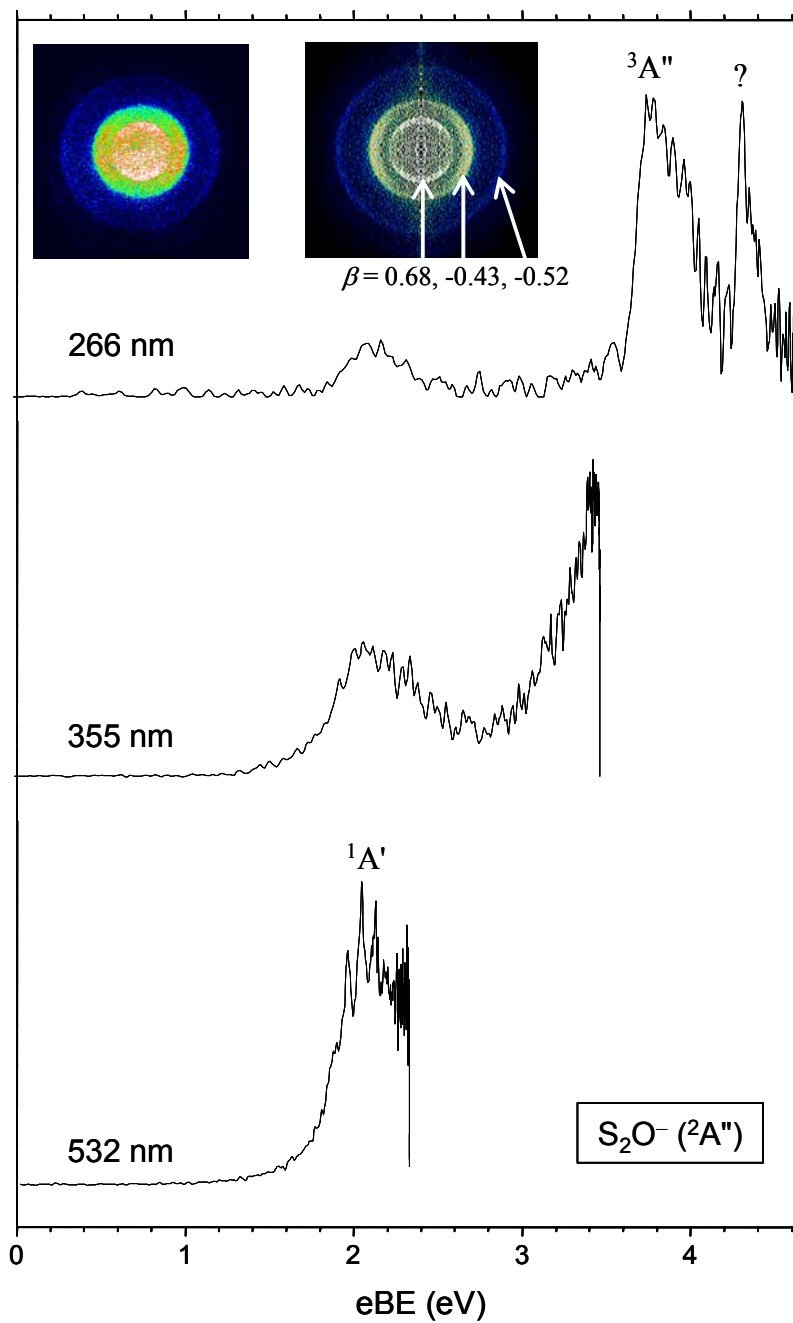


Figure 7.7 Photoelectron images of S_2O^- acquired at 532, 355 and 266 nm. The 266 nm Abel inverted image is shown to the right side of the raw image showing the anisotropy parameter for each transition band.

spacing ($684 \pm 7 \text{ cm}^{-1}$) corresponding to S–S stretching vibrational mode frequency is in good agreement with the literature value (680 cm^{-1}).^{202,203} The photoelectron image of m/z 80 anion was also recorded at 355 and 266 nm. The result is shown in Fig. 7.7 including the 532 nm result from Fig. 7.5(d). The S^- fragment photodetachment transition band was observed in the 355 nm image prominently. The 355 nm photoelectron spectrum shown in Fig. 7.7 is after the S^- fragment transition band is subtracted from the original spectrum. At 266 nm, three transition bands are observed. Comparing the result with the reported 266 nm photoelectron spectrum,²⁰¹ none of the observed prominent bands can be attributed to SO_3^- . Therefore, the three transition bands are attributed to S_2O^- . As indicated on the Abel inverted 266 nm image in Fig. 7.7 the lowest eKE transition band can be characterized as parallel transition with $\beta = 0.68$ in contrast with the other two (higher eKE) transition bands with $\beta = -0.43$ and -0.52 .

Except S_2O^- , the observation of these anions is consistent with the $\text{CS}_2\text{--O}_2$ reaction in the neutral medium as shown in Table 7.1. S_2O^- can be formed through $\text{S}^- + \text{SO}$ and/or $\text{S} + \text{SO}^-$ reactions in the supersonic expansion before anion extraction into the time of flight tube. Similar reactions in the anionic medium can also contribute to the formation of SO^- ($\text{O}^- + \text{S}$ and/or $\text{S}^- + \text{O}$) and SO_2^- ($\text{SO}^- + \text{O}$ and/or $\text{O}^- + \text{SO}$). It is particularly interesting to note that S^- ion formation, nearly absent during supersonic expansion of CS_2/Ar , is intensified when $\text{CS}_2/\text{O}_2/\text{Ar}$ mixture is used. Similarly, the O^- ion is abundantly formed when $\text{CS}_2/\text{O}_2/\text{Ar}$ mixture is expanded instead of O_2/Ar . This signifies the importance of

the reaction between CS₂ and O₂ moieties whether it takes place in the neutral or anionic medium.

7.4.3 Exotic and Novel Anion Formation

7.4.3.1 [CS₂O₂]⁻ versus CS₃⁻ (mass 108)

Unlike the result presented in Fig. 7.2, the photoelectron images of m/z 108 ion formed by expanding ~10% O₂/Ar carrier gas over CS₂ liquid sample exhibits different pattern in a day to day experiment as shown in Fig. 7.8(a)-(c). Although occasionally the photoelectron image reflects the dominant contribution of CS₂⁻·O₂ ion-neutral complex, in most of the cases this species has small contribution to the 355 nm images and the overall photodetachment signal appears low, despite the high intensity of the parent ion. The result suggests that depending on ion source conditions, in addition to the CS₂⁻·O₂ ion-neutral complex, a different isomer or different identity of ion that has high detachment energy is formed. In Chapter 5 the variation of band intensities in the photoelectron spectra of (CS₂)₂⁻ depending on source conditions was attributed to isomer population variation. For the ion with m/z 108 the explanation is more complicated due to the possibility of CS₃⁻ ion formation in addition to [CS₂O₂]⁻ ion where both ion have the same nominal mass and high detachment energy. Therefore, the variation in the pattern of the photoelectron images during different experimental runs can possibly be attributed to formation of the following ions in addition to CS₂⁻·O₂ ion-neutral complex: (i) (S₂C–O₂)⁻ covalent structure, (ii) (OS–COS)⁻/(SO–COS)⁻ through SO⁻ +OCS reaction, (iii) CS₃⁻, or

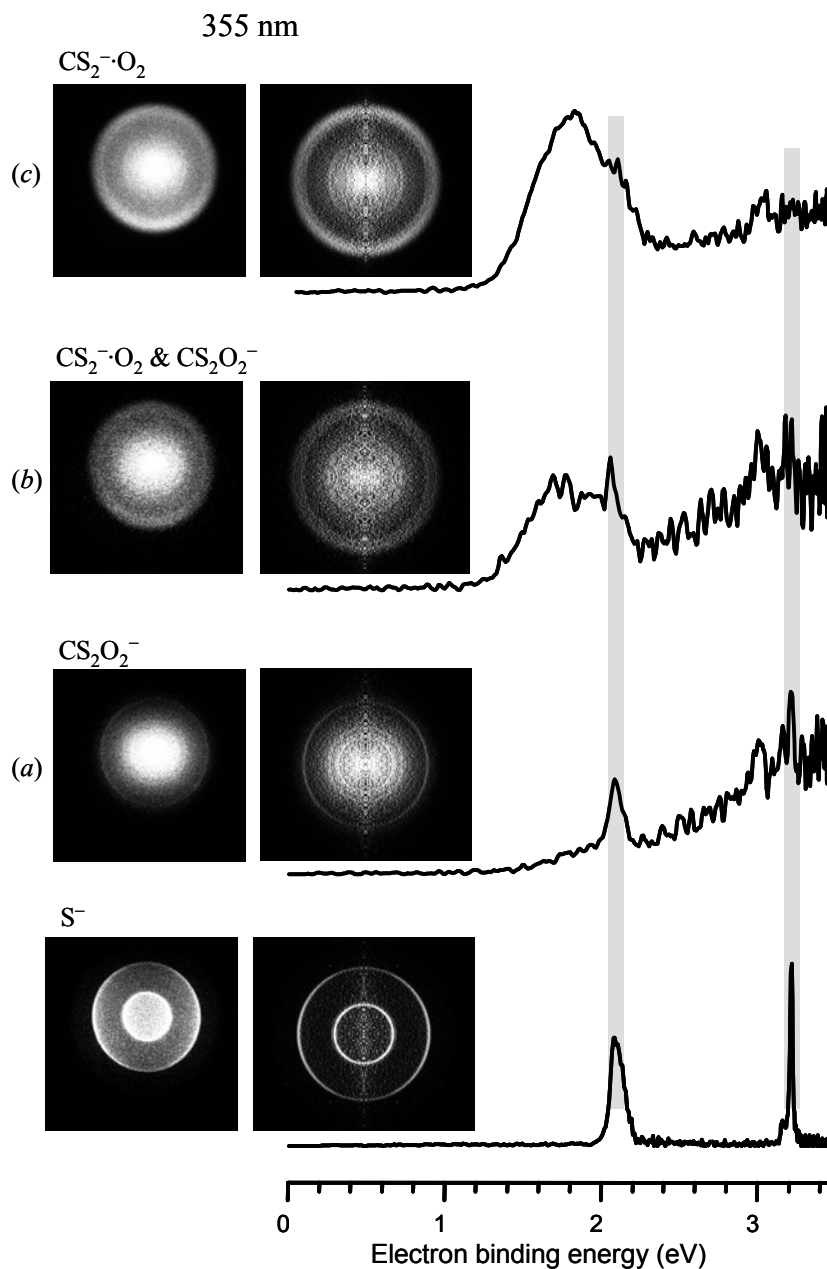


Figure 7.8 The 355 nm photoelectron images/spectra of $[\text{CS}_2\text{O}_2]^-$ formed by expanding 10% O_2/Ar over CS_2 liquid sample. The Abel inverted images are shown on the right side of the raw image. The image for isolated S^- is included for comparison with the S^- fragment image. A shaded bar is included in the spectra to show the energy matching between the isolated and fragment S^- bands. The variations of the transition patterns in the images shown in (a)-(c) is due to the change in the isomer populations distribution depending on source conditions.

(iv) all of the above. The ions in (i) and (ii) differ only in molecular connectivity and for the purpose of our discussion they are represented with a general formula as CS_2O_2^- . The contribution of (ii) may be minimal as the number density of OCS neutral in the plasma, which depends on the $\text{CS}_2\text{-O}_2$ reaction in the neutral medium, is expected to be small. The formation of CS_3^- should involve reaction S^- with abundantly present CS_2 neutral, and hence requires special consideration.

Sülzle *et al.*²⁰⁴ were able to form CS_3^- through electron impact ionization (70 eV) of 4,5-dioxo-1,3-dithiolan, a ring structure containing CS_3 unit. In the experiment of Hiraoka *et al.*,²⁰⁵ a small percentage of CS_3^- ion (accounting for less than 0.5% of the total anion yield) was observed in the CS_2 clustering reaction using a pulsed electron-beam high-pressure mass spectrometer. On the other hand, due to small reaction efficiency (0.18 at 298 K), no CS_3^- ion was observed for $^{34}\text{S}^- + \text{CS}_2$ reaction in the drift tube experiment by Lee and Bierbaum¹⁷³ while isotope exchange and sulfur abstraction reactions took place. In contrast, in our photodissociation experiment on $(\text{CS}_2)_n^-$ clusters, CS_3^- ion was observed presumably through the above association reaction taking place within the cluster (see Chapter 5). The possible mechanism for the CS_3^- ion formation in the supersonic expansion is through $\text{S}^- + \text{CS}_2$ association reaction. Considering the existence of S^- in the beam as depicted in the mass spectrum in Fig. 7.4, the reaction appears plausible. However, the reaction in the supersonic expansion has close resemblance with the reaction in the drift tube, where no CS_3^- was observed. Hence, the contribution of CS_3^- ion (if formed at all) to the ion signal at m/z 108 is expected to be

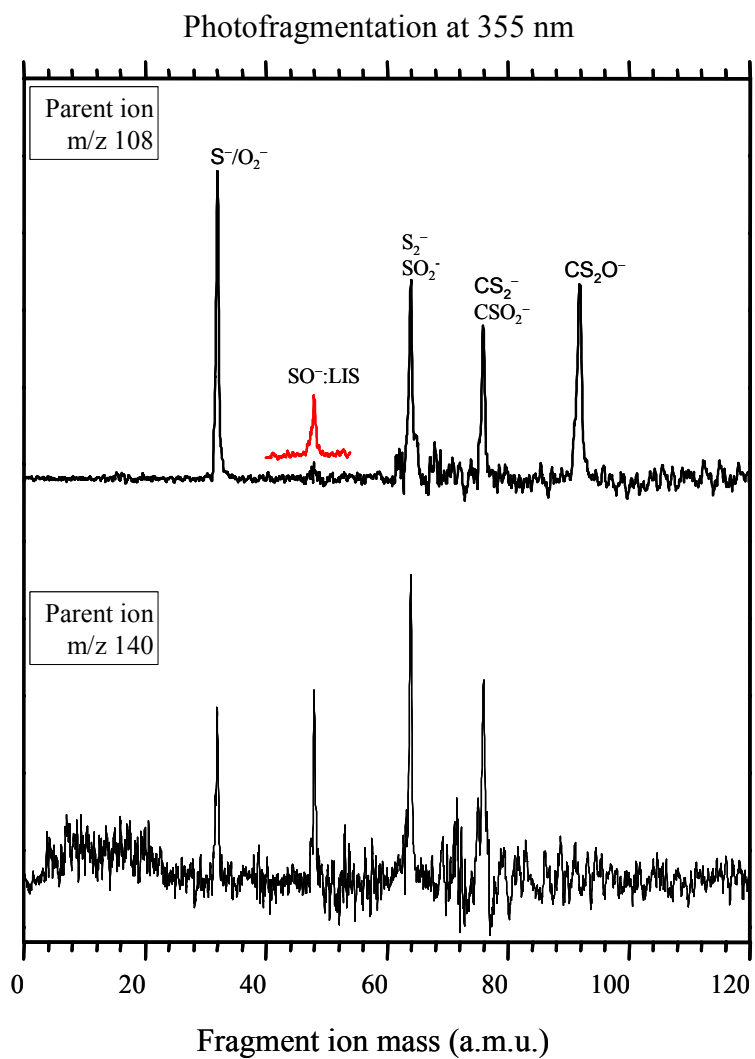


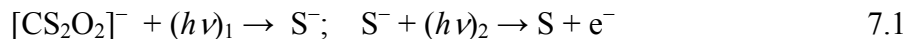
Figure 7.9 Photofragment ion mass spectra of m/z 108 and 140 ions excited at 355 nm laser radiation. LIS is short for laser independent signal.

very small. The isotope pattern of m/z 108 ion signal in the mass spectrum is consistent with $[\text{CS}_2\text{O}_2]^-$ ion (see Fig. 7.4).

Further evidence is obtained from the photofragmentation of the anion. As shown in Fig. 7.9, photoexcitation of m/z 108 anion using 355 nm laser radiation produces ionic fragments with m/z 32 (S^-/O_2^-), 64 ($\text{S}_2^-/\text{SO}_2^-$), 76 ($\text{CS}_2^-/\text{CSO}_2^-$) and 92 (CS_2O^-). A fragment ion with mass 48 (SO^-) was observed independent of the laser. Except for mass 92 (CS_2O^- fragment ion), the m/z assignment is unambiguous at first glance. The observation of the unambiguous CS_2O^- fragment ion is a convincing evidence for the formation of $[\text{CS}_2\text{O}_2]^-$ parent ion as it cannot be produced from CS_3^- . The laser independent SO^- fragment ion is also an evidence for the existence of metastable $[\text{CS}_2\text{O}_2]^-$ parent ion which undergoes spontaneous dissociation in the ion flight tube.

Therefore, the variation of the detachment pattern of the ion with mass 108 during different experimental runs, as seen in Fig. 7.8(a)-(c), should be explained considering the coexistence of the $\text{CS}_2^- \cdot \text{O}_2$ ion-neutral and CS_2O_2^- covalent structure(s). The photoelectron image/spectrum displayed in Fig. 7.8(a) represents the most common case, where the photoelectron signal is very weak. In an attempt to increase the signal, the laser power was increased, which resulted in the photodetachment of the S^- photofragment. The photodetachment transition bands of the S^- fragment appear at the same energy as that of the isolated S^- bands as indicated by the shaded bar in Fig. 7.8. Therefore, the origin of the S^- photodetachment transition in probing m/z 108 anion is attributed to two-photon processes. That is, since the time required for the completion of photodissociation

and fragment photodetachment processes is shorter than the nanosecond laser pulse width, one photon, $(h\nu)_1$, causes dissociation and another photon, $(h\nu)_2$, of the same pulse causes photodetachment from S^- fragment.



Hence, the image/spectrum is dominated by atomic transition band from S^- photofragment ion although the contribution of $CS_2^- \cdot O_2$ ion-neutral complex is noticeable. A case where the S^- fragment and $CS_2^- \cdot O_2$ parent ion transition bands have comparable intensity height is shown in Fig. 7.8(b)]. In Fig. 7.8(c) the $CS_2^- \cdot O_2$ transition band is dominant. In all cases, (a)-(c), there are transition bands in the $eBE > 2.5$ eV regions that cannot be attributed to the $CS_2^- \cdot O_2$ ion-neutral complex or the S^- fragment ion. These transition bands are most likely due to a $CS_2O_2^-$ covalent structure.

The 266 nm photoelectron imaging results for the $[CS_2O_2]^-$ ion for the two extreme cases are shown in Fig. 7.10(a). The dotted line curve is a spectrum characteristics of CS_2^- after accounting for solvation shift, and therefore, it is attributed to $CS_2^- \cdot O_2$ ion-neutral complex. Similar to the corresponding 355 nm imaging result shown in Figs. 7.2 (for $m = 1$) there is no noticeable transition band in this spectrum that can be attributed to the covalent structure. The spectrum shown in solid line is the most commonly observed case where the contribution of the ion-neutral complex is essentially non-existent. The transition bands observed in the $eBE > 2.5$ eV region in the 355 nm spectra in Fig. 7.6 are now clearly seen in the 266 nm spectrum as a partially resolved broad transition band

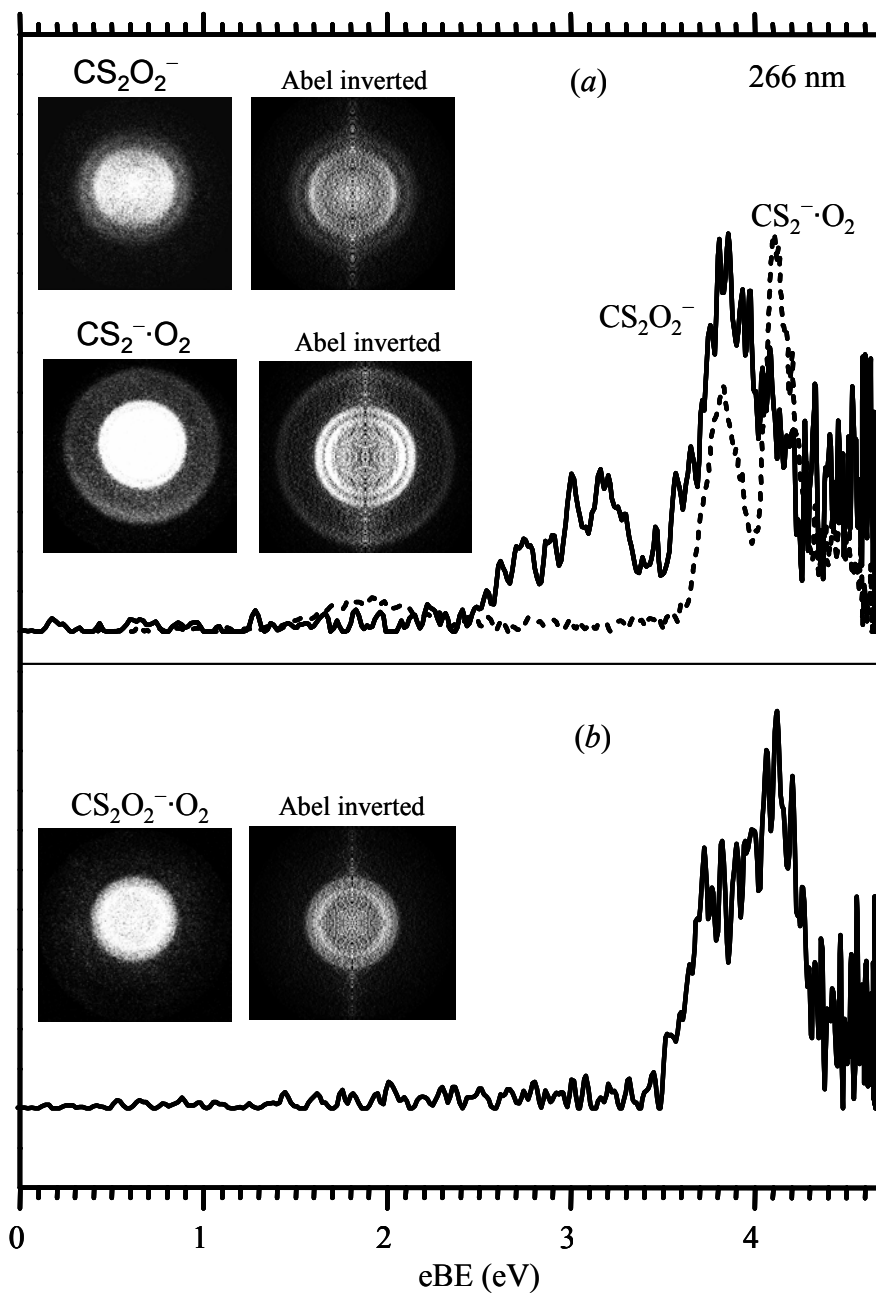


Figure 7.10 Photoelectron images/spectra of anions with m/z 108 and 140 acquired at 266 nm. In (a), the spectra shown in dotted and solid represent two extreme cases indicating the dominance and absence, respectively, of $\text{CS}_2^-\cdot\text{O}_2$ ion neutral complex in the ion beam as a result of existence of other competing isomer presumably CS_2O_2^- covalent structure.

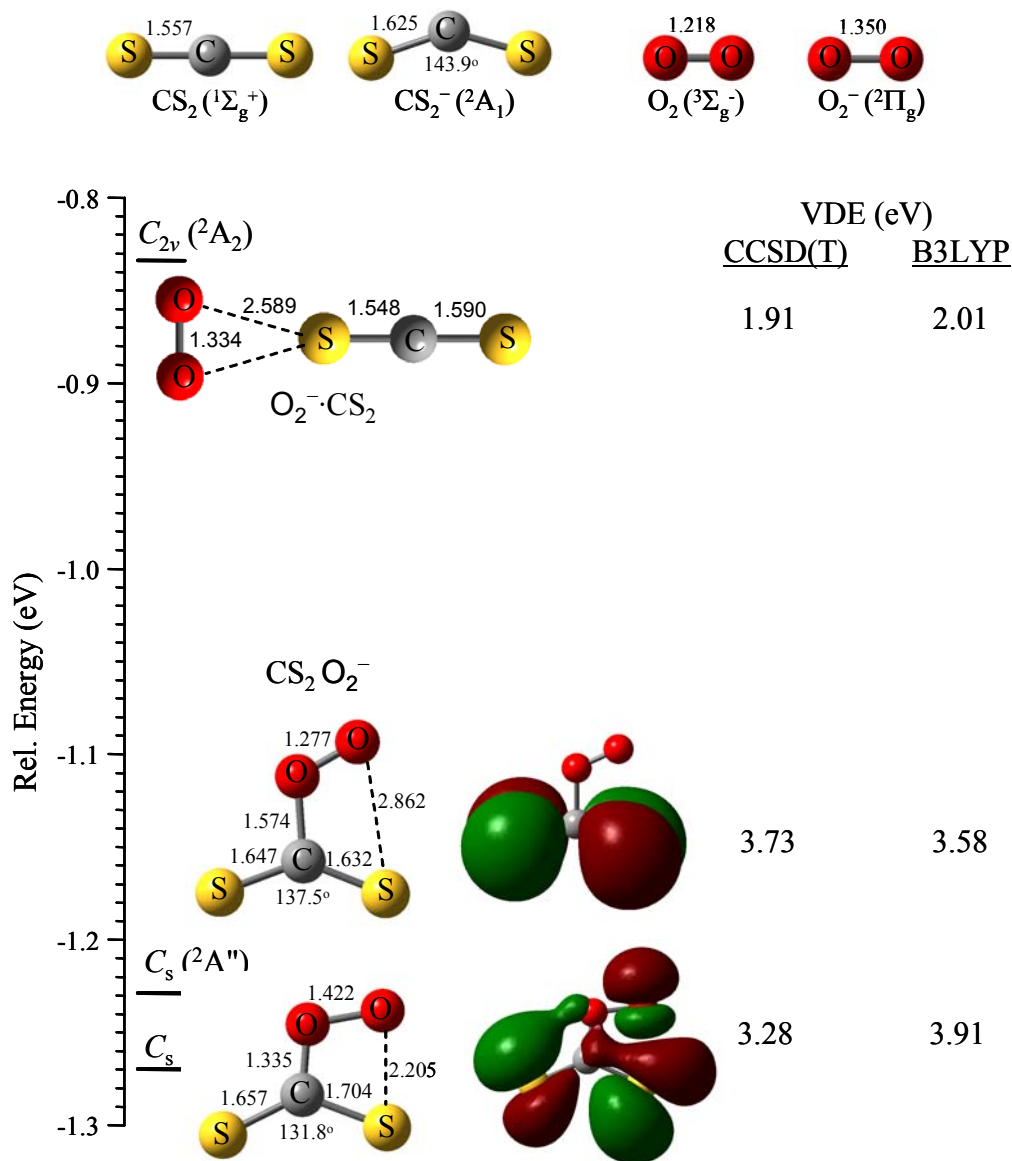


Figure 7.11 Optimized structures and SCF singly occupied molecular orbitals of $[\text{CS}_2\text{O}_2]^-$. The optimization is performed using MP2/6-311+G(3df). For comparison the optimized structures of CS_2 , CS_2^- , O_2 and O_2^- are included. The SCF orbitals are generated using aug-cc-pVTZ basis set. Bond lengths are in angstrom and bond angles are in degrees. The vertical detachment energies are calculated using CCSD(T)/6-311+G(3df)//MP2/6-311+G(3df) and B3LYP/aug-cc-pVTZ.

centered at ~ 3.0 eV. In addition, a strong transition band that peaked at $eBE \approx 3.8$ eV is observed.

The partially resolved broad band centered at ~ 3.0 eV is characteristic of photodetachment transition where the O–O stretching vibrational mode excitation is involved. This may suggest an electronic structure where O_2 and CS_2 molecules are covalently bonded with favorable competition for the excess electron between the two moieties, with greater or comparable probability on the O_2 . The relatively narrow band transition that peaked at ~ 3.8 eV may suggest electron localization on CS_2 which is covalently bonded with O_2 .

Although $[CS_2O_2]^-$ ion was not observed in the past, some structures were predicted from density functional theory calculations using B3LYP method with 6-311+G(d) basis set.²⁰⁶ To assist the interpretation of our experimental results we have re-optimized the geometries using B3LYP and MP2 with 6-311+G(3df) basis set. The MP2 structures are shown in Fig. 7.11. The corresponding singly occupied SCF molecular orbitals are generated using aug-cc-pVTZ basis set. According to CCSD(T)/6-311+G(3df) single point energy calculation, with respect to $O_2^- + CS_2$, the C_s ($^2A'$) and C_s ($^2A''$) structures are stable by 1.27 and 1.23 eV, respectively, and total energy of $CS_2^- + O_2$ is lower by 0.02 eV. The values of the VDEs for the two structures determined from B3LYP and CCSD(T) have opposite order. Based on the charge distribution, which can be visualized from the orbital surfaces, the bands centered at ~ 3.0 and 3.8 eV are temporarily assigned

to the $C_s(^2A')$ and $C_s(^2A'')$ electronic isomers, respectively. This assignment is consistent with the VDEs determined from couple-cluster theory.

Although the formation of $[OS-COS]^-$, through $SO^- + COS$ ion-neutral reaction, is doubtful due to small number density of COS in the free jet we have calculated the VDE for two of the most stable structures. The calculations indicate that the VDE for the $[OS-COS]^-$ anion is above 4.0 eV.

The photoelectron imaging results [see Figs. 7.2, 7.7(b) and 7.7(c)] clearly indicate that $CS_2^- \cdot O_2$ ion-neutral complex is formed, sometimes being the main isomer, depending on the ion source condition. Despite this fact, however, our calculation has failed to predict a stable structure that is consistent with the observation. In the $C_{2v} (^2A_2)$ structure shown in Fig. 7.11 the excess electron primarily resides on O_2 moiety and can be described as $O_2^- \cdot CS_2$ ion-neutral complex. Nevertheless, none of the prominent bands in the photoelectron image/spectra can be attributed to this isomer.

The photoelectron image and spectrum of the ion with m/z 140 is shown in Fig. 7.9(b). The spectra in (b) shares some similarity with the one shown in (a) except that the band at ~ 3.0 eV either has disappeared or shifted significantly and overlap with the higher energy band centered at ~ 4.1 eV. The ~ 4.1 eV band may correspond to the band at ~ 3.8 eV in (a) where the shift is consistent with the solvation energy shift. In this regard, the ion with m/z 140 may be identified as $CS_2O_2^- \cdot O_2$. As seen in Fig. 7.9 similar fragment ions are produced from m/z 108 and 140 which may suggest excitation of the same chromophore in the two ions. Another possible assignment for m/z 140 is $CS_3O_2^-$ that can

be formed through $\text{SO}_2^- + \text{CS}_2$ or $\text{CS}_2^- + \text{SO}_2$ reactions in the expanding plasma before the anions are extracted into the flight tube. However, a covalent CS_3O_2^- structure is expected to have a binding energy higher than the observed band for the m/z 140 ion if not inaccessible at 266 nm.

7.4.3.2 CS_3O^- (mass 124)

Another exotic and novel anion observed in this experiment is the ion with m/z 124. The 266 nm photoelectron image/spectrum of the ion is provided in Fig. 7.11(a). Two partially resolved transition bands, labeled as I and II in Fig. 7.12(a), are seen in the image and the corresponding spectrum. Band I which corresponds to the faster electrons has anisotropy parameter of -0.57 compared to -0.29 for band II. The vertical detachment energies of the two photodetachment transition bands are determined by fitting the sum of two Gaussian functions given below.

$$P(eBE) = C_I \exp\left[-\frac{(eBE - \text{VDE}_I)^2}{\delta_I^2}\right] + C_{II} \exp\left[-\frac{(eBE - \text{VDE}_{II})^2}{\delta_{II}^2}\right] \quad (2.2)$$

where $eBE = h\nu - eKE$, $h\nu$ is the 266 nm photon energy which equals to 4.66 eV, VDE_I and VDE_{II} are the vertical detachment energies corresponding to band I and II, respectively, C_I and C_{II} are normalization factors, and δ_I and δ_{II} are related to the full width at half maximum ($\text{FWHM} = 1.665 \delta$). The dotted line curves in Fig. 7.12(a) are obtained from the individual Gaussian functions corresponding to $\text{VDE}_I = 3.81$ eV, $\delta_I =$

0.18 eV, $VDE_{II} = 4.12$ eV and $\delta_{II} = 0.16$ eV. The solid curve which is the sum of the two functions fits the experimental data points (open circle) satisfactorily.

The most likely assignment for m/z 124 is CS_3O^- , which can plausibly be formed through $SO^- + CS_2$ association reaction in the ion source. The observation of very strong SO^- fragment ion signal in the 355 nm photoexcitation as seen in Fig. 7.12(b) is the reverse of the above association reaction. The other fragment ions at m/z 76 (CS_2^-), 80 (S_2O^-), 92 (CS_2O^-) are all consistent with the CS_3O^- formula. The isotope pattern of the signal in the mass spectrum is also consistent with CS_3O^- atomic composition.

Two stable structures that differ in molecular connectivity as $(OS-CS_2)^-$ and $(SO-CS_2)^-$ corresponding to $C_s(X^2A'')$ and $C_s(X^2A')$ electronic states, respectively, are predicted using *ab initio* calculation with MP2/6-311+G(3df) level of theory (structures are shown in Fig. 7.13). The structures are similar to that of $CS_2O_2^-$ except one oxygen atom is substituted with sulfur. According to the CCSD(T)/6-311+G(3df) single point energy calculation, the $C_s(2A'')$ electronic structure is more stable than $C_s(2A')$ by ~ 0.4 eV. With respect to $SO^- + CS_2$ reactants/products, $C_s(X^2A'')$ and $C_s(X^2A')$ structures are stable by ~ 1.6 and ~ 1.2 eV, respectively. The observed doublet photoelectron band can be assigned either based on the coexistence of the two ions or considering the existence of only one of the two forms attributing the observed bands to photodetachment transition from anion doublet to neutral singlet and neutral triplet states.

In order to assist the band assignment we have calculated the VDEs for both structures using B3LYP/aug-cc-pVTZ, MP2/ aug-cc-pVTZ and CCSD(T)/6-311+G(3df) level of

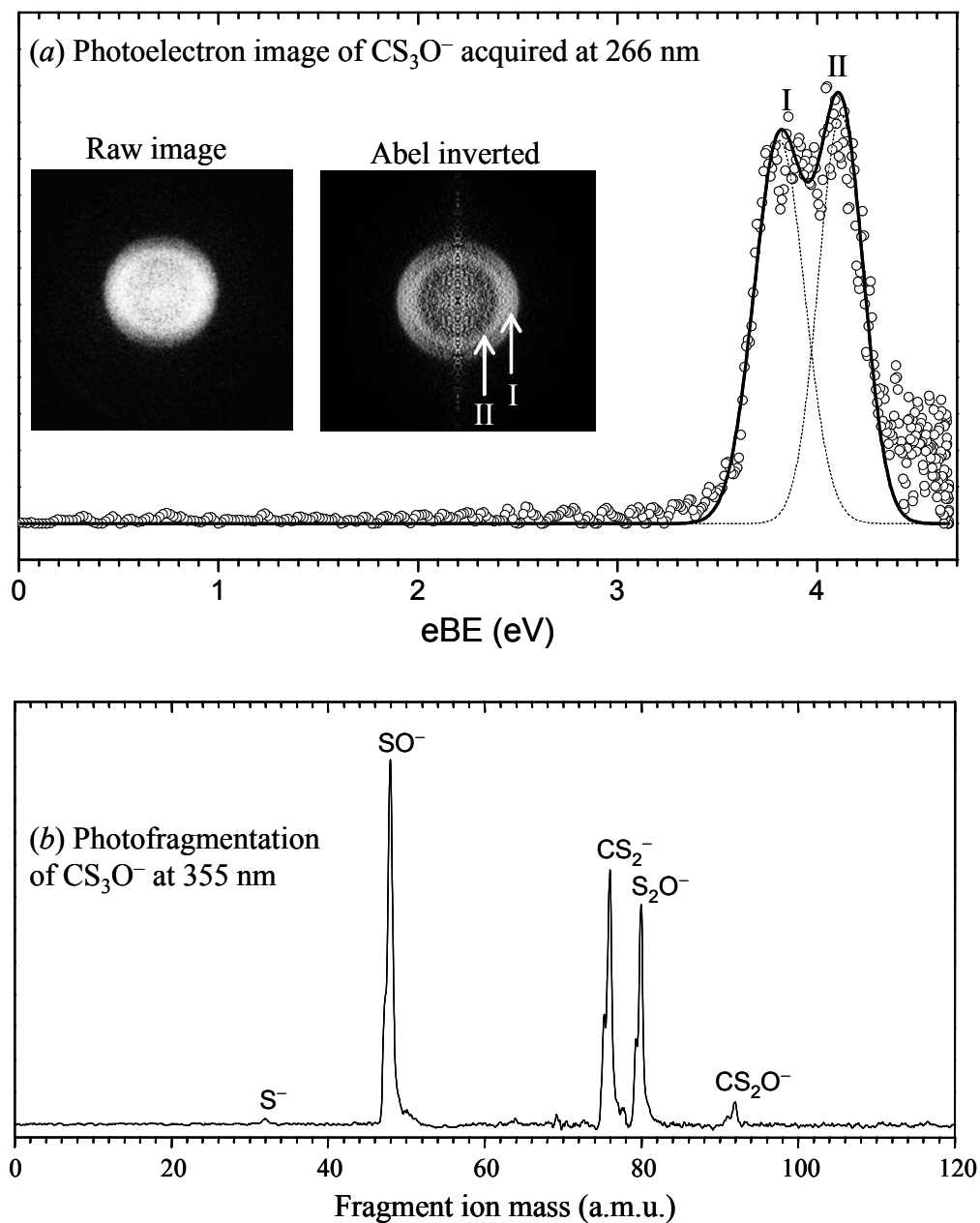


Figure 7.12 (a) Photoelectron image and spectra of CS_3O^- ion acquired at 266 nm. In the spectrum the open circles are the experimental data points; the dotted lines are Gaussian function fits to band I and II separately; and the solid line that fits the over all spectrum is the sum of the two Gaussian functions. (b) 355 nm fragment ions mass spectra for the CS_3O^- parent ions.

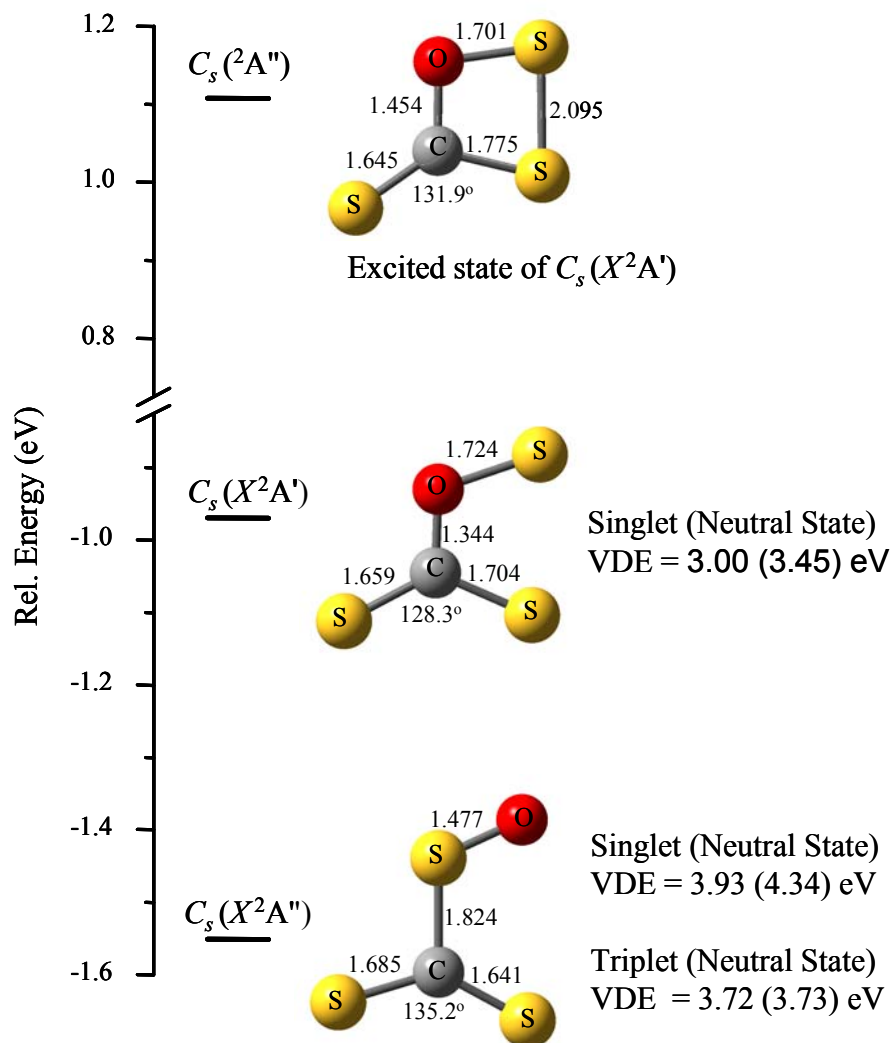
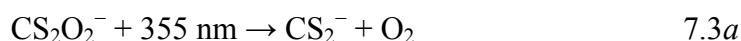
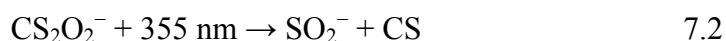
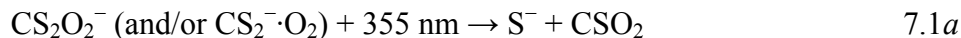


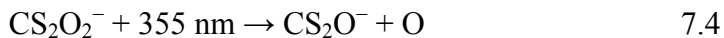
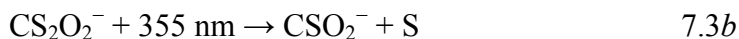
Figure 7.13 Optimized structures of CS_3O^- . Geometries are optimized using MP2/6-311+G(3df). The energies are given with reference to $\text{SO}^- + \text{CS}_2$. Bond lengths are in angstrom. The VDEs are calculated using CCSD(T)/6-311+G(3df) and B3LYP/aug-cc-pVTZ. The B3LYP results are given in parenthesis.

theories. For the $(\text{OS-CS}_2)^- [C_s(X^2A'')]$ structure the neutral singlet \leftarrow anion double transition, the B3LYP, MP2 and CCSD(T) methods give VDEs of 4.34, 3.99 and 3.93 eV, respectively. For the neutral triplet \leftarrow anion double transition, the calculated VDEs are 3.73, 4.08 and 3.72 eV, using the methods in the aforementioned order. On the other hand, for the $(\text{SO-CS}_2)^- [C_s(X^2A')]$ structure the lowest energy transition is found to be neutral singlet \leftarrow anion double with calculated VDEs of 3.45, 3.27 and 3.00 eV, using B3LYP, MP2 and CCSD(T), respectively. The calculated VDEs corresponding to photodetachment transitions from $(\text{OS-CS}_2)^- [C_s(X^2A'')]$ anionic electronic state to the neutral singlet ($^1A'$) and doublet ($^3A''$) states agree favorably with the observed 3.81 and 4.12 eV binding energies.

7.5 Photodissociation Pathways

The 355 nm excitation initiates interesting photochemistry in the newly observed $\text{CS}_2\text{O}_2^-/\text{CS}_2^-\cdot\text{O}_2$ and CS_3O^- anions. The photofragmentation patterns assist in elucidating the structures of the anions. The $\text{CS}_2\text{O}_2^-/\text{CS}_2^-\cdot\text{O}_2$ dissociation mechanisms are suggested in the following photochemical reaction pathways. For m/z 32 and 76 fragment ions, two possible mass assignments are proposed through channels (a) and (b).



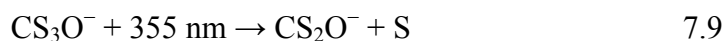
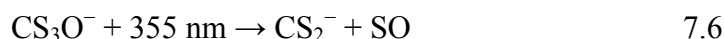


The contribution of channel (7.1*a*) has been confirmed by the photoelectron imaging result which reveals the photodetachment transition band of S^- fragment as shown in Fig. 7.6. The observation of S^- may suggest the importance of channel 7.3*b* where the electron alternatively resides on CSO_2 counterpart. Another mass assignment of m/z 32 involves channel 7.1*b* that has to compete with channel 7.3*a*. Considering the absence of $\text{O}_2^- \cdot \text{CS}_2$ ion-neutral complex in the parent anion as opposed to $\text{CS}_2^- \cdot \text{O}_2$ presence, it is unlikely that $\text{O}_2^- + \text{CS}_2$ product channel competes fairly with $\text{CS}_2^- + \text{O}_2$ product channel.

In the C_s ($^2A'$) structure there is π bond of bond order ~ 0.5 between S and O. In the excited state the potential gradient may lead towards strengthening of this bond leading to SO_2^- ion formation losing CS neutral as shown in channel (7.2). According to the fragment ion mass, formation of $\text{S}_2^- + \text{COO}$ (or $\text{CO} + \text{O}$) products could be an alternative to channel (7.2). However, formation of S_2^- fragment from the predicted isomers requires breaking two C–S bonds and forming S–S bond that involves extreme distortion of SCS bond angle. Energetically, this pathway is expected to be inaccessible at 355 nm photon energy due to high activation energy barrier. The formation of CS_2O^- fragment ion, channel (7.4), involves loss of nascent oxygen. CS_2O^- is also formed in the ion source as reflected in the parent ion mass spectra, Fig. 7.4. This anion is analogous to CO_3^- and

CS_3^- except that one heteroatom is introduced which lowers the symmetry from D_{3h} to C_{2v} .

Similarly, for the CS_3O^- anion the following reaction pathways are proposed.



Despite the structural similarity between CS_2O_2^- and CS_3O^- parent ions (compare structures in Fig. 7.11 and 7.13), no fragment ion with m/z 64, which could only be S_2^- , is observed from the later. The absence of S_2^- from CS_3O^- parent ion may support the above argument that the m/z 64 fragment ion from CS_2O_2^- parent ion is SO_2^- but not S_2^- which is equally expected from CS_3O^- parent ion. According to MP2/6-311+G(3df) calculation $\text{SO}^- + \text{CS}_2$, channel (7.5), is more stable than $\text{CS}_2^- + \text{SO}$, channel (7.6), by ~ 0.7 eV. Consistent with this, the SO^- fragment signal is more intense than that of CS_2^- fragment as seen in Fig. 7.12(b). The S_2O^- fragment ion formation mechanism, channel (7.7) should be similar to SO_2^- ion formation from CS_2O_2^- , channel (7.2). In Fig. 7.13, the $C_s(^2A'')$ ring structure is the excited state of $C_s(X^2A')$ ground state (its existence not confirmed by the photoelectron imaging result). On possible decaying pathway for this excited state is dissociation via channel (7.7) that leads to $\text{S}_2\text{O}^- + \text{CS}$ products. However,

S_2O^- can also be plausibly formed from $C_s(X^2A'')$ without involving $C_s(X^2A')$ isomer. The minor S^- and CS_2O^- products in channel (7.8) and (7.9) can be formed from $C_s(X^2A')$ isomer breaking the S–O bond.

7.6 Summary

In this experiment, $CS_2O_2^-/CS_2^- \cdot O_2$ and CS_3O^- anions are observed for the first time. Photoelectron imaging of $CS_2O_2^-$ ion at 266 nm shows two photodetachment transition bands. Based on the observed spectral features, the transition bands are tentatively attributed to two electronic isomers, in both of which, the O_2 and CS_2 moieties are covalently bonded. This assignment is supported by the *ab initio* calculation that predicts two covalent structures with energy difference in the order of room temperature. In addition, the 355 and 266 nm photoelectron imaging results clearly indicate that the $CS_2^- \cdot O_2$ ion-neutral complex is formed under favorable conditions, although the *ab initio* calculations fail to predict the existence of such stable structure.

The photoelectron image of CS_3O^- ion recorded at 266 nm shows two transition bands with VDE = 3.81 and 4.12 eV. The angular distribution of the 3.81 eV transition band (corresponding to faster electrons) is slightly more anisotropic ($\beta = -0.57$) than that of the 4.12 eV transition band ($\beta = -0.29$). *Ab initio* calculation generates two structures that differ in molecular connectivity as $(OS-CS_2)^-$ and $(SO-CS_2)^-$ corresponding to $C_s(X^2A'')$ and $C_s(X^2A')$ electronic states, respectively. Due to the ambiguity that the two bands could originate from the two coexisting isomers or from the same isomer but different

transitions, we cannot be certain in the assignment of the observed bands.

The photofragmentation CS_2O_2^- and CS_3O^- anion at 355 nm have provided valuable information in the identification and structural elucidation of the anions. The fragment ions that are observed from CS_2O_2^- parent anion include: S^- , SO_2^- , CS_2^- and CS_2O^- . The observed fragment ions from CS_3O^- parent anion are S^- , SO^- , CS_2^- and CS_2O^- .

The formation of small mass ions in the ion source including O^- , S^- , SO^- , S_2^- and SO_2^- is attributed mainly to the $\text{CS}_2\text{-O}_2$ reaction in the neutral medium. The larger anions including the newly observed CS_3O^- ion are believed to be formed through ion-molecule association reactions that take place after the molecular beam is crossed by the electron beam and before the anions are extracted into the time of flight tube. The competition of O_2 and CS_2 molecules for the excess electron is suggested to be the driving force for the formation of CS_2O_2^- anion in which CS_2 and O_2 are covalently bonded.

Although the ion source conditions that favor one type of isomer over the other were not formally optimized, in some cases, when the CS_2 liquid sample was kept in a tight gas delivery line for a long time, the $\text{CS}_2\text{-O}_2$ ion-neutral complex was formed predominantly. However, it appeared that other factors such as impurities tend to affect the isomer population. Optimization of the experimental conditions is the future direction of this project.

Chapter 8

FUTURE DIRECTION

8.1 Broader Perspective

To date the new apparatus has been applied to investigate the electronic structure and dissociation dynamics of molecular and relatively small cluster anions. With small modification of the hardware and the data acquisition system of the machine, the application of photofragmentation spectroscopy and photoelectron imaging can be extended to investigate various chemical systems such as inorganic compounds, semiconductor clusters and biomolecules. One of the required modifications is the ion generating technique. Thus far, the diversity of the ions that can be formed is limited by the availability of the neutral precursor in gas phase or by the vapor pressure (for liquid and solid samples) at room temperature. Therefore, the ion generating mechanism needs to be modified, for example, by introducing a laser ablation or discharge source techniques.

The photofragmentation results presented in the previous chapters enable us to identify the final ionic products and to determine the branching ratios. The best information that can possibly be obtained from detection of the final products is the asymptotic properties of the dissociation process, missing the dynamics between excitation and dissociation. Therefore, in the future by complementing the photofragmentation results with time-

resolved photoelectron imaging, more complete information can be obtained about the dissociation dynamics.

The dissociation of CO_2^- in water cluster (presented in Chapter 3) is an interesting system for the following reasons. The electronic states of CO_2^- that are excited at 355 and 266 nm have potential gradient towards linear geometry. On the other hand, these excited states intersect conically with other states that converge to $\text{O}^- + \text{CO}$ dissociation products. While the conical intersection around the Franck-Condon region leads to the dissociation products presented in Chapter 3, the relaxation of CO_2^- towards linear geometry in the excited states most likely leads to electron autodetachment or loss of CO_2 neutral leaving the excess electron on the water surface. Although, fragment water cluster anions were not observed as final products, transient or metastable fragment water cluster anions might have been formed that can only be probed if time-resolved spectroscopic technique is applied. Therefore, the observation photofragmentation of mass selected $\text{CO}_2^-(\text{H}_2\text{O})_m$ is the beginning of the revelation of the complicated dynamics which is yet to be discovered.

The reflectron and the fragment ion detection system are intended to separate and identify the fragment ions according to their mass. That is, using this technique we cannot measure the product-quantum state distribution even asymptotically. For state-specific detection of smaller fragments, there are several experimental techniques including laser-induced fluorescence, multi-photon ionization, coherent Raman scattering and photofragment ion imaging. Here, we are developing a new technique that involves

probing the mass selected fragment ions via photoelectron imaging at infinite time delay. In addition to its potential to identify the quantum state, photoelectron imaging of fragment ions enables unambiguous identification of the fragment ions when there are more than one possible ionic fragment species with the same nominal mass (see dissociation of the ion with $m/z = 108$ in Chapter 7 for example).

The implementation of the time-resolved photoelectron imaging experiment is presented in the next section considering CO_3^- as a model system. The design for the photoelectron imaging of fragment ions and the corresponding Simion electron trajectory simulation result are summarized in Sec. 8.3.

8.2 Time-Resolved Photoelectron Imaging of CO_3^-

8.2.1 Background

CO_3^- is a stable anion that exists in the Earth's atmosphere.²⁰⁷⁻²⁰⁹ It reacts with various nitrogen oxides^{210,211} including NO, NO₂ and HNO₃ in the atmosphere. There have been numerous experimental²¹²⁻²³⁰ and theoretical^{228,229,231} studies regarding its reaction dynamics, photochemistry and structure. The photodissociation of CO_3^- into $\text{O}^- + \text{CO}_2$ has been studied by several investigators^{219-221,226,227,229}, the most recent report being by Snodgrass et al at photon energies ranging from 2.41 to 2.71 eV.²²⁹ In the gaseous phase, the ground state of CO_3^- corresponds to D_{3h} ($^2A_2'$) electronic state.^{229,231} As it is proposed by Snodgrass et al.²²⁹, the dissociation is initiated by $^2E' \leftarrow ^2A_2'$ electronic transition

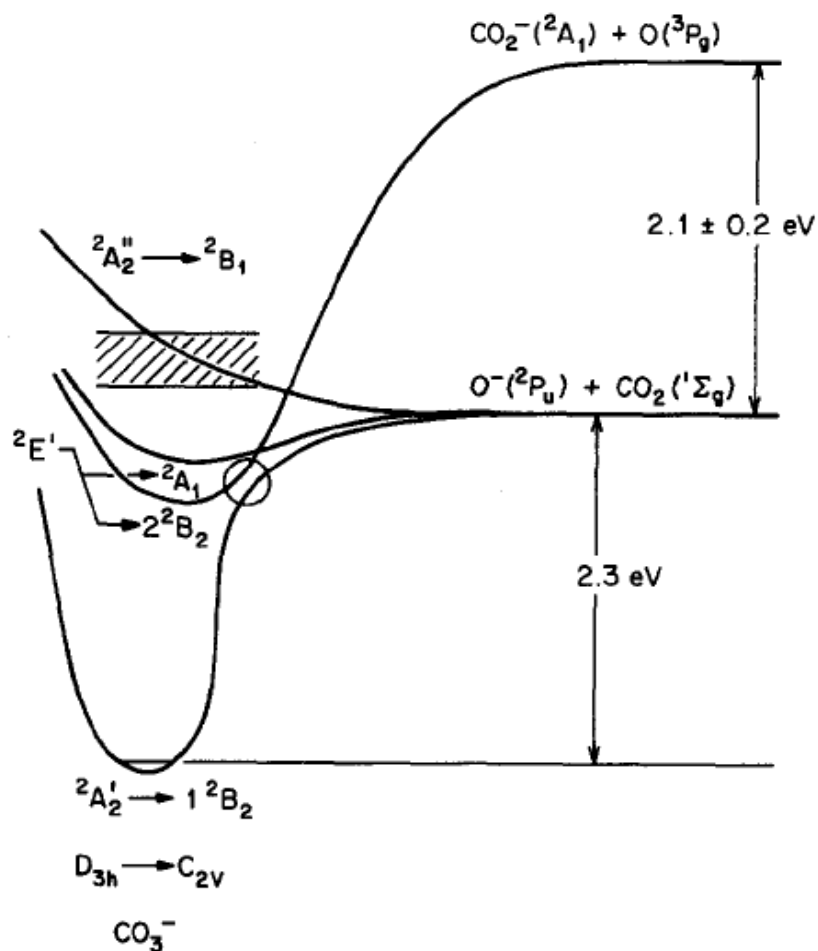


Figure 8.1 Reaction coordinate model of the CO_3^- ion proposed Snodgrass *et al.*²²⁹ It is assumed that the D_{3h} symmetry lowers to C_{2v} as dissociation begins. The cross hatched region indicates the photon energy range covered in the past experiment.²²⁹ The circle indicates a conical intersection (avoided crossing) between $1{}^2B_2$ and $2{}^2B_2$ states.

(Fig. 8.1). As the dissociation proceeds, the symmetry lowers to C_{2v} and hence the ${}^2E'$ state splits to 2A_1 and 2B_2 . Similarly the ground state ${}^2A_2'$ correlates to $1\ {}^2B_2$ state in the C_{2v} symmetry. The avoided crossing interaction between $1\ {}^2B_2$ and $2\ {}^2B_2$ states creates a bound excited state that correlates to $\text{CO}_2^- + \text{O}$ product. The dissociation into $\text{O}^- + \text{CO}_2$ occurs via state-specific interaction between the $2\ {}^2B_2$ and 2B_1 .²²⁹

From their photodissociation study, Hiller and Vestal determined the dissociation threshold for ground state CO_3^- as $2.258 \pm 0.008\ \text{eV}$ ²²⁷ compared to 2.27 eV from thermochemical studies.²²⁴ Based on collision enhanced dissociation of the excited anion, some fractions of the ions excited to the threshold region have been estimated to have a life time as long as microseconds.^{227,232}

Even though important chemical dynamics are involved in the photochemistry of CO_3^- , to date, no time-resolved experimental techniques have been applied to investigate the time evolution of the reaction coordinate. Here, we plan to investigate the $\text{CO}_3^- + h\nu \rightarrow \text{CO}_3^{-*} \rightarrow \text{O}^- + \text{CO}_2$ reaction coordinate applying femtosecond time-resolved photoelectron imaging experiment.

8.2.2 CO_3^- Ion Formation

CO_3^- is formed by expanding ~10% O_2 in CO_2 (total backing pressure of 30-40 psi) over CS_2 liquid sample. The mass spectrum is shown in the top panel of Fig. 8.2. It is interesting to note that when there is no CS_2 vapor in the backing gas mixture, the CO_3^- signal in the mass spectra is either very weak or absent. The O^- ion exhibits similar trend

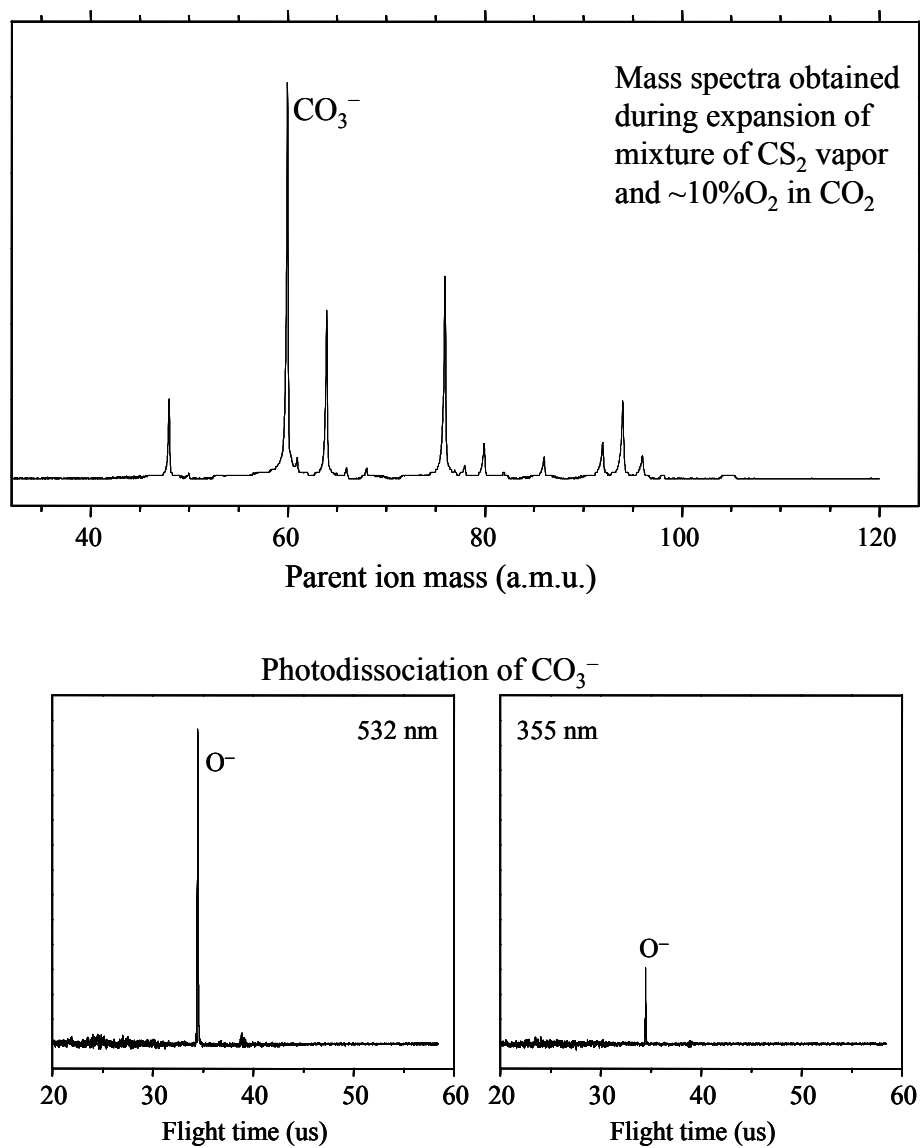


Figure 8.2 The top panel is the parent ion mass spectra obtained during expansion of a mixture of CS_2 vapor and $\sim 10\% \text{O}_2$ in CO_2 . The O^- fragment signal during the photodissociation of CO_3^- at 532 and 355 nm.

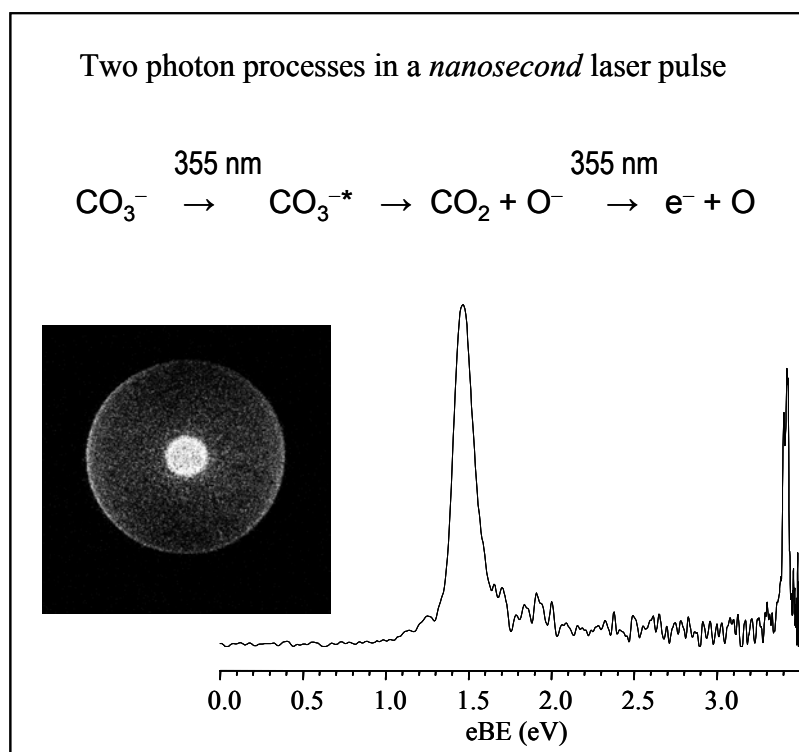


Figure 8.3 Photoelectron image of O^- fragment at 355 nm. Both the dissociation and fragment photodetachment processes occur in a 355 nm laser pulse due to the long pulse width of the laser pulse output (~ 7 ns).

as that of CO_3^- in the mass spectra suggesting that CO_3^- ion be formed through $\text{O}^- + \text{CO}_2 + \text{M} \rightarrow \text{CO}_3^- + \text{M}$ association reaction in the free jet before ion extraction takes place.

8.2.3 Photodissociation of CO_3^- and Fragment Photodetachment

In order to assess the appropriate photon energy for the pump-probe experiment the CO_3^- ion is excited at 532 nm and 355 nm using Nd:YAG laser pulse (~ 7 ns width). The O^- fragment ion signal (detected on the off-axis MCP detector) is shown in Fig. 8.2 (lower panel). Although the fragment signals shown in the figure are not normalized to account for the differences in the experimental conditions (parent ion intensity, photon power, etc), in general the fragment intensity is lower at 355 nm than at 532 nm. The 532 and 355 nm laser radiations are 0.06 eV and 1.22 eV above the dissociation threshold. As Snodgrass et al. have suggested the Franck-Condon factors for transitions to levels above the $\text{O}^- + \text{CO}_2$ dissociation asymptote are expected to be small as the upper state wave function extends to infinity in this energy region.

The photoelectron image shown in Fig. 8.3 is due to two photon processes. That is in a single laser pulse both dissociation and photodetachment take place due to the long pulse width of the nanosecond laser pulse which has a pulse width of ~ 7 ns.

8.2.4 Laser Setup and the Choice of Pump-Probe Wave Lengths

The laser setup for the pump-probe experiment is shown in Fig. 8.4. The details of the procedure was described in the past publications.^{68,233} Based on the O^- photoproduct

signal strength (see Fig. 8.2 lower panel), even though the O^- fragment is observed at 355 nm, the appropriate energy of the pumping laser pulse should be close to the dissociation threshold (480-530 nm). In order to follow the evolution of the electronic structure the ideal probing laser pulse energy needs to be above the detachment threshold of both the CO_3^{*-} excited state complex and the O^- final dissociation product. However, to obtain the time scale of the dissociation process, the probe wavelength can be chosen based on the detachment threshold of O^- product. The O^- ion (eBE = 1.46 eV) detaches at 800 nm (1.55 eV). The photoelectron image for the isolated O^- prepared in the ion source is displayed in Fig. 8.5. The kinetic energy of the detached electron is ~ 0.09 eV which can be turned off even when the O^- is weakly interacting with the departing CO_2 . That is at 800 nm, the O^- photoelectron signal is seen only when the dissociation is essentially complete.

Preliminary pump-probe experiment was performed at 400 nm pump and 800 nm probe wavelengths. The 400 nm initiate the photolysis of CO_3^- and the reaction progress is probed via photodetachment with delayed 800 nm probe laser pulses. At the time of the experiment, the laser was under maintenance. The regeneratively amplified Ti:sapphire laser system (Spectra Physics, Inc.) produces 700 μ J, 100 fs pulses at ~ 800 nm. Half of the fundamental output is used as the probe beam, while the other half is channeled through the LBO crystal of a femtosecond harmonics generator (Super Optronics, Inc.), producing 70 μ J pulses at ~ 400 nm. The 400 nm probe beam passes through a motorized translation stage (Newport ESP300 Universal Motion Controller) to enable controlled

temporal separation of the pump and probe pulses. The pump and probe beam paths are combined before entering the reaction chamber. The polarization vectors of the two beams are parallel to each other and to the ion beam axis. Both laser beams are mildly focused using a 2 m focal length lens positioned ~ 1.4 m before the intersection with the ion beam. The position of zero delay is determined by overlapping the pump and probe pulses in a BBO crystal. The photodetached electrons are detected using velocity-map imaging in the direction perpendicular to the ion and laser beams as described in Chapter 2. Extraneous pump or probe photon detachment signals are removed using computer-controlled shutters in the pump and probe beam paths as described previously.²³⁴

The above 400 and 800 nm pump-probe experiment is an ongoing experiment. Thus far, we are not able to detect the O^- fragment photodetachment channel at any time delay. This can be attributed to different experimental conditions including the small dissociation cross section at 400 nm, small laser power of the pump pulse and poor overlap between the laser and the ion beams. In the next step, in addition to optimizing other experimental conditions, the pump pulse photon energy will be lowered close to dissociation threshold so that the dissociation cross section increases (e.g. 530 nm instead 400 nm).

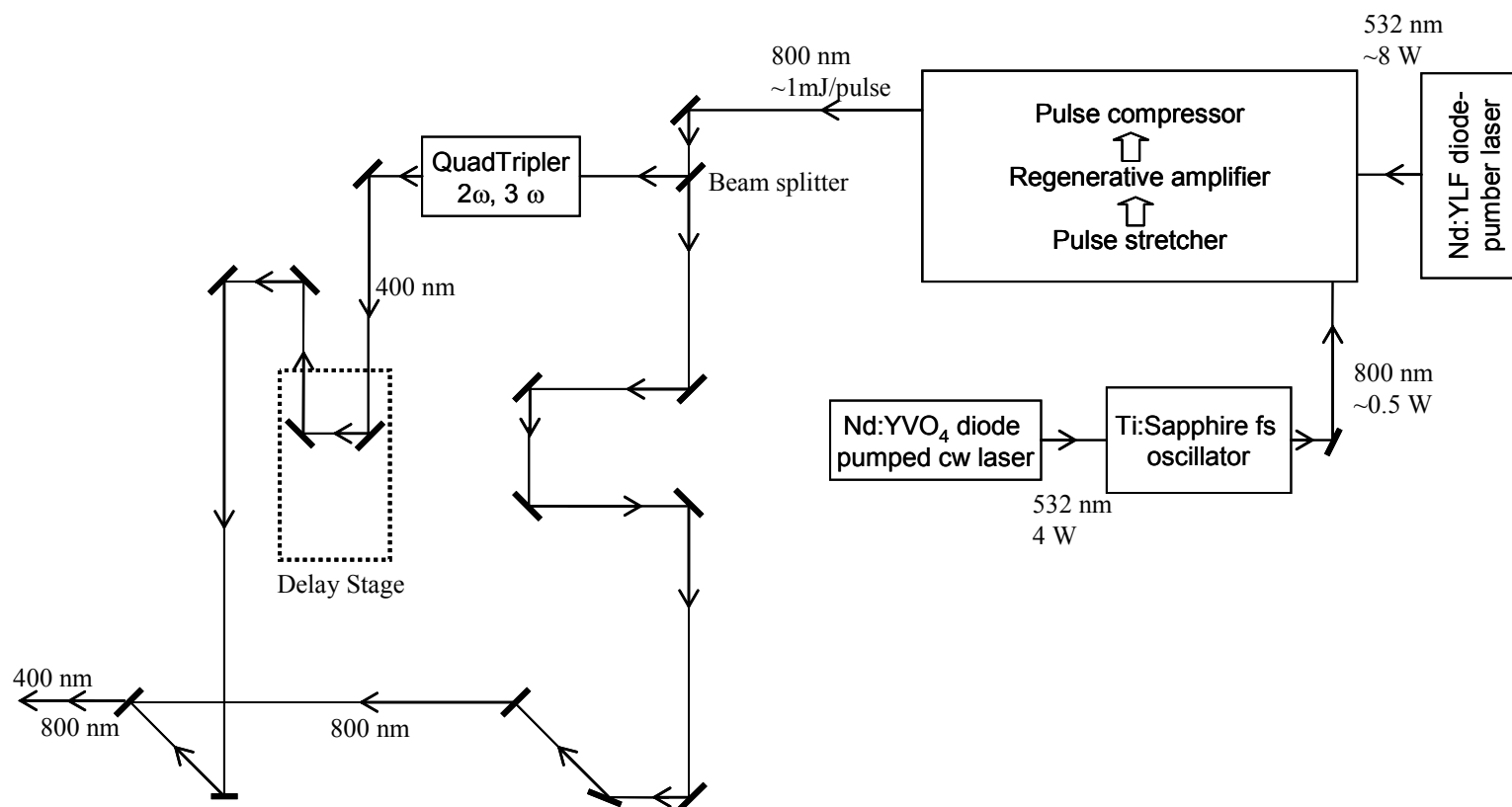


Figure 8.4 The laser setup for pump-probe experiment. The 400 nm laser pulse initiates the dissociation process and the reaction coordinate is sampled at different time delays probing with the 800 nm laser pulse. The progress of the reaction can be followed by photoelectron imaging of the excited complex and the O⁻ dissociation product.

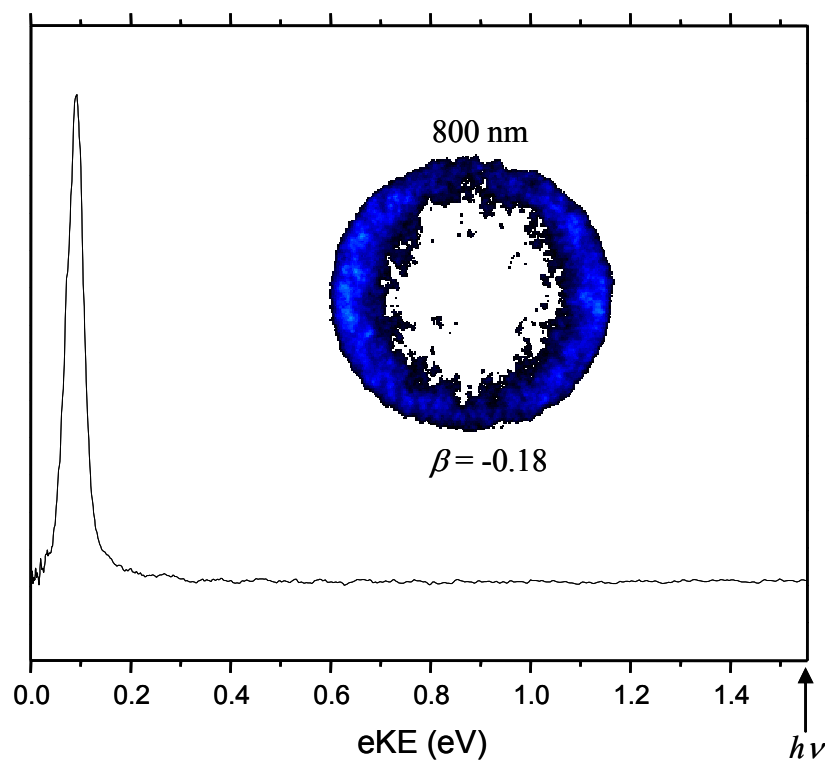


Figure 8.5 Photoelectron image of isolated O^- acquired at 800 nm using the femtosecond laser for a reference.

8.3 Photoelectron Imaging of Fragment Ions at Infinite Time-Delay

In the new apparatus the fragment ions are separated according to their mass using the reflectron TOF-MS. Therefore, as shown in Fig. 8.6, after the photofragmentation takes place with the first laser pulse, the fragment ion can be intercepted with the another laser pulse at infinite time delay as it passes beneath the interaction site of the parent ion and first laser pulse. The photoelectrons detached from the fragment ion can be accelerated towards the same detector that is used for parent ion photoelectron imaging. There are some technical difficulties associated with this approach, but first let us consider how the velocity-mapping of the fragment ion photoelectrons is achieved.

The electron trajectory simulation is performed using Simion 7.0, and the result is shown in Fig. 8.7. The electrostatic lens shown in Fig. 8.6 and 8.7 consists of four electrodes. For photoelectron imaging of fragment ions, electrodes 2 and 3 are referenced to ground while the velocity-mapping is achieved by varying the voltage ratio between electrodes 1 and 4. When the center hole in electrode 2 is not covered by wire mesh as shown in Fig. 8.7(a), the focusing is achieved at $V_1/V_4 = 3.275$. When the hole in electrode 2 is covered by the wire mesh the ratio is 1.725, Fig. 8.7(b). The experimental values are expected to be within ± 0.3 from the simulation result.

The technical difficulty with this design is that the DC potentials that are applied to focus the photoelectrons deflect the fragment ions upward. As a result the fragment ions (and the surviving parent ions) will not enter into the reflectron field. It is observed that

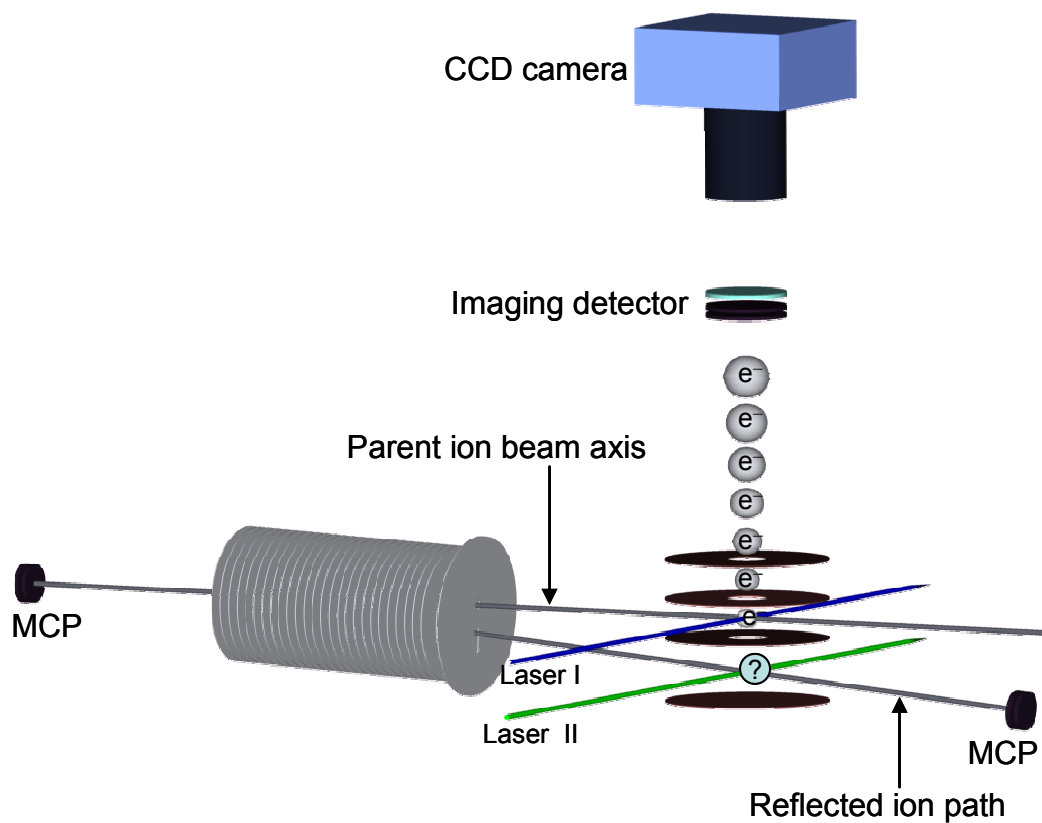


Figure 8.6 Photoelectron imaging of fragment anions. The first laser pulse (Laser I) causes photofragmentation and the photofragments are separated in time and space according to their mass by the reflectron field. The second laser pulse (Laser II) is used to detach electron from the mass selected fragment ion. The detached electrons are accelerated towards the imaging detector.

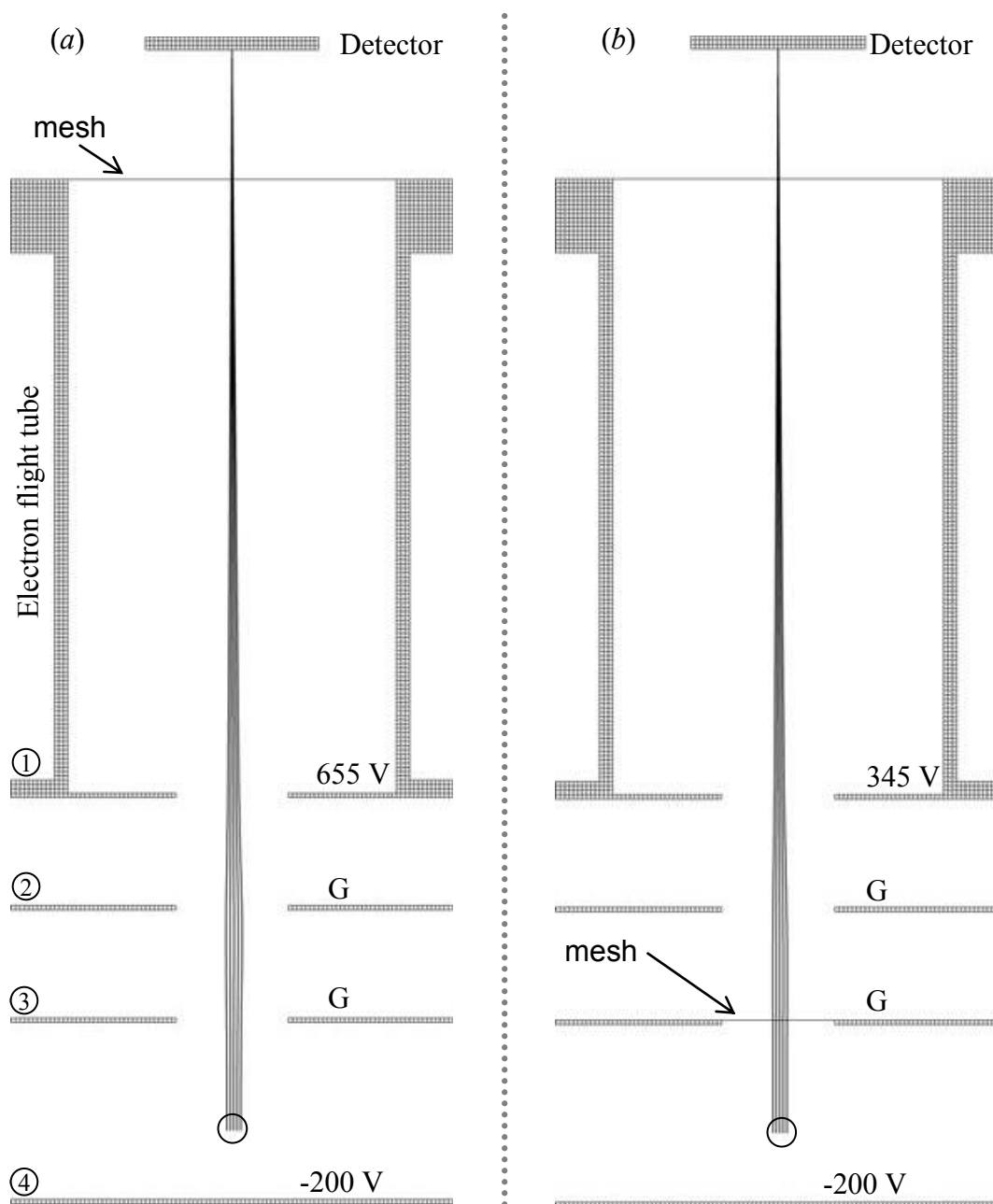


Figure 8.7 Simion trajectory simulation result for fragment ion photoelectron imaging. The circles at the origin of the trajectory indicate the laser light and fragment ion interaction site. The focusing is achieved by varying electrode 1 to electrode 4 voltage ratio while referencing electrodes 2 and 3 to ground (G). When the hole in electrode 3 is open as in (a), the optimum ratio obtained from the simulation is 3.275, but when the hole is covered by a wire mesh as in (b) the ratio is 1.725.

The technical difficulty with this design is that the DC potentials that are applied to focus the photoelectrons deflect the fragment ions upward. As a result the fragment ions (and the surviving parent ions) will not enter into the reflectron field. It is observed that about 100 V is enough to deflect the parent and the fragment ion away from the reflectron entrance hole. Therefore, even when the field from the repeller plate is shielded by the use of the wire mesh on electrode 3, the ions miss the reflectron entrance hole due to the potential applied to electrode 1. The field from electrode 1 could have been shielded by using similar wire mesh on electrode 2, but under this arrangement the velocity-mapping may never be achieved. In addition, when grids (wire mesh) are used far from the detector they are known to create blurring on the image. Therefore, the only viable option to achieve photoelectron imaging of fragment ions is by using a pulse voltage on the electrostatic lens. The pulse voltage can be timed with reference to the laser pulse that is used to interrogate the fragment ions.

8.4 Summary

In summary the following projects can be implemented using the new apparatus with some modifications. (i) Introducing a new ion-generating technique (e.g. laser ablation or discharge source), the application of photofragmentation and photoelectron imaging can be extended to inorganic compounds, semiconductor clusters and biomolecules. (ii) After successfully applying the time-resolved photoelectron imaging on the CO_3^- , the principle can be applied to investigate the dissociation dynamics of CO_2^- in water clusters as well

as other systems. (iii) The fragment ion photoelectron imaging technique will enable to measure the product-quantum state and help to identify fragment ions unambiguously.

Appendix A

ELIMINATION OF NOISE FROM PHOTOELECTRON IMAGES USING DIGITAL FILTERS

A-1 Designing Two Dimensional Filters

The digital filters used in image analysis are two-dimensional (2-D). The 2-D filters can be designed by extending the procedures used in designing 1-D filters. In frequency transformation method, a 2-D zero phase FIR filter is designed from 1-D FIR filter. This can be shown mathematically as

$$H(\omega_1, \omega_2) = H(\omega) \Big|_{\omega=G(\omega_1, \omega_2)} \quad (\text{A-1})$$

where $H(\omega)$ is a 1-D digital filter frequency response, $H(\omega_1, \omega_2)$ is the frequency response of the resulting 2-D digital filter and the $G(\omega_1, \omega_2)$ is the frequency response of the transformation matrix. The frequency transformation method preserves most of the characteristics of the 1-D filter, particularly the transition bandwidth and ripple characteristics.²³⁵ This method uses a transformation matrix, a set of elements that defines the frequency transformation. This can be implemented in Matlab using `ftrans2` function. An example is given in Fig. A-1 where a 1-D bandpass FIR filter is transformed to a 2-D filter using the code given at the end of this appendix.

The Matlab image processing toolbox (IPT) supports a number of predefined 2-D linear filters, obtained by using `fspecial` function. `fspecial` returns a 2-D filter h as a correlation kernel, which is the appropriate form to use with the multidimensional image filtering Matlab function called `imfilter`. The rectangular averaging, the

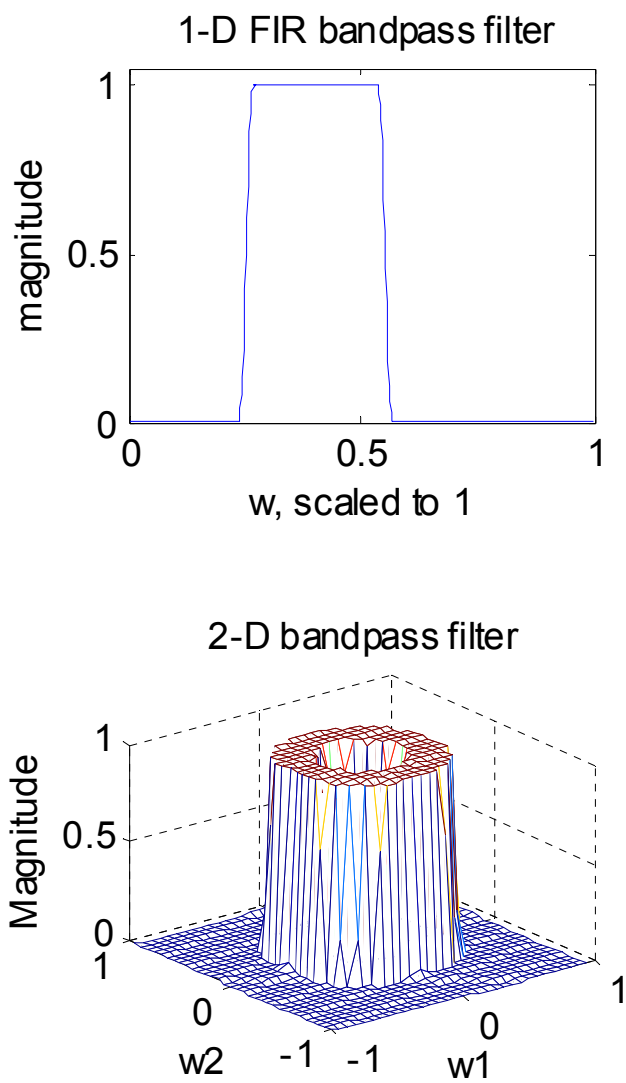


Figure A-1 Transformation of a 1-D bandpass filter to 2-D bandpass filter. w = angular frequency.

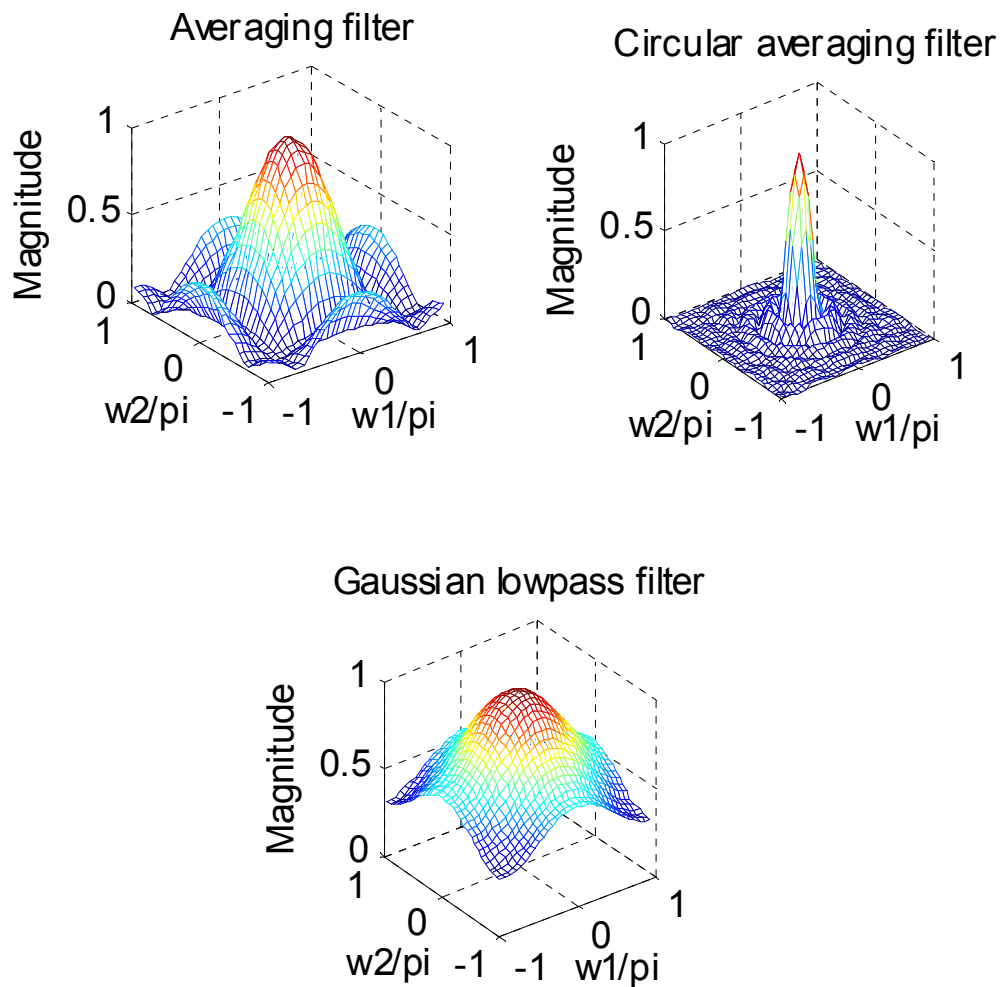


Figure A-2 Magnitude response of (rectangular) averaging, circular averaging and Gaussian lowpass filters. w = angular frequency and $\pi = \pi$.

circular averaging and the Gaussian lowpass filters displayed in Fig. A-2 were generated using `fspecial` function.

A commonly used tool for generating nonlinear spatial filters is the order-statistic filters (also known as rank filters). These are nonlinear filters whose response is based on ordering (ranking) the pixels contained in an image neighborhood and then replacing the value of the center pixel in the neighborhood with the value determined by ranking the result. The best-known order-statistic filter in digital image processing is the median filter which corresponds to the 50th percentile.²³⁶ The IPT provides a specialized implementation of the 2-D median filter through `medfilt2` function name.

Median filtering is a nonlinear process useful in reducing impulsive or salt-and-pepper noise. It is also useful in preserving edges in an image while reducing random noise which can occur due to a random bit error in a communication channel.²³⁵ In a median filter, a window slides along the image, and the median intensity value of the pixels within the window becomes the output intensity of the pixel being processed. Like lowpass filtering, median filtering smoothes the image and is thus useful in reducing noise. Unlike lowpass filtering, median filtering can preserve discontinuities in a step function and can smooth a few pixels whose values differ significantly from their surroundings without affecting the other pixels.

One of the earliest and best known approaches to linear image restoration is Wiener filtering. In a raw image, a signal s is observed superimposed upon an (additive) noisy background w so that s is to be reconstructed from $s + w$. Filtering over square or circular

image segments can be efficient to eliminate the noise but at the same time can smooth out the signal itself beyond recognition especially when larger segment size is used.²³⁷ Therefore, it is natural to seek for an optimal filter that can remove the noise as much as possible while retaining the signal.

A brief summary of the mathematical description of Wiener filter is presented as follows [see ref. ²³⁵ for detail]. Suppose we have a signal $s(n_1, n_2)$ and a noise $w(n_1, n_2)$. The noisy observation $x(n_1, n_2)$ is given by

$$x(n_1, n_2) = s(n_1, n_2) + w(n_1, n_2) \quad (\text{A-2})$$

Then the noise can be determined from noisy signal using a linear estimator given by

$$\hat{s}(n_1, n_2) = x(n_1, n_2) * h(n_1, n_2) \quad (\text{A-3})$$

The linear estimator is linear and shift invariant system, since we are dealing with stationary random processes. The error criterion used is

$$\text{Error} = E[|e(n_1, n_2)|^2] = E[|s(n_1, n_2) - \hat{s}(n_1, n_2)|^2] \quad (\text{A-4})$$

The error can be minimized using the orthogonality principle which requires that $e(n_1, n_2)$ be uncorrelated with any random variable in $x^*(n_1, n_2)$. Applying this principle and assuming that $s(n_1, n_2)$ is uncorrelated with $w(n_1, n_2)$, an expression for a frequency response of noncausal Wiener filter can be found as

$$H(\omega_1, \omega_2) = \frac{P_s(\omega_1, \omega_2)}{P_s(\omega_1, \omega_2) + P_w(\omega_1, \omega_2)} \quad (\text{A-5})$$

where P_s and P_w are the power spectrum of the signal and noise respectively. Application of the noncausal Wiener filter for linear minimum mean square error signal is shown in Fig. A-3. The Wiener filter shown in equation (5) is a zero-phase filter. Since P_s and P_w

are real and nonnegative, $H(\omega_1, \omega_2)$ is also real and nonnegative. Therefore, the Wiener filter affects the spectral magnitude but not the phase. The Wiener filter preserves the high signal-to-noise ratio (SNR) frequency components while attenuating the low SNR frequency components. The Wiener filter is typically a lowpass filter.

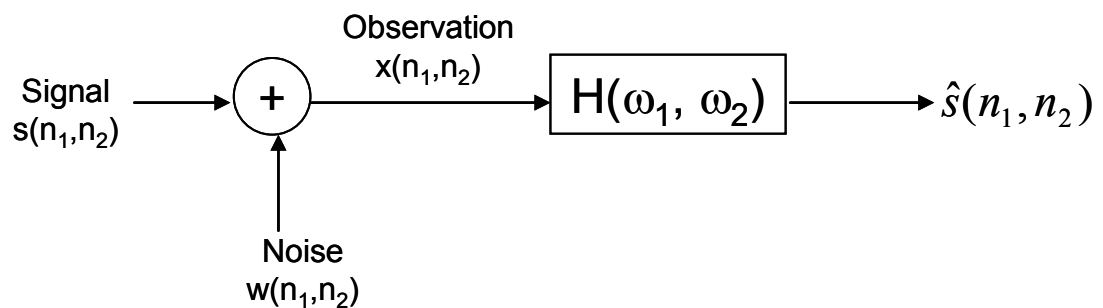


Fig. A-3 Implementation of the noncausal Wiener filter. Adapted from ref. ²³⁵

The Wiener filter was developed under the assumption that the characteristics of the signal and noise do not change over different regions of the image. This has resulted in a space invariant filter. In a typical image, image characteristics differ considerably from one region to another. It is reasonable, then, to adapt the processing to the changing characteristics of the image and degradation. Hence, an adaptive Wiener filter has been developed.

The Matlab image processing toolbox implements the adaptive Wiener filter using the function called `wiener2`. Where the variance is large, `wiener2` performs little smoothing. Where the variance is small, it performs more smoothing. This approach is expected to produce better results than other comparable linear filtering. There are no

design tasks in using `wiener2`. The function handles all preliminary computations and implements the filter for an input image.

A-2 Filter Implementation

To determine the nature of the noise, the raw photoelectron image of S^- anion acquired at 355 nm was sampled by plotting the sum of several rows at different regions. For illustration, the sum of rows from 500 to 520 is plotted as a function of column numbers in pixels as shown in Fig. A-4. The background subtraction is avoided intentionally to see the performance of the filters more clearly. In Fig. A-4, the outputs of the circular averaging filter, median filter and Wiener filter are plotted along with the raw (original) data shown at the very top. For fair comparison, all the filters were used at their default parameters. The spike noise signal at column 385 is partially removed when the circular averaging filter is used and is completely eliminated when the median filter is applied. The circular averaging filter was able to remove noise at bigger window size at the expense of contour resolution. Expectedly, the spike noise signal is not affected by the Wiener filter at all. Wiener filter is known to accomplish little smoothing where the variance is large and more smoothing where the variance is small. In other words, the Wiener filter preserves the high signal-to-noise ratio (SNR) frequency components while attenuating the low SNR frequency components. As shown in the raw data (Fig. A-4 top), the noise can be characterized as “salt and pepper” noise for which the median filter is known to perform best.

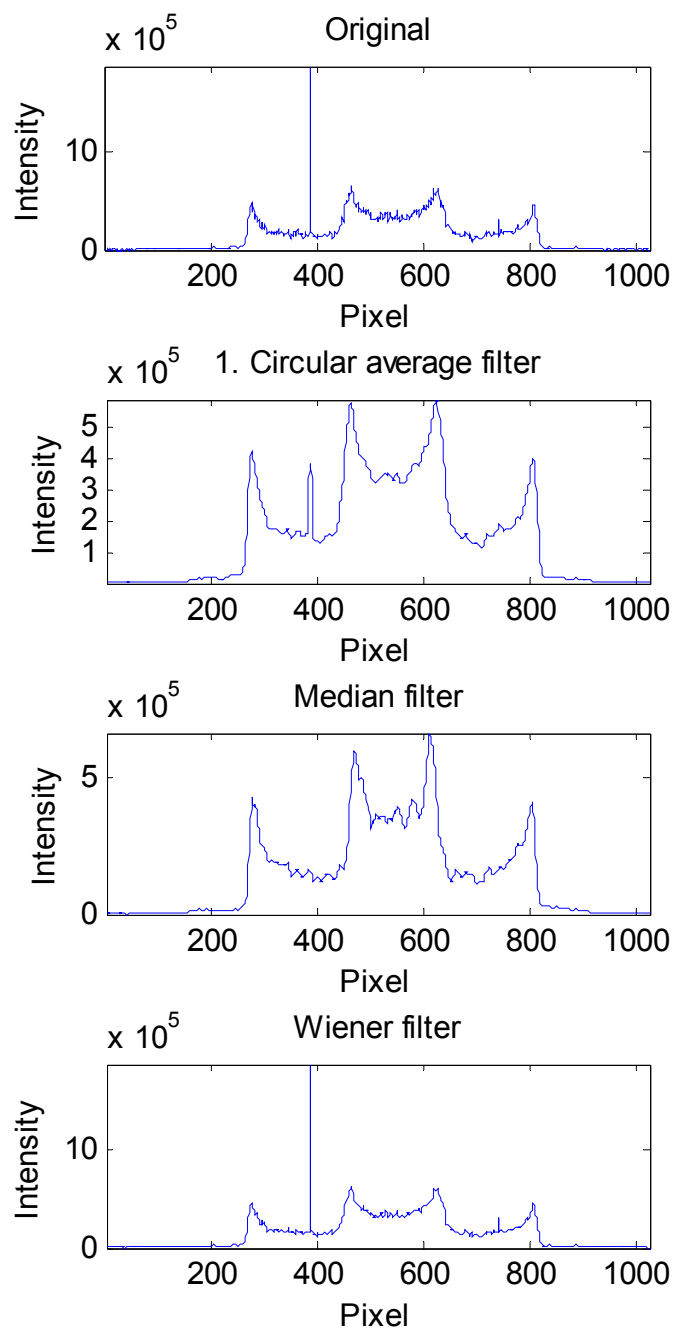
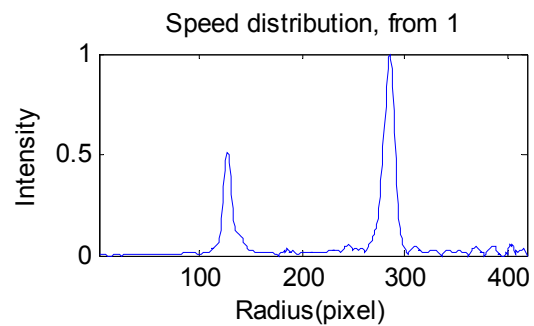
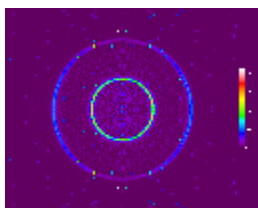
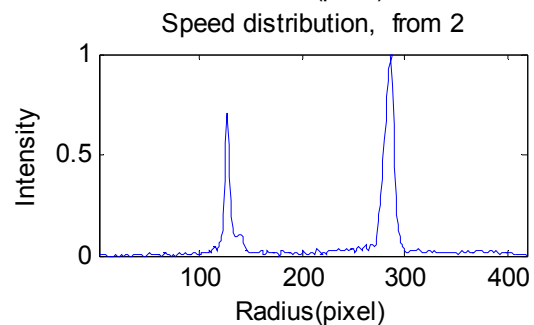
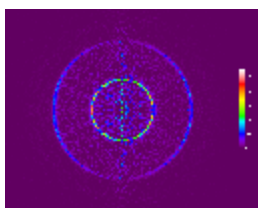


Figure A-4 The examination of the noise by sampling the row data of the image.

1. Circular average filter



2. Median filter



3. Wiener filter

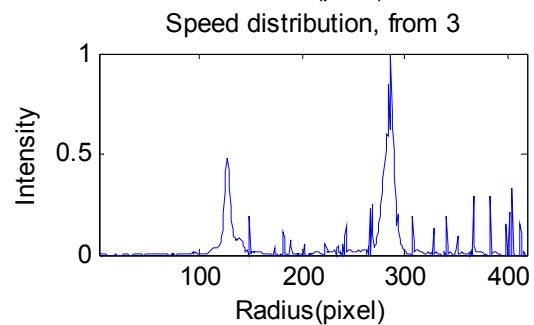


Figure A-5 Comparison of circular averaging, median and Wiener filters. The reconstructed images obtained from the inverse Abel transformation are given on the left side. The corresponding velocity distributions are shown on the right.

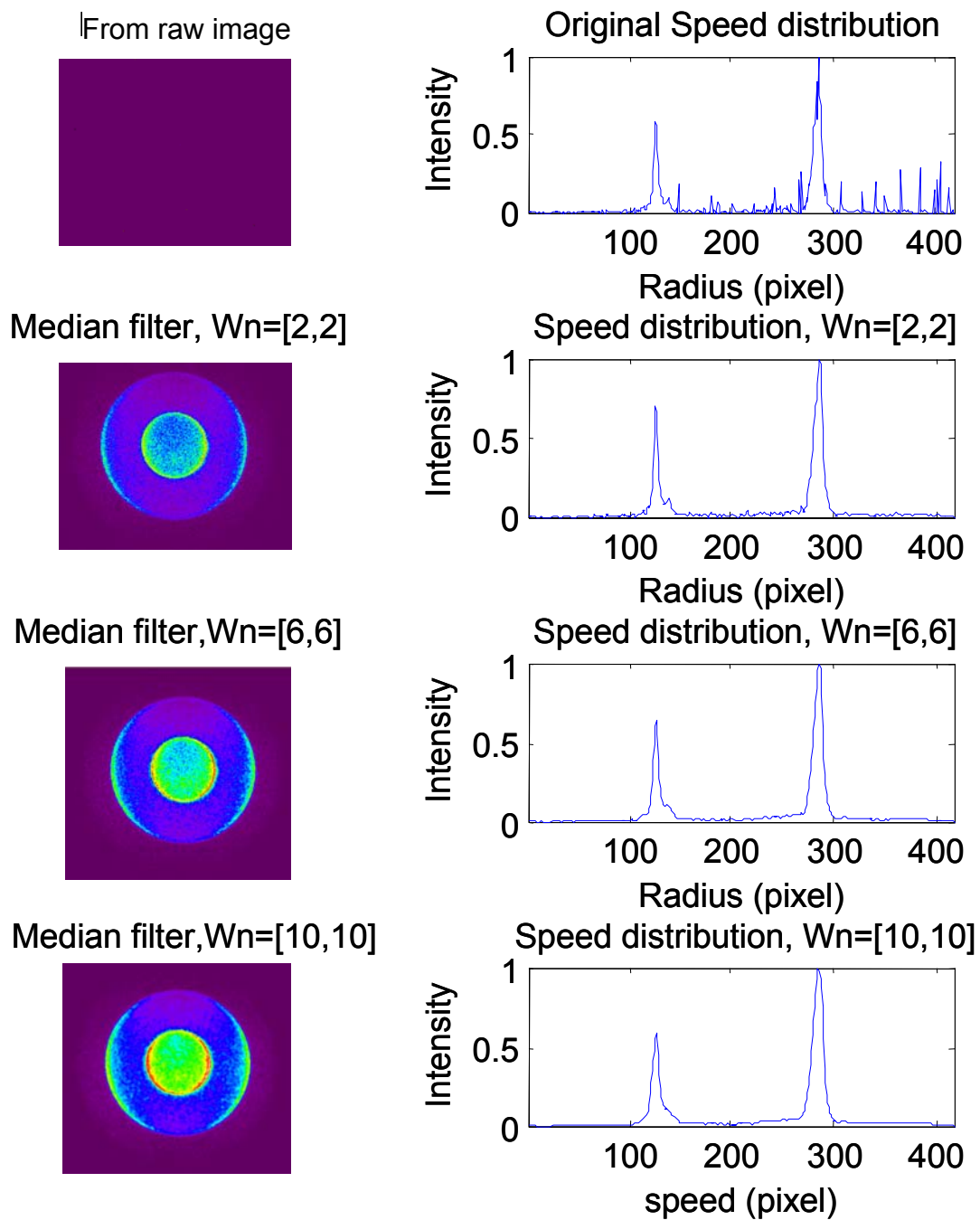


Figure A-6 The effect of segment/window, $W_n=[n,n]$, size on the performance of the median filter.

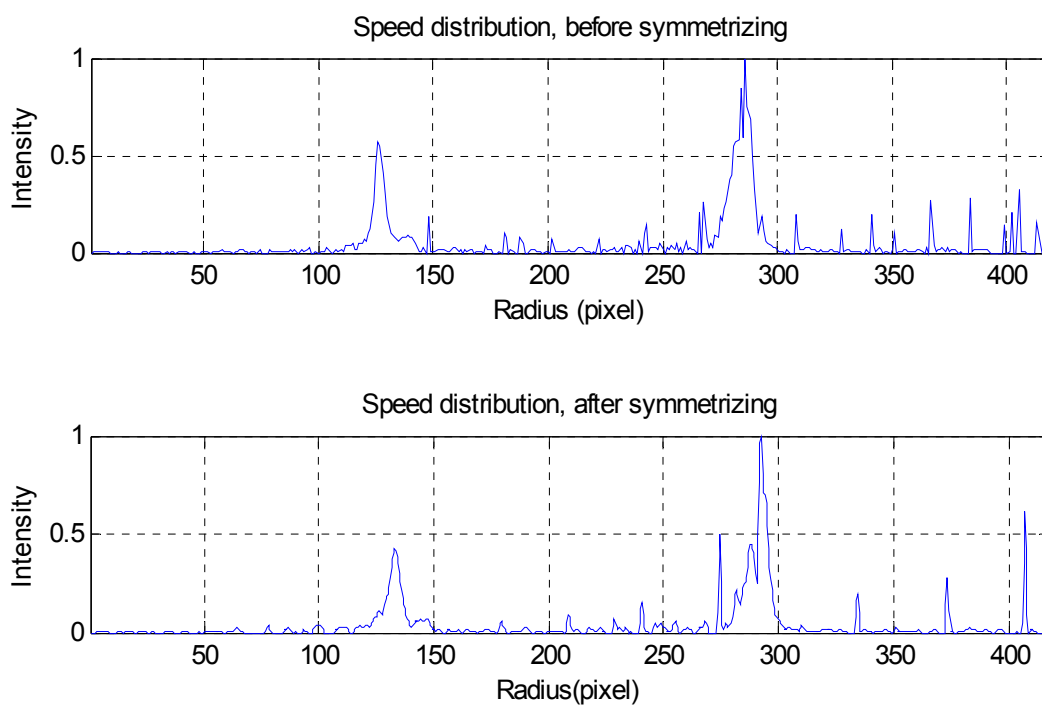


Figure A-7 Effect of symmetrizing the photoelectron image on the resulting spectrum. Notice after symmetrization, the spin-orbit splitting is seen in the $S(3P) \leftarrow S^-(^2P)$ photodetachment transition band.

As shown in Fig. A-5, similar results are obtained when the 3-D distribution of the photoelectron images are reconstructed by taking the inverse Abel transformation of the filtered images using the BASEX program of Dribinski *et al.*⁹⁴ While the outputs of the averaging and median filters have comparable quality, the noise remains essentially unaffected when the Wiener filter is applied. Compared to the median filter output, the averaging filter output suffers from loss of contour resolution. Correspondingly, some important features can be smoothed out by the circular averaging filter in the speed distribution possibly beyond recognition.

In addition to the above filters, a rectangular averaging and Gaussian lowpass filters were implemented using `imfilter` Matlab function at their default parameters. The rectangular and circular averaging filters have similar performance; the former being better in preserving some shoulder peaks. The median filter outperforms all the filters tested in terms of eliminating the noise from our photoelectron images.

An important parameter in using an averaging and a median filter is the size of the window (W_n). Because it is difficult to choose the optimum window size in advance, it is recommended to apply the filters with different window sizes and choose the best of the resulting images. The effect of the window size on the performance of the median filter is illustrated in Fig. A-6. Notice that the inverted image reconstructed from the raw image is barely noticeable from the background. When the median filtering is applied even with the small window size, $W_n=[2,2]$, the noise is essentially eliminated and the signal is visible with excellent contrast. As it can be seen from the figure, large window size results in the loss of contour resolution in the filtered image and correspondingly

important features/peaks can be smoothed out in the resulting velocity distribution. The window size has similar effect on the averaging filters.

A-3 Symmetrization of Photoelectron Image

It is usually not an easy task to find a perfectly symmetric photoelectron image. Experimental settings such as imperfect alignments of electrodes and camera contribute to the asymmetry of photoelectron images. A Matlab code is written to symmetrize the image latitudinally and longitudinally by reflecting the hemispheres. The effect of symmetrization on the velocity distribution is shown in Fig. A-7 by comparing the spectrum extracted from the original (top panel) and symmetrized (lower panel) unfiltered photoelectron images. The resolution of the main peak around 285 pixel is improved after symmetrizing showing the spin-orbit splitting.

A-4 Matlab Programs Used in the Image Analysis

```
%Transformation of 1-D Bandpass FIR filter to 2-D bandpass
%filter
b = fir1(200,[0.25 0.55]); % 1-D bandpass filter
h = ftrans2(b); % 2-D bandpass filter
[H,w]=freqz(b,1,512); % Frequency response of 1-D
filter
subplot(1,2,1),plot(w/pi,abs(H))
axis([0 1 0 1.05])
xlabel('w, scaled to 1'); ylabel('magnitude')
title('1-D FIR bandpass filter')
colormap(jet(64))
subplot(1,2,2), freqz2(h,[32 32]);
%Frequency response of 2-D filter
axis([-1 1 -1 1 0 1])
xlabel('w1'); ylabel('w2')
title('2-D bandpass filter')

%Generating 2-D filters using fspecial
```

```

h = fspecial('average'); %Rectangular averaging filter
subplot(1,3,1), freqz2(h,[32 32])
title('Averaging filter')
xlabel('w1/pi'); ylabel('w2/pi')
h = fspecial('disk'); %Circular averaging filter
subplot(1,3,2), freqz2(h,[32 32])
title('Circular averaging filter')
xlabel('w1/pi'); ylabel('w2/pi')
h = fspecial('gaussian'); %Gaussian lowpass filter
subplot(1,3,3), freqz2(h,[32 32])
title('Gaussian lowpass filter')
xlabel('w1/pi'); ylabel('w2/pi')

% Sampling of raw data
S=load('S.txt');
Seq=0;
for i=500:1:520;
    eq=S(i,:);
    Seq=Seq+eq;
end
p=1:1024;subplot(4,1,1)
plot(p,Seq); axis([1,1024,-inf,inf]);
title('Original'),xlabel('Pixel'); ylabel('Intensity')

h = fspecial('disk');
Scaf=imfilter(S,h);
Seq=0;
for i=500:1:520;
    eq=Scaf(i,:);
    Seq=Seq+eq;
end
subplot(4,1,2), plot(p,Seq); axis([1,1024,-inf,inf])
xlabel('Pixel'); ylabel('Intensity')
title('1. Circular average filter')
Smf = medfilt2(S);
Seq=0;
for i=500:1:520;
    eqm=Smf(i,:);
    Seq=Seq+eq;
end
subplot(4,1,3), plot(p,Seq); axis([1,1024,-inf,inf])
xlabel('Pixel'); ylabel('Intensity')
title('Median filter')
Swf = wiener2(S);
Seq=0;

```

```

for i=500:1:520;
    eq=Swf(i,:);
    Seq=Seq+eq;
end
subplot(4,1,4), plot(p,Seq); axis([1,1024,-inf,inf])
xlabel('Pixel'); ylabel('Intensity')
title('Wiener filter')

%Effect of window size
S=load('S.txt'); %Original data
Sim=imread('S_reconst.bmp'); subplot(4,2,1), imshow(Sim)
title('Reconstructed from raw image')
Srec=load('S_speed.dat'); Sv=Srec(:,1); SI=Srec(:,2);
subplot(4,2,2), plot(Sv,SI); axis([-inf,inf,-inf,inf])
title('Original Speed distribution')
xlabel('Radius (pixel)'); ylabel('Intensity');

Smf = medfilt2(S,[2 2]); %Window size [2,2]
dlmwrite('Smf2.txt', Smf, 'delimiter', '\t');
Srec=load('Smf_speed.dat');
Sim2=imread('Smf2_reconst.bmp');subplot(4,2,3),
imshow(Sim2)
title('Median filter, Wn=[2,2]')
Srec=load('Smf2_speed.dat'); Sv=Srec(:,1); SI=Srec(:,2);
Sv=Srec(:,1); SI=Srec(:,2);
subplot(4,2,4), plot(Sv,SI); axis([-inf,inf,-inf,inf])
title('Speed distribution, Wn=[2,2]')
xlabel('Radius (pixel)'); ylabel('Intensity');
Smf = medfilt2(S,[6 6]); %Window size [6,6]
dlmwrite('Smf6.txt', Smf, 'delimiter', '\t');
Srec=load('Smf_speed.dat');
Sim6=imread('Smf6_reconst.bmp');subplot(4,2,5),
imshow(Sim6)
title('Median filter,Wn=[6,6]')
Srec=load('Smf6_speed.dat'); Sv=Srec(:,1); SI=Srec(:,2);
Sv=Srec(:,1); SI=Srec(:,2);
subplot(4,2,6), plot(Sv,SI); axis([-inf,inf,-inf,inf])
title('Speed distribution, Wn=[6,6]')
xlabel('Radius (pixel)'); ylabel('Intensity')
Smf = medfilt2(S,[10 10]); %Window size [10,10]
dlmwrite('Smf10.txt', Smf, 'delimiter', '\t');
Srec=load('Smf_speed.dat');
Sim10=imread('Smf_reconst.bmp');subplot(4,2,7),
imshow(Sim10)
title('Median filter,Wn=[10,10]')

```

```

Srec=load('Smf10_speed.dat'); Sv=Srec(:,1); SI=Srec(:,2);
Sv=Srec(:,1); SI=Srec(:,2);
subplot(4,2,8), plot(Sv,SI); axis([-inf,inf,-inf,inf])
title('Speed distribution, Wn=[10,10]')
xlabel('speed (pixel)'); ylabel('Intensity')

%Comparison of filters
S=load('S.txt');
%Circular averaging filter
h = fspecial('disk');
Saf=imfilter(S,h);
dlmwrite('Saf.txt', Saf, 'delimiter', '\t')
Sim=imread('Saf_reconst.bmp'); subplot(3,2,1), imshow(Sim)
title('1. Circular average filter')
Srec=load('Saf_speed.dat'); Sv=Srec(:,1); SI=Srec(:,2);
subplot(3,2,2), plot(Sv,SI); axis([-inf,inf,-inf,inf])
title('Speed distribution, from 1')
xlabel('Radius(pixel)'); ylabel('Intensity');
%Median filter
Smf = medfilt2(S,[3 3]);
dlmwrite('Smf.txt', Smf, 'delimiter', '\t');
Srec=load('Smf_speed.dat');
Sim=imread('Smf_reconst.bmp');subplot(3,2,3), imshow(Sim)
title('2. Median filter')
Srec=load('Smf_speed.dat'); Sv=Srec(:,1); SI=Srec(:,2);
Sv=Srec(:,1); SI=Srec(:,2);
subplot(3,2,4), plot(Sv,SI); axis([-inf,inf,-inf,inf])
title('Speed distribution, from 2')
xlabel('Radius(pixel)'); ylabel('Intensity');
%Wiener filter
Swf = wiener2(S,[5,5]);
dlmwrite('Swf.txt', Swf, 'delimiter', '\t');
Srec=load('Smf_speed.dat');
Sim=imread('Swf_reconst.bmp'); subplot(3,2,5), imshow(Sim)
title('3. Wiener filter')
Srec=load('Swf_speed.dat'); Sv=Srec(:,1); SI=Srec(:,2);
Sv=Srec(:,1); SI=Srec(:,2);
subplot(3,2,6), plot(Sv,SI); axis([-inf,inf,-inf,inf])
title('Speed distribution, from 3')
xlabel('Radius(pixel)'); ylabel('Intensity');

%Symmetrization
S=load('S.txt');
Srec=load('S_speed.dat'); Sv=Srec(:,1); SI=Srec(:,2);

```

```

subplot(2,1,1), plot(Sv,SI); axis([-inf,inf,-inf,inf]);
grid
title('Speed distribution, before symmetrizing')
xlabel('Radius (pixel)'); ylabel('Intensity');
[row,col]=size(S);
Nc=col/2+24;
for j=1:1:Nc
    SL(1:row,j)=S(1:1024,j);
    SR(1:row,j)=S(1:1024,Nc-j+1);
end
SSc=[SL,SR];
[row,col]=size(SSc);
Nr=row/2-90;
for i=1:1:Nr;
    St(i,1:col)=SSc(i,1:col);
    Sb(i,1:col)=SSc(Nr-i+1,1:col);
end
SS=[St;Sb];
[row,col]=size(SS);
d=(col-row)/2;
SSS=SS(:,d:col-d-1);
dlmwrite('symm.txt', SSS, 'delimiter', '\t');
Srec=load('symm_speed.dat'); Sv=Srec(:,1); SI=Srec(:,2);
subplot(2,1,2), plot(Sv,SI); axis([-inf,inf,-inf,inf]);
grid
title('Speed distribution, after symmetrizing')
xlabel('Radius (pixel)'); ylabel('Intensity');

```

REFERENCES

- (1) Boyle, R. *The Sceptical Chymist*; University of Pennsylvania Library: <http://oldsite.library.upenn.edu/etext/collections/science/boyle/chymist/>; London, 1661.
- (2) Faraday, M. *Philosophical Transactions of the Royal Society of London* **1857**, *147*, 145.
- (3) Kantrowitz, A.; Grey, J. *Rev. Sci. Instr.* **1951**, *22*, 328.
- (4) Kistiakowsky, G. B.; Slichter, W. P. *Rev. Sci. Instr.* **1951**, - 22.
- (5) Bentley, P. G. *Nature* **1961**, *190*, 433.
- (6) Corradini, P. *J. Chem. Phys.* **1959**, *31*, 1676.
- (7) Bertrand, J. A.; Dollase, W. A.; Cotton, F. A. *Inorganic Chemistry* **1963**, *2*, 1166.
- (8) Castleman, A. W.; Bowen, K. H. *J. Phys. Chem.* **1996**, *100*, 12911.
- (9) Sanov, A.; Lineberger, W. C. *PhysChemComm* **2002**, *5*, 165.
- (10) Johnston, R. L. *Atomic and Molecular Clusters*; Taylor & Francis: New York, 2002.
- (11) Fehlner, T. P.; Halet, J.-F.; Saillard, J.-Y. *Molecular Clusters: A Bridge to Solid-State Chemistry*; Cambridge University Press: New York, 2007.
- (12) Kroto, H. W.; Heath, J. R.; O'Brien, S. C.; Curl, R. F.; Smalley, R. E. *Nature* **1985**, *318*, 163.
- (13) David, W. I. F.; Ibberson, R. M.; Matthewman, J. C.; Prassides, K.; Dennis, T. J. S.; Hare, J. P.; Kroto, H. W.; Taylor, R.; Walton, D. R. M. *Nature* **1991**, *353*, 147.
- (14) Shin, J. W.; Hammer, N. I.; Diken, E. G.; Johnson, M. A.; Walters, R. S.; Jaeger, T. D.; Duncan, M. A.; Christie, R. A.; Jordan, K. D. *Science* **2004**, *304*, 1137.
- (15) Armbruster, M.; Haberland, H.; Schindler, H. G. *Phys. Rev. Lett.* **1981**, *47*, 323.
- (16) Haberland, H.; Ludewigt, C.; Schindler, H. G.; Worsnop, D. R. *J. Chem. Phys.* **1984**, *81*, 3742.

- (17) Hammer, N. I.; Roscioli, J. R.; Johnson, M. A. *J. Phys. Chem. A* **2005**, *109*, 7896.
- (18) Barnett, R. N.; Landman, U.; Cleveland, C. L.; Jortner, J. *J. Chem. Phys.* **1988**, *88*, 4429.
- (19) Coe, J. V.; Lee, G. H.; Eaton, J. G.; Arnold, S. T.; Sarkas, H. W.; Bowen, K. H.; Ludewigt, C.; Haberland, H.; Worsnop, D. R. *J. Chem. Phys.* **1990**, *92*, 3980.
- (20) Bragg, A. E.; Verlet, J. R. R.; Kammrath, A.; Cheshnovsky, O.; Neumark, D. M. *Science* **2004**, *306*, 669.
- (21) Verlet, J. R. R.; Bragg, A. E.; Kammrath, A.; Cheshnovsky, O.; Neumark, D. M. *Science* **2005**, *307*, 93.
- (22) Turi, L.; Sheu, W. S.; Rossky, P. J. *Science* **2005**, *309*, 914.
- (23) Verlet, J. R. R.; Bragg, A. E.; Kammrath, A.; Cheshnovsky, O.; Neumark, D. M. *Science* **2005**, *310*.
- (24) Turi, L.; Sheu, W. S.; Rossky, P. J. *Science* **2005**, *310*.
- (25) Sommerfeld, T.; Jordan, K. D. *J. Am. Chem. Soc.* **2006**, *128*, 5828.
- (26) Surber, E.; Mabbs, R.; Habteyes, T.; Sanov, A. *J. Phys. Chem. A* **2005**, *109*, 4452.
- (27) Alexander, M. L.; Levinger, N. E.; Johnson, M. A.; Ray, D.; Lineberger, W. C. *J. Chem. Phys.* **1988**, *88*, 6200.
- (28) Papanikolas, J. M.; Gord, J. R.; Levinger, N. E.; Ray, D.; Vorsa, V.; Lineberger, W. C. *J. Phys. Chem.* **1991**, *95*, 8028.
- (29) Papanikolas, J. M.; Vorsa, V.; Nadal, M. E.; Campagnola, P. J.; Gord, J. R.; Lineberger, W. C. *J. Chem. Phys.* **1992**, *97*, 7002.
- (30) Papanikolas, J. M.; Vorsa, V.; Nadal, M. E.; Campagnola, P. J.; Buchenau, H. K.; Lineberger, W. C. *J. Chem. Phys.* **1993**, *99*, 8733.
- (31) Vorsa, V.; Nandi, S.; Campagnola, P. J.; Larsson, M.; Lineberger, W. C. *J. Chem. Phys.* **1997**, *106*, 1402.
- (32) Mabbs, R.; Surber, E.; Sanov, A. *Analyst* **2003**, *128*, 765.
- (33) Continetti, R. E. *Int. Rev. Phys. Chem.* **1998**, *17*, 227.

- (34) Bowen, M. S.; Becucci, M.; Continetti, R. E. *J. Chem. Phys.* **2006**, - 125.
- (35) Chandler, D. W.; Houston, P. L. *J. Chem. Phys.* **1987**, *87*, 1445.
- (36) Eppink, A. T. J. B.; Parker, D. H. *Rev. Sci. Instr.* **1997**, *68*, 3477.
- (37) Thoman, J. W.; Chandler, D. W.; Parker, D. H.; Janssen, M. H. M. *Laser Chemistry* **1988**, *9*, 27.
- (38) Chandler, D. W.; Thoman, J. W.; Janssen, M. H. M.; Parker, D. H. *Chem. Phys. Lett.* **1989**, *156*, 151.
- (39) Heck, A. J. R.; Chandler, D. W. *Ann. Rev. Phys. Chem.* **1995**, *46*, 335.
- (40) Houston, P. L. *J. Phys. Chem.* **1996**, *100*, 12757.
- (41) Helm, H.; Bjerre, N.; Dyer, M. J.; Huestis, D. L.; Saeed, M. *Phys. Rev. Lett.* **1993**, *70*, 3221.
- (42) Bordas, C.; Paulig, F.; Helm, H.; Huestis, D. L. *Rev. Sci. Instr.* **1996**, *67*, 2257.
- (43) Wang, L.; Kohguchi, H.; Suzuki, T. *Faraday Disc.* **1999**, *113*, 37.
- (44) Davies, J. A.; LeClaire, J. E.; Continetti, R. E.; Hayden, C. C. *J. Chem. Phys.* **1999**, *111*, 1.
- (45) Suzuki, T.; Wang, L.; Kohguchi, H. *J. Chem. Phys.* **1999**, *111*, 4859.
- (46) Suzuki, T.; Whitaker, B. J. *Int. Rev. Phys. Chem.* **2001**, *20*, 313.
- (47) Tsubouchi, M.; Whitaker, B. J.; Wang, L.; Kohguchi, H.; Suzuki, T. *Phys. Rev. Lett.* **2001**, *86*, 4500.
- (48) Baguenard, B.; Pinaré, J. C.; Bordas, C.; Broyer, M. *Phys. Rev. A* **2001**, *63*, 023204.
- (49) Baguenard, B.; Pinaré, J. C.; Lépine, F.; Bordas, C.; Broyer, M. *Chem. Phys. Lett.* **2002**, *352*, 147.
- (50) Surber, E.; Sanov, A. *J. Chem. Phys.* **2002**, *116*, 5921.
- (51) Li, W.; Huang, C. S.; Patel, M.; Wilson, D.; Suits, A. *J. Chem. Phys.* **2006**, *124*, 011102.

- (52) Ashfold, M. N. R.; Nahler, N. H.; Orr-Ewing, A. J.; Vieuxmaire, O. P. J.; Toomes, R. L.; Kitsopoulos, T. N.; Garcia, I. A.; Chestakov, D. A.; Wu, S. M.; Parker, D. H. *Phys. Chem. Chem. Phys.* **2006**, *8*, 26.
- (53) Townsend, D.; Lahankar, S. A.; Lee, S. K.; Chambreau, S. D.; Suits, A. G.; Zhang, X.; Rheinecker, J.; Harding, L. B.; Bowman, J. M. *Science* **2004**, *306*, 1158.
- (54) Townsend, D.; Li, W.; Lee, S. K.; Gross, R. L.; Suits, A. G. *J. Phys. Chem. A* **2005**, *109*, 8661.
- (55) Tsubouchi, M.; de Lange, C. A.; Suzuki, T. *J. Chem. Phys.* **2003**, *119*, 11728.
- (56) Tsubouchi, M.; de Lange, C. A.; Suzuki, T. *J. Electron Spectrosc. Relat. Phenom.* **2005**, *142*, 193.
- (57) Matsumoto, Y.; Kim, S. K.; Suzuki, T. *J. Chem. Phys.* **2003**, *119*, 300.
- (58) Kim, M. H.; Shen, L.; Suits, A. G. *Phys. Chem. Chem. Phys.* **2006**, *8*, 2933.
- (59) Shu, J. N.; Wilson, K. R.; Ahmed, M.; Leone, S. R. *Rev. Sci. Instr.* **2006**, *77*.
- (60) Wilson, K. R.; Peterka, D. S.; Jimenez-Cruz, M.; Leone, S. R.; Ahmed, M. *Phys. Chem. Chem. Phys.* **2006**, *8*, 1884.
- (61) Plenge, J.; Nicolas, C.; Caster, A. G.; Ahmed, M.; Leone, S. R. *J. Chem. Phys.* **2006**, *125*.
- (62) Nahon, L.; Garcia, G. A.; Harding, C. J.; Mikajlo, E.; Powis, I. *J. Chem. Phys.* **2006**, *125*.
- (63) Romanescu, C.; Loock, H. P. *Phys. Chem. Chem. Phys.* **2006**, *8*, 2940.
- (64) Velarde, L.; Habteyes, T.; Grumbling, E. R.; Pichugin, K.; Sanov, A. *J. Chem. Phys.* **2007**, *127*.
- (65) Davis, A. V.; Wester, R.; Bragg, A. E.; Neumark, D. M. *J. Chem. Phys.* **2003**, *118*, 999.
- (66) Rathbone, G. J.; Sanford, T.; Andrews, D.; Lineberger, W. C. *Chem. Phys. Lett.* **2005**, *401*, 570.
- (67) Sobhy, M. A.; Castleman, A. W. *J. Chem. Phys.* **2007**, *126*.
- (68) Mabbs, R.; Pichugin, K.; Sanov, A. *J. Chem. Phys.* **2005**, *122*, 174305.

- (69) Kammrath, A.; Griffin, G. B.; Verlet, J. R. R.; Young, R. M.; Neumark, D. M. *J. Chem. Phys.* **2007**, *126*.
- (70) Cavanagh, S. J.; Gibson, S. T.; Gale, M. N.; Dedman, C. J.; Roberts, E. H.; Lewis, B. R. *Phys. Rev. A* **2007**, *76*.
- (71) Sanov, A.; Mabbs, R. *Int. Rev. Phys. Chem.* **2008**, *27*, 53.
- (72) Garand, E.; Zhou, J.; Manolopoulos, D. E.; Alexander, M. H.; Neumark, D. M. *Science* **2008**, *319*, 72.
- (73) Engel, V.; Staemmler, V.; Vanderwal, R. L.; Crim, F. F.; Sension, R. J.; Hudson, B.; Andresen, P.; Hennig, S.; Weide, K.; Schinke, R. *J. Phys. Chem.* **1992**, *96*, 3201.
- (74) Weide, K.; Staemmler, V.; Schinke, R. *J. Chem. Phys.* **1990**, *93*, 861.
- (75) Heumann, B.; Duren, R.; Schinke, R. *Chem. Phys. Lett.* **1991**, *180*, 583.
- (76) Hennig, S.; Engel, V.; Schinke, R.; Nonella, M.; Huber, J. R. *J. Chem. Phys.* **1987**, *87*, 3522.
- (77) Schinke, R. *Photodissociation dynamics: spectroscopy and fragmentation of small polyatomic molecules*; Cambridge University Press: Cambridge, New York, 1993.
- (78) Surber, E. Ph.D. Dissertation, University of Arizona, 2005.
- (79) Wiley, W. C.; McLaren, I. H. *Rev. Sci. Instr.* **1955**, *26*, 1150.
- (80) Johnson, M. A.; Lineberger, W. C. Pulsed Methods for Cluster Ion Spectroscopy. In *Techniques for the Study of Ion Molecule Reactions*; Farrar, J. M., Saunders, W. H., Eds.; Wiley: New York, 1988; pp 591.
- (81) Harting, E.; Read, F. H. *Electrostatic Lenses*; Elsevier Scientific Publishing Company: Amsterdam - Oxford - New York, 1976.
- (82) Posey, L. A.; DeLuca, M. J.; Johnson, M. A. *Chem. Phys. Lett.* **1986**, *131*, 170.
- (83) Mamyrin, B. A.; Karataev, V. I.; Shmikk, D. V.; Zagulin, V. A. *Sov. Phys.-JEPT* **1973**, *37*, 45.
- (84) Bergmann, T.; Martin, T. P.; Schaber, H. *Rev. Sci. Instr.* **1989**, *60*, 792.
- (85) Beussman, D. J.; Vlasak, P. R.; McLane, R. D.; Seeterlin, M. A.; Enke, C. G. *Analytical Chemistry* **1995**, *67*, 3952.

- (86) Casares, A.; Kholomeev, A.; Wollnik, H. *Int. J. Mass Spectrom.* **2001**, *206*, 267.
- (87) Wollnik, H.; Casares, A. *Int. J. Mass Spectrom.* **2003**, *227*, 217.
- (88) Scherer, S.; Altwegg, K.; Balsiger, H.; Fischer, J.; Jackel, A.; Korth, A.; Mildner, M.; Piazza, D.; Reme, H.; Wurz, P. *Int. J. Mass Spectrom.* **2006**, *251*, 73.
- (89) Walter, K.; Boesl, U.; Schlag, E. W. *Int. J. Mass Spect. Ion Proc.* **1986**, *71*, 309.
- (90) Boesl, U.; Neusser, H. J.; Weinkauff, R.; Schlag, E. W. *J. Phys. Chem.* **1982**, *86*, 4857.
- (91) Echt, O.; Dao, P. D.; Morgan, S.; Castleman, A. W. *J. Chem. Phys.* **1985**, *82*, 4076.
- (92) Johnson, M. A.; Alexander, M. L.; Lineberger, W. C. *Chem. Phys. Lett.* **1984**, *112*, 285.
- (93) Bracewell, R. *The Fourier Transform and its Applications*; McGraw-Hill: New York, 1965.
- (94) Dribinski, V.; Ossadtchi, A.; Mandelshtam, V. A.; Reisler, H. *Rev. Sci. Instr.* **2002**, *73*, 2634.
- (95) Wigner, E. P. *Phys. Rev.* **1948**, *73*, 1002.
- (96) Arnot, F. L.; Beckett, C. *Proceedings of the Royal Society of London. Series A, Mathematical and Physical Sciences* **1938**, *168*, 103.
- (97) Ropp, G. A.; Melton, C. E. *J. Am. Chem. Soc.* **1958**, *80*, 3509.
- (98) Ovenall, D. W.; Whiffen, D. H. *Mol. Phys.* **1961**, *4*, 135.
- (99) Lunsford, J. H.; Jayne, J. P. *J. Phys. Chem.* **1965**, *69*, 2182.
- (100) Paulson, J. F. *J. Chem. Phys.* **1970**, *52*, 963.
- (101) Keene, J. P.; Raef, Y.; Swallow, A. J. Pulse Radiolysis Studies of Carboxyl and Related Radicals. In *Pulse Radiolysis*; Emert, M., Keene, J. P., Swallow, A. J., Eds.; Academic Press: London, New York, 1965; pp 99.
- (102) Neta, P.; Simic, M.; Hayon, E. *J. Phys. Chem.* **1969**, *73*, 4207.
- (103) Cooper, C. D.; Compton, R. N. *Chem. Phys. Lipids* **1972**, *14*, 29.

- (104) Schulz, G. J. *Phys. Rev.* **1962**, *128*, 178.
- (105) Boness, M. J. W.; Schulz, G. J. *Phys. Rev. A* **1974**, *9*, 1969.
- (106) Allan, M. J. *Phys. B* **2002**, *35*, L387.
- (107) Compton, R. N.; Reinhardt, P. W.; Cooper, C. D. *J. Chem. Phys.* **1975**, *63*, 3821.
- (108) Klots, C. E.; Compton, R. N. *J. Chem. Phys.* **1977**, *67*, 1779.
- (109) Klots, C. E. *J. Chem. Phys.* **1979**, *71*, 4172.
- (110) DeLuca, M. J.; Niu, B.; Johnson, M. A. *J. Chem. Phys.* **1988**, *88*, 5857.
- (111) Mabbs, R.; Surber, E.; Velarde, L.; Sanov, A. *J. Chem. Phys.* **2004**, *120*, 5148.
- (112) Tsukuda, T.; Johnson, M. A.; Nagata, T. *Chem. Phys. Lett.* **1997**, *268*, 429.
- (113) Haberland, H.; Ludewigt, C.; Schindler, H. G.; Worsnop, D. R. **1987**, *36*, 967.
- (114) Balaj, O. P.; Siu, C. K.; Balteanu, I.; Beyer, M. K.; Bondybey, V. E. *Chem-Eur J* **2004**, *10*, 4822.
- (115) Haberland, H.; Langosch, H.; Schindler, H. G.; Worsnop, D. R. *Journal of Physical Chemistry* **1984**, *88*, 3903.
- (116) Tsukuda, T.; Nagata, T. *J. Phys. Chem. A* **2003**, *107*, 8476.
- (117) Habteyes, T.; Velarde, L.; Sanov, A. *Chem. Phys. Lett.* **2006**, *424*, 268.
- (118) Claydon, C. R.; Segal, G. A.; Taylor, H. S. *J. Chem. Phys.* **1970**, *52*, 3387.
- (119) Krauss, M.; Neumann, D. *Chem. Phys. Lipids* **1972**, *14*, 26.
- (120) Sommerfeld, T. *J. Phys. B* **2003**, *36*, L127.
- (121) Sommerfeld, T.; Meyer, H. D.; Cederbaum, L. S. *Phys. Chem. Chem. Phys.* **2004**, *6*, 42.
- (122) Fredin, L.; Nelander, B.; Ribbegard, G. *Chemica Scripta* **1975**, *7*, 11.
- (123) Schriver, A.; Schriver-Mazzuoli, L.; Chaquin, P.; Dumont, E. *J. Phys. Chem. A* **2006**, *110*, 51.

- (124) Dyke, T. R.; Muentner, J. S. **1974**, *60*, 2929.
- (125) Pugliano, N.; Saykally, R. J. **1992**, *257*, 1937.
- (126) Sediki, A.; Lebsir, F.; Martiny, L.; Dauchez, M.; Krallafa, A. **2008**, *106*, 1476.
- (127) Falk, M.; Miller, A. G. *Vibrational Spectroscopy* **1992**, *4*, 105.
- (128) Peterson, K. I.; Klemperer, W. *J. Chem. Phys.* **1984**, *80*, 2439.
- (129) Peterson, K. I.; Suenram, R. D.; Lovas, F. J. *J. Chem. Phys.* **1991**, *94*, 106.
- (130) Tso, T. L.; Lee, E. K. C. *J. Phys. Chem.* **1985**, *89*, 1612.
- (131) Jonsson, B.; Karlstrom, G.; Wennerstrom, H. *Chem. Phys. Lett.* **1975**, *30*, 58.
- (132) Block, P. A.; Marshall, M. D.; Pedersen, L. G.; Miller, R. E. *J. Chem. Phys.* **1992**, *96*, 7321.
- (133) Sadlej, J.; Makarewicz, J.; Chalasinski, G. *J. Chem. Phys.* **1998**, *109*, 3919.
- (134) Makarewicz, J.; Ha, T. K.; Bauder, A. *J. Chem. Phys.* **1993**, *99*, 3694.
- (135) Bowen, K. H.; Eaton, J. G. Photodetachment Spectroscopy of Negative Cluster Ions. In *The Structure of Small Molecules and Ions*; Naaman, R., Vager, Z., Eds.; Plenum: New York, 1988; pp 147.
- (136) Surber, E.; Ananthavel, S. P.; Sanov, A. *J. Chem. Phys.* **2002**, *116*, 1920.
- (137) *CRC Handbook of Chemistry and Physics*, 84 ed.; CRC Press: Boca Raton, Florida, 2004.
- (138) Seta, T.; Yamamoto, M.; Nishioka, M.; Sadakata, M. *J. Phys. Chem. A* **2003**, *107*, 962.
- (139) Chantry, G. W.; Whiffen, D. H. *Mol. Phys.* **1962**, *5*, 189.
- (140) Hartman, K. O.; Hisatsune, I. C. *J. Chem. Phys.* **1966**, *44*, 1913.
- (141) Pacansky, J.; Wahlgren, U.; Bagus, P. S. *J. Chem. Phys.* **1975**, *62*, 2740.
- (142) Hopper, D. G. *Chem. Phys.* **1980**, *53*, 85.
- (143) England, W. B. *Chem. Phys. Lett.* **1981**, *78*, 607.

- (144) Rescigno, T. N.; Isaacs, W. A.; Orel, A. E.; Meyer, H. D.; McCurdy, C. W. *Phys. Rev. A* **2002**, *65*, 032716.
- (145) McCurdy, C. W.; Isaacs, W. A.; Meyer, H. D.; Rescigno, T. N. *Phys. Rev. A* **2003**, *67*, 042708.
- (146) Gillispie, G. D.; Khan, A. U. *J. Chem. Phys.* **1976**, *65*, 1624.
- (147) Kurkal, V.; Fleurat-Lessard, P.; Schinke, R. *J. Chem. Phys.* **2003**, *119*, 1489.
- (148) Jackels, C. F.; Davidson, E. R. *J. Chem. Phys.* **1976**, *65*, 2941.
- (149) Blahous, C. P.; Yates, B. F.; Xie, Y. M.; Schaefer, H. F. *J. Chem. Phys.* **1990**, *93*, 8105.
- (150) Alexander, M. L.; Johnson, M. A.; Levinger, N. E.; Lineberger, W. C. *Phys. Rev. Lett.* **1986**, *57*, 976.
- (151) Fleischman, S. H.; Jordan, K. D. *J. Phys. Chem.* **1987**, *91*, 1300.
- (152) Vorsa, V. Photodissociation Dynamics of Mass-Selected Anions and Anionic Clusters. Ph.D. Thesis, University of Colorado, 1996.
- (153) Velarde, L.; Habteyes, T.; Sanov, A. *J. Chem. Phys.* **2006**, *125*, 114303.
- (154) Oakes, J. M.; Ellison, G. B. *Tetrahedron* **1986**, *42*, 6263.
- (155) Battaglia, M. R.; Buckingham, A. D.; Neumark, D.; Pierens, R. K.; Williams, J. H. *Mol. Phys.* **1981**, *43*, 1015.
- (156) Kalamarides, A.; Walter, C. W.; Smith, K. A.; Dunning, F. B. **1988**, *89*, 7226.
- (157) Suess, L.; Parthasarathy, R.; Dunning, F. B. **2003**, *372*, 692.
- (158) Hiraoka, K.; Fujimaki, S.; Aruga, G.; Yamabe, S. *J. Phys. Chem.* **1994**, *98*, 1802.
- (159) Tsukuda, T.; Hirose, T.; Nagata, T. *Chem. Phys. Lett.* **1997**, *279*, 179.
- (160) Maeyama, T.; Oikawa, T.; Tsumura, T.; Mikami, N. *J. Chem. Phys.* **1998**, *108*, 1368.
- (161) Mabbs, R.; Surber, E.; Sanov, A. *Chem. Phys. Lett.* **2003**, *381*, 479.
- (162) Yu, L. A.; Zeng, A. H.; Xu, Q. A.; Zhou, M. F. *J. Phys. Chem. A* **2004**, *108*, 8264.

- (163) Sanov, A.; Lineberger, W. C.; Jordan, K. D. *J. Phys. Chem. A* **1998**, *102*, 2509.
- (164) Zhang, S. W.; Zhang, C. G.; Yu, Y. T.; Mao, B. Z.; He, F. C. *Chem. Phys. Lett.* **1999**, *304*, 265.
- (165) Frisch, M. J. *et al.* Gaussian 03; Rev. B.01 ed.; Gaussian, Inc.: Wallingford CT, 2004.
- (166) Gutsev, G. L.; Bartlett, R. J.; Compton, R. N. *J. Chem. Phys.* **1998**, *108*, 6756.
- (167) Habteyes, T.; Velarde, L.; Sanov, A. *J. Chem. Phys.* **2007**, *126*.
- (168) Koizumi, S.; Yasumatsu, H.; Otani, S.; Kondow, T. *J. Phys. Chem. A* **2002**, *106*, 267.
- (169) Matsuyama, Y.; Nagata, T. *Chem. Phys. Lett.* **in Press**.
- (170) Surber, E.; Mabbs, R.; Sanov, A. *J. Phys. Chem. A* **2003**, *107*, 8215.
- (171) Keesee, R. G.; Castleman, A. W. *J. Phys. Chem. Ref. Data.* **1986**, *15*, 1011.
- (172) Vandoren, J. M.; Barlow, S. E.; Depuy, C. H.; Bierbaum, V. M. *Int. J. Mass Spect. Ion Proc.* **1991**, *109*, 305.
- (173) Lee, H. S.; Bierbaum, V. M. **1994**, *101*, 9513.
- (174) Habteyes, T.; Velarde, L.; Sanov, A. *J. Phys. Chem. A* **2008**.
- (175) Habteyes, T. Ph. D. dissertation. Ph.D., University of Arizona, 2008.
- (176) Ervin, K. M.; Anusiewicz, W.; Skurski, P.; Simons, J.; Lineberger, W. C. *J. Phys. Chem. A* **2003**, *107*, 8521.
- (177) Myerson, A. L.; Taylor, F. R. *J. Am. Chem. Soc.* **1953**, *75*, 4348.
- (178) Howgate, D. W.; Barr, T. A. *J. Chem. Phys.* **1973**, *59*, 2815.
- (179) Homann, K. H.; Krome, G.; Wagner, H. G. *Berichte Der Bunsen-Gesellschaft Fur Physikalische Chemie* **1970**, *74*, 654.
- (180) Wright, F. J. *J. Phys. Chem.* **1960**, *64*, 1648.
- (181) Sheen, D. B. *J. Chem. Phys.* **1970**, *52*, 648.

- (182) Wood, W. P.; Heicklen, J. *J. Phys. Chem.* **1971**, *75*, 854.
- (183) Wood, W. P.; Heicklen, J. *J. Phys. Chem.* **1971**, *75*, 861.
- (184) Graham, R. E.; Gutman, D. *J. Phys. Chem. A* **1977**, *81*, 207.
- (185) Murakami, Y.; Kosugi, M.; Susa, K.; Kobayashi, T.; Fujii, N. *Bull. Chem. Soc. Jpn.* **2001**, *74*, 1233.
- (186) Azatyan, V. V. *Kinetics and Catalysis* **2003**, *44*, 459.
- (187) Suart, R. D.; Dawson, P. H.; Kimbell, G. H. *J. Appl. Phys.* **1972**, *43*, 1022.
- (188) Babarogic, Z.; Konjevic, N.; Trtica, M. *Rev. Sci. Instr.* **1980**, *51*, 658.
- (189) Dudkin, V. A. *Journal of Russian Laser Research* **1999**, *20*, 362.
- (190) Chemistry WebBook; NIST Standard Reference Database Number 69, June 2005 Release ed.
- (191) Arnold, D. W.; Cangshan, X.; Kim, E. H.; Neumark, D. M. *J. Chem. Phys.* **1994**, *101*, 912.
- (192) Polak, M. L.; Fiala, B. L.; Ervin, K. M.; Lineberger, W. C. *J. Chem. Phys.* **1991**, *94*, 6926.
- (193) Huber, K. P.; Herzberg, G. *Constants of Diatomic Molecules*; Van Nostrand Reinhold Company: New York, NY, 1979.
- (194) Yamada, C.; Kawaguchi, K.; Hirota, E. *J. Chem. Phys.* **1978**, *69*, 1942.
- (195) Cooper, J.; Zare, R. N. *J. Chem. Phys.* **1968**, *48*, 942.
- (196) Hanstorp, D.; Bengtsson, C.; Larson, D. J. *Phys. Rev. A* **1989**, *40*, 670.
- (197) Akin, F. A.; Schirra, L. K.; Sanov, A. *J. Phys. Chem. A* **2006**, *110*, 8031.
- (198) Moran, S.; Ellison, G. B. *J. Phys. Chem* **1988**, *92*, 1794.
- (199) Nimlos, M. R.; Ellison, G. B. *J. Phys. Chem. A* **1986**, *90*, 2574.
- (200) Herzberg, G. *Molecular Spectra and Molecular Structure III. Electronic Spectra and Structure of Polyatomic Molecules*; Van Norstrand: Princeton, NJ, 1967.

- (201) Dobrin, S.; Boo, B. H.; Alconcel, L. S.; Continetti, R. E. *J. Phys. Chem. A* **2000**, *104*, 10695.
- (202) Muller, T.; Vaccaro, P. H.; Perez-Bernal, F.; Iachello, F. *J. Chem. Phys.* **1999**, *111*, 5038.
- (203) Zhang, X. Y.; Wu, J.; Cui, Z. F. *Chem. Phys. Lett.* **2006**, *428*, 1.
- (204) Sulzle, D.; Egsgaard, H.; Carlsen, L.; Schwarz, H. **1990**, *112*, 3750.
- (205) Hiraoka, K.; Fujimaki, S.; Aruga, K.; Yamabe, S. *J. Phys. Chem.* **1994**, *98*, 8295.
- (206) Shao, L. M.; Chen, M. H.; Zhou, M. F. *Journal of Molecular Structure-Theochem* **2001**, *542*, 57.
- (207) Arnold, F.; Kissel, J.; Krankowsky, D.; Wieder, H.; Zahringer, J. *Journal of Atmospheric and Terrestrial Physics* **1971**, *33*, 1170.
- (208) Narcisi, R. S.; Bailey, A. D.; Lucca, L. D.; Sherman, C.; Thomas, D. M. *Journal of Atmospheric and Terrestrial Physics* **1971**, *33*, 1159.
- (209) Viggiano, A. A.; Hunton, D. E. *Journal of Mass Spectrometry* **1999**, *34*, 1107.
- (210) Arnold, S. T.; Morris, R. A.; Viggiano, A. A. *J. Chem. Phys.* **1995**, - 103.
- (211) Mohler, O.; Arnold, F. *Journal of Atmospheric Chemistry* **1991**, *13*, 33.
- (212) Chantry, G. W.; Horsfield, A.; Morton, J. R.; Whiffen, D. H. *Mol. Phys.* **1962**, *5*, 589.
- (213) Moll, N. G.; Clutter, D. R.; Thompson, W. E. *J. Chem. Phys.* **1966**, *45*, 4469.
- (214) Serway, R. A.; Marshall, S. A. *J. Chem. Phys.* **1967**, *47*, 868.
- (215) Olsen, J. F.; Burnelle, L. *J. Am. Chem. Soc.* **1970**, *92*, 3659.
- (216) Burt, J. A. *J. Chem. Phys.* **1972**, *57*, 4649.
- (217) Burt, J. A. *J. Chem. Phys.* **1973**, *59*, 1567.
- (218) Jacox, M. E.; Milligan, D. E. *J. Mol. Spectrosc.* **1974**, *52*, 363.
- (219) Moseley, J. T.; Bennett, R. A.; Peterson, J. R. *Chem. Phys. Lett.* **1974**, *26*, 288.

- (220) Cosby, P. C.; Moseley, J. T. *Phys. Rev. Lett.* **1975**, *34*, 1603.
- (221) Moseley, J. T.; Cosby, P. C.; Peterson, J. R. *J. Chem. Phys.* **1976**, *65*, 2512.
- (222) Beyer, R. A.; Vanderhoff, J. A. *J. Chem. Phys.* **1976**, *65*, 2313.
- (223) So, S. P. *Journal of The Chemical Society-Faraday Transactions II* **1976**, *72*, 646.
- (224) Dotan, I.; Davidson, J. A.; Streit, G. E.; Albritton, D. L.; Fehsenfeld, F. C. *J. Chem. Phys.* **1977**, *67*, 2874.
- (225) Hong, S. P.; Woo, S. B.; Helmy, E. M. *Phys. Rev. A* **1977**, *15*, 1563.
- (226) Vestal, M. L.; Mauclaire, G. H. *J. Chem. Phys.* **1977**, *67*, 3758.
- (227) Hiller, J. F.; Vestal, M. L. *J. Chem. Phys.* **1980**, *72*, 4713.
- (228) Hunton, D. E.; Hofmann, M.; Lindeman, T. G.; Castleman Jr., A. W. *J. Chem. Phys.* **1985**, *82*, 134.
- (229) Snodgrass, J. T.; Roehl, C. M.; Vankoppen, P. A. M.; Palke, W. E.; Bowers, M. T. *J. Chem. Phys.* **1990**, *92*, 5935.
- (230) Bopp, J. C.; Diken, E. G.; Headrick, J. M.; Roscioli, J. R.; Johnson, M. A. *J. Chem. Phys.* **2006**, *124*.
- (231) Cappa, C. D.; Elrod, M. J. *Phys. Chem. Chem. Phys.* **2001**, *3*, 2986.
- (232) Moseley, J. T. In *Photodissociation and photoionization* Lawley, K. P., Ed.; Wiley: New York, 1985; pp pp. 290.
- (233) Mabbs, R.; Pichugin, K.; Surber, E.; Sanov, A. *Virt. J. Ultrafast Sci.* **2004**, *3*.
- (234) Mabbs, R.; Pichugin, K.; Surber, E.; Sanov, A. *J. Chem. Phys.* **2004**, *121*, 265.
- (235) Lim, J. S. *Two-Dimensional Signal and Image Processing*, 1989.
- (236) Gonzalez, R. C.; Woods, R. E.; Eddins, S. L. *Digital Image Processing Using MATLAB*, 1st ed., 2003.
- (237) Teuber, J. *Digital Image Processing*, 1993.